DROPLETS AS MODEL SYSTEMS FOR INVESTIGATING 2D CRYSTALS, GLASSES AND THE GROWTH DYNAMICS OF GRANULAR AGGREGATES

DROPLETS AS MODEL SYSTEMS FOR INVESTIGATING 2D CRYSTALS, GLASSES AND THE GROWTH DYNAMICS OF GRANULAR AGGREGATES

By

JEAN-CHRISTOPHE ONO-DIT-BIOT, B.Sc., M.Sc.

A Thesis
Submitted to the School of Graduate Studies
in Partial Fulfillment of the Requirements
for the Degree
Doctor of Philosophy

McMaster University

DOCTOR OF PHILOSOPHY (2021) McMaster University
(Physics) Hamilton, Ontario

TITLE: Droplets as model systems for investigating 2D crystals, glasses and the growth dynamics of granular aggregates

AUTHOR: Jean-Christophe Ono-dit-Biot, B.Sc., M.Sc.(McMaster University)

SUPERVISOR: Dr. Kari Dalnoki-Veress

NUMBER OF PAGES: x, 143

Abstract

The research presented in this thesis focusses on the experimental study of two fundamental questions: the crystal-to-glass transition and how aggregates of adhesive droplets spread on a surface. Aggregates made of lightly adhesive oil droplets are used as models for crystals or amorphous glasses. The force applied on the aggregates can be directly measured as they are compressed.

A large portion of the work focusses on the crystal-to-glass transition and tries to answer the following question: how many defects are needed in a crystal for its mechanical response to be like a glass? To answer this question, the mechanical response of a perfect mono-crystal is measured. It is found that crystals deform elastically until they fail catastrophically in a single event once the force exceeds a critical value: the yield stress. The force measured during the compression of a crystal shows a well defined number of peaks which only depends on the initial geometry of the aggregate. As defects are added (the amount of disorder increased) the number of peaks in the force measurement increases rapidly before it saturates at a value obtained for model glasses. The magnitude of the force peaks also decreases as disorder is introduced. This work concludes that even a small amount of disorder in a crystal has a significant impact on its mechanical properties.

In the second project, the spreading of a monodisperse aggregate of oil droplets is studied. Droplets are added one-by-one to a growing aggregate and the area covered on the interface is measured. It is found that after an initial 3D growth, the height of the aggregate saturates and the growth only happens in 2D along the horizontal direction. The growth is analogous to a puddle of liquid. In analogy with the capillary length in liquids, the "granular capillary length" is introduced to characterize the balance between buoyancy acting on the droplets and the adhesion strength. The height of the aggregates, in the later stage of the growth, is set by this length scale. A method was developed to characterize the adhesion between two droplets, a key parameter in this experiment, as a function of the relevant experimental parameters.

Preface

This is a "sandwich" thesis based on the papers published during my Ph. D. The first chapter is an introduction which covers the key concepts needed to understand the research presented in this thesis. Chapter 2 provides experimental details and describes the different data analysis methods. This chapter comes in addition to the description of the experiments provided in each paper and is particularly relevant to someone wanting to replicate the experiments or techniques used in the different projects. Chapter 3 is a collection of the main papers of this thesis. Each paper is introduced by a short summary of the research and key results as well as the contributions of each author. The last chapter summarizes the most important results and conclusions from the three studies presented. Potential follow-up projects or directions are briefly discussed. Finally, a list of additional papers I have been involved with is provided in the Appendix. These papers are not part of the main thesis either because I am not the main contributor or the subject is tangential to the main theme of this thesis.

Acknowledgements

As I am writing this paragraph it has been, almost exactly, six years that I boarded a plane to Canada. At this time, I had only committed to a MSc but it quickly became clear that this would turn into a Ph. D. Reflecting back, I can confidently say that this was the best decision I have ever made. I have learnt so much in the last years, both on a personal level and about soft matter physics, and I have several people to thank for helping me get to where I am today.

First and foremost, thank you Kari for being such an amazing supervisor and mentor. I will forever remember your first lecture at the ESPCI, even if I had no idea what was coming next, and our skype meeting where you convinced me to join your group. Your love for physics is what struck me instantly and I do not think I have ever met anybody who gets so excited about simple things like silly-putty, spaghettis, sand or oil droplets. Your advice in the lab, but also outside the field of physics, is always valuable and has helped me countless times. I could not be happier to be able to continue working with you but most importantly having you as a friend.

I would also like to thank An-Chang and James for being on my committee and for all the discussions we had on the different projects. I also had the chance to work with multiple collaborators: Cécile, Elie, Eric Lauga, Eric Weeks and Tom. Thank you for your valuable advice.

My next thanks go to all the grad students in the KDV lab for making everyday in the lab enjoyable: Paul, Raffi, John, Carmen, Adam, Ben, Clementine, Johnathan, Hamza, Lauren and Sara. Special thanks to Ben and Raffi for being great squash partners and John for the countless coffee walks. I was lucky to work with talented undergraduate students that are responsible for some of the work presented here.

My family has always supported my decision even when this meant flying overseas for my studies. Thank you for teaching me these values of hard work and helping me become who I am today.

Last but not least, my partner Flo who joined me in this journey with no doubts. I cannot express how grateful I am to have you by my side. I can always count on your support, you have listened to countless practice talks and we have been on many adventures to discover Canada. I simply could not have done this without you. You and I make a great team and I cannot wait to see what the future brings.

Contents

Abstract . . . iii
Preface . . . iv
Acknowledgements . . . v

1 Introduction **1**
- 1.1 Suspensions . . . 2
  - 1.1.1 Emulsions . . . 5
  - 1.1.2 Colloids . . . 6
  - 1.1.3 Foams . . . 6
- 1.2 Interactions in solution . . . 7
  - 1.2.1 Hard spheres . . . 8
  - 1.2.2 Soft spheres . . . 8
  - 1.2.3 Van der Waals . . . 9
  - 1.2.4 Depletion interaction . . . 10
  - 1.2.5 Double layer repulsion . . . 10
- 1.3 Granular materials . . . 13
  - 1.3.1 Angle of repose . . . 13
- 1.4 Liquids and surface tension . . . 16
  - 1.4.1 The Laplace pressure . . . 18
  - 1.4.2 The capillary length . . . 19
  - 1.4.3 Liquid on a surface . . . 20
  - 1.4.4 Measuring the surface tension . . . 23
- 1.5 Properties of suspensions . . . 25

1.5.1 Jamming . . . 26
1.5.2 Yield stress materials . . . 28
1.5.3 Force network . . . 29
1.5.4 Dynamical heterogeneities . . . 30
1.5.5 Ageing . . . 31
1.6 Suspensions as model systems . . . 31
1.6.1 Geological model . . . 32
1.6.2 Biology . . . 33
1.6.3 Glass transition . . . 34
1.6.4 Crystal-to-glass transition . . . 36
1.7 Liquid-like properties in collections of particles . . . 38

2 Experimental Details 41
2.1 Experimental chambers . . . 41
2.1.1 Aqueous solutions . . . 43
2.1.2 Micropipettes . . . 44
2.2 Production of droplets and aggregates . . . 49
2.2.1 Snap-off technique . . . 50
2.2.2 Assembly of crystals and bi-disperse aggregates . . . 51
2.3 Image analysis . . . 51
2.3.1 Force measurement . . . 52
2.3.2 Area measurement . . . 56

3 Papers 59
Paper I . . . 60
Paper II . . . 71
Paper III . . . 85

4 Conclusions 93

5 Appendix A 99
Paper AI . . . 100
Paper AII . . . 116

List of Figures

1.1 Phase separation of oil and vinegar emulsion 4
1.2 Depletion interaction between colloids 10
1.3 Double layer repulsion in aqueous solution between colloids 12
1.4 Free body diagram of a block on an incline 14
1.5 Potential energy between molecules in a liquid and origin of the surface tension 17
1.6 Origin of the Laplace pressure 18
1.7 Partial wetting of a liquid on a solid surface 20
1.8 Geometry of a puddle of liquid on a solid 21
1.9 Pendant drop experiment to measure the surface tension of a liquid . 24

2.1 3D schematics of the experimental chamber 42
2.2 Schematics of the experimental chamber used for the aggregate compression experiments 45
2.3 Accordion pipette geometry 46
2.4 Pushing pipette geometry 47
2.5 Experimental chamber used for measure of the adhesion between droplets and chronograph of the experiment 48
2.6 Different geometries and composition for the oil droplet aggregates . . 51
2.7 Illustration of the crosscorrelation technique used to measure the pipette deflection or displacement 54
2.8 Pipette calibration using the water droplet technique 55

2.9 Pipette calibration using a pipette of known spring constant 56
2.10 Image analysis process to measure the area covered by the oil droplet aggregates 57

4.1 Hexagonal packing of oil droplets confined on a curved interface . . . 96

Chapter 1

Introduction

From shaving foam or whipped cream to salad dressing or even paint, suspensions of particles into a continuous phase are familiar to all. Even though these examples do not seem to have a lot in common, they all belong to the family of suspensions: small particles of a substance A dispersed into a continuous phase B [1]. Industrial applications for suspensions are endless: ranging from the food industry [2,3] to high-tech applications such as the formulation of vaccines [4] or enhanced oil recovery [5]. In addition to being widely used in industry, suspensions have been proven to be particularly accurate models for real materials. Among other fundamental questions, colloidal suspensions have helped better understand the glass transition [6], droplets are used as models to study the cell-cell adhesion [7] and bubble rafts are used as models for metallic glasses [8].

Suspensions also offer a platform to study the connection between microscopic properties, such as the arrangement of particles, and the macroscopic consequences, such as the elastic properties of aggregates or how the collection of particles spreads on a surface. As discussed later in this thesis, the particles constituting the suspension can be imaged with multiple techniques, including optical microscopy [6]. The microscopic structure can thus be imaged over time and particles tracked individually as they deform or move [9]. Finally the forces between particles can be quantitatively measured experimentally [10, 11]. Being able to link all these local properties to the response of the global suspension to external stress, further improves our fundamental understanding of elastic and plastic properties of molecular materials.

The main purpose of this thesis is to present how we have used suspensions of oil droplets as model systems to study: i) the crystal-to-glass transition using the mechanical properties of aggregates with various amounts of disorder; and ii) the spreading of an aggregate of adhesive oil droplets on an interface.

This Chapter provides the necessary background to fully understand the research conducted during my Ph. D. This includes the key concepts and mathematical models used in the research but also the review of characteristic properties of suspensions. I first discuss the different types of suspensions that exist and their specificities (Section 1.1), including the different stabilization techniques of such particles which would aggregate or merge otherwise. Section 1.2 describes the interactions between particles in solution and the mathematical models used to describe such interactions. Properties of granular materials, a collection of grains such as rice or sand, are discussed in Section 1.3. The focus is on the role that inter-particle friction plays in the shape of piles of grains and the consequences of removing friction between grains on the structure of the aggregates. Section 1.4 provides the essential concepts and equations needed to understand the wetting and the spreading of a liquid on a surface. In Section 1.5, characteristic properties of suspensions or granular materials and their implications are reviewed. As discussed in the first paragraph, suspensions are widely used as model systems, Section 1.6 gives examples of various fields in which suspensions are used. This section also gives more details regarding the question of the glass transition which has extensively been studied using suspensions. Several studies on the crystal-to-glass transition are discussed to give the reader the necessary background for Paper I and II. Finally, in Section 1.7, various examples of liquid-like properties observed in suspensions and granular materials, such as instabilities or capillary waves, are discussed. This last section gives some context to the research described in Paper III.

1.1 Suspensions

Suspension is a generic term which describes a mixture of small particles of a substance A into a continuous phase B [1]. Particle size ranges from a couple of nanometers up to a couple of millimetres. Here, we are particularly interested in particles dispersed in a liquid. Different names are given to suspensions depending on the nature of the dispersed phase. Solid particles in liquids are referred to as colloids. As discussed in Section 1.3, the term colloid typically refer to particles smaller than 1 μm. An example is paint which is a suspension of solid particles in a liquid. If the particles are liquid droplets, the suspension is called an emulsion. A typical emulsion is salad dressing where droplets of vinegar or lemon juice are dispersed in oil. Foams are a suspension of air bubbles in a liquid, for example shaving foam.

Suspensions have generated a lot of interest for both fundamental research and industrial applications. For example, colloidal gels have been used as model for geological flows [12], emulsions are commonly used to model biological systems [7, 13] and also to study more fundamental phenomena such as the glass transition or the transition from a crystal to a glass. A detailed discussion on the role of suspensions in fundamental research, and how suspensions are used as model systems, is conducted in Section 1.6. Suspensions are also commonly used in industrial applications. For example, silica particles or carbon black are typically added to elastomers to make tires. The addition of these particles, called fillers, can improve the mechanical properties of the rubber for a given application [14, 15]. Most cosmetic products consist of two or more phases mixed together with a stabilizer, typically called emulsifier, to create an emulsion [16, 17]. Emulsions and nanoparticles are used in various medical applications such as vehicles for drugs [18] or vaccine delivery [4].

The size of the particles and in particular their size distribution is one of the principle characteristics of a suspension as it has important consequences on their properties. If the particles all have the same size, the suspension is said to be monodisperse. If particles all have different sizes, the suspension is polydisperse. The size distribution of the particles can be characterized by the coefficient of variance CV defined as the ratio between the standard deviation in the particle radii and the mean value of the radius [19]. Polydispersity has been shown to prevent colloidal glasses from crystallizing [20, 21].

Finally, suspensions always create a large interface between two immiscible phases. If nothing is done to stabilize a suspension, particles will typically aggregate or coalescence, in the case of liquid droplets and air bubbles, to minimize the interface. Taking a closer look at the example of vinegar droplets dispersed in oil and its evolution over

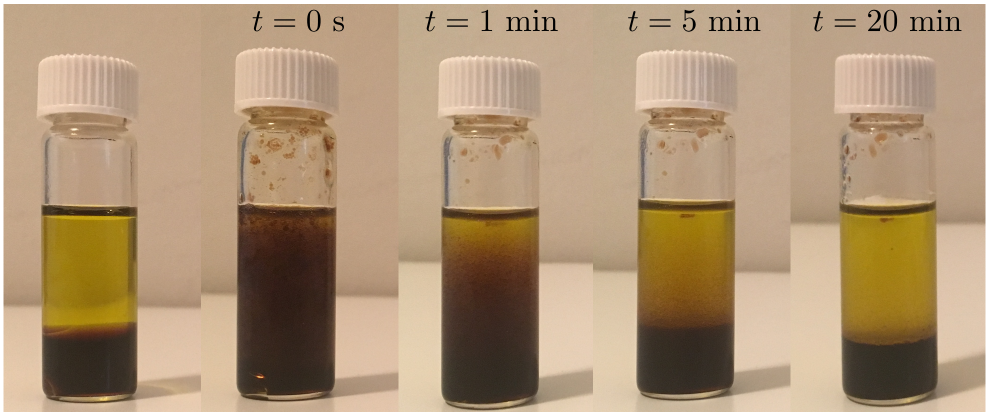

Figure 1.1: Mixture of oil and balsamic vinegar (salad dressing). The left picture shows the two phases separate. Time is taken to be 0 s just after shaking, second picture from the left. The solution looks cloudy as droplets of vinegar are suspended in oil. If the solution is let to rest (from left to right), the two phases separate to return to their original state: two phases on top of one another.

time, shown in Fig. 1.1, provides insight into this mechanism. Just after shaking, vinegar, black, droplets are dispersed in oil, yellow and the solution appears cloudy. If the mixture is let to rest for a couple minutes, vinegar droplets coalesce and eventually the mixture returns to its original state with two distinct phases. The mixture phase separates due to the large energy cost of maintaining the interface between two phases which is not favourable. In section 1.4, interfacial tension phenomena are discussed in detail for liquids, but any interface between two phases comes with an energy cost per unit area. The lowest energy state corresponds to the smallest area of contact. For a given volume, this always corresponds to two separate phases: A rich and B rich. Breaking up phase A in many small droplets results in a larger total surface area. Let us consider a droplet of oil with radius 1 cm dispersed into 10^9 micro-droplets of radius 10 μm. The total volume remains constant but the surface area of contact between the two phases is increased by a factor of 10^3 and is of the order of 1 m^2. Since the energy cost is directly proportional to the surface area, the cost of keeping the micro-droplets suspended is a thousand times larger than having two separate phases. It is also particularly interesting to realize that dispersing a droplet with a radius of 1 cm in 10-micron particles results in a total surface area of 1 m^2. Due to the large energy cost, oil droplets spontaneously coalesce to form larger and larger droplets until the mixture phase separates into two volumes with minimal contact. The same argument could be carried with colloidal suspensions or foams. Different techniques are used to stabilize suspensions and prevent phase separation. In the following paragraphs, we take a closer look at the different suspensions in liquids and ways to obtain stable suspensions.

1.1.1 Emulsions

Emulsions are the dispersion of a liquid phase into another liquid. Common examples of emulsions are salad dressing, mayonnaise or milk. While salad dressing simply made of vinegar and oil phase separates rapidly (see Fig. 1.1), mayonnaise, which is also an emulsion of water in oil, is stable. Mayonnaise is not strictly a mixture of water and oil, proteins contained in the egg yolk stabilize the water droplets suspended in oil. Another common example is milk: a suspension of fat in water. Again the proteins in the milk stabilize the emulsion. The proteins effectively decrease the interfacial tension between both liquids, reducing the energy cost of maintaining such a large interfacial area.

This stabilization can be reproduced in the laboratory by adding molecules called surfactants to an emulsion. These molecules typically have a long carbonated backbone and a polar head. The carbonated backbone is hydrophobic, does not mix in water, and will mix in the oily phase. The polar head is hydrophilic and will stay in the aqueous phase. As a result, these molecules will migrate to the interface so each part of the molecule mixes with its preferred phase. As in the case of stabilizing proteins, the surfactant reduces the interfacial tension between both phases and thus the energy cost of maintaining the interface is reduced [22]. Examples of commonly used surfactants are Sodium Dodecyl Sulfate (SDS) or cetrimonium bromide (CTAB). All experiments discussed in this thesis use emulsions of oil in water, stabilized using SDS. Emulsions can also be sterically stabilized using solid particles adsorbing at the interface and forming a shell around the droplets [23–26]. This type of emulsion is called a pickering emulsion.

Emulsions can be produced by mechanically mixing phases A and B together in presence of a stabilization agent [27]. More sophisticated methods have been developed to control the size of the droplets. In particular, with the emergence of microfluidic devices, multiple methods and geometries have been developed to produce large quantities of droplets which size can be controlled [28–30]. The droplets used in the experiments presented in this thesis are produced using the snap-off instability [19] as discussed in section 2.2.1.

1.1.2 Colloids

Colloids are solid particles suspended in a liquid. Colloidal particles are found in paint for example, or in tires, to modify the mechanical properties of the elastomers. They can be made of inorganic material such as silica or carbon black particles (used in tires) or polymers such as polystyrene (PS) or poly(methyl methacrylate) (PMMA). The polymer particles are commercially available and come with precise sizes and size distributions. Colloids typically have a size under 1 μm and the particles are subject to Brownian motion.

Colloidal particles are attracted to one another due to van der Waals forces (see section 1.2.3 for details). As colloids come close to one another they stick together in a process called aggregation to reduce their total surface area [31]. Van der Waals forces are particularly strong if the colloids are in close contact but drop significantly with distance. Two strategies can be used to prevent aggregation in colloids: electrostatic stabilization and steric stabilization [31]. The electrostatic stabilization can only be used if the surface of the particles is charged and depends on the composition of the liquids. More details regarding the interaction between charged particles are given in section 1.2.5. The steric stabilization of colloids consists in grafting long polymer chains to the surface. As particles come closer, the polymer chains interact and are confined in a small volume. This confinement reduces the entropy of the chains which results in repulsive forces between the colloids. Due to the polymer chains, particles cannot come into close contact reducing the aggregation due to van der Waals forces. PMMA particles are commonly grafted with poly-(12 hydroxystearic acid) and used as model for particles interacting as hard spheres [6, 32, 33].

1.1.3 Foams

Foams are bubbles of gas in a liquid phase. A typical example is the foam that forms at the surface of a carbonated drink as bubbles rise to the top of the glass due to buoyancy. Foams are also widely used in the food industry [2,3]. In fact, the study of stability of foams is strongly driven by the food industry as the foam properties and stability are essential to the texture of products. Similarly to emulsions, foams can be stabilized using surfactants, proteins and biosurfactant [34] or particles adsorbing at the interface [2]. The stabilization by solid particles depends on the affinity between the particles and the gaseous and liquid phase. Particles adsorb at the interface and prevent the coalescence of the bubbles due to steric repulsion [3, 26]. Foams are also used in high-tech applications such as drug-delivery [18, 35] or as scaffolds for cell transplantation and tissue growth [36].

In addition to having multiple industrial applications, foams were historically one of the first suspensions to be used as model materials. Bragg and Nye, in 1947, used 2D bubble rafts to model the behaviour of metallic glasses [8]. Using bubbles to model atoms, dislocation and grain boundaries could be observed directly and linked to material properties [37]. This work pioneered the use of suspensions as model materials to study fundamental questions.

1.2 Interactions in solution

Individual particles in solution interact with one another over time. The nature of the inter-particle interaction directly impacts the mechanical properties of the suspension. Interactions can either be attractive or repulsive. If the sum of the interactions is attractive, the suspension can be unstable and particles aggregate with one another. If the sum of the interactions is repulsive, particles remain suspended in solution. Note that interactions between particles can depend on the distance between particles: attractive interactions at long distance can become repulsive at short distance and *vice versa*. As mentioned in section 1.1.2, colloidal suspensions must be stabilized using steric repulsion in order to prevent the particles from aggregating. On the other hand, attractive interactions can be purposefully introduced in order to study particular behaviours. Finally, suspensions are often studied in numerical simulations and the forces between particles are calculated using a mathematical model.

1.2.1 Hard spheres

The hard spheres interaction is considered as the simplest interaction between particles. In this model, the only constraint is that particles cannot overlap. If the distance between the center of two particles, r_{ij}, is less that the sum of the radii of each droplet, $(R_i + R_j)$, their potential energy is infinite. The hard sphere interaction can be mathematically modelled by the potential:

$$V(r_{ij}) = \begin{cases} \infty, & \text{if } r_{ij} \leq (R_i + R_j) \\ 0, & \text{otherwise.} \end{cases} \tag{1.1}$$

The hard sphere model was proven to be a good approximation for sterically stabilized colloids with polymer chains such as PMMA [6]. Despite being the simplest model for suspensions, the hard sphere model was shown to capture the main properties of bulk metallic glasses [38, 39].

1.2.2 Soft spheres

While the hard sphere model considers that particles simply cannot overlap, certain particles can deform. For example, air bubbles in foams can be deformed to increase their packing fraction [40, 41]. Instead of preventing the deformation and overlap completely, particles can be modelled as soft spheres which can virtually overlap. The cost of deforming a particle can be modelled as an energy cost which depends on how close two particles are compared to the sum of their radii which is quantified by the overlap parameter:

$$\delta_{ij} = 1 - \frac{r_{ij}}{R_i + R_j}, \tag{1.2}$$

with r_{ij} the center-to-center distance between particles i and j and R_i and R_j the radii of the particles [41]. Particles are in contact if $\delta_{ij} \geq 0$. The interaction between particles can be mathematically modelled by the following potential [41]:

$$V_{ij} = \begin{cases} \epsilon_{ij}\delta_{ij}^{\alpha}, & \text{if } \delta_{ij} \geq 0 \\ 0, & \text{if } \delta_{ij} \leq 0 \end{cases} \tag{1.3}$$

The exponent α can be adjusted as a function of the nature of the interaction. For harmonic interactions, $\alpha = 2$ and ϵ_{ij} sets the spring constant of the interaction.

Hertzian mechanics between two solid particles can be modelled using an exponent $\alpha = 5/2$. In Paper I, oil droplets are considered deformable and modelled as springs.

1.2.3 Van der Waals

Van der Waals forces are attractive forces between two molecules or atoms. The attraction originates from dipolar moments in molecules. The dipolar moment can either be permanent in polar molecules or induced due to fluctuations in the electronic clouds. As a result, even non-polar molecules experience van der Waals attractive forces. The potential energy scales with the distance between particles as $U_{\mathrm{VdW}} \propto -1/r^6$. From the potential interaction between molecules, the interaction forces between macroscopic objects can be calculated. In the context of suspensions, the interaction between two spheres is of particular interest. The exact calculation was first carried out by Hamaker [42]. For two spheres of radius R_i and R_j, close to one another, the force simplifies to:

$$F_{\mathrm{VdW}}(r) = -\frac{AR_iR_j}{6r^2(R_i + R_j)}, \tag{1.4}$$

with A the Hamaker constant which depends on the material constituting the spheres. The order of magnitude of the Hamaker constant is $A \sim 10^{-19}$ J [31]. For two spheres of same radii, $R = R_i = R_j$, the force simplifies to:

$$F_{\mathrm{VdW}}(r) = -\frac{AR}{12r^2}. \tag{1.5}$$

It is interesting to calculate the order of magnitude of such a force in the case of an emulsion. Let us consider particles with radius $R \approx 10$ μm and a contact distance $r \approx 0.2$ nm [31], the force required to separate the particles is $F_{\mathrm{VdW}} \sim 2$ μN. The order of magnitude of F_{VdW} seems low but in fact is much larger than the typically nano-Newton depletion force measured between two droplets in Paper III. Note that to calculate this order of magnitude, the distance between droplets is taken as perfect contact at the atomic level and the van der Waals forces drop significantly as the distance between particles increases.

1.2.4 Depletion interaction

The depletion interaction is an attractive force between two large particles when smaller particles, depletants, are co-dispersed in solution. The origin of the force is from the entropy of the small particles in solution. Consider two large particles, for example oil droplets, far from one another. As particles cannot interpenetrate, each large droplet is surrounded by a volume, called the excluded volume, that is not accessible to the small particles (grey area in Fig. 1.2 (a)). As the droplets come closer to one another, the excluded volumes can overlap resulting in a smaller total excluded volume for the small particles as shown in Fig. 1.2 (b). There are now more configurations accessible to the small particles and thus they have a greater entropy. As a result, large particles are attracted to one another in order to maximize the entropy of the system. Experimentally, depletants can be dissolved polymer chains in solution [31,43] or surfactant micelles [44]. Depletion interactions can be described by the Asakura-Oosawa potential [45, 46] and the depletion forces between two oil droplets are precisely measured in Paper III.

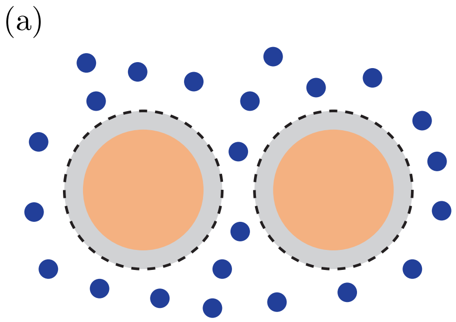

Figure 1.2: (a) Two particles (orange) are surrounded by depletant particles (blue) which cannot enter the excluded volume (shown by the grey area). (b) As the large particles come closer to one another, the excluded areas overlap (shaded grey area), resulting in less excluded volumes for depletants. Small particles can access more configurations which increases their entropy. As a result, large particles are attracted to one another to minimize the excluded volume and increase the entropy of depletants.

1.2.5 Double layer repulsion

The double layer repulsion occurs when charged particles are dispersed in solution. As indicated by the name, two charged particles will experience repulsive interactions.

However, the repulsion is not caused by electrostatic interactions alone. Instead, the origin of the interaction is entropic. If charged particles are dispersed in solution, counter-ions will be attracted to the particle. For example, if the particles are negatively charged, positive counter-ions will preferentially stay in the vicinity of the particle and on average, the concentration of positive ions will be larger than the concentration of negative ions, as shown in Fig. 1.3 (a). The concentration in ions i at a distance, x, from the particle follows a Boltzmann distribution [47]:

$$\rho_{xi} = \rho_{\infty i} \exp\left(-\frac{z_i e \psi_x}{kT}\right), \tag{1.6}$$

where $\rho_{\infty i}$ and z_i are respectively the concentration in the bulk (infinite distance from the particle) and the valency of ions i, e the charge of an electron, ψ_x the electrical potential at distance x, k the Boltzmann factor and T the temperature. If NaCl is dissolved in the solution the number $z_i = +1$ for Na^+ ions and $z_i = -1$ for Cl^-. The electrical potential, ψ, created by a charge is directly linked to the charge density of ion, ρ, with valency z via the Poisson's equation:

$$ze\rho = -\epsilon\epsilon_0 \frac{d^2\psi}{dx^2}, \tag{1.7}$$

with ϵ the relative permittivity of a material and ϵ_0, the relative permittivity of vacuum. Equation 1.7 can be generalized to the case where the solution contains more than one type of ions [47]. A schematic of the concentration of co-ions and counter-ions as a function of x is shown in Fig. 1.3 (b). The positive counter-ions screen the charge of the suspended particle. Now, if two charged particles are brought closer to each other, the counter-ions are confined into a smaller space and less configurations are available to them. This decreases their entropy which is not favourable and as a result the charged particles experience a repulsive force.

It is important to know the range of the double layer repulsion. The particles only experience a repulsive force if the two layers of counter-ions interpenetrate. In the limit of small potential, the Debye-Hückel approximation, the potential, $\psi(x)$, in the vicinity of the particle can be shown to decay exponentially: $\psi(x) = \psi_0 \exp(-\kappa_{\mathrm{D}} x)$ [47]. The length κ_{D}^{-1} is called the Debye length and characterize the extent of the double layer. The Debye length depends on the concentration

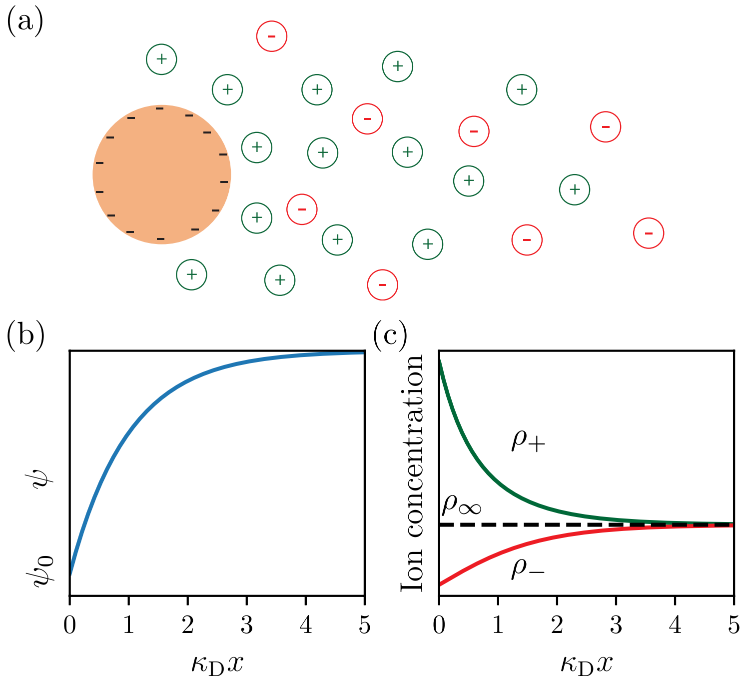

Figure 1.3: (a) Schematic of the distribution of charged counter-ions around a negatively charged colloid (orange particle). The concentration of positive ions is greater in the neighbourhood of the particle. (b) Electrical potential as a function of the dimensionless distance to the particle. The potential at the surface ψ_0 is negative and exponentially increases to zero in the bulk. (c) Ion concentration as a function of the dimensionless distance to the particle. The black dashed line shows the unperturbed concentration in ions in the bulk of the solution. The counter-ions (green) are attracted to the colloids while the co-ions are repelled. The effect of the negatively charged colloid vanishes at about five Debye lengths, $\sim 5\kappa_{\mathrm{D}}^{-1}$, for both the electrical potential and the concentration in ions.

of ions in the solutions: the more ions in the solution, the shorter the Debye length. The interactions between charged particles are screened by the double layer of ions over the typical length scale κ_{D}^{-1}. A short Debye length means that the particles only experience the repulsive force if they come in close contact. The role and the order of magnitude of the Debye length for the experiments conducted in Paper I and Paper II are discussed in details in section 2.1.1

1.3 Granular materials

A granular material is a particulate matter that consists of an assembly of solid particles [48]. As we have seen earlier, solid particles under 1 μm are referred to as colloids [48]. Assemblies of particles with size between 1 μm and 100 μm are called powders and van der Waals forces play an important role. The terminology granular material typically refers to particles that are larger than 100 μm. Due to the particle size, Brownian motion is negligible for granular materials and particles interact through collision and friction. The definition of granular materials is broad and while most people would immediately picture a sand pile when talking about granular materials, it also encompasses assemblies of rice, or coffee grains, or even much larger structures, like Saturn's rings and asteroid belts. The physics of granular materials is extremely rich. At the macroscopic level, they can behave as solids, liquids, or gas [49]. For example, sand will take the shape of its container as a liquid would but poured on a surface, it will assume a conical shape which is not the case of a liquid (see section 1.4.3). In this section, we are particularly interested in how granular materials accumulate at an obstacle, and the structures that they form.

1.3.1 Angle of repose

The typical conical shape that sand takes when poured onto a surface or the shape of sand dunes in the desert is familiar to all. The slope of the sand pile defines a characteristic angle with the bottom surface. This angle is called the angle of repose, θ_{R}. Another way to think about the angle of repose is to place granular materials on a surface and continuously increase the angle the surface makes with the horizontal. For small angles, the pile behaves as a solid and does not move. If the angle exceeds a critical value, $\theta > \theta_{\mathrm{R}}$, the grains start to flow [49]. This technique is called the tilting box method and is used to measure the coefficient of static friction [50] which is directly related to the angle of repose. For regular granular materials, with friction between grains, the angle of repose takes values ranging from $\sim 20°$ to $\sim 45°$ [50].

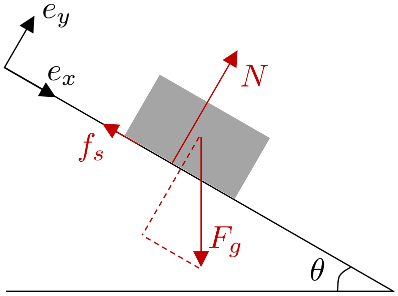

Figure 1.4: Free body diagram of a block of mass, m, on an incline at an angle θ. The coefficient of static friction between the ramp and the block is μ_s. Looking at the maximum angle at which the block starts sliding provides insight into the maximum angle a pile of grain can sustain.

Inter-particle friction

The angle of repose is, among other parameters, linked to the friction between grains. Reasoning in analogy with a solid block on a ramp gives significant insight into how the angle of repose and static friction are related [48]. Fig 1.4, shows the free body diagram of a solid block, of mass m on a ramp, at angle θ with coefficient of static friction μ_s. In this scenario, we are calculating the maximum angle before the block starts moving. Just before the motion starts: $\overrightarrow{F_{\text{net}}} = \overrightarrow{0}$ and the force of static friction is maximal: $f_s^{\text{max}} = \mu_s N$. Using the force balance along the vertical and horizontal directions:

$$\begin{aligned} N &= mg\cos(\theta), \qquad \text{and} \\ f_s^{\text{max}} &= mg\sin(\theta). \end{aligned} \tag{1.8}$$

Using the relationship between N and f_s^{max}:

$$\mu_s mg\cos(\theta) = mg\sin(\theta), \tag{1.9}$$

and finally

$$\mu_s = \tan(\theta). \tag{1.10}$$

Equation 1.10, gives the connection between the angle at which the block starts to slide and the friction between the ramp and the block. This analogy suggests that the maximum angle, called friction angle, at which the pile is stable is given by the friction coefficient of the material. In a granular material, the friction occurs between grains and thus μ_s is taken as the inter-particle coefficient of friction. The friction angle is directly related to the maximum angle of a pile of grains. However, the trigger of an avalanche, when the pile becomes unstable and grains start to flow, does not only depend on the friction between grains. The angle of repose was shown to not only be a function of the inter-particle friction. Parameter such as the shape of particles [51] or the surface roughness [52] also influence the angle of repose.

Frictionless particles

A natural question to ask is what happens to the sand pile geometry if the inter-particle friction is removed? One would expect that frictionless particles cannot sustain a conical shape and the angle of repose drops to zero. While removing the friction between particles can be easily done in numerical simulations, experimentally, one must use a different type of particle or interaction between particles. Numerical results obtained with frictionless particles still evidence a small but non-zero angle of repose [53, 54]. On the experimental side, several groups have studied this question using frictionless particles or repulsive colloids. First, Ortiz *et al.* [55] have studied how repulsive colloids transported by a liquid accumulate against an obstacle in the flow. In this experiment, the static friction between particles is expected to play a minimal role. Colloids aggregate into a sandpile-like structure with a finite angle of repose which depends on the flow speed of the continuous phase. The authors measured small angles of repose ranging from 0.5° to 7° which is consistent with the results from numerical studies and thus with the assumption that static friction is minimal. The colloids being repulsive, the aggregate breaks up if the flow of the continuous phase is turned off. Another study was conducted with foams by Shorts and Feitosa [56]. Bubbles are produced in a liquid and rise to the top of the container where they accumulate. The interface between the foam and the liquid is not flat and shows a finite angle of repose. As the production of bubble is interrupted, the interface flatten and $\theta_{\mathrm{R}} \rightarrow 0$. Finally, Lespiat *et al.* [57] used a 3D foam with various thicknesses driven up an inclined plane (at angle θ) due to buoyancy. The solid-like behaviour for the foam is defined as the sheet sliding up the slope as a whole while in the liquid-like regime, the top layer (in contact with the wall) of the foam moves slower than the bottom layer. The angle at which the transition from solid-like to liquid-like happens is defined as the angle of repose in the limit where the number of layers of bubbles is large. Again, despite the lack of friction between bubbles, the author measured a finite angle of repose in good agreement with values from numerical simulations [53,54]. All these studies show that the absence of friction between particles does not prevent the particles to form sandpile-like structures. While the angle of repose is relatively small, $\theta_{\mathrm{R}} < 8°$, compared to typical frictional granular materials [58], it remains different from zero. A similar experiment to [57] with immersed granular material lead to an angle of repose of about 22° [59] versus 4.6° in the case of foams.

1.4 Liquids and surface tension

In this section, we discuss fundamental properties of liquids and in particular properties that result from having an interface between two liquids, a liquid and a gas, or a liquid in contact with a solid surface. Any interface between two distinct phases leads to an interfacial energy cost referred to as surface tension. Rigorously speaking, the interfacial tension should be defined between phase A and phase B. The term surface tension is commonly used to describe the interfacial tension between a liquid, for example water, and air. In this section, we mostly focus on the interfacial tension between two fluids. Interfacial tension has major consequences on liquid properties. Evidence of surface tension effects can be observed in everyday life: water striders walking on the surface of a water pound, the spherical shape of droplets on windows or even water coming out of the kitchen tap breaking up into droplets. All these macroscopic observations are direct consequences of microscopic molecular interactions.

Molecules in a typical liquid are disordered and interact with their neighbours through van der Waals forces or hydrogen bonds. As discussed in section 1.2.3, even non-polar molecules will experience van der Waals forces and the attraction force scales as $U_{\mathrm{VdW}} \propto -1/r^6$, with r the distance between molecules. At shorter range, molecules experience a repulsive force as they cannot occupy the same space. The repulsive force scales as $U_{\mathrm{rep}} \propto 1/r^{12}$. The addition of the attractive and repulsive potentials results in a potential well, see curve shown in Fig. 1.5 (a), with an interac-

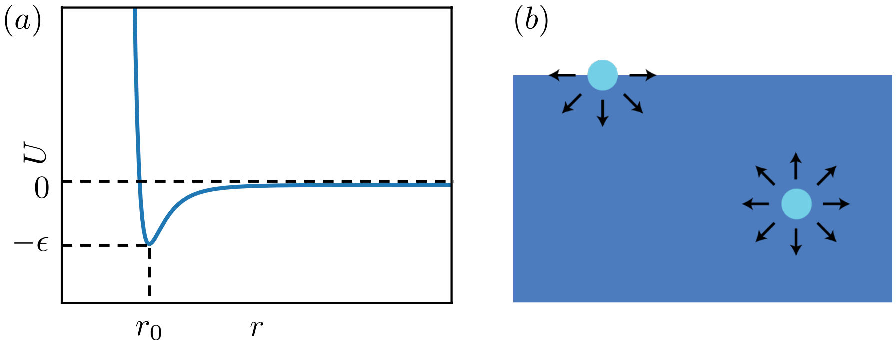

Figure 1.5: (a) Potential energy between two liquid molecules separated by a distance r. A minimum in the potential energy is found when particles are at a distance r_0 from one another. (b) Schematics of the difference in interactions with neighbouring molecules felt by a molecule at the interface compared to a molecule in the bulk.

tion energy ϵ when particles are at a distance r_0. Molecules will, on average, be found at a distance r_0 from one another and are bound to their neighbours by a stabilizing energy ϵ. If a molecule is placed on an interface as shown in Fig. 1.5 (b), it is missing approximately half of its neighbours in comparison to being in the bulk. The missing interactions with neighbours result in the molecules at the interfaces having a larger free energy than their counterpart in the bulk. This creates an energy cost per unit area associated with the creation of an interface between two phases: the surface tension. This argument can be generalized to the interfacial tension between any two phases A and B being placed in contact. In fact, following the derivation from R. A. L. Jones [31], the interfacial tension can be related to the pairwise relative interaction energies ϵ_{AA}, ϵ_{BB} and ϵ_{AB} for a sharp interface. In this model, molecules have a volume v and are placed on a lattice with Z nearest neighbours. The interfacial tension can be expressed as

$$\gamma_{AB} = \frac{1}{2v^{2/3}}(2\epsilon_{AB} - \epsilon_{AA} - \epsilon_{BB}). \tag{1.11}$$

Equation 1.11 clearly shows the energy cost of bringing two phases A and B in contact and can be rewritten in terms of the $\chi = \frac{Z}{2kT}(2\epsilon_{AB} - \epsilon_{AA} - \epsilon_{BB})$ parameter which quantifies the relative strength of the different pairwise interactions:

$$\gamma_{AB} = \frac{\chi kT}{Zv^{2/3}}. \tag{1.12}$$

The above discussion shows that any interface between phases leads to an energy cost per unit area, provided $\chi > 0$. To minimize the energy cost, any surface will minimize its area. For a given volume, the smallest area is obtained if the material takes a spherical shape; this explains why oil droplets in an emulsion take a perfect spherical shape or rain drops form spherical caps on the windshield. Finally, the surface tension can also be treated as a tensile force at the interface and has the units of N/m.

1.4.1 The Laplace pressure

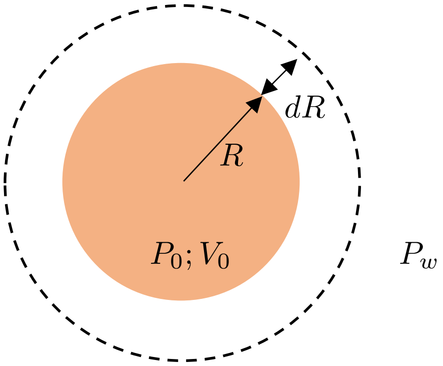

Figure 1.6: Origin of the Laplace pressure in a droplet of oil in water. The expression for the Laplace pressure can be obtained by considering the energy cost of increasing the droplet size by dR

The Laplace pressure refers to the jump in pressure across a curved surface and is directly proportional to the surface tension of the liquid. The expression of the Laplace pressure can be obtained by considering the energy cost of increasing the size of an oil droplet in water by dR, as shown in the schematics Fig 1.6. The work done by the pressure is given by [60]:

$$\delta W = -P_o dV_o - P_w dV_w + \gamma_{ow} dA, \tag{1.13}$$

where P_o and P_w are the pressures in the oil and water, γ_{ow} is the interfacial tension between oil and water. The change in volume for the oil phase is the inverse of the change in volume of water: $dV_o = -dV_w = 4\pi R^2 dR$ and the change in area is

$dA = 8\pi R dR$. At equilibrium, the work is equal to zero which leads to:

$$\Delta P = P_o - P_w = \frac{2\gamma_{ow}}{R}. \tag{1.14}$$

This expression corresponds to the jump in pressure across the interface: the Laplace pressure. If the interface is not a sphere, it can be described by two principle radii of curvature, R_1 and R_2, and Eq. 1.15 can be generalized as:

$$\Delta P = P_o - P_w = \gamma_{ow}\left(\frac{1}{R_1} + \frac{1}{R_2}\right) = \gamma_{ow} C, \tag{1.15}$$

where C is the curvature. Gradients in Laplace pressure can cause flow in polymer films for example in order to minimize the curvature of the interface [61–64]. The Laplace pressure is responsible for the Ostwald ripening [60]: a phenomenon by which small droplets empty into large droplets.

1.4.2 The capillary length

The surface tension of liquids can have consequences that go against the action of gravity. For example the formation of menisci results in liquid being pulled up along a capillary tube or a glass wall. However, the liquid cannot rise indefinitely and at equilibrium the meniscus is established over a given length scale. This length scale is established by the balance between gravity, or the hydrostatic pressure in the liquid, and the surface tension of the liquid. The length scale at which gravity and surface tension become equivalent is called the capillary length, κ^{-1}. The expression for κ^{-1} can be obtained by comparing the Laplace pressure (Eq. 1.15), γ/κ^{-1}, and the hydrodynamic pressure at depth κ^{-1}: $\rho g \kappa^{-1}$, with ρ the density of the liquid and g the acceleration due to gravity. Setting these two pressures equal leads to:

$$\kappa^{-1} = \sqrt{\frac{\gamma}{\rho g}}. \tag{1.16}$$

If a droplet of radius, R, is smaller than the capillary length, the effect of gravity can be neglected while for droplets larger than κ^{-1}, gravity must be taken into account. The typical length scale for the capillary length of most liquids is a couple of millimetres and a simple calculation for pure water with $\gamma = 72$ mN/m gives a capillary length of 2.7 mm.

1.4.3 Liquid on a surface

When a droplet is deposited on a surface, a solid or another liquid, the droplet will spread in a process called wetting. The spreading depends on the spreading parameter S [60]:

$$S = \gamma_{\mathrm{sv}} - \gamma_{\mathrm{sl}} - \gamma, \tag{1.17}$$

where γ_{sv} and γ_{sl} are the interfacial tensions of the solid-vapour and solid-liquids interfaces respectively. The spreading parameter quantifies the difference in energy per unit area between a dry solid and a solid covered by a liquid film. In the case where $S > 0$, referred to as "total wetting", it is energetically favourable for the liquid to completely spread into a film on top of the solid. If $S < 0$, which corresponds to "partial wetting", the liquid will form a spherical cap on the solid substrate to minimize the total interfacial free energy. Equation 1.17 can be generalized to a liquid A deposited onto a bath of another immiscible fluid B as follow: $S = \gamma_{\mathrm{B}} - \gamma_{\mathrm{AB}} - \gamma_{\mathrm{A}}$.

Contact angle

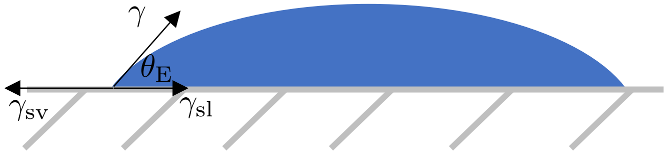

Figure 1.7: Partial wetting of a liquid on a solid surface. It assumes the shape of a spherical cap with a contact angle θ_{E}. The force balance at the contact line is used to derive the Young's equation.

In the case of the partial wetting of a liquid on a solid surface, a spherical cap of liquid will form with a well-defined contact angle θ_{E} commonly known as Young's angle, as shown in Fig. 1.7. The contact angle can be predicted by a simple horizontal force balance along the contact line:

$$\gamma \cos \theta_{\mathrm{E}} + \gamma_{\mathrm{sl}} = \gamma_{\mathrm{sv}} \tag{1.18}$$

$$\cos\theta_{\mathrm{E}} = \frac{\gamma_{\mathrm{sv}} - \gamma_{\mathrm{sl}}}{\gamma}. \tag{1.19}$$

The contact angle is directly set by the relative surface energies of the different materials in contact with each other. In fact, depositing a droplet on a surface and measuring the contact angle can be used to characterize the energetics of the solid-liquid and solid-vapour interface.

The vertical component $\gamma\sin\theta_{\mathrm{E}}$ seems unbalanced on the schematics in Fig. 1.7. The balancing force to this vertical component is provided by the elasticity of the substrate itself [60, 65, 66]. The solid is considered infinitely rigid in this case so remains undeformed. This assumption does not hold in the case of soft solids and soft substrates can be deformed by a liquid droplet [67–69]. Finally, measuring the contact angles between a liquid and a solid can be used as an indirect way to measure surface tension. Suppose the surface tension γ_{sv} and γ_{sl} are known, one can calculate γ and vice-versa. However measuring independently the solid-liquid or solid-vapour is particularly challenging as they appear as a difference in Eq. 1.19. A recent study looked at measuring the contact angle of capped droplets on an elastomer and showed that this method could be used to measure the surface energy between the elastomer and the liquid: $\gamma_{\mathrm{el,l}}$ [70].

Height of a puddle

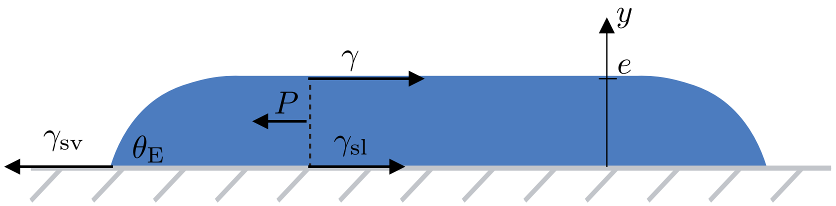

Figure 1.8: Schematics of a puddle of liquid with height e and contact angle θ_{E}. The force balance on the left section of the puddle (delimited by the dashed line) is used to derive the height of the puddle, e. The pressure P corresponds to the hydrostatic pressure in the puddle given by Eq. 1.20

The droplet will maintain the shape of a spherical cap until its radius becomes comparable to the capillary length κ^{-1}. For larger radii, gravity starts playing a role and the droplet will take a pancake-like shape called a puddle. The contact angle remains unchanged but the height of the puddle becomes constant, as shown in Fig. 1.8. If more liquid is added to the puddle, it will simply spread horizontally keeping its height constant. The thickness of the puddle, e, can be obtained by balancing the different surface tension forces and the hydrostatic pressure integrated over the entire thickness of the puddle. The different forces acting on a portion of the liquid puddle are labelled in Fig. 1.8. The hydrostatic pressure, integrated over the thickness of the puddle, is given by:

$$P = \int_0^e \rho g(e-y)dy = \frac{1}{2}\rho g e^2, \tag{1.20}$$

with ρ the density of the fluid and g the acceleration due to gravity. The total force per unit length balance on a section of the puddle leads to:

$$\frac{1}{2}\rho g e^2 + \gamma_{\mathrm{sv}} - \gamma - \gamma_{\mathrm{sl}} = 0. \tag{1.21}$$

Using Young's law, Eq. 1.19, the above equation can simply be rewritten as:

$$\gamma(1-\cos\theta_{\mathrm{E}}) = \frac{1}{2}\rho g e^2, \tag{1.22}$$

and finally, the thickness of the puddle is given by:

$$e = 2\sqrt{\frac{\gamma}{\rho g}}\sin\frac{\theta_{\mathrm{E}}}{2} = 2\kappa^{-1}\sin\frac{\theta_{\mathrm{E}}}{2}. \tag{1.23}$$

The thickness of the puddle is directly proportional to the capillary length which captures the relative importance of the surface tension against gravity. One could imagine increasing the size of a water droplet over time. As long as the radius of the spherical cap is less than κ^{-1}, the spherical cap is growing as a self similar object in 3D. Once the volume is such that the height of the spherical cap is equal to $2\kappa^{-1}\sin\frac{\theta_{\mathrm{E}}}{2}$, the liquid will simply spread on the surface as a puddle in 2D, keeping its height constant. This result is particularly relevant for the results discussed in Paper III where we compare the spreading of aggregates of droplets on a surface to the spreading of a liquid.

1.4.4 Measuring the surface tension

Significant efforts have been made in order to measure the surface tension precisely. In this section, we discuss two methods that are commonly used.

Pendant drop

The concept behind this measurement is rather intuitive. Liquid is slowly pushed out of a capillary tube and forms a drop at the opening as depicted in Fig. 1.9. At equilibrium the Laplace pressure in the drop must equal hydrostatic pressure at any height y: $\gamma C = \rho g y$ where C is the curvature [60]:

$$C = -\frac{r_{yy}}{(1+r_y^2)^{3/2}} + \frac{1}{r(1+r_y^2)^{1/2}}, \tag{1.24}$$

with r_y and r_{yy}, the first and second derivatives of the radius with respect to y respectively. By solving these two equations numerically using the shape of the droplet, one can measure the surface tension of the liquid.

A back-of-the-envelop calculation also provides an easy way to estimate the surface tension of a liquid. If enough liquid is pushed out of the pipette, the force of gravity will detach the drop from the capillary. When the drop detaches the weight of the droplet, W, is equal to the tension force holding the droplet at the edge of the capillary: T (labeled on Fig. 1.9). When the droplet detaches:

$$2\pi R_c \gamma = W, \tag{1.25}$$

where R_c is the radius of the capillary and the weight can be measured using a scale. Ignoring the exact shape, the pendant drop can be coarse-grained into a sphere of radius R_d. Its weight can be written as $W = \frac{4}{3}\pi R_d^3 \rho g$ and the surface tension can be expressed as:

$$\gamma = \frac{2R_d^3}{3R_c}\rho g. \tag{1.26}$$

Equation 1.26 provides a convenient and straightforward way to measure the surface tension of the liquid. However, Equation 1.26 neglects the fact that the drop is not a perfect sphere. As it detaches, the droplet forms a neck and only a fraction of the total weight detaches. As a consequence, it can only be used to estimate the surface

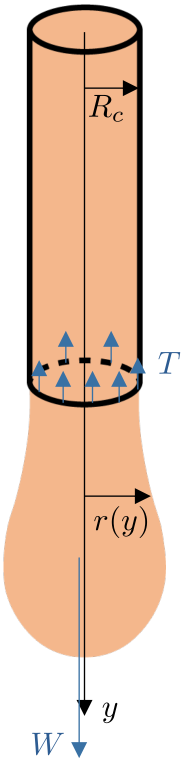

Figure 1.9: Schematics of oil being pushed out of a pipette with radius R. A pendant drop which can be described by its radius $r(z)$ forms at the opening. The drop is pulled down by its own weight W and held in contact with the capillary by surface tension $T = \gamma(2\pi R_c)$ with $2\pi R_c$ the perimeter of the pipette opening. The droplet detaches from the capillary if it weight becomes larger than the surface tension force.

tension and more complex geometry must be taken into account to obtain a precise measurement of γ. It is worth noting that the pendant drop method can be extended to measuring the interfacial tension between two fluids as a drop of fluid A can be pushed into a bath of fluid B, provided that the difference of density between the two fluids is known.

Wilhelmy plate

Another commonly used method is the Wilhelmy plate. A plate of known geometry can be dipped into a liquid bath. The liquid forms a meniscus along the perimeter of the plate, l. The contact line between the solid and liquid phase is characterized by the contact angle, θ_{E} (see discussion in section 1.4.3) and the liquid effectively pulls down on the solid plate with the force:

$$f = l\gamma \cos\theta_{\mathrm{E}}. \tag{1.27}$$

By using a material with very low surface energy, the liquid wets the solid plate resulting in the angle $\theta_{\mathrm{E}} \approx 0$ which simplifies the above equation to $f = l\gamma$. Alternatively, the plate can be pulled out slowly so that the force is perpendicular to the surface when the plate detaches from the water. In this case, the force also simplifies to $f = l\gamma$. Practically, the plate is dipped into the liquid of interest and then pulled out slowly while measuring the force exerted on the plate. Commercial equipment is readily available to conduct such measurements but a scale can be used to measure the decrease in normal force exerted by the liquid bath. Indeed, a simple free body diagram shows that the force $f = N$, the normal force of the bath on the scale. Note that in this discussion, the buoyancy of the plate is ignored which is a good approximation only if the plate is not dipped in the liquid too deep. This is the strategy we adopted to measure the surface tension of water in Paper AI. As mentioned above, the surface tension of ultra pure water is $\gamma = 72$ mN/m but the water used for the experiment was simply tap water and exposed to dirt in the lab. Any impurity in the water decreases the surface tension. We designed an home-made Wilhelmy plate experiment to measure the surface tension of the water used in the experiments and obtained a lower value: $\gamma_{\mathrm{exp}} = 50 \pm 10$ mN/m.

1.5 Properties of suspensions

Suspensions are typically described by their volume fraction ϕ which represents the volume occupied by the suspended phase compared to the total volume. Flow and mechanical properties are strongly affected by the volume fraction of the sample as we will see in the following. At low ϕ, the suspension behaves as a liquid. As the volume fraction is increased above a critical value, suspensions behave as soft solids [71–73]. Depending on the size distribution of the particles, the suspension will either form a glass or a crystal. In the case of hard spheres in 3D, if thermal monodisperse particles reach a volume fraction $\phi = 0.494$, the sample will form a crystal with $\phi = 0.545$ [31]. For any volume fraction $0.454 \leq \phi \leq 0.545$, the sample will undergo a true phase transition and will separate into two coexisting phases [6,31]. A polydisperse assembly of thermal hard sphere forms a glass at a volume fraction $\phi_g \sim 0.58$ [6]. The glassy state requires the width of the distribution of particle radii to be at least 8% of the average radius otherwise the sample will eventually crystallize [21,74]. The maximum volume fraction for a suspension of hard spheres corresponds to the regular close-packed structure with $\phi_{\mathrm{HCP}} \sim 0.74$ in the case of a monodisperse sample. The upper bound for the glassy region is reached for a random close packing of hard spheres with $\phi_{\mathrm{RCP}} \sim 0.64$. In 2D, crystalline packing corresponds to the hexagonal packing of disks and $\phi^{2D}_{\mathrm{hex}} = \pi/2\sqrt{3}$ while the volume fraction at random close packing in 2D is $\phi^{2D}_{\mathrm{RCP}} \sim 0.84$. Particles that are deformable such as bubbles or droplets can pack with volume fraction larger than ϕ_{RCP}. In the following, we discuss the process by which suspensions become solid-like and their resulting mechanical properties.

1.5.1 Jamming

Jamming refers to the transition of a suspension from the liquid state to a rigid state which responds elastically to small applied stress [75]. Jamming traditionally refers to athermal particles while the terminology of colloidal glass transition refers to thermal particles [76]. If the applied stress exceeds a certain value, the jammed suspension can unjam and flow (see more details in section 1.5.2).We first focus on the effect of volume fraction of spherical particles only; *i.e.* what happens to a suspension as ϕ is increased. The temperature of the system is set to zero (athermal particles) and no external shear is applied.

An important parameter in the jamming transition is the average number of contacts per particles, z. For the system to become fully rigid, each particle must have a minimum number of contacts between particles called the isotactic contact number z_{iso}. The isotactic number of contacts can be precisely calculated and depends on the number of constrains on the system. Below this critical number of contacts, collective motion of particles can happen. However, the jamming transition does not necessarily corresponds to $z = z_{\mathrm{iso}}$ [41]. Systems can be described by their distance to the isostatic number of contact: $z - z_{\mathrm{iso}}$. Let us first consider frictionless spherical particles, for example emulsions and foams which can be modelled as soft spheres (see section 1.2.2). The jamming transition for these particles as ϕ increases occurs when the volume fraction exceeds a critical volume fraction: $\phi > \phi_\mathrm{c}$. At this critical volume fraction, the number of contacts suddenly jumps from 0 to a critical value, z_c, and the pressure in the system becomes different from zero. This specific point is commonly called "point J" [41]. In the limit of infinite size system the onset of jamming is a sharp transition at point J [40, 77]. For finite size system, the width of the transition decreases with the number of particles as a power law [77]. The transition at point J, for frictionless particles, corresponds to an isotactic point: $z_c = z_\mathrm{iso} = 2d$ where d is the dimensionality of the system. The volume fraction can increase beyond this critical volume fraction and particles start to deform. The physics of systems approaching the unjamming transition ($\Delta\phi = \phi - \phi_\mathrm{c} > 0$) is extremely rich. Multiple studies have looked at the power law scaling of various properties, such as the excess number of contacts $z - z_\mathrm{iso}$, the pressure in the system, or the shear modulus, as a function of the distance to point J (measured by $\Delta\phi$) [40,78,79]. Finally, it was shown that the mechanical properties of such systems are closely linked to the geometry of the system, for example the number of excess contacts.

Let us now consider packing of frictional particles, for example granular materials. By adding friction between the spheres, the critical number of contact, z_c and the critical volume fraction, ϕ_c are no longer unique and depend on the coefficient of friction between the particles and the history of the sample [41]. The value for both parameters are lower than for frictionless sphere, meaning the jamming transition happens sooner (lower volume fraction) when friction is added. Also, the jamming transition no longer corresponds to isostaticity as z_c ranges from $z_\mathrm{iso}^\mu = d + 1$ and $2d$.

The previous paragraphs focus solely on the effect of volume fraction. It is known that applied shear or even temperature have an impact on the jamming transition. Lui and coworkers [80] proposed a unified phase diagram for the jamming transition in various systems: foams, colloids, emulsions, granular materials. The original phase diagram had three axis: temperature, density ($\propto 1/\phi$) and shear stress. Trappe and coworkers further generalized this phase diagram by adding a fourth axis which takes into account the adhesion between particles [81]. Experimental proofs support this unified phase diagram. This unified frame of work can help study the connection between the different parameters that can be used to unjam a suspension, such as shear stress in foams and emulsions or temperature in thermal colloidal suspensions.

Such a phase diagram suggests a strong correlation between thermal systems that undergo a colloidal glass transition and athermal systems that becomes solid-like at the jamming transition. However, the glass transition in thermal colloids occurs at $\phi_g \sim 0.58$ and jamming at $\phi_c \sim 0.63$. Experiments on emulsions have shown that the solid-liquid transition happened at ϕ_g and the modulus of the emulsion becomes larger for $\phi > \phi_c$ [75]. Recent work also suggests that thermal droplets can undergo both a glass transition and a jamming transition while athermal droplets only show a jamming transition [76]. These results, along with others [82–84], suggest that the glass-transition and jamming may be two distinct phenomena.

1.5.2 Yield stress materials

While suspensions above a critical volume fraction respond elastically to small applied stress [75], suspensions flow if the stress exceeds a critical value called yield stress [73]. Typical examples of yield stress materials are tooth paste, a colloidal suspension, or whipped cream, a foam. Both act as solids if left at rest but become liquid when sheared. The existence of yield stress for a material can be evidenced by rheological measurements. In these studies, the stress, σ is measured against the shear rate $\dot{\gamma}$. For a Newtonian liquid, like water, $\sigma = \eta\dot{\gamma}$, where η is the viscosity of the liquid. For non-Newtonian liquids, the viscosity is a function of the shear rate $\sigma = \eta(\dot{\gamma})\dot{\gamma}$ [31]. If a material becomes less viscous as it is sheared, it is called a shear-thinning material (toothpaste or ketchup), while a material which viscosity increases with shear rate is called shear-thickening (cornstarch with water). The simplest model capturing a finite yield stress is called the Bingham model [85]. Below the yield stress ($\sigma < \sigma_y$), the shear rate is equal to zero: $\dot{\gamma} = 0$ and:

$$\sigma = \sigma_y + \eta\dot{\gamma}, \text{ if } \sigma \geq \sigma_y. \tag{1.28}$$

The fitting parameter η describes the viscosity of the material in the fluid region. Another model used to describe rheological properties of yield materials is the Herschel-Bulkley [86], which is a generalization of the Bingham model:

$$\sigma = \sigma_y + K\dot{\gamma}^n. \tag{1.29}$$

Equation 1.28 is a specific case of Eq. 1.29, with $n = 1$. The exponent n, called the flow index, is typically less than unity which is characteristic of a shear-thinning fluid. At low shear rate, Herschel-Bulkley model predicts $\sigma = \sigma_y$ and a power low for large shear rate. The existence of a yield stress can be used to study the glass transition [87] or jamming [83]. For both thermal and athermal suspensions, below a critical volume fraction, the suspensions behave as Newtonian liquids. The yield stress appears above a given volume fraction, ϕ_g for thermal colloids or ϕ_c for athermal particle. Similar rheology measurements were used to show the existence of two transitions in thermal emulsions: a glass transition ($\phi_g \sim 0.58$) followed by the jamming transition ($\phi_c \sim 0.64$) [76]. In these studies, the rheology curves are typically fitted well by the Herschel-Bulkley model which describes both the yield stress and the shear thinning behaviour. Finally, the yield stress depends on the volume fraction of the suspensions wether or not the particles are thermal or not. The scaling of the yield stress with volume fraction depends on the nature of the particles and in particular if they are deformable (soft spheres such as foams or emulsions) or not (hard spheres) [73].

1.5.3 Force network

When an external load is applied on suspensions or granular material, forces between particles are not homogeneously distributed. While some particles experience no force from a neighbour, others will experience large forces. These high forces between particles tend to align forming chains between particles [88] known as force networks.

As we will discuss in section 1.6.3, numerical simulations have evidenced similar force distributions between particles, or molecules, in suspensions and molecular glass formers respectively [89]. Numerical simulation offers a convenient way to study force chains. The probability distribution of forces between particles can be directly calculated and the nature of interactions, such as friction, is easily tuneable [89–91]. The probability distribution of individual contact force $P(F)$, is a simple method to characterize a force network. In typical granular packing, $P(F)$ has an exponential tail for large forces and a plateau at small forces [91]. However, the probability distribution does not show the spacial distribution of force chains.

Suspensions and granular materials offer a tool to study force chains experimentally as one can take advantage of the larger particle size, compared to molecules, to image individual particles. Emulsions and foams are ideal candidates as the force between particles can indirectly be measured from the shape of the droplets. Droplets or bubbles can deform when an external force is applied, resulting in a change in their surface area which has an energy cost associated. The force between particles depends in the radii of the droplets and the contact patch that forms between the droplets [10, 92]. Inter-particle forces in emulsions have been experimentally measured in 2D [11] and 3D [10, 93] using this indirect method. Force chain persistence length has been measured to be around 10 particle diameters in emulsions and the microscopic distribution of forces was linked to the elastic properties of suspensions at a macroscopic level [10]

Another good candidate for measuring inter-particle forces are granular materials, which are also known to develop force chains under external load. One of the key differences in granular materials is that the inter-particle force has two components: normal and tangential (friction) compared to emulsions and foams which only interact through normal forces [93]. Forces between granular particles can be directly measured using photo-elastic disks [94, 95]. These disks are made of a material that becomes birefringent when a force is applied: the index of refraction is different along the two principle stress directions. When placed between two crossed polarizer, the particles display white and black bands. Force chains can readily be observed in packing of photo-elastic disks without further analysis. The magnitude and the direction of the force can then be qualitatively calculated from the fringe pattern [96]. Other methods have been used to measure the distribution of forces at bottom or the top of packings of granular beads under external loads [97, 98].

1.5.4 Dynamical heterogeneities

Dynamical heterogeneities refers to the difference in dynamics for different parts of the sample: some particles can have fast dynamics while other parts of the sample are barely moving [6]. This concept is connected to the idea of cooperative motion where several particles need to move together in order to rearrange. These spacial heterogeneous dynamics can take the form of strings of particles following one another [99]. Cooperative motion has been observed with microscopy in sheared foams [100], colloidal suspensions [32, 101, 102], and granular systems [103]. The need for cooperative motion of particles results from a particle being trapped in a cage by its neighbours. In order to rearrange, the cage must relax and the particle can escape [103]. Of course the particle under consideration also cages neighbours. By moving cooperatively, a particle can move and the others follow. Weeks and Weitz [104] studied the dynamics of colloidal particles and cage rearrangements using the mean squared displacement (MSD) of particles. For purely Brownian motion, the MSD should scale linearly with time: $< \Delta r^2 > \propto t$. For very short time, the colloidal suspension shows a diffusive behaviours: they have not diffused far enough to “feel” the cage. The MSD shows a plateau for longer times which corresponds to particles being trapped in a cage. For even longer time, the particles can escape from the cage and become diffusive again with a reduced coefficient of diffusion. The authors also show that the displacement observed in the plateau of MSD are smaller for larger volume fraction indicating a smaller cage. Finally, the cages take longer to rearrange as ϕ increases and approaches the colloidal glass transition.

1.5.5 Ageing

The properties of amorphous materials such as colloidal glasses ($\phi > \phi_g$) are also time dependent and these systems are known to age over time [105]. A glassy system ages because it is out of equilibrium and evolves over time towards its equilibrium configuration. On a short experimental time scale, the system may appear solid and not changing but if one waits long enough, rearrangements will happen. Ageing was studied by using confocal microscopy to measure the MSD of colloidal suspension [106]. Depending on the wait time, defined as the time since the last rearrangement occurred, the MSD is different and the dynamics are slowed down with increased wait time. Similar studies of ageing were conducted using dynamic light scattering (DLS) [107] or with fluorescent recovery after photobleaching [108]. All these studies conclude that the dynamics are slowed down as colloidal glasses age.

1.6 Suspensions as model systems

Suspensions have been extensively used as model systems to study fundamental questions. The main advantage of colloidal particles, droplets or bubbles compared to atoms is their size. As mentioned in section 1.1.3, bubble rafts were used to model metallic glasses [8]. Using bubbles instead of atoms, dislocations and grain boundaries could be directly observed and linked to material properties. A large variety of techniques have since been developed and used to characterize suspensions. As the particles are larger than atoms, they can be directly observed by microscopy [32] and information at the single particle level can be accessed. Particle tracking was first introduced by Crocker and Grier [9] and is now a standard technique used to study suspensions. Particles can be tracked with a spacial resolution of ~ 20 nm [6] and more recent algorithms have pushed the spacial resolution down to ~ 5 nm [109]. Imaging individual particles is especially important to study dynamical heterogeneities (Section 1.5.4) that are typically observed in systems such as colloidal glasses [99, 101]. The size of the particles being of the same order of magnitude as the wavelength of light, suspensions can be studied using light scattering. While particle tracking and microscopy are used to access information at the particle level, light scattering experiments provide average structural and dynamical properties of the sample [6].

Another interesting use of emulsions or colloids is to simplify the study of certain properties of more complex systems such as geological flows or biological systems. Next, we discuss the emulsions, foams and colloids as simplified model systems as well as the role they have played in the study of fundamental questions.

1.6.1 Geological model

The Earth's surface can be seen as a mixture of fluid and particulate matter: a colloidal suspension or a granular material. Materials constituting the Earth exhibit properties commonly studied in soft-matter such as aging in colloids and granular matter, glassy dynamics or jamming [12]. This observation generated a lot of interest in the soft-matter physics community as key concepts observed with simple colloidal systems or granular matter can help predict or understand geological flows. The rheology of geological materials can be studied and modelled by colloidal systems. For example, the rheology of sediment transported by a laminar flow was studied using acrylic particles suspended in oil [110].

Another connection between particulate matter and geophysics is the study of earthquakes. Earthquakes happen as tectonic plates move with respect to one another. As they cannot move freely, stress builds up and eventually relaxes into a catastrophic event: an earthquake. Hayman *et al.* used a granular material under an external load as a model to study these events [111]. In their study, particles are sandwiched between two plates, one is stationary while the other is pulled to simulate a fault. The force exerted on the pulled boundary and its position are monitored. When the force exceeds the static friction at the imposed fault, the plate starts moving and the force decreases. This process repeats and results in a stick-slip behaviour. The authors study the statistics of the stick-slip events in this model system to give insight into fault mechanics which are responsible for earthquakes. The literature also suggests that the statistics of such discreet events are independent of the length scale and applies to systems ranging from nanocrystals to paper crumpling or earthquakes [112–115]. These discrete, sudden events are gathered under the same terminology: crackling noise. As they share statistical properties such as slip size distribution, these behaviours are likely independent of their microscopic nature and can be studied using simplified models.

1.6.2 Biology

Biology is another example of field where suspensions can be used as tool to study complex systems. Specific tissue behaviours have also been explained by analogies with suspensions [13]. Analogies with foams were made to study the patterning of cells in developing retina. The cone cells pack together the same way as soap bubbles would, suggesting that the mechanism driving the packing is the minimization of total surface area [116]. Another study showed that actin/fascin bundle network viscoelastic properties are age-dependent, much like soft glassy materials such as colloidal gels [117].

Suspensions can also be used to mimic cellular behaviour. Indeed, cells are complex living organisms that can be difficult to manipulate or study. For example the cell-cell adhesion is a rather complex phenomenon that involves multiple mechanisms. To isolate the role of mechanical forces in adhesion, Pontani and coworkers used oil droplets to model cells [7]. The droplet surface is functionalized with biotin–streptavidin–biotin complexes to replicate cell-cell adhesion. The model developed on these biomimetic emulsions leads to predictions which are consistent with values for binder concentration observed in real cells. Mechanical properties of cell aggregates can also be studied using methods and models typically applied to droplets. Cell aggregates can be grabbed using a micropipette by applying suction. The deformation of the cell aggregate can be measured over time as a function of the suction pressure applied [118]. The mechanical behaviour of cell aggregates can be modelled as a viscoelastic droplet.

Finally, tissues can be described as liquids with various properties, such as surface tension or viscosity, which depend on the specific interactions between cells [13]. This description of tissues as continuous media was inspired by the following observation: two populations of cells mixed together typically separate into two distinct populations in a process called segregation. Cell segregation is driven by the difference in cell adhesion molecules which generates an interfacial tension between two cell populations [119, 120]. The equilibrium configuration minimizes the total interfacial energy. This phenomenon is reminiscent of oil and water phase separating to minimize their interfacial energy.

1.6.3 Glass transition

The glass transition refers to the phenomenon by which a viscous liquid becomes an amorphous solid as the temperature is lowered below the glass transition temperature, T_g [121]. The glass transition is observed in glass forming materials such as polymers. The glass transition temperature is defined as the temperature at which the relaxation time of the material, for example polymer chains, is comparable to the time scale of the experiment. The glass transition is a kinetic phase transition as the value of T_g depends on the cooling rate [31]. The glass transition is a well known phenomenon but its microscopic origin still is not fully understood [122]. Empirical laws have been developed in order to study the transition. For example the Volgel-Fulcher law captures the divergence of viscosity for molecular glasses at T_g [121]:

$$\eta(T) = \eta_0 \exp\left(\frac{T_A}{T - T_V}\right), \tag{1.30}$$

where η_0, T_A and T_V are constants which depend on the molecular glass.

As explained in section 1.5, the control parameter in colloidal suspensions is the volume fraction ϕ. Upon increase of the volume fraction, the viscosity of a colloidal suspension also increases and diverges at a given volume fraction ϕ_g. This transition is analogous to the glass transition in molecular glasses and is called the colloidal glass transition or jamming [6]. The glass transition in colloidal glasses not only resembles qualitatively the transition in a molecular material, the equations governing the change in viscosity are also similar. The Doolittle equation describes the divergence in viscosity in colloidal systems [123]:

$$\eta(\phi) = \eta_0 C \exp\left(\frac{D\phi}{\phi_m - \phi}\right), \tag{1.31}$$

where η_0, C, D and ϕ_m are fitting parameters. Another control parameter is the shear stress applied to the suspension. Emulsions and foams have been shown to undergo a transition analogous to the glass transition when sheared and the governing equation are analogous to Eq. 1.30 where temperature is replaced by parameter depending on the applied shear [124]. These similarities justify the use of suspensions as model systems to study complex fundamental questions like the glass transition. Due to the size of the particles, a wider range of experimental techniques is available to study colloidal glasses compared to their molecular counterpart.

The divergence of the viscosity as colloidal systems approach the glass transition is not the only similarity with molecular systems. As mentioned in section 1.5.4, colloidal systems display dynamical heterogeneities. Simulations of liquids, below their melting point, have also evidenced dynamical heterogeneities in molecular glass formers [125–127]. As colloidal suspensions approach the glass transition the size of the dynamical heterogeneities regions grows: more particles must move cooperatively [32]. This observation is consistent with results from numerical simulations in liquids [125]. The characteristic relaxation time scale also grows as the system approaches the glass transition [32]. However, the connection between the increase in spacial length scale and the increase in time scale remains unclear [128]. As discussed in section 1.5.5, ageing is a characteristic of jammed suspensions but is also observed in polymers below T_g [121, 129]. Finally, the force distribution between particles, $P(F)$, is directly compared in simulations between model supercooled liquids and foams [89]. The authors show that the force distributions, $P(F)$, in both systems have similar shapes. Similar features in the force distribution on granular material are observed experimentally [89, 130]. The authors suggest that the resemblance in the force distributions, and in particular the presence of a peak in $P(F)$ as the system approach jamming or the glass transition, may be linked to force chains. All these similarities between molecular and colloidal glasses are evidence that modelling materials by suspensions can help answer fundamental questions about the microscopic origin of the glass transition.

1.6.4 Crystal-to-glass transition

Monodisperse spheres can pack nicely to form a perfectly ordered crystal. However, disorder, such as polydisperse colloidal particles, prevents glasses from crystallizing [20, 21]. The crystal-to-glass transition remains an outstanding fundamental question. Glassy, disordered materials cannot be described as simply as crystals with defects [131]. Recently, Goodrich *et al.* [132] addressed this question using simulations. In this work, authors compare a crystal, a glass and a slightly disturbed crystal, obtained by adding a small number of defects in the crystalline packing. Crystalline and glassy behaviours were defined using both microscopic information about sphere packing and macroscopic properties, such as bulk and shear modulus. Despite a small percentage of defects in the disturbed crystal, it was found to be better described as a glassy material. This result is in agreement with several other numerical simulations [40, 82, 133–136].

Studying the crystal-to-glass transition experimentally is much more challenging. Most experimental studies focus on microscopic properties such as the packing of particles [137–139]. Several mathematical functions can be used to describe the amount of disorder in a system. By looking at its six closest neighbours, the bond orientation order parameter ψ_6 can be calculated for each particle [137]. A particle in a perfectly ordered crystal has an order parameter ~ 1 and the order parameter decreases as disorder is introduced. Another useful mathematical function is the correlation function $g_6(r)$ with r the distance between particles [137]. In a crystalline packing, the correlation function shows several peaks at regular spacing corresponding to the lattice spacing between ordered particles. Studying the impact of adding disorder on these mathematical functions helps understand how crystals transition to amorphous materials. Results from these studies are in agreement with the numerical simulations discussed above.

Unfortunately, these experimental studies do not yield direct conclusions on the difference in mechanical properties between a crystal and a glass. Different approaches have been explored to characterize suspensions mechanically. The force distribution between particles can be measured as suspensions, with varying amounts of disorder, are submitted to external stress [97, 140]. Both studies concluded that even lightly polydisperse, almost crystalline suspensions have a mechanical response closer to the one of an amorphous material. The rheology of jammed suspensions was also measured by Keim and coworkers [141]. The authors compared the rheological properties of a monodisperse suspension (model for a crystal) and a bidisperse (model for a glass) and showed that they were similar.

The real challenge in these experiments is the definition of a perfectly crystalline system. Indeed, it is extremely challenging to create a single perfect monocrystal. Most studies of colloidal crystals focus on polycrystals [71,142,143] and only few experimental studies have been able to produce ideal monocrystal [144,145]. It is known that the mechanical properties of polycrystals are mostly impacted by dislocations and structural disorder [146]. This could explain why, in the previously mentioned studies, even the suspensions used as models for crystal have too much disorder to display a true crystalline behaviour and their mechanical properties are often similar to amorphous materials.

Paper I shows how we produce ideal monocrystals using monodisperse oil droplets produced with the snap-off instability [19]. The mechanical response of these crystals under compression is measured. The force required to break the crystals is used to define the mechanical behaviour of an ideal crystal. In Paper II, we study the impact of disorder on the mechanical properties by systematically adding defects to the aggregates. The compression force required to break the aggregates is used as a signature of the aggregate composition. We find that the mechanical properties are significantly affected by the addition of even a small number of defects, which is consistent with previous studies. The main advantage of these finite size aggregates used in these studies is our ability to define a purely crystalline behaviours and directly measure the rapid shift in mechanical behaviour when disorder is introduced.

1.7 Liquid-like properties in collections of particles

Despite being composed of discrete particles, some granular materials have been shown to display properties similar to those of simple liquids. In particular, even though flows of granular materials have been shown to lack surface tension [147, 148], assemblies of particles can exhibit liquid-like properties that are typically attributed to their surface tension.

A well known example is capillary fluctuations which are typically observed at the interface between any two liquids or a liquid and its vapour. Molecules at the surface undergo thermal motion resulting in a rough interface which can be described in terms of thermal capillary waves [149, 150]. This phenomenon is driven by thermal motion and mediated by the surface tension of the liquid. The roughness of the interface is set by the balance between these two quantities and is directly proportional to $\sqrt{kT/\gamma}$, with k the Boltzmann constant, T the temperature and γ the surface tension of the liquid [151]. Analogous phenomena have been observed in colloidal systems subject to thermal motion [151]. The surface tension for such colloidal system has been shown to scale like $\gamma \sim kT/a^2$, with a the size of the particles [151–153]. As the size of the particle increases, the system becomes athermal and particles are no longer subject to Brownian motion. Despite the physics of granular materials (where thermal fluctuations can be neglected) being intrinsically different from colloidal materials, capillary-like fluctuations have been observed at the interface of a falling granular jet [154] or at the solid-liquid interface of a quasi-2D assembly of particles under vibration [155].

In addition to being responsible for capillary fluctuations at an interface, the surface tension in liquids leads to different kinds of instabilities. A well known example is a falling stream of water, for example coming out of a kitchen tap, breaking up into droplets in a process driven by surface tension. This instability is known as the Plateau-Rayleigh instability [60]. For a given volume, the surface area and thus the surface energy cost is lower for a collection of droplets compared to a column of liquid. Similar observations were made with a falling granular stream breaking up into clusters of grains [156, 157]. In that case, the clustering of particles is driven by weakly cohesive forces between the grains instead of surface tension in the case of liquids. In this example, the weak adhesion between particles results in an apparent surface tension, and a granular material exhibits properties commonly seen in continuous media.

Another example of liquid instabilities is the Rayleigh-Taylor (RT) instabilities which occurs between two liquids of different densities. If the denser liquid, A, is placed above the less dense fluid, B, equally space fingers of A will form into B and vice versa. Analogues to the RT instabilities have been reported with both thermal colloids and granular materials for which Brownian motion can be neglected. Typical RT patterns are observed both experimentally and numerically in a sedimenting suspension of colloids [158]. Wysocki *et al.* showed that the characteristic wavelength of the instability corresponds to the fastest growing wavelength for the instability. They also applied a linear stability analysis based on a continuum hydrodynamics approach to capture the main experimental features, such as the wavelength, in the early stage of the experiment. This study is a perfect example of using the physics of continuous media to understand certain behaviours in colloidal suspensions. Similar observations were made by looking at sand particles sedimenting in glycerin [159]. In this case, the system exhibits a single wavelength growing faster than the other from the start. In other cases, the interface between grains and a gas layer grows through the coarsening of cusp and the merging of fingers [160]. Finally, by tapping a monolayer of fine particles on a plate, small heaps of particles can form with a regular spacing between them [161]. The formation of the heaps is reminiscent of a liquid film dewetting on a surface and a close connection between the pattern formed by the heaps of particles and the RT instability can be established.

Chapter 2

Experimental Details

Experimental details are clearly outlined in each manuscript presented in Chapter 3, however, the experimental descriptions are concise. In this chapter, additional details about the experimental procedures are provided, focussing in particular on aspects that are not discussed in the papers. The experimental chambers for the three projects were similar in design, consisting of two glass slides spaced by a gap of 2.5 mm. The chambers are filled with an aqueous solution with Sodium Chloride, NaCl, and a surfactant, Sodium Dodecyl Sulfate (SDS). Oil droplets are produced *in situ* and accumulate under the top glass slide due to buoyancy. Pulled glass micropipettes are inserted in the chamber to manipulate individual droplets or aggregates. Pipettes are made with different geometries, discussed in section 2.1.2, to accommodate the needs of each experiment. A recent review by Backholm and Bäumchen [162] covers the different aspects of the Micropipette Deflection (MD) technique. Section 2.3.1 summarizes the key aspects of the MD technique as well as the methods used to calibrate micropipettes. Images are collected using an inverted microscope and the different techniques used to extract quantitative information from the images are discussed in section 2.3.

2.1 Experimental chambers

Experimental chambers are designed to hold the aqueous solution in which the various experiments are conducted. They are made of two glass slides spaced by a 2.5 mm gap. The spacer used between the glass slides is a 3D printed wall (polylactic acid - PLA) glued with caulking to the bottom glass slide. Figure 2.1 shows a 3D schematics of a typical chamber. The addition of the wall significantly reduces the evaporation of the solution, keeping the concentrations of SDS and NaCl approximatively constant over several hours. The strength of the adhesion between droplets is directly linked to the concentration of the different compounds in the solution. The strength of adhesion between droplets has been measured over the course of several hours and was found to stay constant for at least three hours. As a consequence, chambers were typically used for up to three hours before being thoroughly cleaned and filled with new solution. Openings are designed into the wall in order to insert the micropipettes. The number and position of the openings depend on the needs of the experiment.

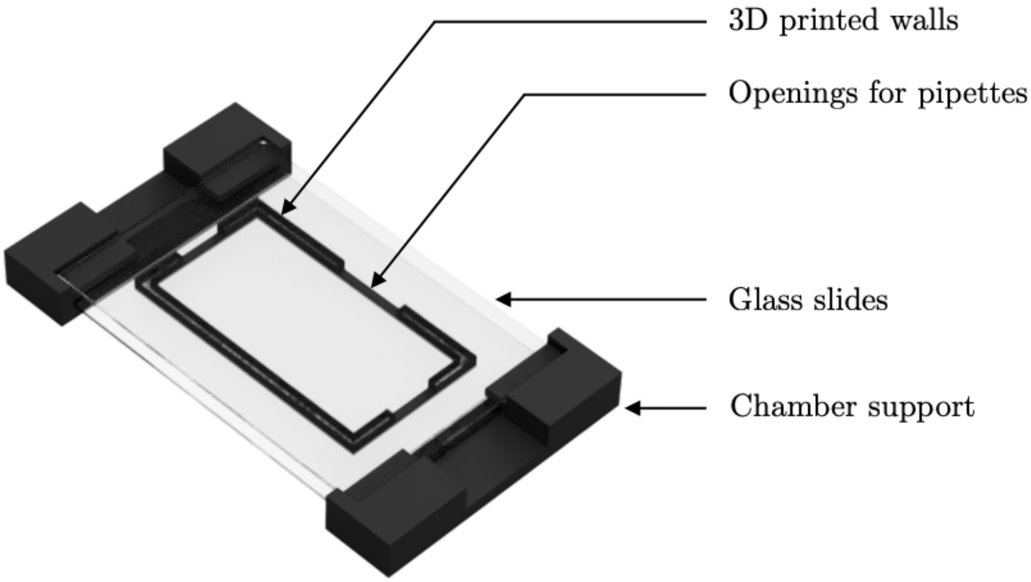

Figure 2.1: 3D render of the experimental chamber. The 3D printed walls are glued to the bottom glass slide. The top glass slide is placed after the pipettes have been inserted in the chamber. The top glass slide is not glued to the wall but is held in place by capillary forces once the chamber is filled with the aqueous solution. The chamber holders prevent sliding from the top glass slide with respect to the bottom. Small openings are designed in the walls to insert the pipettes.

2.1.1 Aqueous solutions

Surfactant, SDS, is added to the solution to both stabilize the emulsion, as explained in section 1.1.1 and induces attractive depletion interactions between the droplets (see section 1.2.4). The concentration in SDS, C, is varied from 0.07 to 0.21 mol/L which is at least one order of magnitude greater than the critical micelle concentration (CMC) of SDS: $C_{\mathrm{CMC}} = 8$ mmol/L [44]. Due to the depletion interactions, droplets stick to each other and aggregates form. SDS being an anionic surfactant, the surface of the oil droplets is charged leading to double-layer repulsive forces between the droplets, as explained in section 1.2.5. The competition between depletion attraction and double layer repulsive forces results in weak attraction between oil droplets. To increase the adhesion between droplets, sodium chloride is added to the solution to screen electrostatic interactions.

In order to quantify the importance of the electrostatic repulsion interactions, the Debye length can be calculated. If only SDS is added to the solution, the Debye length is given by [163]:

$$\kappa_{\mathrm{D}}^{-1} = (0.430 \text{ nm} \cdot \text{mol}^{1/2} \cdot \text{L}^{-1/2})(2C_{\mathrm{CMC}} + (C - C_{\mathrm{CMC}})Q)^{-1/2}, \tag{2.1}$$

with Q the percentage of dissociated SDS molecules in a micelle. Q is approximately 25% for CTAB [164], a cationic surfactant, and one can assume the value for SDS to be similar. As Sodium Chloride is added to the solution, Eq. 2.1 must be slightly modified:

$$\kappa_{\mathrm{D}}^{-1} = (0.430 \text{ nm} \cdot \text{mol}^{1/2} \cdot \text{L}^{-1/2})(2C_{\mathrm{CMC}} + (C - C_{\mathrm{CMC}})Q + 2C_{\mathrm{NaCl}})^{-1/2}. \tag{2.2}$$

Using typical values for $C = 0.1$ mol/L and $C_{\mathrm{NaCl}} = 0.26$ mol/L, which corresponds to 1.5% by mass, the Debye length is $\kappa_{\mathrm{D}}^{-1} \approx 0.6$ nm. Double-layer forces are screened on any length scale larger than the Debye length. Separate experiments were also conducted with concentration in NaCl ranging from 0.5% to 2% by mass and no difference in the strength of the interaction between droplets was observed. This supports the screening role of NaCl: once the repulsive interactions are screened, adding more NaCl does not affect the interaction between droplets. In the following, it is assumed that the electrostatic interactions are negligible, as the Debye length is small in comparison to the size of the droplets, and only the depletion interactions are relevant. The concentration of NaCl is set to 0.26 mol/L for all the experiments presented in Chapter 3

2.1.2 Micropipettes

Hollow glass capillaries (World Precision Instruments, USA, outer diameter 1 mm, inner diameter 0.58 mm) are pulled with a PN-31 pipette puller (Narishige, Japan) to an outer diameter of about 10 μm. The capillaries are passed through a $\sim$ 1 mm wide platinum ribbon bent into an annulus shape. Current is applied to heat the ribbon and locally melt the glass capillary. Capillaries are then pulled using electromagnets. Parameters, such as the temperature of the ribbon or the strength of the magnets, can be adjusted as a function of the desired diameter and length of the pulled pipette. The purpose of the micropipettes used in the studies presented in Chapter 3 is to measure forces of the order of 100 pN. The force measurement being related to the deflection of the micropipette, see discussion in section 2.3.1, the more flexible a pipette is, the more sensitive it is to small forces. Parameters on the puller are set in order to maximize the length of the pulled section of the pipette and minimize its radius. Typically, a consistent radius of $\sim$ 10 μm is achieved over the length of $\sim$ 3 cm. Some experiments required stiffer pipettes, in which case the pulled section was simply cut shorter. The pipettes used for the production of droplets are discussed in section 2.2.1. In the following, the general method for bending pipette is discussed as well as the different pipette geometries for force sensing and droplet manipulations.

Pipette microforging

The MD technique relies on the measurement of the deflection of a micropipette under an external forces. As mentioned in the previous paragraph, longer and thinner pipette are more flexible and thus deflect under smaller forces. The order of magnitude of forces measured in Paper I and II is $\sim 1 - 10$ nN. To achieve this sensitivity, the length of the pipette must be maximized while keeping the pipette compact enough to fit in the confined space of the chamber. Micropipettes are bent into various shapes depending on the needs of the experiment. The sensitivity of the pipette is set by the radius and the total length perpendicular to the force applied. The bending of pipettes is referred to as microforging. Pipettes are locally heated using a 0.5 mm diameter Platinum:Iridium (90:10) wire from Alpha Aesar. Bends are typically performed on the pulled section of the pipette but thicker Pt:Ir wires can be used to bend pipettes with larger diameters. Current is applied to heat the wire until it turns to a faint red: the temperature of the wire should barely be high enough to melt the glass. If the temperature is too high, the glass sticks to the wire and the pipette often breaks. Once the bend in the pipette is performed, the temperature of the wire must be lowered slowly before taking the pipette away from the wire to avoid quenching the glass and prevent the pipette from breaking.

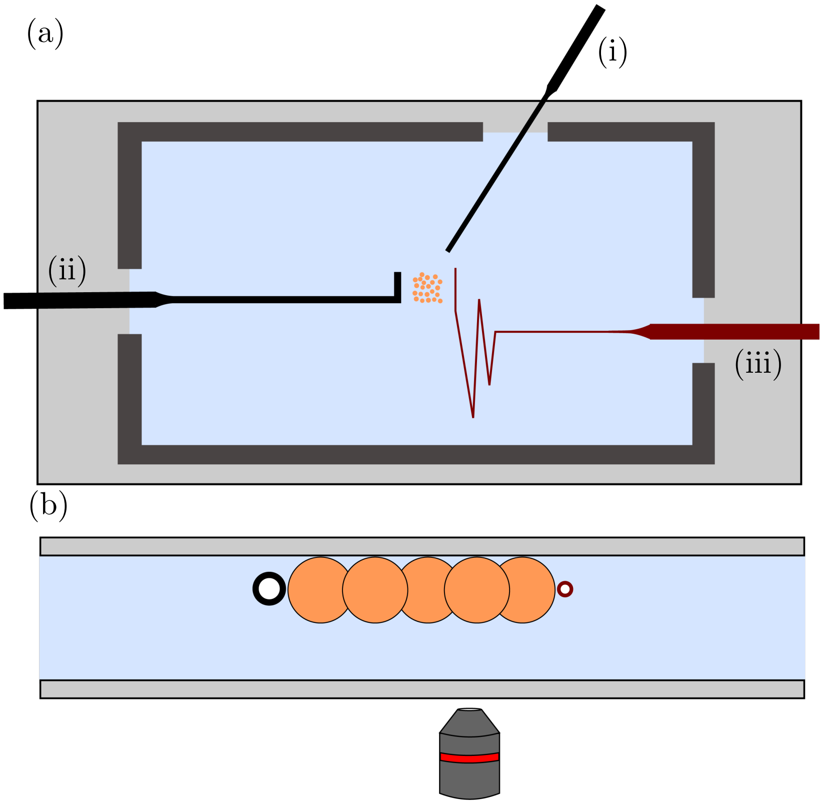

Figure 2.2: (a) Schematic top view of the experimental chamber. The dimensions of the wall (dark grey) are 55 × 30 × 2.5 mm. Three pipettes are inserted in the chamber: (i) the “droplet pipette”, (ii) the “pushing pipette”, and (iii) the “force-sensing pipette”. (b) Schematic side view (not to scale). The buoyant oil droplets form a quasi 2D aggregate under the top glass slide. The pushing pipette (black circle on the left) and the force-sensing pipette (red circle on the right) are placed near the average equatorial plane of the droplets.

Compression of aggregates

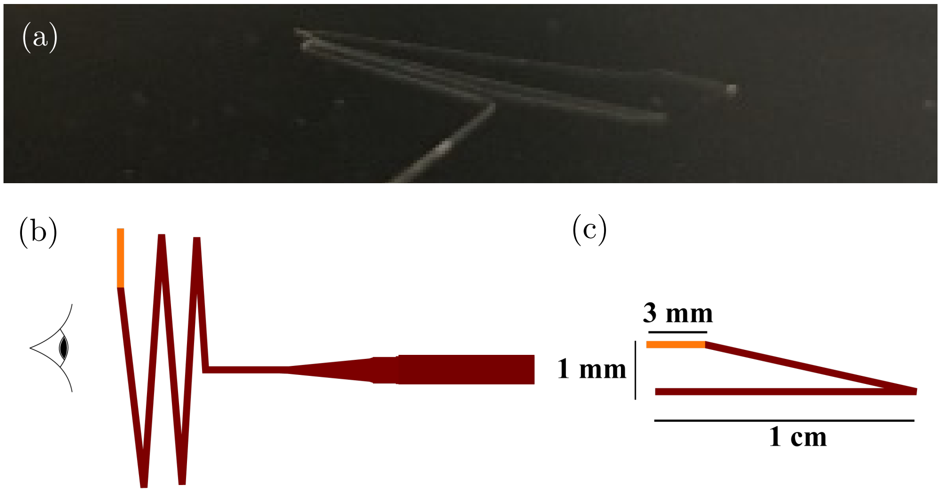

Figure 2.3: (a) Picture of the accordion pipette. The flat tip, top right on the picture, is in contact with the droplets. (b) Top view schematic of the accordion pipette. Several 180° bends are performed every centimetres to keep most of the length of the pipette perpendicular to the applied force while creating a compact pipette that fits in the chamber. (c) Front on view of the accordion pipette. The section in contact with the droplets is shown in orange. Most of the pipette is deep in the liquid chamber while only ~ 3 mm is aligned with the top glass slide.

Paper I and Paper II use the same force sensing pipette geometry referred to as the accordion pipettes, because of their shape. The force sensing and pushing pipettes are facing each other as shown on the schematics in Fig. 2.2. The accordion pipette is made of multiple in-plane 180° bends, as shown in Fig. 2.3. The 180° bends keep most of the length of the pipette perpendicular to the applied force. The sensitivity of the bent pipette is almost equivalent to the straight pipette (before bending). Another bend of $\sim 45°$ is performed about 5 mm from the tip of the pipette and finally the tip, ~ 3 mm, is flattened to be parallel to the main plane of the pipette. The last couple millimetres of the pipette, shown in orange in Fig. 2.3, are used to compress the aggregate of droplets and need to be in a slightly higher plane compared to the rest of the pipette. Indeed, the part in contact with the aggregate must be in the equatorial plane of the droplets, only ~ 10 μm away from the top coverslip. Keeping the entire pipette so close and strictly parallel to the top coverslip is extremely challenging. Giving a small offset to the part in contact with the droplets reduces this technical challenge, as only ∼ 3 mm of the glass pipette is close to the top glass slide while the most part of the pipette is deep in the chamber. It is important to realize that any contact between the pipette and the chamber will prevent it from deflecting and therefore forces cannot be measured.

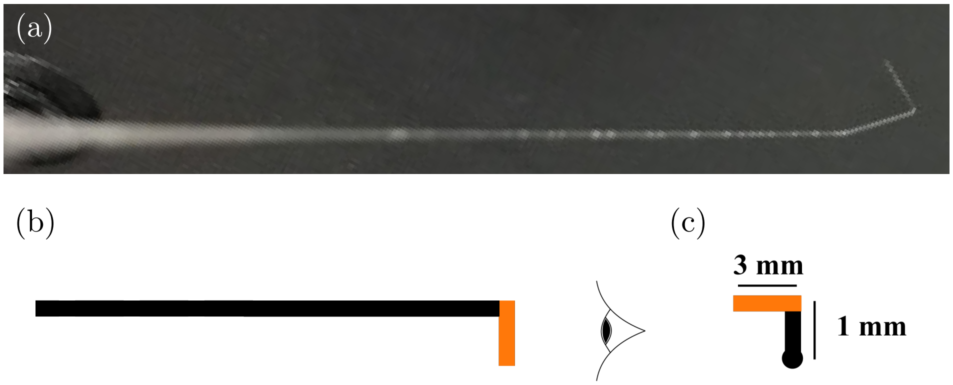

Figure 2.4: (a) Picture of the pushing pipette. The last millimetres, which make a 90° angle with the rest of the pipette, is used to compress the aggregates. (b) Top view schematic of the pushing pipette. (c) Front on view of the pushing pipette. The section in contact with the droplets is shown in orange. Due to the ∼ 45° bend to offset the compression part of the pipette, only 3 mm must be perfectly aligned with the top glass slide.

The "pushing pipette" is the second pipette used to compress the aggregates. It is a stiffer pipette made of a 90° bend about 3 mm from the tip and a ∼ 45° to offset the compressing section of the pipette (shown in orange in Fig 2.4). This is done for the same reason as for the accordion pipette: only the last couple of millimetres of the pipette, used for compression, are close to the top glass slide, while most of the pipette remains deep in the chamber. The length of the pipette, perpendicular to the applied force, is small in comparison to the length of the force sensing pipette and does not deflect noticeably under the small forces applied.

Adhesion strength measurement

In Paper III, the adhesion strength between two oil droplets is measured as a function of their size and the concentration in surfactant. The experimental chamber was similar in design, (two glass slides separated by a 3 mm gap), but the space constraint

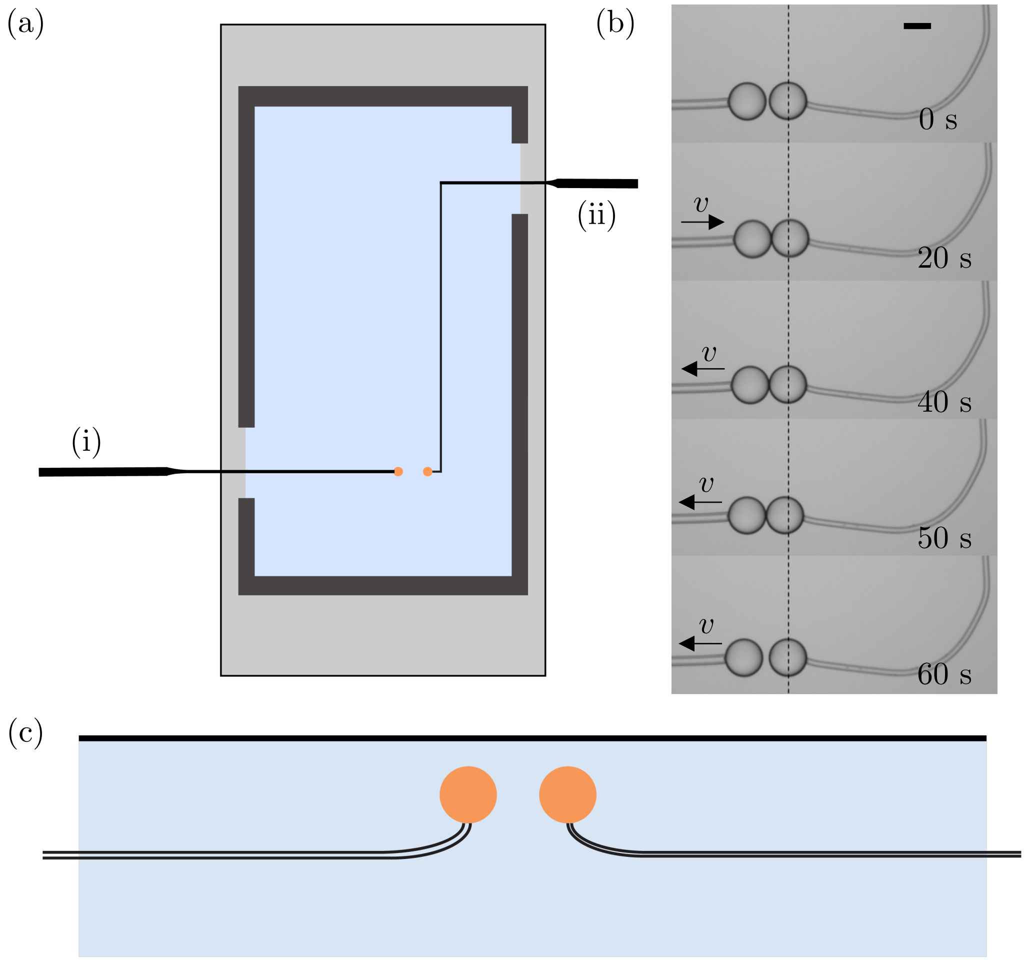

Figure 2.5: (a) Schematic top view of the experimental chamber. Two pipettes are inserted in the chamber: a straight pipette (i) which can be translated at constant speed, v, and a force sensing pipette (ii) to measure the strength of adhesion. (b) Chronograph of the adhesion strength measurement. The left droplet is brought in contact with the other droplet at constant speed before pulling them apart. The dashed line shows the undeflected position of the force sensing pipette. As droplets are pulled apart, the droplet moves further to the left compared to its equilibrium position: a negative force is applied on the pipette. The maximum negative force corresponds to the adhesion force between droplets. Once the adhesion force is overcome, the bond between droplets breaks. The scale bar corresponds to 100 μm. (c) Schematic side view (not to scale). Droplets are grabbed by applying a light suction with the pipettes. The droplets are lowered in the chamber to avoid any interaction with the top glass slide.

was less as only two droplets were pushed against one another before being pulled apart. Openings in the 3D-printed wall for the pipettes are offset so the tips of the pipettes are facing each other, as shown in Fig. 2.5 (a). The force sensing pipette (right, (ii)) is made of two 90° bends, one close to the base of the pulled part of the pipette and one close to the tip. These micropipettes are typically ten times more flexible than the accordion pipettes.

The opening of this force sensing pipette must be flat and not broken irregularly. Suction will be applied to this pipette in order to grab oil droplets. If the opening is irregular the contact between the pipette and the droplet will not be sufficient to hold the droplet and manipulate it. To break the tip of the pipette with clean edges, the thin part of the pipette is wrapped several times around the hot Pt:Ir wire. Current is turned off suddenly to apply a large amount of stress to the glass which breaks, leaving a flat opening. Another advantage of breaking the tip of the pipette using this method is that it typically leaves a short hook upward, see Fig. 2.5 (c), which helps when manipulating the droplets: the droplets can be grabbed on the lower hemisphere instead of the equatorial plane. As droplets accumulate at the top glass slide during the production phase, it can be challenging to bring the pipette close enough to grab the droplets, in particular with small droplets. The small upward hook simplifies the process of grabbing droplets by bringing the pipette from underneath. The second pipette used in this experiment is simply a straight pipette with a flat opening, obtained using the method described above. Once droplets are well adhered to the pipettes, they are lowered in the chamber to avoid any contact between the pipettes and the top glass slide.

2.2 Production of droplets and aggregates

A third pipette is typically used to produce droplets directly in the chamber at the beginning of the experiment. These pipettes, called “droplet pipettes”, are pulled using the pipette puller to a radius of ~ 10 μm. This pipette does not require to be bent and this method of production can be used with both straight or bent pipettes. The pipette is connected to a syringe filled with mineral oil via a needle and plastic tubing. Constant and high pressure must be applied on the syringe plunger in order to push oil through the micropipette. A small oil droplet forming at the tip of the pipette is a sign of a successfully filled pipette. The "snap-off" method, used to produce highly monodisperse droplets, is described in detail below.

2.2.1 Snap-off technique

The droplet pipette is used to create oil droplets in the aqueous solution using the snap-off instability. The details of the snap-off instability are extensively discussed in two studies by Barkley *et al.* [19,165]. This section summarizes the main findings and the method to produce droplets using this instability. One of the main advantages of the snap-off method is the production of droplets without any flow of the continuous phase. This is particularly important as droplets are produced directly in the chamber in all experiments. Most common microfluidic techniques require the continuous phase to flow using syringe pumps [28–30]. The snap-off technique also results in the production of highly monodisperse droplet, with a particularly low coefficient of variability: typically less than 0.7% [165]. The droplet size depends directly on the size of the micropipette opening. As a consequence, a given pipette always produces the same size droplets. The radius of the droplets, R, is equal to double the radius of the pipette [165]. A pulled pipette has a long section with constant radius and a conical section toward its base. By cutting the pipette at different lengths in the conical section, the radius of the pipette, and thus the radius of the droplets, is easily tunable.

Practically, once the pipette, filled with oil, is introduced in the aqueous phase, the tip of the pipette must be pre-wet by the aqueous phase before pushing oil out of the pipette. This is typically achieve by sucking a small amount of aqueous solution. The oil is then pushed out using the syringe plunger. This process usually initiates the snap-off instability. It has been found that using an irregularly broken tip for the droplet pipette facilitate the production of droplet via the snap-off instability. The irregularities allow the continuous phase to enter the pipette and thus the instability to occur. The easiest method to obtain an irregular opening is simply to break the tip of the pipette using tweezers. In the experiment presented in Paper III, it is important for the rate at which droplets are produced to be constant. The needle is disconnected from the syringe creating an open oil "reservoir" in the base of the needle. This reservoir can be risen (lowered) to increase (decrease) the hydrostatic pressure and speed up (slow down) the production of droplets.

2.2.2 Assembly of crystals and bi-disperse aggregates

Once produced, the droplets rise to the top of the chamber due to buoyancy and accumulate under the top glass slide. Droplets are manipulated with the pushing and force sensing pipette to be assembled into an aggregate before being compressed. If only monodisperse droplets are used, crystals of different geometries can be assembled as shown in Fig. 2.6 (a) and (b). In Paper II, defects are introduced in the crystalline structure to study the impact of disorder on the mechanical properties of the aggregates. Defects are droplets with a different size compared to the majority of the aggregate. For example, large droplets can be substituted by a smaller one and *vice versa* (see Fig. 2.6 (c)). To build these bidisperse aggregates, two droplet pipettes with different radii are used to produce two distinct sizes of droplets. Because droplets are placed one-by-one to build the aggregate, the position and the number of defects can be controlled and varied easily.

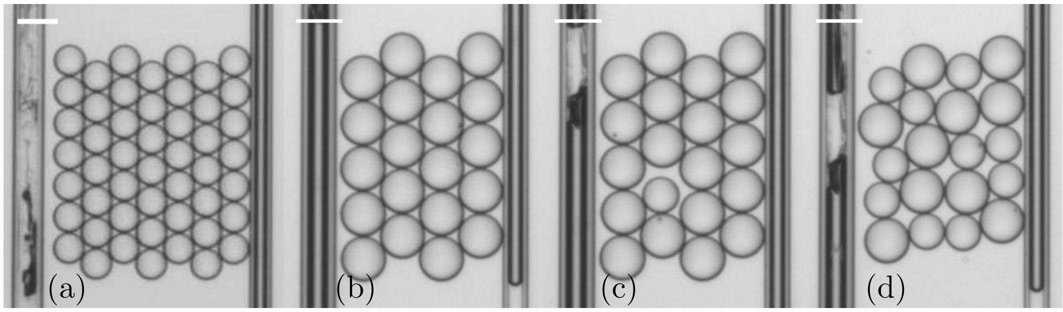

Figure 2.6: (a) - (b) Monodisperse aggregates form perfect monocrystals, the geometry of these crystals can be controlled. (c) A defect, in the form of a smaller droplet, is introduced in the crystalline structure. Its position can be chosen during the assembly. (d) Bi-disperse aggregates made of 50% small and 50% large droplets. These kinds of aggregates are used as model glasses. Scale bars correspond to 50 μm.

2.3 Image analysis

Images are collected using an inverted microscope using a 5x or 10x objective before being analyzed to extract quantitative information. In Papers I and II, the data of interest is the force required to break the aggregates during compression. The force is calculated from the deflection of the force sensing pipette. The deflection is measured using a 1D cross-correlation algorithm. To convert this deflection into a force, pipettes are calibrated using known forces. The cross-correlation analysis as well as the calibration methods are discussed in section 2.3.1. In Paper III, the area covered by the droplets on the top glass slide is measured over time. The image analysis used in this study is discussed in section 2.3.2.

2.3.1 Force measurement

The technique for measuring small forces using a micropipette was developed in the Dalnoki-Veress lab. It was used for a wide range of purposes: from measuring the adhesion and membrane tension of single vesicles [166], or the viscoelastic properties of the nematode *C. elegans* [167] to the propulsive force of *C. elegans* as it swims [168]. This section summarizes the key aspects of the MD technique and additional details, including trouble shooting tips, can be found in the review article by Backholm and Bäumchen [162] .

Cross-correlation technique

The displacement of both the force sensing pipette and the pushing pipette between two images is measured using 1D discrete cross-correlation. The order of magnitude of the displacements typically ranges from less than 1 to about 10 pixels. The cross-correlation offers sub-pixel resolution and in the case of the studies presented in Papers I and II, a resolution of about 0.1 μm.

Mathematically, the cross-correlation measures how similar a vector and its lagged copies are to a reference vector. The cross-correlation between two vectors of length L can be calculated using the following formula:

$$C_{\mathrm{1D}}(j) = \sum_{i=-L}^{L} X(i)Y(i+j). \tag{2.3}$$

The cross-correlation is applied to intensity profiles of a cross-section of the pipette between a reference image (undeflected pipette at $t = 0$ s) and the pipette at instant t. The left inset in Fig. 2.7 shows the cross section of the pipette at $t = 0$ s (top) and time t (bottom). For clarity, the images show 10 pixels in height for each profile while the cross correlation algorithm uses a single line of pixels. The displacement of the pipette between the two images can clearly be seen. Let us consider a simple example: the reference intensity profile of the cross section is $X = [255; 255 \ldots 255; 200; 100; 200; 255 \ldots 255; 255]$ and the intensity profile at time t is $Y = [255; 255 \ldots 255; 255; 200; 100; 200 \ldots 255; 255]$ where each index corresponds to the pixel intensity. In this example the pipette has deflected by 1 pixel. The best match between Y and a lagged copy of X is obtained by shifting all indexes in Y by 1 to the left. The cross-correlation function between X and Y would show a global maximum for a lag of $j = -1$. Shifting the indexes to find the closest match between two vectors corresponds to measuring the deflection of the pipette at time t with respect to a reference (undeflected position). In this example, the pipette has deflected by one pixel. Of course, the pipette does not necessarily deflect by integer numbers of pixels. Because the cross correlation is carried discretely, the data points near the maximum of the curve are locally fitted to a gaussian curve. The maximum of the gaussian fit can now be between two pixels. Finding the location of this maximum allows to measure the deflection with sub-pixel resolution.

This process is illustrated in Fig. 2.7. The autocorrelation (blue curve), correlation of X with itself, is performed on the reference image to find the initial position of the pipette and the cross-correlation between the reference and the image at time t (red curve) measures the deflection of the pipette. The right inset shows a zoom on the global maxima and the gaussian fits (black lines) used to achieve sub-pixel resolution. Initial routines to measure the cross-correlation between two vectors were written in Matlab and have been translated to Python.

Pipette calibration

The cross-correlation technique only measures the displacement of the force sensing pipette. The deflection in microns must be converted to a force in Newtons. This is achieved by calibrating force sensing pipettes using known forces. There are two main methods to calibrate pipettes depending on their shapes.

The most direct methods is to measure the deflection of the pipette under the

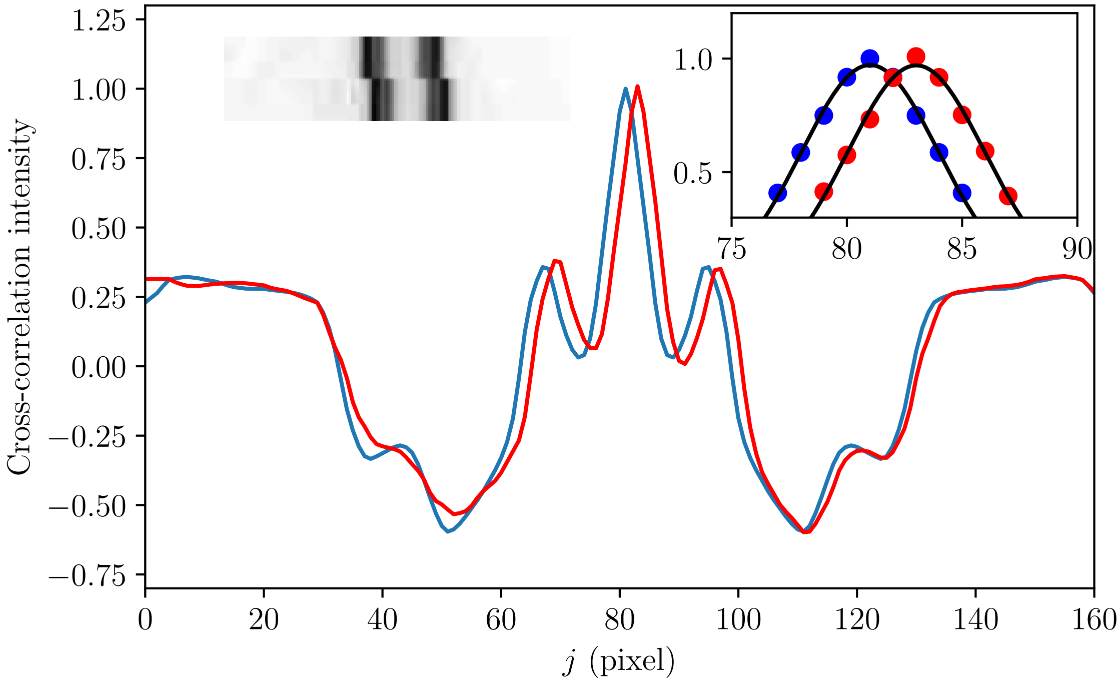

Figure 2.7: Autocorrelation of the reference pipette profile is shown in blue. The cross-correlation between the pipette cross section at time $t = 0$ s and time t is shown in red. The right inset shows a zoom on the global maxima and the gaussian fits (black lines) used to find the position of the maxima with sub-pixel resolution. The measured deflection is the distance between maxima. The left inset illustrates the cross sections used in the cross-correlation measurements. For clarity, each profile shows 10 pixels in height when the algorithm uses a single line of pixels. The displacement between $t = 0$ s (top) and time t (bottom) can be seen directly on the images.

weight of a water droplet. The pipette is filled with water until a droplet of water forms at the tip. The droplet grows as more water is pushed out or shrinks as it evaporates and thus the force exerted on the pipette increases or decreases. Assuming the droplet has an axisymmetric shape around the pipette, the volume of the droplet can be measured and the force due to gravity is calculated. The deflection, obtained by the cross correlation method, as a function of the applied force is shown in Fig. 2.8. For small deflections, the relationship between force, F, and deflection, Δd, is linear and analogous to an Hookean spring. The slope of the fitted line corresponds to the spring constant of the pipette, k. For any deflection of a calibrated pipette, the force is: $F = k\Delta d$. Unfortunately, this method is more challenging to use with complex

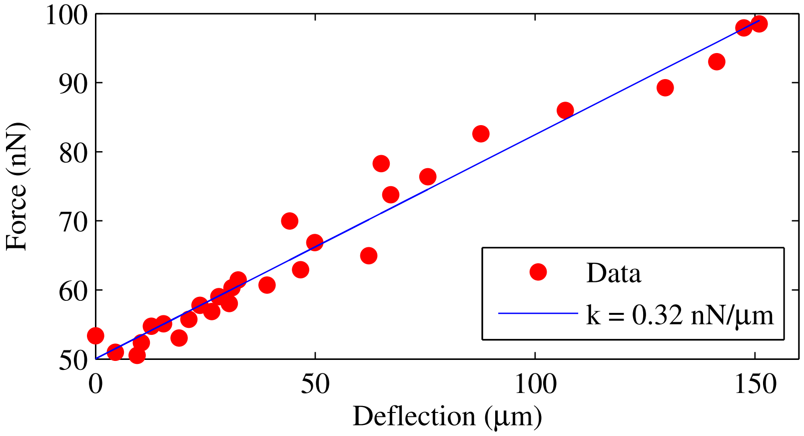

Figure 2.8: Force as a function of the pipette deflection. The force, F, applied on the pipette is calculated based on the volume of the water droplet and the deflection is measured using the cross-correlation technique. The force is linear with the deflection of the pipette and the slope of the linear regression (blue line) is the spring constant of the pipette.

shape pipettes such as the accordion pipettes.

An alternative method is to push a pipette with known spring constant against the accordion pipette. The pipette of known spring constant, called the reference pipette, is typically calibrated using the water droplet method. Its shape is similar to the one used for the adhesion measurement (see section 2.1.2). The pipettes start away from one another (not in contact) and the reference pipette is moved at a constant speed towards the accordion pipette (red data points in Fig. 2.9 (a)). Once the contact is made, pushing two pipettes against one another is equivalent to pushing two springs against one another. The force applied to both pipettes must be equal:

$$k_{\mathrm{ref}}\Delta x_1 = k_{\mathrm{p}}\Delta x_2, \tag{2.4}$$

where k_{ref} is the spring constant of the reference pipette, k_{p} the unknown spring constant and Δx_1 and Δx_2 the deflection of the reference pipette and the accordion pipette respectively. The deflection of the accordion pipette, Δx_2, can be measured directly with the cross-correlation method. Before contact, the reference pipette moves at a constant speed given by the slope of the displacement curve, red data points in Fig. 2.9 (a). As contact is made, both pipettes deflect and the slope of the displacement curve for the reference pipette decreases (blue data points in Fig. 2.9 (a)). The difference between the observed (blue data points) and the extrapolated (black dashed line) displacements corresponds to the deflection of the reference pipette, Δx_1. The force on the reference pipette, $k_{\mathrm{ref}}\Delta x_1$, is then plotted against Δx_2 as shown in Fig. 2.9 (b). The slope corresponds to the unknown spring constant k_{p}.

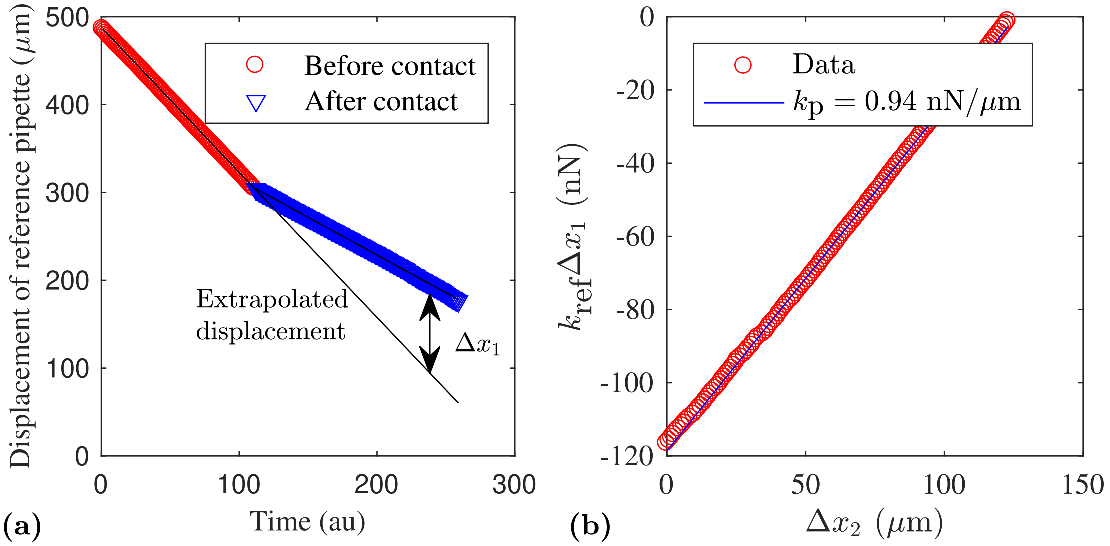

Figure 2.9: (a) Displacement of the reference pipette with known spring constant k_{ref} at a constant speed. The slope decreases when the pipettes come into contact (blue data points) and the reference pipette starts deflecting. The black line is obtained by linear regression on the red data points and corresponds to the extrapolated displacement of the reference pipette (if it did not deflect). The deflection of the known pipette Δx_1 is the difference between the measured and extrapolated displacements. (b) Force applied on the reference pipette, $k_{\mathrm{ref}}\Delta x_1$, as a function of the deflection of the unknown pipette. The slope of the straight line is the spring constant of the unknown pipette: k_{p}

2.3.2 Area measurement

To study the spreading of droplet aggregates on a surface in Paper III, the area covered by the droplets on the top glass slide is monitored over time. Images are collected with an optical microscope which only shows the 2D projection of a three dimensional object. The different shades of grey correspond to the number of droplets along the vertical direction (perpendicular to the top glass slide). Darker area correspond to thicker aggregates, *i.e.* several layers of droplets. A raw image is shown in Fig. 2.10 (a). Because droplets appear as black annuli, applying a threshold algorithm results in detecting the edges of the droplets [Fig. 2.10 (b)]. Each white patch is labelled and its area measured. This includes the outside region but also the inside of each droplets as well as bare patches within the limits of the aggregate. If the area if smaller than the projected area of a droplet, πR^2, the area is filled in black so each droplet appears as a black disk. With this analysis, portions that are not covered by droplets within the contour of the aggregate are not counted towards the total covered area. Finally, the image is inverted so the covered area appears in white on a black background [Fig. 2.10 (c)] and the area is measured by counting the number of white pixels.

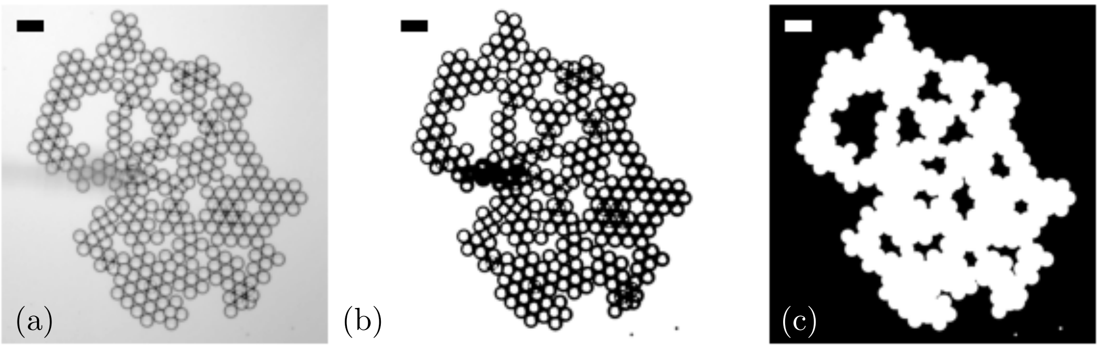

Figure 2.10: (a) Raw picture of the aggregate of oil droplets. Pictures are collected with an optical microscope, as a result images are a 2D projections of a 3D object. Darker shades of grey correspond to several layers of droplet along the vertical direction (perpendicular to the glass slide). (b) Aggregate after the threshold algorithm is applied. (c) The inside of the droplets is filled and the image is inverted. The area covered by the droplets is shown in white. Scale bars correspond to 100 μm.

Chapter 3

Papers

This chapter contains the main papers discussed in this thesis. Each paper is prefaced by a brief summary, the main results and the conclusions. My contribution to each manuscript is also stated. Two additional papers for which I am not the main contributor or are slightly disconnected to the main focus of the thesis are included in Appendix A.

Paper I

Mechanical properties of 2D aggregates of oil droplets as model mono-crystals

J.-C. Ono-dit-Biot, P. Soulard, S. Barkley, E. R. Weeks, T. Salez, E. Raphaël and K. Dalnoki-Veress, Soft Matter, **17**, 1194 (2021).

In this paper, we study the mechanical response of ideal mono-crystals made of lightly attractive oil droplets to compression. Taking advantage of the small sample size and the high degree of monodispersity of the droplets, the aggregate can form a perfectly ordered, defect-free crystal. The aggregates are compressed between two glass rods and the force required to break the aggregates is measured. The force measurement is coupled with the imaging of the plastic rearrangements that occur during the compression. Crystals behave elastically until the force reaches a critical value and the crystal fractures. All bonds break simultaneously in a catastrophic event and the crystal can no longer sustain any stress, the force decreases to zero. We find that the minimal number of bonds that must be broken to allow rearrangement of the crystal corresponds to forming equilateral triangles of droplets. Once the aggregate breaks, droplets slide past one another to rearrange into a new crystal with one less row, and the process repeats. A crystal with p initial rows will undergo $(p-1)$ transitions. During the compression phase, droplets are modelled as individual Hookean springs and the resulting aggregate can be modelled by an assembly of springs with an equivalent spring constant. This simple model captures well the elastic properties of the aggregates. Finally, by equating the stored elastic energy during compression with the adhesion energy released by breaking bonds between droplets, we can predict the yield properties of the crystal for each transition.

Initial versions of this experiment were designed by Solomon Barkley and Kari Dalnoki-Veress. Solomon wrote the first data analysis scripts and conducted preliminary experiments. I improved the experimental setup to reduce evaporation of the aqueous phase and improve the reproducibility of the experiment. I collected all experimental data presented in this manuscript, in collaboration with Kari Dalnoki-Veress, and wrote additional scripts to analyze the data. I proposed the first theoretical model to capture the elastic and yield properties of the aggregate with the guidance of Kari Dalnoki-Veress. The theoretical model was improved upon by Pierre Soulard, Thomas Salez and Elie-Raphaël. I prepared the first draft of the manuscript which was subsequently edited by all contributors.

Volume 17
Number 5
7 February 2021
Pages 1109–1446

Soft Matter

rsc.li/soft-matter-journal

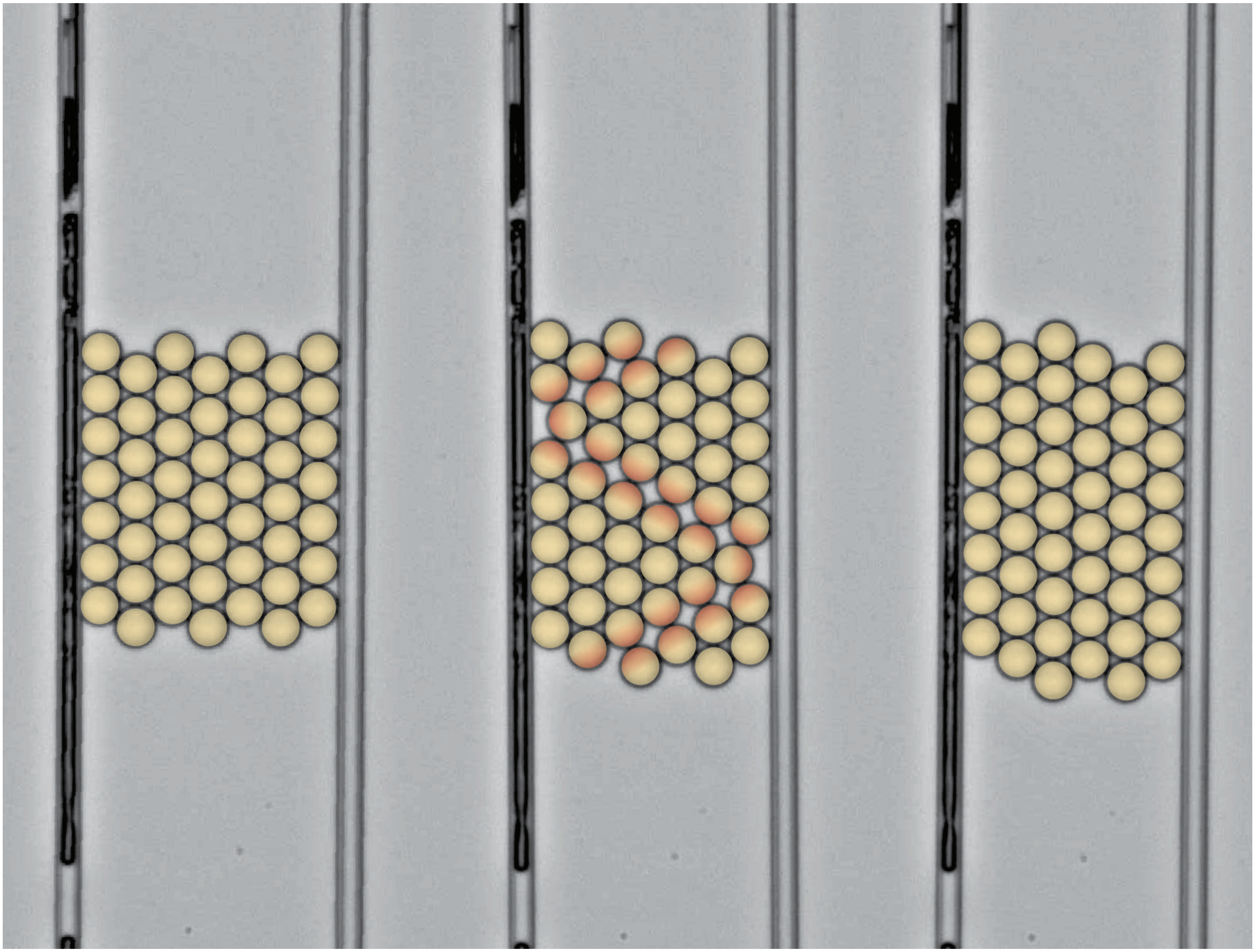

ISSN 1744-6848

ROYAL SOCIETY
OF **CHEMISTRY**

PAPER
Kari Dalnoki-Veress *et al.*
Mechanical properties of 2D aggregates of oil droplets as model mono-crystals

Soft Matter

PAPER

View Article Online
View Journal | View Issue

Cite this: *Soft Matter*, 2021, **17**, 1194

Mechanical properties of 2D aggregates of oil droplets as model mono-crystals†

Jean-Christophe Ono-dit-Biot,[a] Pierre Soulard,[b] Solomon Barkley,[a] Eric R. Weeks,[c] Thomas Salez,[de] Elie Raphaël[b] and Kari Dalnoki-Veress*[ab]

Received 25th June 2020,
Accepted 1st December 2020

DOI: 10.1039/d0sm01165g

rsc.li/soft-matter-journal

We investigate the elastic and yielding properties of two dimensional defect-free mono-crystals made of highly monodisperse droplets. Crystals are compressed between two parallel boundaries of which one acts as a force sensor. As the available space between boundaries is reduced, the crystal goes through successive row-reduction transitions. For small compression forces, the crystal responds elastically until a critical force is reached and the assembly fractures in a single catastrophic global event. Correspondingly there is a peak in the force measurement associated with each row-reduction. The elastic properties of ideal mono-crystal samples are fully captured by a simple analytical model consisting of an assembly of individual capillary springs. The yielding properties of the crystal are captured with a minimal bond breaking model.

1 Introduction

Historically, foams have often been used as model materials, with an especially inspiring example being the use of bubble rafts to model the behaviour of a metallic structure proposed by Bragg and Nye.[1] Using bubbles instead of atoms, dislocations and grain boundaries were imaged directly and mechanical properties of the assembly were studied.[2] The use of foams, emulsions, and colloids has become a powerful tool to study fundamental questions such as the glass transition,[3–8] formation and melting of crystals,[9–12] the order-to-disorder transition[13–18] and jamming.[19–24] Complex biological systems can also be modeled using foams and emulsions.[25–28] One of the important characteristics of these model systems is their mechanical response to external stress such as compression or shear. The mechanical properties of such systems depend strongly on the volume fraction of suspended particles[29,30] as well as the interaction between particles.[31–34] Above a critical volume fraction, foams and emulsions behave as soft solids.[33,35–38] For small applied stress, the assembly deforms elastically.[2,30] When the magnitude of the applied stress exceeds a critical value, given by the yield stress, plastic deformations occur and the material flows as a liquid. Several theoretical[39–42] and simulation[43–46] works have studied the connection between local plastic events and macroscopic flow. As the particles constituting the foam or the emulsion can be resolved individually,[4] studies linking microscopic plastic events to flow properties can also be conducted experimentally.[34,46–51]

In foams and emulsions, the nature of the constituting particles is also a key parameter in understanding the properties of the assembly. For example, the relevant scale for the elastic modulus of an assembly of oil droplets is set by the Laplace pressure.[30] Thus changing the size of the droplets or the interfacial tension modifies the elastic properties of the structure. The size distribution of the particles is also particularly important. Indeed, monodisperse particles can assemble into a crystal while polydispersity prevents crystallization.[52,53] Due to their perfect arrangement and periodicity, defect-free monodisperse crystals are well understood theoretically.[29] However, these mono-crystals are more challenging to study experimentally, as perfect monodispersity and crystalline order are difficult to achieve. Most experimental studies on colloidal crystals have focused on the study of polycrystals[34,35,51,54] and in particular plastic deformations resulting from shear imposed on structurally disordered materials.[55,56] For crystals, it is known that the mechanical properties, and in particular the yield stress, is dictated by dislocations or local structural disorder.[57] To date, only a small number of experimental studies have been able to produce ideal defect-free mono-crystals[58,59] and the study of their elastic and yielding properties warrants further attention.

In this study we use lightly attractive oil droplets in water with low polydispersity to create mono-crystals made of tens of droplets. Due to the droplets being monodisperse combined with a small sample size, the aggregates are defect-free crystals.

---

[a] *Department of Physics & Astronomy, McMaster University, Hamilton, ON, L8S 4L8, Canada. E-mail: dalnoki@mcmaster.ca*
[b] *UMR CNRS Gulliver 7083, ESPCI Paris, PSL Research University, 10 rue Vauquelin, 75005 Paris, France*
[c] *Department of Physics, Emory University, Atlanta, GA 30322, USA*
[d] *Univ. Bordeaux, CNRS, LOMA, UMR 5798, F-33405 Talence, France*
[e] *Global Station for Soft Matter, Global Institution for Collaborative Research and Education, Hokkaido University, Sapporo, Japan*

† Electronic supplementary information (ESI) available. See DOI: 10.1039/d0sm01165g

In the experiments we simultaneously measure the mechanical response of these ideal mono-crystals under compression between two glass capillaries and image the rearrangements that cause yielding and plastic deformation of the structure. We find that crystals behave elastically until a critical force is applied and the crystal fractures. The bonds between droplets are broken in a coordinated manner, after which the aggregate can no longer sustain any stress. Upon further compression the structure rearranges into a new crystal with one less row of droplets. The elastic response and the yield properties are fully captured by a simple analytical model.

2 Experimental methods

The experimental chamber (55 × 30 mm^2), shown in Fig. 1, is made of two glass slides separated by a 3D-printed spacer of thickness 2.5 mm [dark grey wall in Fig. 1(a)]. This gap between the glass slides is 10^3 times larger than the size of the droplets. The chamber is filled with an aqueous solution with 3% (w/w) sodium dodecyl sulfate (SDS) and 1.5% (w/w) NaCl. The 3D-printed wall reduces evaporation of the solution and ensures a concentration that is approximately constant over the course of the experiments. At this concentration, the surfactant, SDS, assembles into micelles acting as a depletant resulting in a short-range attraction between the droplets.[60] Glass capillaries (World Precision Instruments, USA) are pulled to a diameter of about 10 μm over several centimeters in length using a pipette puller (Narishige, Japan). One of these pipettes, the "droplet pipette" is used to produce highly monodisperse droplets of mineral oil, with size proportional to the tip radius of the pipette, using the snap-off instability.[61] The droplets used in this experiment have a radius R = 18.9 ± 0.3 μm. The uncertainty on the radius corresponds to the precision on the measurement of the droplet size. As droplets are produced using the snap-off instability, the droplet polydispersity is less than 0.7%.[61] Droplets are buoyant and accumulate under the top glass slide. Aggregates of oil droplets are assembled droplet-by-droplet into 2D crystals with arbitrary shapes (see Movie M1 in ESI†). The crystals are made up of p rows and q droplets per row, with the initial aggregate defined as $p = p_{\text{ini}}$ and $q = q_{\text{ini}}$ [see Fig. 1(c)]. Under compression, the crystal rearranges with corresponding values of p and q, while keeping the total number of droplets, N_{tot}, constant. Aggregates are compressed between two micropipettes: the "pushing pipette" and the "force-sensing pipette". The "pushing pipette" is a short and stiff pipette used to compress the aggregates. The pushing pipette is affixed to a motorized translation stage and moved at a constant speed, v = 0.3 μm s^{-1}, for all experiments. The "force-sensing pipette" is a long compliant pipette. Its deflection is used to measure the forces applied to the aggregate as it is compressed.[62] The pipette is pulled to a diameter of ~10 μm over a length of ~3 cm to be sensitive to forces as small as ~100 pN. The thin section of the pipette is locally and temporarily heated to soften the glass such that the pipette can be bent into a shape that fits in the small chamber while maximizing its total length [see pipette (iii) in Fig. 1(a)]. The pushing and force-sensing pipettes are aligned to be as parallel as possible in order to compress the aggregate uniformly. A misalignment would result in one side of the aggregate breaking earlier than the other. The chamber is placed atop of an inverted optical microscope for imaging while the aggregates are compressed and images are collected at a frame rate of 1.8 Hz.

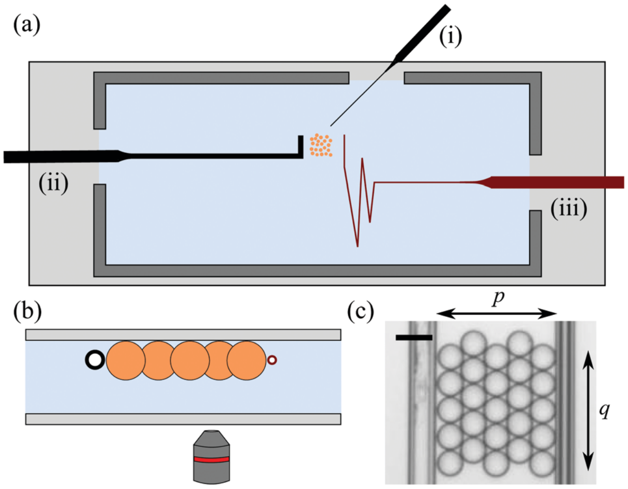

Fig. 1 (a) Schematic top view of the experimental chamber. The typical dimensions of the wall (dark grey) are 55 × 30 × 2.5 mm^3. The "droplet pipette", "pushing pipette", and "force-sensing pipette" are labelled as (i), (ii) and (iii) respectively. (b) Schematic side view (not to scale). The buoyant droplets are assembled into a quasi 2D crystal under the top glass plate. The pushing pipette (black circle) is moved at speed v = 0.3 μm s^{-1} to compress the aggregate and the force-sensing pipette (red circle) is used to measure forces. Both pipettes are placed near the equatorial plane of the droplets so forces are applied horizontally. (c) Optical microscopy image of a typical crystal (scale bar is 50 μm). p refers to the number of rows of droplets and q the number of droplets per row. In this example $p = q = 5$.

The distance between the pushing pipette and the force-sensing pipette, δ, is measured using cross-correlation analysis between images. This analysis leads to a sub-pixel resolution and in this study a precision of ~0.1 μm.[62] The deflection of the pipette is measured using the cross-correlation analysis and converted into a force using the calibrated spring constant k_{p} = 1.3 ± 0.1 nN μm^{-1} of the force-sensing pipette.[62] The crystal is fractured and rearranges under compression by breaking adhesive bonds between droplets. Using the optical microscopy images, fracture events observed directly can be linked to features in the measured force-distance curves.

3 Results and discussion

3.1 Compression of colloidal crystals

Fig. 2(a) shows the measured force as a function of the distance between the pipettes, δ, for a crystal with initial geometry (p_{ini} = 7; q_{ini} = 7). As the crystal is compressed, the distance δ decreases over time; thus, in the plots the experiment progresses from right to left as indicated by the time arrow in Fig. 2(a). The trace shows six distinct peaks corresponding to six fracture events (see movie M2 in ESI†). To accommodate for the decreasing space between the pipettes, the number of rows of droplets, p, must be reduced.

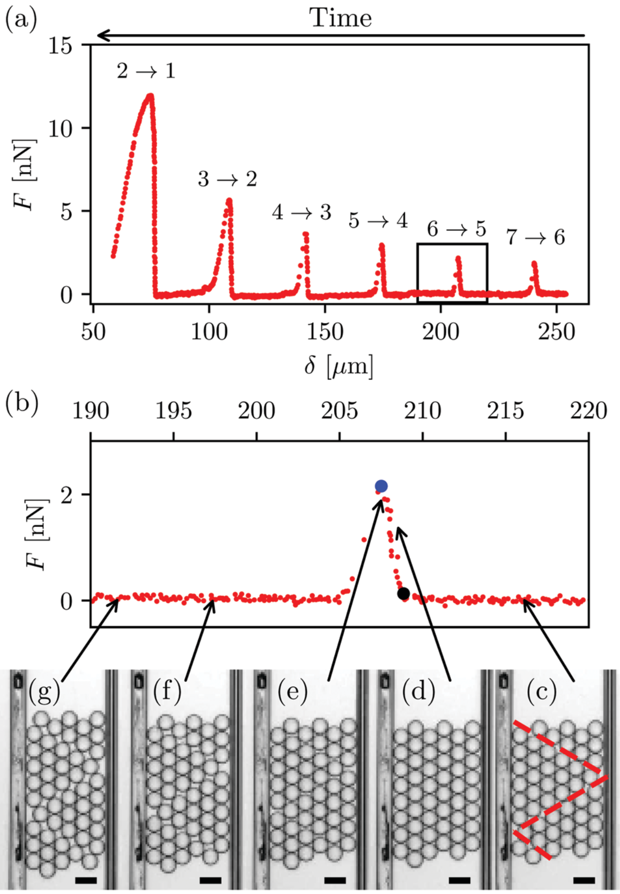

Fig. 2 (a) Measured force, F, as a function of the distance between the pipettes, δ for a crystal with an initial configuration given by $p_{\text{ini}} = 7$; $q_{\text{ini}} = 7$, and a droplet size R = 18.9 ± 0.3 μm. The distance between pipettes, δ, decreases over time as the aggregate is compressed. The crystal undergoes six well defined transitions $p \rightarrow (p - 1)$ evidenced by six local maxima in the force curve. (b) Zoom of the 6 → 5 transition force peak, corresponding to the black square shown in panel (a). The right side of the peak, rising of the force, occurs during the compression of the crystal. The onset of the peak is shown by the black dot. The force reaches a maximum F_c, shown by the blue dot, as the crystal fractures. (c–g) Sequence of microscopy images of the crystal being compressed (scale bar is 50 μm). During a fracture event, all bonds are broken in a single catastrophic and coordinated manner along fracture lines shown by the red dashed lines in (c). The fracture patterns for 2D crystals consist of equilateral triangles with $(p - 1)$ droplets on the triangle's side [see (c), (f) and (g)].

These breaking events are referred to as row-reduction transitions: from $p = 7$ to $p = 6$ rows of droplets [designated as 7 → 6 in Fig. 2(a)], followed by 6 → 5, 5 → 4, *etc.*, until the last transition 2 → 1. A zoom of the second transition (6 → 5) is shown in Fig. 2(b) along with an optical image sequence corresponding to this specific transition. To undergo a transition, adhesive bonds between droplets that arise from SDS-induced depletion forces must be broken. The droplet assembly maximizes the total number of bonds between droplets, creating a hexagonal structure. We find that bonds break in a catastrophic and coordinated manner. As the crystal transitions from p to $(p - 1)$ rows, bonds are broken along 60° fracture lines with respect to the pipettes [red dashed lines on Fig. 2(c)], resulting in equilateral triangles with $(p - 1)$ droplets on their side. This breaking pattern corresponds to the least number of broken bonds – and thus the minimum energy cost – for the aggregate to undergo the row reduction transition. A simple geometrical calculation, ignoring edge effects, shows that the number b of broken bonds satisfies $b = 2q$ (see Appendix for more details). We emphasize that the crystal structures studied here are not infinite, and hence ignoring edge effects is an important simplifying approximation.

The bond breaking events observed are T1 events during which four droplets exchange neighbours[50,51] resulting in a slip-line (the 2D equivalent of a slip-plane in 3D). T1 events along a fracture line at 60° have also been reported as monodisperse droplets flow through a tapered channel.[51,63] Similar observations for simulations of lightly repulsive colloids under compression have been made.[64] After the fracture, the $(p - 1)$-sided equilateral triangles slide past each other to rearrange into a new crystal with $(p - 1)$ rows of droplets accommodated between the pushing and the force-sensing pipettes. During the sliding of the structure between two fracture events the force is nearly zero as can be seen in Fig. 2(b). This indicates that the compression is conducted at low enough speed (0.3 μm s^{-1}) to ensure that the viscous drag is negligible. Nevertheless, the sharp decay of the force peak corresponds to the resolved relaxation of the force-sensing pipette as the entire system evolves through a viscous medium [Fig. 2(a) and (b)]. Separate experiments have shown that the relaxation of the force-sensing pipette in absence of droplets is almost instantaneous on the relevant timescale. Therefore, the decay of the force mentioned above is mainly due to the viscous damping experienced by the droplets, though it remains fast compared to the timescale of the experiment. For example, for the peak shown in Fig. 2(b), the decay occurs over 5 s while the experiment takes 10 min (the frame rate is 1.8 Hz). The relaxation of the pipette takes longer for later transitions, for example the 2 → 1 transition, as more droplets must flow over a larger distance.

As a crystal aggregate is compressed, the force builds and the system is elastically deformed. The elastic energy stored eventually reaches the point of breaking the adhesive bonds. Another interesting feature of the force trace is the evolution of the peak magnitude with the transition index. From Fig. 1(a), it is clear that the force required to fracture the structure becomes larger from one transition to the next, as p diminishes. This force increase can be explained by the number of bonds that need to be broken to enable the transition. In going from one transition to the next, the number of rows, p, decreases and thus q increases ($N_{\text{tot}} = pq$ is constant). Since q increases and the minimal number of broken bonds is given by $b = 2q$, a larger force is required with each subsequent transition.

3.2 Equivalent spring model

To quantitatively understand the evolution of the magnitude of the peaks for subsequent transitions, we developed a minimal analytical model. Let us focus on the onset of fracture, for example the peak shown in Fig. 2(b). If droplets were strict hard spheres, one would expect the rise of the peak (*i.e.* upon decreasing δ) to have an infinite slope. The fact that the force increases with a finite slope indicates that droplets are slightly deformable and the aggregate can withstand a certain amount of elastic deformation before breaking. However, the deformation of individual droplets remains extremely small and cannot be seen on optical microscopy images (see movie M2 in ESI†). To account for this capillary deformation, we model individual droplets as identical springs with spring constant k_1. This is consistent with previous studies that have investigated the deformation of a droplet under external forces.[27,65] At lowest order in the deformation, the restoring force can indeed be modelled as that of a capillary spring with a spring constant $k_1 = \mathscr{G}\gamma$ (see discussion in the appendix) directly proportional to the interfacial tension γ between oil and the SDS aqueous solution.[66] The proportionality constant $\mathscr{G}$ depends on the exact contact geometry between the droplets. The aggregates are thus made of q springs in parallel (along the same row) and p rows of springs in series. The resulting crystal can thus be represented by an equivalent spring with constant:

$$k_{\mathrm{eq}} = k_1 q/p. \tag{1}$$

Under compression, the restoring force is linear with slope k_{eq}. To validate this model, we measure the evolution of the equivalent spring constant of a crystal for the different transitions as the aspect ratio q/p changes from one transition to another.

Fig. 3(a) shows the rise of the force peaks as a function of the compression of the crystal for the six $p \rightarrow (p-1)$ transitions. For each peak, the compression is defined as $\Delta x = \delta_0^p - \delta$ with δ_0^p the onset of compression for each transition, corresponding to the black dot in Fig. 2(b). Within the resolution of the experiment, the force is linear with the compression. The peaks flatten and deviate from the early linear behaviour for larger values of Δx. This is particularly noticeable on the curve corresponding to the $2 \rightarrow 1$ transition and can be explained by a slight misalignment of the pushing and force-sensing pipette. The misalignment results in parts of the crystal breaking earlier than the rest (movie M2 in ESI†). The experiment is more sensitive to misalignment for the later transitions as the lateral extent of the crystal is larger (increasing number q of droplets per rows). The non-linear part of the curve that deviates from the linear behaviour is excluded from the linear fit as the model is only valid in the limit where all droplets are in contact and prior to the onset of fracture events. This non-linear behaviour is especially obvious in the case of the $2 \rightarrow 1$ transition in Fig. 3(a) where at high forces the crystal fracture initiates at one edge of the structure (see Movie M2 in ESI†). The slope of each force curve k_{eq} is extracted and plotted against the ratio q/p as suggested by eqn (1) and shown in Fig. 3(b). The equivalent spring constant k_{eq} is found to scale linearly with q/p, as predicted by eqn (1), with a slope corresponding to $k_1 \approx 1.46$ mN m^{-1}. The value of surface tension extracted for the relation $k_1 = \mathscr{G}\gamma$ depends on the geometrical factor $\mathscr{G}$. Literature values for the interfacial tension are in the $\sim$5–10 mN m^{-1} range,[30,67] which is consistent with what we find for a geometrical pre-factor, $\mathscr{G}$, on the order of 1. The assembly of droplets thus behaves like a perfect 2D Hookean solid, where the 2D-equivalent applied stress $\sigma = F/(2qR)$ is equal to the strain $\varepsilon \sim \Delta x/(2pR)$ times a 2D-equivalent Young's modulus $E \sim \mathscr{G}\gamma$.

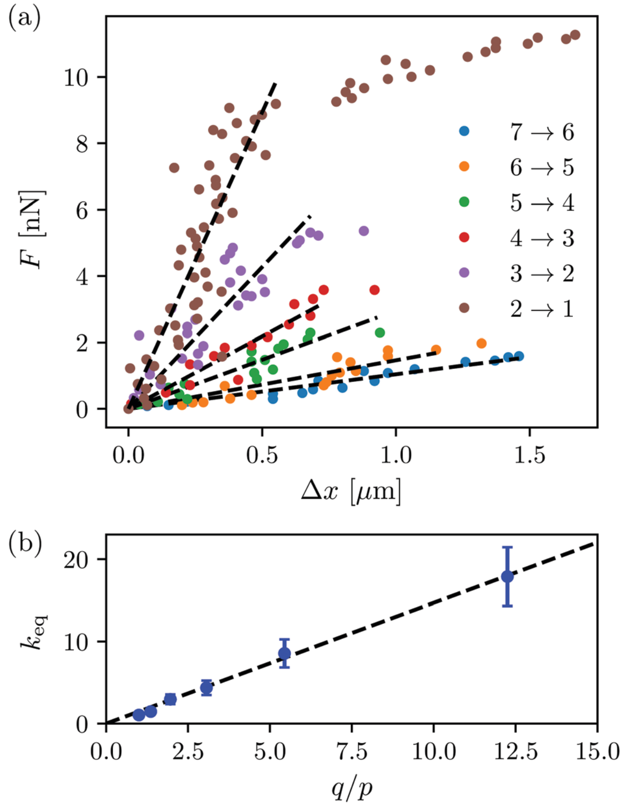

Fig. 3 (a) Force as a function of the compression Δx of the aggregate for the six different transitions. The part of the force shown is the rising one, that corresponds to the force between the black and blue dot in Fig. 2(b), from onset to peak. The compression is defined to be equal to zero at the onset. The black dashed lines are linear best fits to the data. Each dashed line is only fitted to the elastic part of the compression. The slopes of these lines are the equivalent spring constants of the cluster, k_{eq}. (b) Evolution of k_{eq} with the aspect ratio q/p. The black dashed line is the best fit to eqn (1). The error bars correspond to the uncertainty on the slopes of the linear fits in panel (a). Indeed, these linear fits are sensitive to the first and last data points included in the fit.

In the equivalent spring model, it is assumed that the droplets can store elastic energy under compression and the stretching of adhesive bonds is neglected. Indeed, the adhesion comes from the depletion forces induced by the SDS micelles and can be described by the Asakura-Oosawa potential.[68] This potential has a negative curvature which means that as soon as the adhesive force is overcome, the bond between droplets breaks completely. The range of the depletion forces is set by the nanometric size of the SDS micelles ($\sim$5 nm) and is thus short-ranged compared to the elastic deformation of the droplets, and the strength of adhesion is dependant on the concentration of SDS, which is kept fixed here to simplify the system.

Having validated the equivalent spring model, if the aggregate maintains a compressed hexagonal configuration the droplets deform, and the stored elastic energy increases with compression as $E_{\mathrm{s}} = k_{\mathrm{eq}}\Delta x^2/2$. In order for the cluster to fracture, bonds between droplets must be broken. As mentioned above, the minimum number of bonds that must break for a 2D hexagonal crystal to rearrange is $b = 2q$. As a result, crystals fracture when the stored elastic energy, $k_{\text{eq}}\Delta x_c{}^2/2$, reaches the threshold $2qE_1$, where E_1 is the depletion-induced adhesive energy associated with breaking a single bond. This criterion corresponds to a critical yield force $F_c = k_{\text{eq}}\Delta x_c$, which is equal to:

$$F_c = 2N_{\text{tot}}\sqrt{\frac{k_1E_1}{p^3}}. \tag{2}$$

The model developed in this study assumes an ideal experiment where the pushing and the force-sensing pipettes are strictly parallel and the b bonds are broken simultaneously for every transition. As such, eqn (2) represents an upper bound for the measured real force. It can be tested experimentally by recording F_c, for each transition $p \to (p - 1)$, and with aggregates of different initial geometries (p_{ini}, q_{ini}). For example, the compression experiment shown in Fig. 2(a) for droplets with radius $R = 18.9 \pm 0.3$ μm, leads to six values of F_c for $p = 7$ to $p = 2$. After a compression experiment is completed, the same droplets can be reassembled into a new crystal with a different initial geometry. By using the same droplets from one experiment to another, we ensure that the energy per bond E_1 and spring constant k_1 remain constant.

In Fig. 4(a), we plot the experimentally measured force at failure normalized by N_{tot} as a function of $p^{-3/2}$ for five different experiments with different initial geometries, as suggested by eqn (2). The best fit of eqn (2) to all the data (dot-dash line) corresponds to a bond energy of $E_1 = 0.096$ fJ. The depletion energy per unit area that must be overcome to break an adhesive bond can be expressed as $W = \rho kTa$,[69] with $\rho \sim 5 \times 10^{23}$ m^{-3} the number concentration of SDS micelles, $a \sim 5$ nm the radius of a micelle and k the Boltzmann constant. With an estimate of the contact patch to be $R_p \sim 0.1R$, one can obtain the order of the energy per unit bond to be $E_1 = W\pi R_p{}^2 \sim \rho kTa\pi R_p{}^2 \sim 0.13$ fJ, an approximate value that is consistent with the best fit value. However, any imperfections in the experiment or thermal fluctuations, ensure that one can never measure a force greater than that corresponding to the ideal crystal. For comparison we also show eqn (2) with $E_1 = 0.2$ fJ (dashed line) corresponding to a bond energy adjusted such that all the data lies below the upper bound given by the theory.

Using the experimental estimated value of $E_1 \approx 0.2$ fJ, and the spring constant $k_1 \approx 1.46$ nN m^{-1} of individual droplets, one can construct the theoretical force curve for an ideal system through the various transitions. Fig. 4(b) shows the force trace for a ($p_{\text{ini}} = 7$; $q_{\text{ini}} = 7$) crystal (red curve). Eqn (2) predicts the upper-bound values of the force peaks which are shown with the blue dots. Additionally, from eqn (1) we have that upon compression the force rises linearly with slope $k_{\text{eq}} \approx (1.46q/p)$ mN m^{-1}, which is shown with the black dashed lines for the various transitions. We find good agreement between the simple analytical model proposed in this study and the experimental results. The discrepancy between the measured and the predicted maximum forces is larger for the later transitions (for example 2 → 1). This is expected since the experiment is more sensitive to imperfections as the lateral extent of the crystal becomes larger (increasing q).

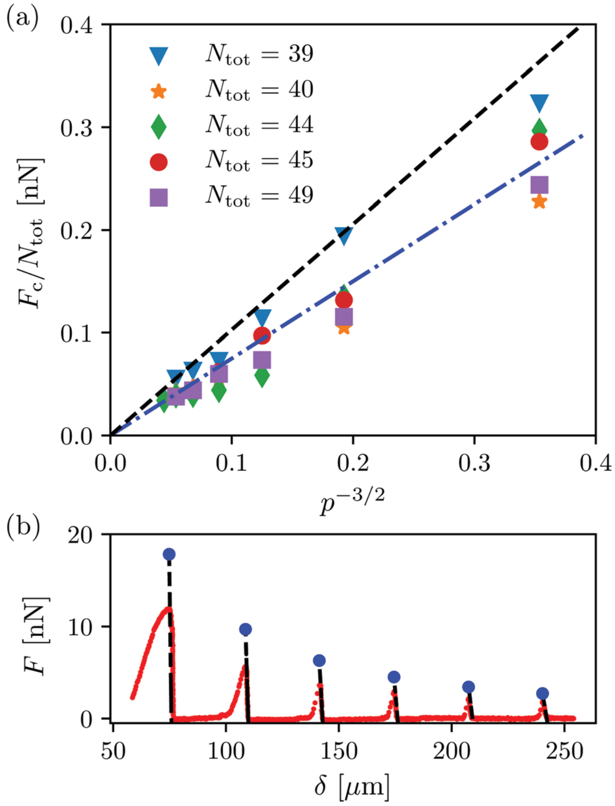

Fig. 4 (a) Evolution of the peak force, F_c normalized by N_{tot}, as a function of $p^{-3/2}$ for five different compression experiments with different initial geometries. The size of the droplets is kept constant to $R = 18.9 \pm 0.3$ μm. The initial geometries are: (▼) 7 alternating rows of 6 and 5 droplets; (★) $p_{\text{ini}} = 5$; $q_{\text{ini}} = 8$; (♦) 8 alternating rows of 6 and 5 droplets; (●) $p_{\text{ini}} = 5$; $q_{\text{ini}} = 9$; (■) $p_{\text{ini}} = 7$; $q_{\text{ini}} = 7$. The dash-dot line corresponds to the best fit of eqn (2) to all the data with the energy per bond $E_1 = 0.096$ fJ, while the dashed line ensures all measured maximal forces fall below the line with $E_1 \approx 0.2$ fJ. (b) Measured force as a function of the distance between pipettes for a ($p_{\text{ini}} = 7$; $q_{\text{ini}} = 7$) crystal. The blue data points correspond to the maximal forces, predicted from eqn (2) with $E_1 \approx 0.2$ fJ, which would be expected for an ideal experiment. The black dashed lines correspond to the theoretical predictions from eqn (1) with $k_1 \approx 1.46$ mN m^{-1}.

The study presented here focusses on the mechanical properties of mono-crystals. In reality, most crystals are poly-crystalline with defects in their structure. Introducing defects in mono-crystals has been investigated with the model system described here, and the results are presented in Ono-dit-Biot *et al.*[18] Defects are added through the introduction of smaller or larger droplets into the aggregate. It was found that even a small number of defects has a significant impact on the mechanical properties of the assembly.

4 Conclusions

In summary, we prepared 2D defect-free colloidal mono-crystals by assembling highly monodisperse droplets into small size aggregates. The force trace measured during compression shows a well defined number of peaks corresponding to row-reduction transitions. Using our experimental apparatus, we are able to measure macroscopic mechanical properties while monitoring individual droplets. Under small applied forces, crystals respond elastically. A simple assembly of capillary springs, representing individual droplets, captures the elastic properties of the crystal. As the aggregate is further compressed and a critical yield force is reached, the crystal fails catastrophically, but in a coordinated manner. Plastic T1 events occur simultaneously along 60° fracture lines, resulting in equilateral triangles of droplets which slide past each other. This defect is a slip-line, the 2D equivalent of a slip-plane in 3D. The droplets eventually reassemble into a new crystal with one less row. An analytical model balancing the stored elastic energy upon compression with the released depletion-induced adhesion energy during bond breaking, allows us to predict the yield point. The satisfactory agreement between the model and experiments highlights the validity of assuming that the edge effects of the finite crystals can be ignored. We expect this assumption to break down for smaller aggregates. While here the attraction between droplets is caused by depletion forces, the model is expected to remain valid for other sources of adhesion. The low-polydispersity droplet system with controllable adhesion strength provides an ideal platform for investigating material properties while individual constituents can be directly imaged.

Conflicts of interest

There are no conflicts to declare.

Appendix

Spring constant of a droplet

Individual droplets are modeled as capillary springs of constant k_1, directly proportional to the surface tension γ between the oil and the aqueous solution. In this section, we provide details to justify this model analytically. Consider two oil droplets, with initial radius R, compressed against one another as shown in Fig. 5.

During compression, the volume of the droplet is conserved but the radius, R_1, and thus the surface area of the droplet is modified. The change in surface area results in a capillary energetic cost. Following the work by Pontani *et al.*,[27] one can show that the change in energy is $\Delta E = \gamma\pi R^2\theta^4/2$. For the spring model developed in this study, the change in energy must be expressed as a function of the compression of an individual droplet, x. Using simple geometrical arguments, the compression can be written as[69] $x \simeq {R_\text{p}}^2/R$, with R_p the radius of the patch between droplets (see Fig. 5). In the limit of small deformations: $\theta \simeq R_\text{p}/R$. Using these two expressions, the change in surface energy can be written as:

$$\Delta E \simeq \tfrac{1}{2}\gamma\pi x^2. \tag{3}$$

Comparing eqn (3) to the energy $E_\text{s} = k_1x^2/2$ stored in a spring naturally leads to $k_1 = \pi\gamma$. Taking into account the hexagonal geometry of our droplet assemblies would lead to a different pre-factor for the effective individual spring constant $k_1 = \mathscr{G}\gamma$. Nevertheless, this simple analytical calculation justifies why droplets can be modelled as springs, and that the associated spring constant is directly proportional to the surface tension γ.

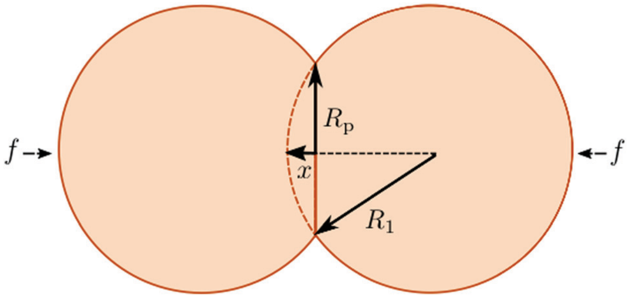

Fig. 5 Schematic of two oil droplets being pushed against one another with force f. The droplets deform by an amount x during compression and a patch with radius R_p is formed between the two droplets. The volume of the droplet is conserved during compression and thus the initial radius, R, increases to a different value, R_1.

Minimal bond breaking model

As explained in the main text and evidenced by Fig. 1, the aggregates break forming equilateral triangles. This geometry minimizes the number of bonds that needs to be broken. To justify why the number of bonds that must be broken is equal to $2q$, one considers the number of droplets per triangle:

$$d = \sum_{i=1}^{p-1} i = \frac{p(p-1)}{2}. \tag{4}$$

Therefore, the number of triangles t for a transition (excluding edge effects) is:

$$t = \frac{N_\text{tot}}{d} = \frac{2q}{p-1}. \tag{5}$$

The bonds are broken along the edge of the triangles only, leading to $(p - 1)$ bonds broken per triangle. Only one side of the triangle is considered to avoid double counting. The total number of bonds b broken during a transition is thus given by:

$$b = t(p - 1) = 2q. \tag{6}$$

Acknowledgements

We gratefully acknowledge financial support by the Natural Science and Engineering Research Council of Canada. The work of E. R. W. was supported by the National Science Foundation (CBET-1804186). We also thank Maxence Arutkin for preliminary discussions.

References

1 W. L. Bragg and J. F. Nye, *Proc. R. Soc. A*, 1947, **190**, 474–481.
2 W. L. Bragg and W. M. Lomer, *Proc. R. Soc. A*, 1949, **196**, 171–181.

3 P. N. Pusey and W. van Megen, *Phys. Rev. Lett.*, 1987, **59**, 2083.
4 E. R. Weeks, J. C. Crocker, A. C. Levitt, A. Schofield and D. A. Weitz, *Science*, 2000, **287**, 627–631.
5 G. L. Hunter and E. R. Weeks, *Rep. Prog. Phys.*, 2012, **75**, 066501.
6 V. N. Manoharan, *Science*, 2015, **349**, 1253751.
7 B. Illing, S. Fritschi, H. Kaiser, C. L. Klix, G. Maret and P. Keim, *Proc. Natl. Acad. Sci. U. S. A.*, 2017, **114**, 1856–1861.
8 S. Vivek, C. P. Kelleher, P. M. Chaikin and E. R. Weeks, *Proc. Natl. Acad. Sci. U. S. A.*, 2017, **114**, 1850–1855.
9 D. W. Schaefer and B. J. Ackerson, *Phys. Rev. Lett.*, 1975, **35**, 1448.
10 P. N. Pusey and W. van Megen, *Nature*, 1986, **320**, 340–342.
11 A. M. Alsayed, M. F. Islam, J. Zhang, P. J. Collings and A. G. Yodh, *Science*, 2005, **309**, 1207–1210.
12 Z. Wang, F. Wang, Y. Peng, Z. Zheng and Y. Han, *Science*, 2012, **338**, 87–90.
13 P. J. Yunker, Z. Zhang and A. G. Yodh, *Phys. Rev. Lett.*, 2010, **104**, 2–5.
14 M. Hanifpour, N. Francois, S. M. V. Allaei, T. Senden and M. Saadatfar, *Phys. Rev. Lett.*, 2014, **113**, 1–5.
15 C. P. Goodrich, A. J. Liu and S. R. Nagel, *Nat. Phys.*, 2014, **10**, 1–4.
16 N. C. Keim and P. E. Arratia, *Soft Matter*, 2015, **11**, 1539–1546.
17 P. Charbonneau, E. I. Corwin, L. Fu, G. Tsekenis and M. van Der Naald, *Phys. Rev. E*, 2019, **99**, 020901.
18 J.-C. Ono-dit Biot, P. Soulard, S. Barkley, E. R. Weeks, T. Salez, E. Raphaël and K. Dalnoki-Veress, *Phys. Rev. Res.*, 2020, **2**, 023070.
19 A. J. Liu and S. R. Nagel, *Nature*, 1998, **396**, 21–22.
20 V. Trappe, V. Prasad, L. Cipelletti, P. Segre and D. A. Weitz, *Nature*, 2001, **411**, 772–775.
21 C. S. O'Hern, L. E. Silbert, A. J. Liu and S. R. Nagel, *Phys. Rev. E: Stat., Nonlinear, Soft Matter Phys.*, 2003, **68**, 011306.
22 E. I. Corwin, H. M. Jaeger and S. R. Nagel, *Nature*, 2005, **435**, 1075–1078.
23 A. J. Liu and S. R. Nagel, *Annu. Rev. Condens. Matter Phys.*, 2010, **1**, 347–369.
24 D. Bi, J. Zhang, B. Chakraborty and R. P. Behringer, *Nature*, 2011, **480**, 355–358.
25 T. Hayashi and R. W. Carthew, *Nature*, 2004, **431**, 647–652.
26 D. Gonzalez-Rodriguez, K. Guevorkian, S. Douezan and F. Brochard-Wyart, *Science*, 2012, **338**, 910–917.
27 L.-L. Pontani, I. Jorjadze, V. Viasnoff and J. Brujic, *Proc. Natl. Acad. Sci. U. S. A.*, 2012, **109**, 9839–9844.
28 S. Douezan and F. Brochard-Wyart, *Soft Matter*, 2012, **8**, 784–788.
29 H. Princen, *J. Colloid Interface Sci.*, 1983, **91**, 160–175.
30 T. Mason, J. Bibette and D. Weitz, *Phys. Rev. Lett.*, 1995, **75**, 2051.
31 E. Irani, P. Chaudhuri and C. Heussinger, *Phys. Rev. Lett.*, 2014, **112**, 188303.
32 M. Grob, C. Heussinger and A. Zippelius, *Phys. Rev. E: Stat., Nonlinear, Soft Matter Phys.*, 2014, **89**, 050201.
33 D. Bonn, M. M. Denn, L. Berthier, T. Divoux and S. Manneville, *Rev. Mod. Phys.*, 2017, **89**, 035005.
34 I. Golovkova, L. Montel, E. Wandersman, T. Bertrand, A. M. Prevost and L.-L. Pontani, *Soft Matter*, 2020, **16**, 3294–3302.
35 T. Mason, J. Bibette and D. Weitz, *J. Colloid Interface Sci.*, 1996, **179**, 439–448.
36 P. Coussot, J. Raynaud, F. Bertrand, P. Moucheront, J. Guilbaud, H. Huynh, S. Jarny and D. Lesueur, *Phys. Rev. Lett.*, 2002, **88**, 218301.
37 J. Goyon, A. Colin, G. Ovarlez, A. Ajdari and L. Bocquet, *Nature*, 2008, **454**, 84–87.
38 B. Dollet and C. Raufaste, *C. R. Phys.*, 2014, **15**, 731–747.
39 G. Picard, A. Ajdari, F. Lequeux and L. Bocquet, *Eur. Phys. J. E: Soft Matter Biol. Phys.*, 2004, **15**, 371–381.
40 L. Bocquet, A. Colin and A. Ajdari, *Phys. Rev. Lett.*, 2009, **103**, 036001.
41 K. Kamrin and G. Koval, *Phys. Rev. Lett.*, 2012, **108**, 178301.
42 A. Nicolas and J.-L. Barrat, *Phys. Rev. Lett.*, 2013, **110**, 138304.
43 A. Kabla and G. Debrégeas, *Phys. Rev. Lett.*, 2003, **90**, 258303.
44 S. Tewari, B. Tithi, A. Ferguson and B. Chakraborty, *Phys. Rev. E: Stat., Nonlinear, Soft Matter Phys.*, 2009, **79**, 011303.
45 V. Mansard, A. Colin, P. Chaudhuri and L. Bocquet, *Soft Matter*, 2013, **9**, 7489–7500.
46 B. Dollet, A. Scagliarini and M. Sbragaglia, *J. Fluid Mech.*, 2015, **766**, 556–589.
47 P. Schall, D. A. Weitz and F. Spaepen, *Science*, 2007, **318**, 1895–1899.
48 P. Jop, V. Mansard, P. Chaudhuri, L. Bocquet and A. Colin, *Phys. Rev. Lett.*, 2012, **108**, 148301.
49 E. D. Knowlton, D. J. Pine and L. Cipelletti, *Soft Matter*, 2014, **10**, 6931–6940.
50 D. Chen, K. W. Desmond and E. R. Weeks, *Phys. Rev. E: Stat., Nonlinear, Soft Matter Phys.*, 2015, **91**, 062306.
51 Y. Gai, C. M. Leong, W. Cai and S. K. Y. Tang, *Proc. Natl. Acad. Sci. U. S. A.*, 2016, **113**, 12082–12087.
52 P. N. Pusey, *J. Phys.*, 1987, **48**, 709–712.
53 S. Auer and D. Frenkel, *Nature*, 2001, **413**, 711–713.
54 A. Van der Net, W. Drenckhan, D. Weaire and S. Hutzler, *Soft Matter*, 2006, **2**, 129–134.
55 P. Schall, I. Cohen, D. A. Weitz and F. Spaepen, *Science*, 2004, **305**, 1944–1948.
56 D. Vecchiolla and S. L. Biswal, *Soft Matter*, 2019, **15**, 6207–6223.
57 C. Kittel, *et al.*, *Introduction to Solid State Physics*, Wiley, New York, 1976, vol. 8.
58 M. E. Rosa and M. Fortes, *Philos. Mag. A*, 1998, **77**, 1423–1446.
59 A. Gouldstone, K. J. Van Vliet and S. Suresh, *Nature*, 2001, **411**, 656.
60 J. Bibette, D. Roux and B. Pouligny, *J. Phys. II*, 1992, **2**, 401–424.
61 S. Barkley, S. J. Scarfe, E. R. Weeks and K. Dalnoki-Veress, *Soft Matter*, 2016, **12**, 7398–7404.
62 M. Backholm and O. Bäumchen, *Nat. Protoc.*, 2019, **14**, 594–615.

63 Y. Gai, A. Bick and S. K. Tang, *Phys. Rev. Fluids*, 2019, **4**, 014201.

64 D. McDermott, C. J. O. Reichhardt and C. Reichhardt, *Phys. Rev. E*, 2016, **93**, 1–12.

65 J. Brujić, S. F. Edwards, D. V. Grinev, I. Hopkinson, D. Brujić and H. A. Makse, *Faraday Discuss.*, 2003, **123**, 207–220.

66 P. Attard and S. J. Miklavcic, *Langmuir*, 2001, **17**, 8217–8223.

67 S. J. Rehfeld, *J. Phys. Chem.*, 1967, **71**, 738–745.

68 J. C. Crocker, J. A. Matteo, A. D. Dinsmore and A. G. Yodh, *Phys. Rev. Lett.*, 1999, **82**, 4352.

69 J. N. Israelachvili, *Intermolecular and Surface Forces*, Academic press, 2011.

Paper II

Rearrangement of two dimensional aggregates of droplets under compression: Signature of the energy landscape from crystal to glass

J.-C. Ono-dit-Biot, P. Soulard, S. Barkley, E. R. Weeks, T. Salez, E. Raphaël and K. Dalnoki-Veress, Phys. Rev. Res., **2**, 023070 (2020).

This paper presents our study of the crystal-to-glass transition using the mechanical properties of a model suspension made of lightly attractive oil droplets in water. Aggregates can be built with precise geometry and a precise fraction and location for the defects. As in the previous study, aggregates are compressed and the force required to break them is recorded. By systematically adding defects, the evolution of the force curve is monitored and compared to the reference force curve obtained for a defect free mono-crystal. The number of peaks in the force measurement, which each corresponds to a bond breaking event, is measured as the aggregates transition from an ideal mono-crystal to a bidisperse aggregate (model for a glass). We find that the number of force peaks increases sharply with the defect fraction before saturating at the glassy value. The yield energy as a function of disorder is also investigated. A single large energy barrier must be overcome for crystals to break, while glasses fracture through several smaller steps. The fracture events and the associated energy dissipated reflects the substructure introduced by disorder in the energy landscape. A minimal analytical model captures the different features observed experimentally.

This project is the natural extension of the former study. Solomon Barkley developed the early version of the experimental setup with Kari Dalnoki-Veress and looked at the impact of adding defects on the force measurement. I improved the experimental setup to reduce evaporation of the aqueous phase and improve the reproducibility of the experiment. My main contribution was the systematic investigation of the force measurement as disorder is increased in the structure. I collected all experimental data presented in this manuscript, in collaboration with Kari Dalnoki-Veress, and wrote scripts to analyze the data. The theoretical model which describes the evolution of the number of peaks in the force measurement as well as the change in work dissipated during the compression was developed by Pierre Soulard, Thomas Salez and Elie-Raphaël in collaboration with Kari Dalnoki-Veress, Eric Weeks and myself. I prepared the first draft of the manuscript which was subsequently edited by all contributors.

PHYSICAL REVIEW RESEARCH **2**, 023070 (2020)

Editors' Suggestion

Rearrangement of two dimensional aggregates of droplets under compression: Signatures of the energy landscape from crystal to glass

Jean-Christophe Ono-dit-Biot,[1] Pierre Soulard,[2] Solomon Barkley,[1] Eric R. Weeks,[3] Thomas Salez,[4,5]
Elie Raphaël,[2] and Kari Dalnoki-Veress[1,2,*]
[1]*Department of Physics & Astronomy, McMaster University, Hamilton, Ontario, Canada L8S 4L8*
[2]*UMR CNRS Gulliver 7083, ESPCI Paris, PSL Research University, 10 Rue Vauquelin, 75005 Paris, France*
[3]*Department of Physics, Emory University, Atlanta, Georgia 30322, USA*
[4]*Univ. Bordeaux, CNRS, LOMA, UMR 5798, F-33405 Talence, France*
[5]*Global Station for Soft Matter, Global Institution for Collaborative Research and Education, Hokkaido University, Sapporo, Japan*

(Received 22 September 2019; revised manuscript received 7 February 2020; accepted 12 March 2020;
published 23 April 2020)

We study signatures of the energy landscape's evolution through the crystal-to-glass transition by compressing two dimensional (2D) finite aggregates of oil droplets. Droplets of two distinct sizes are used to compose small aggregates in an aqueous environment. Aggregates range from perfectly ordered monodisperse *single* crystals to disordered bidisperse glasses. The aggregates are compressed between two parallel boundaries, with one acting as a force sensor. The compression force provides a signature of the aggregate composition and gives insight into the energy landscape. In particular, crystals dissipate all the stored energy through single catastrophic fracture events whereas the glassy aggregates break step by step. Remarkably, the yielding properties of the 2D aggregates are strongly impacted by even a small amount of disorder.

DOI: 10.1103/PhysRevResearch.2.023070

I. INTRODUCTION

Glassy materials are drastically different from crystals in their properties and cannot simply be described as crystals with defects [1]. The intrinsic disorder associated with molecules that do not neatly pack, or polydisperse colloidal spheres, prevents glasses from crystallizing [2,3]. Intense effort has been devoted to understanding glasses and the transition from an ordered crystal to a disordered glass. Microscopic properties such as the packing configuration can be accessed experimentally and provide insight into the crystal-to-glass transition [4–8]. But, these studies did not yield any conclusion regarding the difference in mechanical properties between crystals and glasses. To answer this question several numerical studies have been conducted, with a consistent conclusion: adding even a small amount of disorder to a system with crystalline packing results in properties, including mechanical properties, that are similar to those of amorphous structures [9–17]. However, conducting an equivalent experimental study is challenging. A beautiful experiment by Keim *et al.* showed that a small amount of disorder in a colloidal polycrystal results in a shear modulus similar to the one observed with a binary mixture of colloids [18]. However, an experimental characterization of the transition from a perfectly ordered single crystal to a disordered glass probed using mechanical properties is still lacking, since experimental systems are often polycrystalline and their properties dominated by grain boundaries. Here, we experimentally study the yielding properties of two dimensional (2D) finite-size aggregates of droplets that vary in the extent of disorder from a perfect crystal to a glass.

We use an emulsion since individual particles can easily be imaged to obtain both structural and dynamical information [19–21]. Colloids and emulsions are proven model systems for the study of glasses and jamming [19,22–25], force chains [26,27], and phase transitions in crystals [28]. Specifically, we use an emulsion of oil-in-water confined to a 2D finite-size aggregate. The droplets have a short-range attraction due to the depletion force, with an attraction energy much greater than thermal energy. When the droplets come into contact, they have an even stronger short-range repulsion. In our experiment, they act as hard spheres, given that the forces we exert are much less than those needed to deform the particles [27]. Such interactions are typical and generic to many systems. Furthermore, while many glass formers have greater complexity, it has been shown that even the simplest hard sphere model captures the main properties of bulk metallic glasses [29,30]. Thus, the experiments presented stimulate systems such as metallic and colloidal glasses. The amount of disorder is tuned by changing the relative fraction of large and small droplets in aggregates with a total of $N_{\text{tot}} = 20$ or 23 droplets. We investigate the transition from a perfectly ordered monodisperse crystal [31] to a disordered bidisperse glass [32–34] by systematically adding defects to the crystalline structure. The transition is studied through the

---

[*] dalnoki@mcmaster.ca

force required to globally compress and fracture the 2D aggregates while simultaneously monitoring microscopic reorganization.

While there are several advantages to the idealized model system presented, it is important to address how the inherent simplifications relate to real bulk systems. First, the droplets are large (~20 μm radius) so the system must be treated as athermal. The results presented are then the analogs of molecular systems which correspond to an adhesive glass or a crystal that is well below the solid-melt transition temperature. A second simplification is the 2D nature of the model system and it is certainly the case that dimensionality will influence the results. However, recent works [24,25,35] suggest that the glass transitions in 2D and 3D are fundamentally the same. While there may be differences due to the dimensionality, the underlying physics of the crystal-to-glass transition is expected to be common. A last point is that the number of particles studied is small compared to the bulk. However, the small system provides a unique "bottom-up" opportunity which complements bulk or many-particle approaches. Specifically, with the system studied, it is possible to (i) prepare perfect single crystals, rather than a polycrystal as is typical, (ii) add defects to the single crystals *one by one*, and (iii) obtain aggregate-scale force responses during compression, while (iv) *simultaneously* observing local structural re-arrangements. With the addition of even a small number of defects, we find (1) a rapid increase in the number of fracture events upon compression and (2) that the yield energy is distributed over many small steps in comparison to a single large step for a crystal. These experimental findings provide a signature of the increasingly complex energy landscape as the system transitions from crystal to glass. Finally, we develop an analytical model which supports the experimental data.

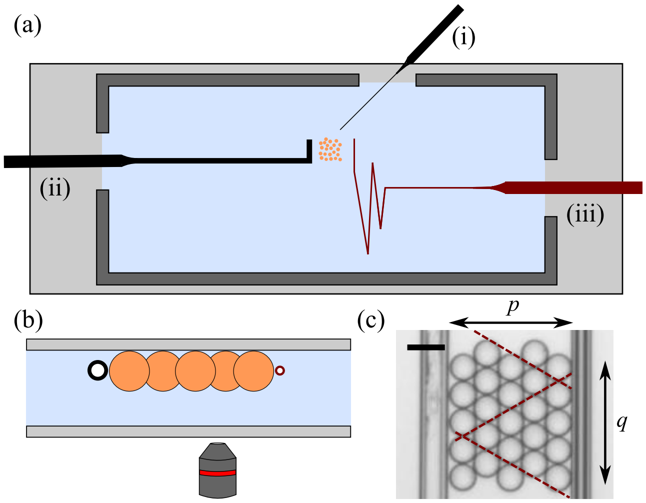

FIG. 1. (a) Schematic top view of the experimental chamber. The typical dimensions of the wall (dark grey) are 55 × 30 × 2.5 mm^3. The "droplet pipette," "pushing pipette," and "force-sensing pipette" are labeled as (i), (ii), and (iii) respectively. (b) Schematic side view (not to scale). The buoyant droplets form a quasi-2D aggregate bounded by the top glass plate. The pushing pipette (black circle on the left) and the force-sensing pipette (red circle on the right) are placed near the average equatorial plane of the droplets so forces are applied horizontally. (c) Optical microscopy image of a typical crystal (scale bar is 50 μm). Red dashed lines show observed fracture lines for a crystal when compressed.

II. EXPERIMENTAL DETAILS

The experimental setup, illustrated in Fig. 1(a), is a chamber (55 × 30 mm^2) is made of two glass slides separated by a gap of 2.5 mm, which is 10^3 times greater than the size of droplets. The chamber is filled with an aqueous solution of sodium dodecyl sulfate (SDS) at 3% and NaCl at 1.5%. This concentration of SDS leads to the formation of micelles acting as a depletant resulting in a short-ranged attraction between the droplets [36]. The adhesion between droplets can be clearly seen in Movie M1 in Supplemental Material [37]. In the absence of SDS, the adhesion is insufficient for the droplets to stick to each other and the aggregates cannot be assembled. Three small micropipettes are inserted into the chamber: the "droplet pipette," "pushing pipette," and "force-sensing pipette." Pipettes were pulled from glass capillaries (World Precision Instruments, USA) with a pipette puller (Narishige, Japan) to a diameter of about 10 μm over several centimeters in length. The "droplet pipette" produces monodisperse droplets, with size directly proportional to the tip radius of the pipette, using the snap-off instability [38]. The droplets are buoyant and form a 2D aggregate under the top glass slide [Fig. 1(b)]. The "pushing pipette" is short and stiff and is used to compress the aggregate. The pushing pipette is affixed to a translation stage and its speed set to $v = 0.3$ μm/s for all experiments. The "force-sensing pipette" is a long compliant pipette, and its deflection is used to measure forces applied to the aggregate [39,40]. To be sensitive to forces as small as ≈100 pN, the force-sensing pipette needs to be long (≈3 cm) and thin (≈10 μm). This long straight pipette is locally and temporarily heated to soften the glass such that it can be shaped to fit within the small chamber [see pipette (iii) in Fig. 1(a)]. Aggregates of oil droplets are assembled droplet by droplet and thus can be prepared into any arbitrary shape (see Movie M1 in Supplemental Material [37]). We use p_{ini} to refer to the initial number of rows of droplets, defined as parallel to the pipettes as shown in Fig. 1(c), while q_{ini} refers to the initial number of droplets per row. Under compression the aggregate rearranges to have p rows and q columns, while N_{tot} remains fixed. Using two "droplet pipettes" with different tip radii facilitates the preparation of well controlled bidisperse aggregates [38]. To increase the disorder in an aggregate, large droplets are replaced by small droplets (or vice versa). The chamber is placed atop an inverted optical microscope for imaging while the aggregates are compressed.

The distance between the pushing pipette and the force-sensing pipette, δ, is measured using cross-correlation analysis between images with a precision of ~0.1 μm [39,40]. Additionally, correlation analysis provides the deflection of the force-sensing pipette, which is converted to a force using the calibrated spring constant $k_{\text{p}} = 1.3 \pm 0.1$ nN/μm of the pipette [39,40]. The typical uncertainty on the force is $\delta F/F \approx 2\%$. The aggregate rearranges under compression by breaking adhesive bonds between droplets. These fracture events can be directly monitored with optical microscopy and related to the force measurement.

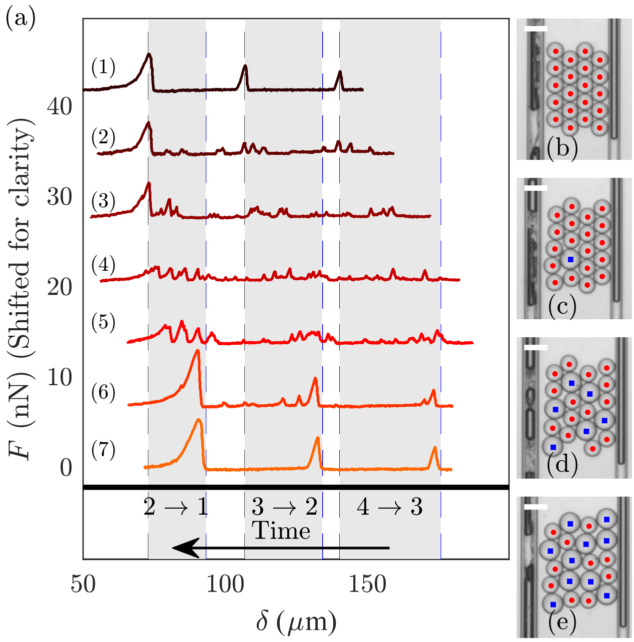

FIG. 2. (a) Force measurements, F, as a function of the distance between the pipettes, δ, for seven aggregates sharing the same lattice but with different compositions of small ($\mathcal{R} = 19.2 \pm 0.3$ μm) and large ($\mathcal{R} = 25.1 \pm 0.3$ μm) droplets. Here δ decreases with time as the aggregate is compressed and the aggregate changes from $p = 4$ to 1 as indicated at the bottom. Traces 1 to 7 correspond to $\{0; 1; 6; 10; 14; 19; 20\}$ large droplets with $N_{\text{tot}} = 20$. The black dashed lines correspond to the positions δ^p_{min} of the peak maxima for the crystal made of small droplets, while the blue dashed lines correspond to the positions δ^p_{max} of the peak onsets (i.e., upon compression as δ decreases) for the crystal made of large droplets. The shaded area highlights the different transitions during the compression. (b)–(e) Optical microscopy images of the aggregates, before compression, corresponding to traces 1 to 4. Blue squares correspond to large droplets and red circles to small droplets (scale bar is 50 μm).

Our droplets are essentially athermal. This can be seen by calculating the Péclet number Pe, the nondimensional ratio between the timescale for diffusive motion τ_D and the timescale for the pipette motion τ_v. τ_D is the typical time it takes a droplet to diffuse its own radius, $\tau_D = R^2/(2D)$ with $R \approx 20$ μm for our experiments and D the diffusion constant. For D, we consider the diffusion constant based on three dimensional diffusion in water, leading to $\tau_D \approx 18\,000$ s. τ_v is the time it takes the pushing pipette to move a distance R, thus $\tau_v = R/v \approx 67$ s. This leads to $\text{Pe} = \tau_D/\tau_v = 270$, and as this is much larger than 1, it confirms that motion within our experiment is athermal (driven by the pushing pipette rather than due to diffusion). Given that our droplets also have adhesive forces which further diminish diffusion-driven rearrangements, we are safely in the $\text{Pe} \gg 1$ limit.

III. RESULTS AND DISCUSSION

A. Effect of disorder on the force curves

Figure 2(a) shows the force measurements as a function of the distance between the pipettes, δ, for seven different aggregates with $p_{\text{ini}} = 4$ and $q_{\text{ini}} = 5$. The proportion of large and small droplets is varied from aggregate to aggregate. The top trace (1) corresponds to a crystal (i.e., a monodisperse aggregate) made of small droplets with radius $\mathcal{R} = r = 19.2 \pm 0.3$ μm [Fig. 2(b)], and the bottom trace (7) to a crystal of large droplets with radius $\mathcal{R} = R = 25.1 \pm 0.3$ μm. These traces show three force peaks corresponding to three fracture events: the transition from $p = 4$ to $p = 3$, which we designate as $4 \rightarrow 3$, followed by $3 \rightarrow 2$, and finally $2 \rightarrow 1$ (see Movie M2 in Supplemental Material [37]). The peak height is directly linked to the number of bonds broken. Each fracture event corresponds to a local maximum in the force-distance curve of Fig. 2(a) and to a corresponding interbasin barrier in the energy landscape. Clearly, for a $p \rightarrow (p-1)$ transition, a crystal made of small droplets will fracture at a smaller spacing between the pipettes (trace 1), compared to a crystal of larger droplets (trace 7). All the bonds are broken in a catastrophic and coordinated manner, in agreement with other studies of crystals under compression [41,42]. The largest system that shows this catastrophic failure in a crystal was made of 49 droplets with $p = 7$ (see Movie M3 in Supplemental Material [37]). Larger aggregates were not studied but we expect this result to hold even for large values of p as long as the droplets are monodisperse enough to form a perfect single crystal. For 2D crystals we find that the fracture patterns consist of equilateral triangles with $(p-1)$ droplets on a triangle's side as shown in Fig. 1(c). These equilateral triangles arise because they minimize the number of broken bonds between droplets as $p \rightarrow (p-1)$. After fracture, the triangles slide past each other and reassemble into a new crystal with $(p-1)$ rows of droplets. By design, the force sensor does not register a friction force during sliding, nor are we sensitive to viscous drag during compression, because slow compression (0.3 μm/s) ensures that viscous drag forces are negligible.

With the introduction of defects in the structure compression forces are no longer homogeneously distributed within the aggregate [see Figs. 2(c)–2(e)]. Thus, rather than a single catastrophic fracture, additional fracture events occur and extra peaks appear in the force data, as seen in the traces 2 to 6 of Fig. 2(a). When a single defect is introduced (traces 2 and 6), extra peaks are observed but peaks corresponding to the fracture of the crystalline portion of the aggregate can still be identified (large peaks at the same values of δ). Defects are systematically introduced up to trace 4, which corresponds to the most disordered system that we use to model a glass (equal fraction of large and small droplets). The force-distance curves are strongly impacted by increasing disorder: (i) the number of peaks increases, (ii) the overall magnitude of the force peaks decreases, and (iii) the peaks corresponding to the underlying crystalline structure can no longer be differentiated from the others. In order to identify peaks as corresponding to a specific transition from p to $(p-1)$ one can invoke the fact that a restructuring event in a bidisperse aggregate must occur within the compression range set by the *onset* of fracture associated with a crystal of big droplets and the *completion* of fracture in an aggregate of small droplets. Thus, we invoke the following criterion: a peak corresponds to the $p \rightarrow (p-1)$ transition if the peak is found in the compression range $\delta \in [\delta^p_{\text{min}}, \delta^p_{\text{max}}]$, where δ^p_{max} is defined by the onset of the force peak upon compression of aggregates only made of large droplets and $\delta^p_{\rm min}$ is defined by the completion of the fracture event in aggregates made of only small droplets [i.e., corresponding to the compression value at the maximum force as detailed in Fig. 2(a)]. This criterion is ideal for the small aggregates used in this study. For larger aggregates, stacking i large droplets may result in a smaller height than $i+1$ small droplets for large values of i. The value of i for which overlapping regions could be seen depends on the size ratio r/R. However, peaks can still be attributed to a given transition $p \to (p-1)$ by correlating specific fracture events to bond breaking events in the microscopy pictures.

From Fig. 2 it is evident that fracture properties are strongly dependent on the aggregate composition. In the simplest case, that of compressing a crystal cluster, the droplets deform and the stored elastic energy increases with compression. Eventually the stored elastic energy exceeds the depletion-induced adhesive energy, and a coordinated fracture occurs as discussed above [shown in Fig. 1(c)], such that a minimal number of bonds are broken. We now turn to the more complex bidisperse aggregates. As defects are introduced, the most striking feature is the rapid increase in the number of force peaks [Fig. 2(a)]. To further quantify this observation, we perform experiments for two different aggregate geometries: (i) $p_{\rm ini}=4$ with $q_{\rm ini}=5$ and (ii) $p_{\rm ini}=3$ with the three rows initially made of 8, 7, and 8 droplets. The composition of the cluster is given by the number fraction of small droplets in the aggregate, $\phi = N_{\rm small}/N_{\rm tot}$, which varies from zero to one. Both $\phi=0$ and $\phi=1$ correspond to crystals while $\phi=0.5$ corresponds to the maximum amount of disorder: a model glass. The defects are purposely distributed throughout the whole structure to avoid clumps of defects. In Fig. 3(a), we plot the total (i.e., until we reach $p=1$) number $N^{p_{\rm ini}\to 1}$ of detectable force peaks as a function of the defect fraction.

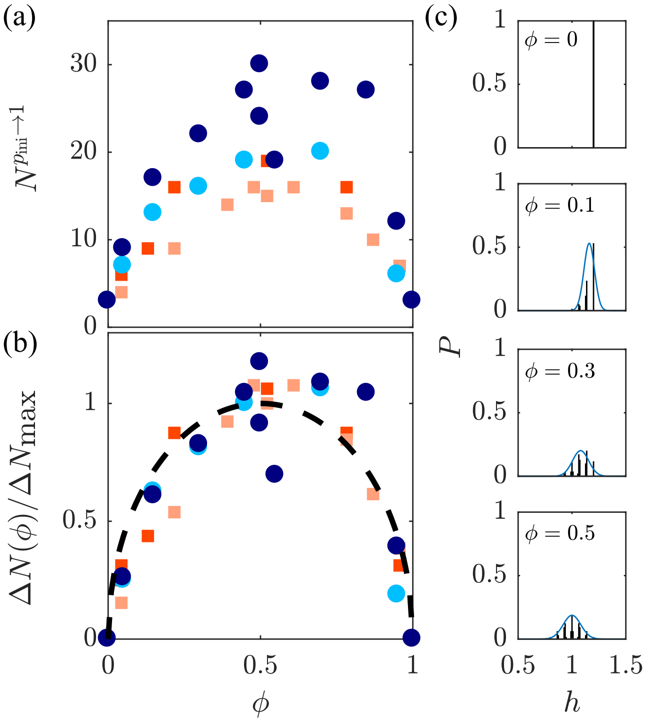

FIG. 3. (a) Measured total number of force peaks as a function of defect fraction, for a compression from $p_{\rm ini}$ to $p=1$. (●) $p_{\rm ini}=4$ with $q_{\rm ini}=5$ from two data sets (different colors); (■) $p_{\rm ini}=3$ with the three rows initially made of 8, 7, and 8 droplets each, from two data sets (different colors). (b) Evolution of the normalized excess number of peaks compared to a crystal, with the black dashed line corresponding to Eq. (2). (c) Theoretical probability distribution of the dimensionless column height h, in an aggregate with $q \to \infty$ and $p=4$, for four defect fractions $\phi = \{0; 0.1; 0.3; 0.5\}$ (see Appendix B). Gaussian curves (blue solid lines) with same standard deviation, σ, and average, μ, as the discrete distribution are overlayed as a guide to the eyes. Typical radii of large and small droplets are ≈22 μm and ≈18 μm (see Appendix D).

B. Analytical model

We propose a minimal model that rationalizes the experimental observations. A given (p, q) aggregate is approximated by an ensemble of q independent columns, each with p rows of droplets. By allowing this simplification, one can treat each column as a random packing of droplets belonging to two different species which correspond to the two different radii: small droplets with $\mathcal{R}=r$ and large droplets with $\mathcal{R}=R$. Since droplets are arranged in a nearly hexagonal lattice, each column consists of alternating layers of a single droplet or two droplets side by side (see Appendix A). The probabilities associated with finding a small or large droplet at a specific site are given by the number fractions ϕ and $1-\phi$. The total resulting height, H, of a given column depends on the specific composition in that column, and takes values ranging from H_r to H_R, for columns made of small ($\phi=1$) and large ($\phi=0$) droplets. We define the dimensionless height $h = 2H/(H_R + H_r)$. One can compute (see Appendix B) the associated probability distribution, $P(h)$, plotted in Fig. 3(c) for various ϕ (black bars). Compression of an aggregate then proceeds as follows: First, the tallest columns are compressed and broken, which creates a force peak whose magnitude reflects the abundance of these highest columns in the aggregate. Then, the pushing pipette starts compressing the second highest columns and the process repeats.

The simple model predicts that the average number of force peaks observed during the $p \to p-1$ transition of an aggregate can be identified with the average number $N^p(\phi, q)$ of different column heights present in the aggregate composed of q columns. For a monodisperse aggregate, there is only one possible column height, and thus $N^p(0,q) = N^p(1,q) = 1$ resulting in one force peak for the $p \to p-1$ transition. In contrast, as the defect fraction increases, the number of possible different heights and thus the number of force peaks increase. The number of different heights can be calculated numerically according to the scheme described above (see Appendix B). In addition, a simple argument provides an analytical estimate for the average number of force peaks in a sample with a given ϕ. The increase in the average number of different column heights in comparison to a crystal is expected to be proportional to the standard deviation, $\sigma(\phi, p) \propto \sqrt{\phi(1-\phi)}$, of the height distribution centered at $\mu(\phi, p)$ shown in Fig. 3(c). This results from the random packings of the columns described above and gives

$$N^p(\phi, q) - 1 = [N^p(\phi = 0.5, q) - 1]2\sqrt{\phi(1-\phi)}. \qquad (1)$$

Finally, in order to determine all the force peaks encountered on average as the aggregate is compressed, we sum Eq. (1) over all the transitions starting from a cluster with $p_{\rm ini}$ rows to one row, in order to construct $N_{q_{\rm ini}}^{p_{\rm ini}\to 1}(\phi) = \sum_{p=2}^{p_{\rm ini}} N^p(\phi, q)$, where $q = N_{\rm tot}/p$. Defining the average number of peaks compared to a crystal, $\Delta N(\phi, p_{\rm ini}, q_{\rm ini}) = N_{q_{\rm ini}}^{p_{\rm ini}\to 1}(\phi) - N_{q_{\rm ini}}^{p_{\rm ini}\to 1}(0)$, we obtain (see Appendix C)

$$\frac{\Delta N}{\Delta N_{\rm max}}(\phi) = 2\sqrt{(1-\phi)\phi}, \qquad (2)$$

where $\Delta N_{\rm max} = \Delta N(\phi = 0.5, p_{\rm ini}, q_{\rm ini})$ corresponds to the average maximum excess number of peaks, observed when compressing the most disordered aggregate. The experimental value of $\Delta N_{\rm max}$ is obtained by fitting Eq. (2) to each set of data presented in Fig. 3(a). Figure 3(b) shows that this simple model captures well the rapid increase of the number of force peaks as defects are added. The derivative of Eq. (2) at $\phi = 0$ is infinite; thus, a small change in the fraction of defects in an aggregate results in a drastic change in the yield properties as observed in experiments. We note that the minor discrepancy between the data and the model reflects experimental error as well as three main departures of the real aggregate from the proposed idealization: (i) neighboring columns are not independent, (ii) the real aggregate has a finite number of columns, and (iii) some peaks may not be detected.

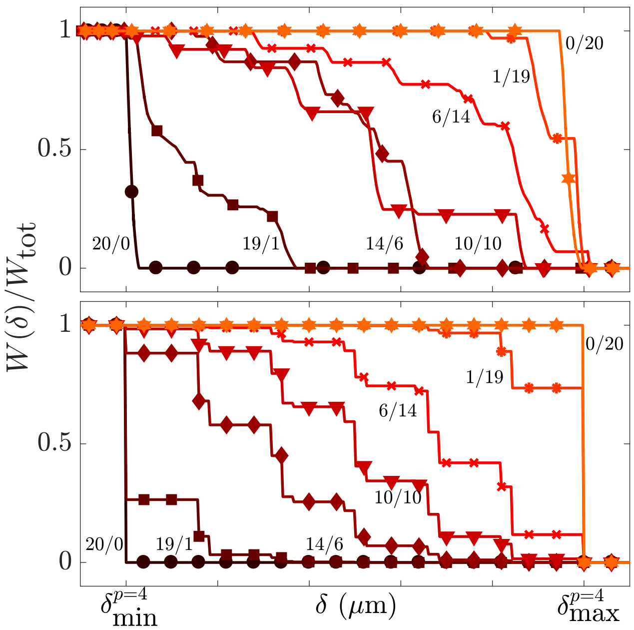

FIG. 4. Normalized partial work (see definition in text) as a function of distance, for the $p = 4 \to p = 3$ transition, for aggregates of different relative compositions (number of small droplets / number of large droplets) as indicated. Top: Experimental results corresponding to the force curves shown in Fig. 2(a). Bottom: Corresponding theoretical results, according to Eq. (3).

C. Probing the energy landscape through the crystal-to-glass transition

The compression experiments can also be used to measure the yield energy of the aggregate as a function of the defect fraction, which reflects the character of the underlying energy landscape. The energy landscape is a high dimensional space, and we observe one specific pathway through this space as the system is compressed. The changes in these pathways as the sample is varied from a crystal to a glass reveal hints of how the energy landscape changes based on the sample structure. Specifically, the work $W_{\rm tot}$ exerted (and then fully dissipated in the fluid) in order to generate a $p \to (p-1)$ rearrangement is obtained by integrating the force-distance curve [Fig. 2(a)], for the corresponding transition; this gives the height of the barrier traversed in the energy landscape. As explained previously, a $p \to (p-1)$ transition corresponds to $\delta \in [\delta_{\rm min}^p, \delta_{\rm max}^p]$, so the integration is performed over this interval. Moreover, we only consider the rising (along the compression orientation, i.e., upon decreasing δ) elastic part $F_{\rm s}$ of the force peaks, as the subsequent decay corresponds to the viscous relaxation of the force-sensing pipette. The overlap of a decaying part of a peak and a rising part of the following peak constitute a possible source of uncertainty in the measurement. However, because of the small size of the aggregate, these overlapping events are in fact extremely rare. For this analysis, we focus on the collection of force traces presented in Fig. 2(a) and in particular the transition $p = 4 \to p = 3$. Within our resolution, the total work $W_{\rm tot} = \int_{\delta_{\rm min}^p}^{\delta_{\rm max}^p} d\delta'\, F_{\rm s}(\delta') = 2.2 \pm 0.7$ fJ is found to be nearly constant for all the different experiments and is not correlated to the composition of the aggregate when the initial geometry ($p_{\rm ini}$, $q_{\rm ini}$) is kept constant (see Appendix E). The remarkable result that the work is nearly independent of the composition of the aggregate is an indication that the number of bonds broken must be nearly constant.

While the total work may be nearly constant, there is an important distinction between the disordered and crystalline systems in how that work is distributed during a $p \to (p-1)$ transition of the aggregate. To access that information, we consider the partial work $W(\delta) = \int_{\delta}^{\delta_{\rm max}^p} d\delta'\, F_{\rm s}(\delta')$, with $\delta \in [\delta_{\rm min}^p, \delta_{\rm max}^p]$. For the crystals, the bonds are broken simultaneously as the system is driven out of a deep minimum in the landscape. For instance, the crystal made of large droplets breaks near $\delta = \delta_{\rm max}^p$ [Fig. 2(a)], with the normalized partial work going abruptly from zero to one upon compression (i.e., decreasing δ) near that point. This fracture event is detailed in the top panel of Fig. 4 where we plot the normalized work as a function of the interpipette distance, δ. The crystal made of small droplets exhibits a similar sudden transition, except that the fracture event happens at $\delta = \delta_{\rm min}^p$. In contrast, when defects are introduced, several intermediate steps are observed. For an aggregate with a single defect, a major step (corresponding to the crystalline fraction) is still observed but rapidly fades away as more defects are added. The curves for six defects ($\phi = 0.3$) and for the model glass ($\phi = 0.5$) both show many discrete jumps in the work; thus, the failure of disordered systems is more progressive and has a much lower yield threshold than for crystals. These compression experiments give a microscopic view into well-known macroscopic

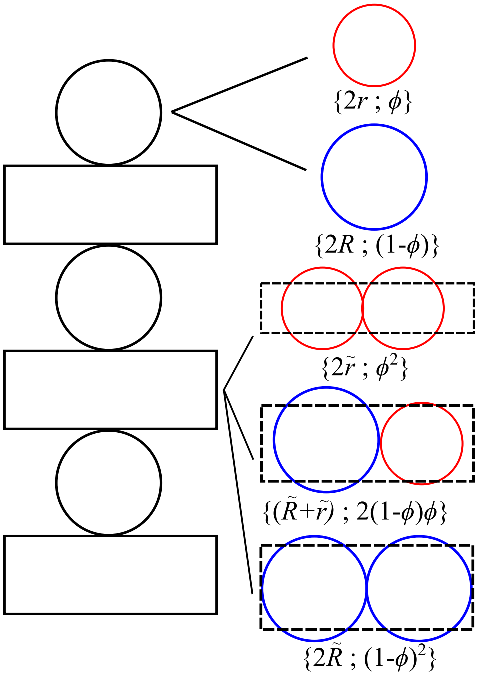

FIG. 5. Schematics of the columns with $p = 6$ considered in the theoretical model. The left part shows how rectangles and circles are assembled to build a column. The right part shows the different choices for circles and rectangles along with their probability of appearing.

properties. Finally, one can compare the experiment to the theoretical model developed above. In the model, the average normalized partial work is given by the fraction of columns that have a height H larger than δ. Invoking the probability distribution P of column heights, one gets on average

$$\frac{W(\delta)}{W_{\rm tot}} = \int_{\frac{\delta}{\Lambda}}^{\frac{\delta^p_{\rm max}}{\Lambda}} dh\, P(h, \phi, p), \tag{3}$$

where $\Lambda = \mu(p, \phi = 0.5) = (H_r + H_R)/2$. This expression is plotted in the bottom panel of Fig. 4 for various compositions, and is consistent with the experimental data. The theory predicts more steps than the experiment; this is because the experiment probes one configuration, while the theory is an average over all the configurations. We have thus shown that model 2D crystals and glasses are markedly different under compression: crystals deform elastically until a catastrophic global fracture event occurs, whereas glasses rearrange locally with many intermediate fracture events that each have lower individual yield thresholds. This deviation from the well-established response of a crystal to an external stress has also been observed in a recent analytical study [43], and it was shown numerically that materials go from brittle to ductile when transitioning from crystal to glass [13]; a fact that is tested here directly with the idealized microscopic experiments.

IV. CONCLUSIONS

In summary, we present a study of aggregates composed of a finite number of athermal particles which provide a unique bottom-up opportunity to investigate the transition from crystal to glass by systematically adding disorder to 2D colloidal crystals. Upon addition of defects the mechanical properties of the aggregates rapidly transition from crystalline to glassy. The number of force peaks, corresponding to fracture events, increases steeply with the defect fraction, before saturating to the glass value. Additionally, the yield energy as a function of disorder has been investigated. We find that for a 2D crystal a high energy barrier must be overcome, while glasses fracture progressively through failure in many small steps. In the system studied the adhesion energy between particles exceeds the thermal energy, thus the aggregates correspond to a glass or a crystal well below the solid-melt transition temperature. In a system that is closer to the solid-melt transition, the thermal energy would trigger the rearrangements we observe with less compression than observed in the experiments and would blur the energy landscape. The peaks of our force measurement would shift to smaller compressions and have reduced magnitude. This does not change the physics of such thermal clusters, but would make the precise force spectra harder to observe. Nonetheless, the major finding of our work would remain: perfect crystals require more force to compress, and adding in a dilute amount of defects dramatically decreases the force necessary to deform and rearrange a material, even at finite temperatures. The fracture events observed reflect the substructure introduced by disorder in the underlying energy landscape. The observations are consistent with the brittle failure of crystals as opposed to the plasticity of glasses. A minimal analytical model captures the essential experimental features. From the combination of experiments and theory, we quantify the crystal-to-glass transition using macroscopic yield observables that are consistent with a simple microscopic picture.

ACKNOWLEDGMENTS

The authors thank Maxence Arutkin, Matilda Backholm, and James Forrest for valuable discussions, as well as Yilong Han for sharing a preliminary draft on a similar topic. Financial support from NSERC (Canada), the Joliot chair from ESPCI Paris, and the Global Station for Soft Matter, a project of Global Institution for Collaborative Research and Education at Hokkaido University, is gratefully acknowledged. The work of E.R.W. was supported by the National Science Foundation (CBET-1804186).

APPENDIX A: HEIGHT OF A COLUMN AND PROBABILITY

In this section, the theoretical model used to predict the number of peaks in the force measurement as a function of ϕ is derived. In this calculation, each transition from p rows of droplets to $(p - 1)$ rows is studied individually. In the following, p and q are constant values.

The theoretical model developed for this study is based on geometrical arguments. An assembly of droplets is compressed if its lateral unstrained extent is larger than the spacing between the pipettes. The aggregate is modeled as q independent columns of height H_i stacked next to each other, the index i, going from 1 to q, labels the columns. The total height of a column depends the composition of droplets. For a crystal, all the columns are the same so they break at the same time, which results in a single peak in the force measurement. When defects are introduced, large droplets are substituted by small ones (or vice versa). Columns constituting the aggregate now have different heights and break for different values of δ, resulting in several peaks in the force measurement.

A column is made of alternating layers of two droplets, which are modeled as a *rectangle*, and single droplets, modeled as *circles*, as shown in Fig. 5. The number fraction ϕ of small droplets in an assembly of $N_{\rm small}$ small droplets and $N_{\rm tot} - N_{\rm small}$ large droplets is defined as $\phi = N_{\rm small}/N_{\rm tot}$. Depending on the composition of the two droplets, the rectangles can take three heights $\{2\tilde{R},\ 2\tilde{r},\ (\tilde{R}+\tilde{r})\}$ with probabilities $\{(1-\phi)^2,\ \phi^2,\ 2(1-\phi)\phi\}$ respectively. The circles can only have two diameters resulting in two distinct heights $\{2R,\ 2r\}$ with probabilities $\{(1-\phi),\ \phi\}$ respectively. Finally, we take the relation between (R, r) and $(\tilde{R}, \tilde{r})$ to be a geometrical factor α. It is the sum of the heights of the rectangles and the heights of the circles that determine the overall height of a column, as shown in Fig. 5.

Random walk statistics can be applied to this model. To simplify, we consider p being even. The results for p being odd would be similar. Thus, for the even case, building such a column is equivalent to two random walks of $p/2$ steps: one with the circles and one with the rectangles. Using the random walk statistics formalism [44], we can express the probability $P_{\rm circ}(H_1, \phi, p, r, R)$ of finding a height H_1 by stacking $p/2$ circles of two different sizes for a given ϕ, and $P_{\rm rect}(H_2, \phi, p, \tilde{r}, \tilde{R})$, the probability of finding a height H_2 by stacking $p/2$ rectangles of three different heights:

$$P_{\rm circ}(H_1, \phi, p, r, R) = \frac{1}{2\pi}\int_{-\pi}^{\pi}[\phi e^{2i\theta r} + (1-\phi)e^{2i\theta R}]^{\frac{p}{2}} e^{-i\theta H_1} d\theta,$$

$$P_{\rm rect}(H_2, \phi, p, \tilde{r}, \tilde{R}) = \frac{1}{2\pi}\int_{-\pi}^{\pi}\underbrace{[\phi^2 e^{2i\theta\tilde{r}} + (1-\phi)^2 e^{2i\theta\tilde{R}} + 2\phi(1-\phi)e^{i\theta(\tilde{R}+\tilde{r})}]}_{[\phi e^{i\theta\tilde{r}}+(1-\phi)e^{i\theta\tilde{R}}]^2}{}^{\frac{p}{2}} e^{-i\theta H_2} d\theta, \tag{A1}$$

$$P_{\rm circ}(H_1, \phi, p, r, R) = \sum_{k=0}^{\frac{p}{2}} \binom{\frac{p}{2}}{k} \phi^k (1-\phi)^{\frac{p}{2}-k} \delta\big[2kr + 2\big(\tfrac{p}{2}-k\big)R - H_1\big],$$

$$P_{\rm rect}(H_2, \phi, p, \tilde{r}, \tilde{R}) = \sum_{l=0}^{p} \binom{p}{l} \phi^l (1-\phi)^{p-l} \delta[l\tilde{r} + (p-l)\tilde{R} - H_2]. \tag{A2}$$

It turns out that the random walk of $p/2$ steps with three different step sizes is equivalent to p steps of two different sizes [see Eq. (A1)]. The Dirac δ function in Eq. (A2) is a geometrical constraint on the total height. Only the combinations of droplets that lead to the right total heights H_1 and H_2 are considered. The distribution of probability of the total height H is the convolution product of $P_{\rm circ}(H_1, p, \phi, r, R)$ and $P_{\rm rect}(H_2, p, \phi, \tilde{r}, \tilde{R})$:

$$P(H, \phi, p, r, R, \tilde{r}, \tilde{R}) = \int_0^{\infty} P_{\rm circ}(H - H_2, \phi, p, r, R) P_{\rm rect}(H_2, \phi, p, \tilde{r}, \tilde{R})\, dH_2. \tag{A3}$$

Using Eq. (A2) we find

$$P(H, \phi, p, r, R, \tilde{r}, \tilde{R}) = \sum_{k=0}^{\frac{p}{2}} \sum_{l=0}^{p} \binom{\frac{p}{2}}{k} \binom{p}{l} \phi^{k+l} (1-\phi)^{\frac{3p}{2}-k-l} \delta\big[l\tilde{r} + (p-l)\tilde{R} + 2kr + 2\big(\tfrac{p}{2}-k\big)R - H\big]. \tag{A4}$$

To simplify the notation we consider r, R, $\tilde{r}$, and $\tilde{R}$ fixed so the probability distribution is $P(H, \phi, p)$. Equation (A4) is used to calculate numerically the discrete distribution presented in the main text [Figs. 3(c)–3(e) histograms]. The height H can take discrete values H_i, with probability $P_i = P(H_i, \phi, p)$, ranging from H_r for a column made of small droplets ($\phi = 0$) to H_R for a column made of large droplets ($\phi = 1$). The total number of different heights H_i only depends on p and is denoted m_p. Finally, the height H is renormalized as $h = 2H/(H_r + H_R)$. With this renormalization, a column made of 50% large droplets and 50% small droplets ($\phi = 0.5$) has a dimensionless height $h = 1$.

APPENDIX B: NUMBER OF PEAKS

The column model gives access to the probability P_i of finding the height H_i in an aggregate for any fraction of defects ϕ. The number of peaks in the force measurement is calculated from the height distribution. Let us denote the average number of force peaks during the compression of an aggregate with p rows to an aggregate with $(p-1)$ rows by $N^p(\phi, q)$. Observing a single peak in the force measurement means that all the columns share the same height. Measuring two peaks means that there are two and only two different heights. Thus $N^p(\phi, q)$ corresponds to the average number of *different* heights composing an aggregate of p rows and q columns.

For a given fraction of defects ϕ, an aggregate of size $p \times q$ is built by choosing randomly q columns from a pool of columns. Correlation between two adjacent columns are neglected. Experimentally, a small fraction of the peaks in the force measurement is due to the correlation between columns, but most of the peaks are indeed due to compression of independent columns. From the discrete probability distribution, Eq. (A4), there is a finite number m_p of possible heights H_i with a nonzero probability. To predict the number of peaks we calculate the probability $A_n(\phi, p, q)$ of finding strictly n different columns heights in an aggregate of size $p \times q$ at a given fraction of defects ϕ.

Building an aggregate is equivalent to drawing q columns which can take m_p different heights H_i with probability P_i. $\{ijk\cdots\}_n$ defines n different numbers between 1 and m_p. Let $\tilde{P}_{\{ijk\cdots\}_n}$ denote the probability that the aggregate is composed only of the n heights $\{H_i, H_j, H_k, \dots\}$ and each height appears at least once. As the order in which the heights are drawn is not important, one gets

$$A_n(\phi, p, q) = \frac{\Theta(q-n)}{n!} \sum_{\{ijk\cdots\}_n \subset [\![1,m_p]\!]} \tilde{P}_{\{ijk\cdots\}_n}, \tag{B1}$$

where Θ is the Heaviside function and $\sum_{\{ijk\cdots\}_n \subset [\![1,m_p]\!]}$ denotes the sum over all the n-tuples $\{ijk\cdots\}_n$ in $[\![1, m_p]\!]$. We define $P_{\{ijk\cdots\}_n}$ as the probability of drawing one of the n heights $\{H_i, H_j, H_k, \dots\}$, and obtain

$$P_{\{ijk\cdots\}_n} = \sum_{\kappa \in \{ijk\cdots\}} P_\kappa. \tag{B2}$$

Hence, the probability that an aggregate of q columns is composed only of the heights $\{H_i, H_j, H_k, \dots\}$ is given by $(P_{\{ijk\cdots\}_n})^q$. However, this probability is not equal to $\tilde{P}_{\{ijk\cdots\}_n}$ since it does not take into account that each height must appear at least once. The difference between $(P_{\{ijk\cdots\}_n})^q$ and $\tilde{P}_{\{ijk\cdots\}_n}$ is the probability that one or more of the heights $\{H_i, H_j, H_k, \dots\}$ does not appear. To calculate $\tilde{P}_{\{ijk\cdots\}_n}$ we subtract from $(P_{\{ijk\cdots\}_n})^q$ the probabilities that the aggregate is only composed of $n-\kappa$ different types of columns of heights $\{H_a, H_b, H_c, \dots\}$ with $\{abc\cdots\} \subset \{ijk\cdots\}_n$ summed over all the possible $(n-\kappa)$-tuples in $\{ijk\cdots\}_n$ and summed over all the κ from 1 to $n-1$:

$$\tilde{P}_{\{ijk\cdots\}_n} = \left(P_{\{ijk\cdots\}_n}\right)^q - \sum_{\kappa=1}^{n-1} \sum_{\{abc\cdots\}_{n-\kappa} \subset \{ijk\cdots\}_n} \tilde{P}_{\{abc\cdots\}_{n-\kappa}}. \tag{B3}$$

Noticing that the sum over the κ and the other sums can be switched, and using Eq. (B1), one finds

$$\begin{aligned} &A_n(\phi, p, q) \\ &= \frac{\Theta(q-n)}{n!} \sum_{\{ijk\cdots\}_n \subset [\![1,m_p]\!]} \left(P_{\{ijk\cdots\}_n}\right)^q \\ &\quad - \frac{1}{n!} \sum_{\kappa=1}^{n-1} \underbrace{\sum_{\{ijk\cdots\}_n \subset [\![1,m_p]\!]} \sum_{\{abc\cdots\}_{n-\kappa} \subset \{ijk\cdots\}_n} \tilde{P}_{\{abc\cdots\}_{n-\kappa}}}_{B_\kappa}. \end{aligned} \tag{B4}$$

Let us focus on the second term of the right-hand side, called B_κ, in Eq. (B4). $\tilde{P}_{\{abc\cdots\}_{n-\kappa}}$ depends on $n-\kappa$ indices and it is summed over n indices. So if we fix the $n-\kappa$ indices that $\tilde{P}_{\{abc\cdots\}_{n-\kappa}}$ depends on, it will appear $\binom{n}{\kappa}$ times. Thus

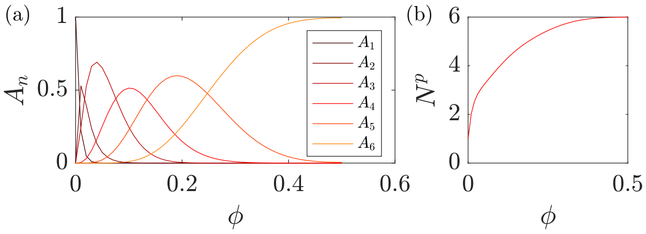

FIG. 6. (a) Probability distribution A_n as a function of ϕ for an aggregate made of $p = 2$ rows and $q = 50$ droplets per row. (b) Prediction of the average number of peaks in the force measurement as a function of ϕ based on the distribution A_n. Note that we only plot the function for $\phi \in [0, 0.5]$ by symmetry about $\phi = 0.5$.

$$B_\kappa = \sum_{\{ijk\cdots\}_n \subset [\![1,m_p]\!]} \binom{n}{\kappa} \tilde{P}_{\{ijk\cdots\}_{n-\kappa}}. \tag{B5}$$

By splitting the sum into two parts, one finds

$$B_\kappa = \kappa! \binom{n}{\kappa} \left[\prod_{\beta=\kappa}^{n-1} (m_p - \beta) \right] A_\kappa, \tag{B6}$$

leading to

$$\begin{aligned} A_n(\phi, p, q) = &\frac{\Theta(q-n)}{n!} \sum_{\{ijk\cdots\}_n \subset [\![1,m_p]\!]} (P_{\{ijk\cdots\}_n})^q \\ &- \frac{1}{n!} \sum_{\kappa=1}^{n-1} \binom{n}{\kappa} \kappa! \left[\prod_{\beta=\kappa}^{n-1} (m_p - \beta) \right] A_\kappa. \end{aligned} \tag{B7}$$

The average number of peaks $N^p(\phi, q)$ is given by

$$N^p(\phi, q) = \sum_{n=1}^{m_p} n A_n(\phi, p, q). \tag{B8}$$

Equations (B7) and (B8) can be evaluated numerically, see Fig. 6. The importance of this distribution $A_n(\phi, p, q)$ can be easily understood for both extreme values of ϕ. If $\phi = 0$, there is only one possible height for the column, meaning that $A_n(\phi = 0, p, q) = \delta_{1n}$, where δ_{ij} is the Kronecker symbol. On the other hand, if $\phi = 0.5$, it is unlikely to find only one height so $A_1 \simeq 0$. It is more likely to find all the different heights in the aggregate leading to $A_{m_p} \simeq 1$. This is illustrated in Fig. 6(a) which shows the probabilities, A_n, for $p = 2$ (with n takes values from 1 to $m_2 = 6$) as a function of ϕ. Note that in Figs. 6(a) and 6(b) we restrict the range to $\phi \in [0, 0.5]$ as the function is symmetric about $\phi = 0.5$. For $\phi = 0$, only $A_1 \neq 0$. As ϕ increases, finding two different heights becomes more likely and A_2 becomes dominant. For $\phi = 0.5$, it is very likely to find the maximum number of columns, $m_2 = 6$, in the aggregate and $A_6 \simeq 1$.

1. Finite-size effect

The number of force peaks is a function of the size of the cluster: in the model, the number of force peaks depends explicitly on the number of columns q since A_n depends on

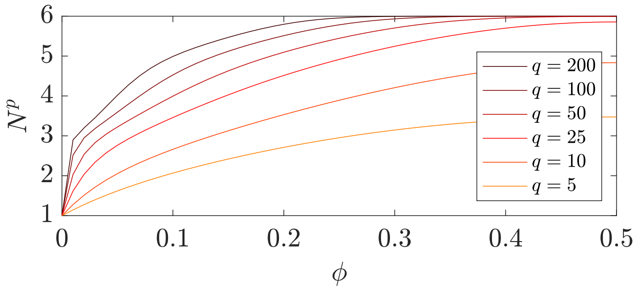

FIG. 7. Impact of the size of the aggregate on the number of peaks in the force measurement for $p = 2$ and different values of q.

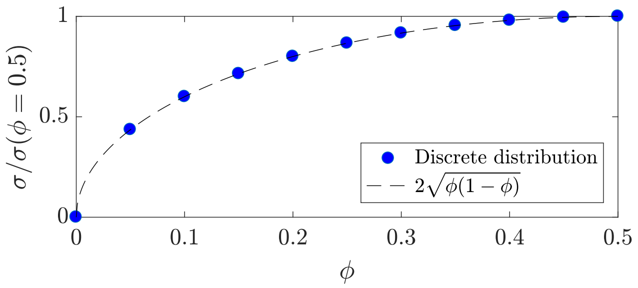

FIG. 8. Comparison between the analytical expression for the standard deviation of the height distribution and the numerically calculated values for different ϕ for $p = 2$.

q (in Fig. 6, $q = 50$). In an infinitely large cluster ($q \to \infty$) all the heights will appear and so $N^p(\phi > 0, q \to \infty) = m_p$, with m_p the number of possible heights one can get with the random packing described previously at a given p. For a finite q, one has $N^p(\phi, q) < m_p$ because all the possible heights will not appear simultaneously in the same cluster. As a simple consequence, one has $N^p(\phi, q_1) < N^p(\phi, q_2)$, for $q_1 < q_2$.

Moreover, even if the total number of different possible heights m_p is large, we cannot find more different heights than the number of columns, q. This is the reason for the Heaviside function in the definition of A_n. For the experimental aggregates, q varies from 3 to 15. In particular for $p = 3$ or $p = 4$, the number of columns is usually ~5 and the value of q gives an upper limit for the number of force peaks. Figure 7 shows the impact of the number of columns on the number of peaks for $p = 2$.

2. A simpler approach to estimate the number of force peaks

The approach discussed above predicts accurately the average number of force peaks observed during the compression of an aggregate. However the number of force peaks estimated for a transition $p \to p - 1$ is strongly dependent of the size of the cluster. In this section, we take a simpler approach that leads to an analytical expression for the number of force peaks observed during the compression of a cluster. In addition, with this approach we are able to define a quantity that allows us to renormalize our results with respect to the size of the cluster. This analytical expression characterizes the transition of a cluster from being crystal-like to glass-like.

We define the excess number of force peaks as the number of force peaks for a given ϕ compared to the number of force peaks observed in the crystal case $N^p(\phi = 0, q) = 1$ for the same transition $p \to p - 1$: $N^p(\phi, q) - 1$. This quantity can be normalized by its value for a glassy case where $\phi = 0.5$: $N^p(\phi = 0.5, q) - 1$. The normalized quantity quantifies how crystalline or glassy a cluster is, and takes values ranging from 0 for a crystal to 1 for a glass.

Instead of numerically calculating the average number of different column heights in a $p \times q$ cluster, we propose the following statistical argument: the average number of different heights in a $p \times q$ cluster is well approximated by the number of different *highly probable heights* in the probability distribution of heights. To define if a height H_i is highly probable, one has to invoke a threshold for the probability, $P(H_i)$, which is strongly dependent on the total number of columns, q, in the cluster. The larger q is, the smaller the threshold must be, and should go to zero in the limit of infinitely large clusters ($q \to \infty$). Since the columns are built as a 1D random walk, the distribution follows a binomial law and the number of probable heights can be characterized using the standard deviation σ of the height distribution. Using σ to define the threshold, the excess number of peaks is then directly proportional to the width of the height distribution. As we are interested in the ratio between the excess number of peaks at a given fraction of defects, ϕ, and its maximum value, observed at $\phi = 0.5$, the choice of the threshold is not critical, for the range of q values explored in the experiments. This leads to

$$\frac{N^p(\phi, q) - 1}{N^p(\phi = 0.5, q) - 1} \simeq \frac{\sigma(\phi, p)}{\sigma(\phi = 0.5, p)}. \tag{B9}$$

The standard deviation, σ, as well as the average value, μ, of the continuous height distribution can be calculated analytically in this simplified approach. We find $\mu(\phi, p) = p(\alpha + 1)[(1 - \phi)R + r\phi]$ and $\sigma^2(\phi, p) = p(2 + \alpha^2)(R - r)^2\phi(1 - \phi)$. The analytical expression for σ as a function of ϕ is tested against the numerically calculated values from the discrete model, described in the previous sections, for different values of ϕ. Figure 8 shows perfect agreement between both approaches for $p = 2$.

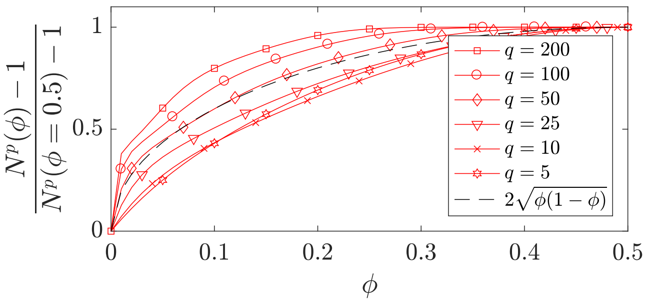

FIG. 9. Comparison between the average number of peaks predicted by the discrete calculation (for different values of q) and the continuous approximation, for $p = 2$. The continuous model does not take into account the number of droplets per row q in the aggregate.

Using the expression found for the standard deviation, σ, Eq. (B9) can be rewritten as

$$\frac{N^p(\phi, q) - 1}{N^p(\phi = 0.5, q) - 1} \simeq 2\sqrt{\phi(1-\phi)}. \tag{B10}$$

Note that the result is now independent of the size of the cluster. Indeed, this ratio simply compares the excess number of peaks to its maximum value, but it does not predict the exact number of peaks observed in the force curves. This simplified approach can be tested against the discrete model by comparing the number of peaks predicted by each model with $p = 2$. The left-hand side of Eq. (B10) is calculated numerically for the discrete model and compared to $2\sqrt{\phi(1-\phi)}$ as shown in Fig. 9. Both models are in good agreement for the number of peaks as long as $q < 50$. The analytical prediction overestimates the number of force peaks in the range of q values experimentally explored.

APPENDIX C: TOTAL NUMBER OF PEAKS $N_{q_{\mathrm{ini}}}^{p_{\mathrm{ini}}\to 1}(\phi)$

In the main text, we compare the experimental results and the total number of peaks when compressing a cluster initially made of p_{ini} rows and q_{ini} columns to a single row ($p = 1$), at a given percentage in defects ϕ: $N_{q_{\mathrm{ini}}}^{p_{\mathrm{ini}}\to 1}(\phi)$. Equation (2) in the main text is obtained by summing Eq. (B10) over the different transitions:

$$\begin{aligned} N_{q_{\mathrm{ini}}}^{p_{\mathrm{ini}}\to 1}(\phi) &= \sum_{p=2}^{p_{\mathrm{ini}}} N^p(\phi, q) \\ &= 2\sqrt{(1-\phi)\phi}\sum_{p=2}^{p_{\mathrm{ini}}}[N^p(\phi = 0.5, q) - 1] + \sum_{p=2}^{p_{\mathrm{ini}}} 1. \end{aligned} \tag{C1}$$

During these transitions, the total number of droplets N_{tot} is conserved and thus $p \times q = p_{\mathrm{ini}} \times q_{\mathrm{ini}}$. Noticing that $\sum_{p=2}^{p_{\mathrm{ini}}} 1$ is the number of peaks observed when compressing a crystal initially made of p_{ini} rows, this quantity is independent of q_{ini} and will be denoted $N^{p_{\mathrm{ini}}\to 1}(\phi = 0)$. Equation (C1) can then be written as

$$\begin{aligned} N_{q_{\mathrm{ini}}}^{p_{\mathrm{ini}}\to 1}(\phi) = {}& 2\sqrt{(1-\phi)\phi}\big[N_{q_{\mathrm{ini}}}^{p_{\mathrm{ini}}\to 1}(\phi = 0.5) - N^{p_{\mathrm{ini}}\to 1}(0)\big] \\ &+ N^{p_{\mathrm{ini}}\to 1}(0), \end{aligned} \tag{C2}$$

leading to

$$\frac{N_{q_{\mathrm{ini}}}^{p_{\mathrm{ini}}\to 1}(\phi) - N^{p_{\mathrm{ini}}\to 1}(0)}{N_{q_{\mathrm{ini}}}^{p_{\mathrm{ini}}\to 1}(\phi = 0.5) - N^{p_{\mathrm{ini}}\to 1}(0)} = 2\sqrt{(1-\phi)\phi}. \tag{C3}$$

TABLE I. Size of the droplets used for the crystal-to-glass transition study; Fig. 4 in the main text.

Data set	Point color	R (μm)	r (μm)
1	red	21.5 ± 0.2	19.1 ± 0.2
2	salmon	21.4 ± 0.4	19.1 ± 0.4
3	light blue	20.9 ± 0.3	17.3 ± 0.5
4	dark blue	25.1 ± 0.3	19.2 ± 0.3

TABLE II. Total work needed to transition from $p = 4$ to $p = 3$ for different compositions.

Composition	ϕ	W_{tot} (fJ)
20/0	0	1.2
19/1	0.05	2.8
14/6	0.3	2.8
10/10	0.5	2.1
6/14	0.3	3.1
1/19	0.05	1.5
0/20	0	2.0

Finally, we define $\Delta N(\phi, p_{\mathrm{ini}}, q_{\mathrm{ini}}) = N_{q_{\mathrm{ini}}}^{p_{\mathrm{ini}}\to 1}(\phi) - N^{p_{\mathrm{ini}}\to 1}(0)$ as the average excess number of peaks observed when compressing an aggregate with a defect fraction ϕ in comparison to a crystal of same geometry $p_{\mathrm{ini}} \times q_{\mathrm{ini}}$. The maximum excess number of peaks $\Delta N_{\mathrm{max}} = N_{q_{\mathrm{ini}}}^{p_{\mathrm{ini}}\to 1}(\phi = 0.5) - N^{p_{\mathrm{ini}}\to 1}(0)$ corresponds to the excess number of peaks observed when compressing the most disordered aggregates (model for a glass, $\phi = 0.5$). The ratio of these two quantities $\Delta N/\Delta N_{\mathrm{max}}$ does not depend on the size of the cluster $p_{\mathrm{ini}} \times q_{\mathrm{ini}}$ but only on the fraction of defects ϕ. We can thus write Eq. (C3) in a simpler form and obtain Eq. (2) of the main text

$$\frac{\Delta N}{\Delta N_{\mathrm{max}}}(\phi) = 2\sqrt{(1-\phi)\phi}. \tag{C4}$$

The maximum number of peaks, $N_{\mathrm{max}}^{p_{\mathrm{ini}}\to 1}(q) = N^{p_{\mathrm{ini}}\to 1}(\phi = 0.5, q)$, depends on the system size as shown in the previous section. The experimental value is obtained by fitting Eq. (C4) to each set of data presented in Fig. 3(a).

APPENDIX D: SIZE OF THE DROPLETS IN THE CRYSTAL-TO-GLASS TRANSITION STUDY

The data shown in Figs. 4(a) and 4(b), in the main text, come from four different sets of experiments. The droplets used during a given set of experiments are the same, while the defect fraction is varied. New droplets were produced for each new set. Table I summarizes the sizes of the droplets used in these experiments.

APPENDIX E: WORK ANALYSIS

In the main text, we study how the work is distributed along a compression as a function of the composition of the aggregate. This analysis relies on the assumption that the total work for a given transition does not depend on ϕ. We found that, within the uncertainty of the experiments, the total work for the transition $p \to (p-1)$ is constant and is not correlated to the fraction of defects ϕ. Table II summarizes the total work, W_{tot}, exerted to go from four to three rows for the different aggregates.

[1] A. W. Philips, *Amorphous Solids: Low-Temperature Properties* (Springer, Berlin, 1981).

[2] P. N. Pusey, The effect of polydispersity on the crystallization of hard spherical colloids, J. Phys-Paris **48**, 709 (1987).

[3] S. Auer and D. Frenkel, Suppression of crystal nucleation in polydisperse colloids due to increase of the surface free energy, Nature (London) **413**, 711 (2001).

[4] P. J. Yunker, Z. Zhang, and A. G. Yodh, Observation of the Disorder-Induced Crystal-To-Glass Transition, Phys. Rev. Lett. **104**, 015701 (2010).

[5] P. J. Yunker, K. Chen, M. D. Gratale, M. A. Lohr, T. Still, and A. G. Yodh, Physics in ordered and disordered colloidal matter composed of poly(*N*-isopropylacrylamide) microgel particles, Rep. Prog. Phys. **77**, 056601 (2014).

[6] R. Higler, J. Appel, and J. Sprakel, Substitutional impurity-induced vitrification in microgel crystals, Soft Matter **9**, 5372 (2013).

[7] M. Hanifpour, N. Francois, S. M. V. Allaei, T. Senden, and M. Saadatfar, Mechanical Characterization of Partially Crystallized Sphere Packings, Phys. Rev. Lett. **113**, 148001 (2014).

[8] J. Comtet, A. Lainé, A. Niguès, L. Bocquet, and A. Siria, Atomic rheology of gold nanojunctions, Nature (London) **569**, 393 (2019).

[9] C. S. O'Hern, L. E. Silbert, A. J. Liu, and S. R. Nagel, Jamming at zero temperature and zero applied stress: The epitome of disorder, Phys. Rev. E **68**, 011306 (2003).

[10] C. P. Goodrich, A. J. Liu, and S. R. Nagel, Solids between the mechanical extremes of order and disorder, Nat. Phys. **10**, 578 (2014).

[11] R. Mari, F. Krzakala, and J. Kurchan, Jamming Versus Glass Transitions, Phys. Rev. Lett. **103**, 025701 (2009).

[12] H. Tong, P. Tan, and N. Xu, From crystals to disordered crystals: A hidden order-disorder transition, Sci. Rep. **5**, 15378 (2015).

[13] J. S. Babu, C. Mondal, S. Sengupta, and S. Karmakar, Excess vibrational density of states and the brittle to ductile transition in crystalline and amorphous solids, Soft Matter **12**, 1210 (2016).

[14] H. Zhang and Y. Han, Compression-Induced Polycrystal-Glass Transition in Binary Crystals, Phys. Rev. X **8**, 041023 (2018).

[15] P. Charbonneau, E. I. Corwin, L. Fu, G. Tsekenis, and M. van der Naald, Glassy, Gardner-like phenomenology in minimally polydisperse crystalline systems, Phys. Rev. E **99**, 020901(R) (2019).

[16] H. Mizuno, S. Mossa, and J.-L. Barrat, Elastic heterogeneity, vibrational states, and thermal conductivity across an amorphisation transition, Europhys. Lett. **104**, 56001 (2013).

[17] M. Ozawa, L. Berthier, G. Biroli, and G. Tarjus, The role of fluctuations on the yielding transition of two-dimensional glasses, arXiv:1912.06021.

[18] N. C. Keim and P. E. Arratia, Role of disorder in finite-amplitude shear of a 2D jammed material, Soft Matter **11**, 1539 (2015).

[19] E. R. Weeks, J. Crocker, A. C. Levitt, A. Schofield, and D. Weitz, Three-dimensional direct imaging of structural relaxation near the colloidal glass transition, Science **287**, 627 (2000).

[20] J. Crocker and D. Grier, Methods of digital video microscopy for colloidal studies, J. Colloid Interface Sci. **179**, 298 (1996).

[21] A. Kose, M. Ozaki, K. Takano, Y. Kobayashi, and S. Hachisu, Direct observation of ordered latex suspension by metallurgical microscope, J. Colloid Interface Sci. **44**, 330 (1973).

[22] I. Jorjadze, L.-L. Pontani, K. A. Newhall, and J. Brujic, Attractive emulsion droplets probe the phase diagram of jammed granular matter, Proc. Natl. Acad. Sci. USA **108**, 4286 (2011).

[23] G. Hunter and E. R. Weeks, The physics of the colloidal glass transition, Rep. Prog. Phys. **75**, 066501 (2012).

[24] B. Illing, S. Fritschi, H. Kaiser, C. L. Klix, G. Maret, and P. Keim, Mermin-Wagner fluctuations in 2D amorphous solids, Proc. Natl. Acad. Sci. USA **114**, 1856 (2017).

[25] S. Vivek, C. P. Kelleher, P. M. Chaikin, and E. R. Weeks, Long-wavelength fluctuations and the glass transition in two dimensions and three dimensions, Proc. Natl. Acad. Sci. USA **114**, 1850 (2017).

[26] J. Brujić, S. F. Edwards, D. V. Grinev, I. Hopkinson, D. Brujić, and H. A. Makse, 3D bulk measurements of the force distribution in a compressed emulsion system, Faraday Discuss. **123**, 207 (2003).

[27] K. W. Desmond, P. J. Young, D. Chen, and E. R. Weeks, Experimental study of forces between quasi-two-dimensional emulsion droplets near jamming, Soft Matter **9**, 3424 (2013).

[28] B. Li, D. Zhou, and Y. Han, Assembly and phase transitions of colloidal crystals, Nat. Rev. Mater. **1**, 15011 (2016).

[29] D. V. Denisov, K. A. Lorincz, W. J. Wright, T. C. Hufnagel, A. Nawano, X. Gu, J. T. Uhl, K. A. Dahmen, and P. Schall, Universal slip dynamics in metallic glasses and granular matter – linking frictional weakening with inertial effects, Sci. Rep. **7**, 43376 (2017).

[30] K. Zhang, M. Fan, Y. Liu, J. Schroers, M. D. Shattuck, and C. S. O'Hern, Beyond packing of hard spheres: The effects of core softness, non-additivity, intermediate-range repulsion, and many-body interactions on the glass-forming ability of bulk metallic glasses, J. Chem. Phys. **143**, 184502 (2015).

[31] P. N. Pusey and W. van Megen, Phase behaviour of concentrated suspensions of nearly hard colloidal spheres, Nature (London) **320**, 340 (1986).

[32] Z. Zhang, N. Xu, D. T. N. Chen, P. J. Yunker, A. M. Alsayed, K. B. Aptowicz, P. Habdas, A. J. Liu, S. R. Nagel, and A. G. Yodh, Thermal vestige of the zero-temperature jamming transition, Nature (London) **459**, 230 (2009).

[33] J. M. Lynch, G. C. Cianci, and E. R. Weeks, Dynamics and structure of an aging binary colloidal glass, Phys. Rev. E **78**, 031410 (2008).

[34] L. Assoud, F. Ebert, P. Keim, R. Messina, G. Maret, and H. Löwen, Ultrafast Quenching of Binary Colloidal Suspensions in an External Magnetic Field, Phys. Rev. Lett. **102**, 238301 (2009).

[35] H. Shiba, Y. Yamada, T. Kawasaki, and K. Kim, Unveiling Dimensionality Dependence of Glassy Dynamics: 2D Infinite Fluctuation Eclipses Inherent Structural Relaxation, Phys. Rev. Lett. **117**, 245701 (2016).

[36] J. Bibette, D. Roux, and B. Pouligny, Creaming of Emulsions - the Role of Depletion Forces Induced By Surfactant, J. Phys. II **2**, 401 (1992).

[37] See Supplemental Material at http://link.aps.org/supplemental/10.1103/PhysRevResearch.2.023070 for Movies M1 and M2. Movie M1 illustrates the preparation of an aggregate of oil droplets in a droplet-by-droplet manner. Movie M2 shows the

compression of a perfect single crystal (left panel) while simultaneously measuring the compression force (right panel).

[38] S. Barkley, S. J. Scarfe, E. R. Weeks, and K. Dalnoki-Veress, Predicting the size of droplets produced through Laplace pressure induced snap-off, Soft Matter **12**, 7398 (2016).

[39] M. Backholm, W. S. Ryu, and K. Dalnoki-Veress, Viscoelastic properties of the nematode Caenorhabditis elegans, a self-similar, shear-thinning worm, Proc. Natl. Acad. Sci. USA **110**, 4528 (2013).

[40] M. Backholm and O. Bäumchen, Micropipette force sensors for in vivo force measurements on single cells and multicellular microorganisms, Nat. Protoc. **14**, 594 (2019).

[41] Y. Gai, C. M. Leong, W. Cai, and S. K. Y. Tang, Spatiotemporal periodicity of dislocation dynamics in a two-dimensional microfluidic crystal flowing in a tapered channel, Proc. Natl. Acad. Sci. USA **113**, 12082 (2016).

[42] D. McDermott, C. J. O. Reichhardt, and C. Reichhardt, Avalanches, plasticity, and ordering in colloidal crystals under compression, Phys. Rev. E **93**, 062607 (2016).

[43] G. Biroli and P. Urbani, Breakdown of elasticity in amorphous solids, Nat. Phys. **12**, 1130 (2016).

[44] I. M. Sokolov and J. Klafter, *First Steps in Random Walks: From Tools to Applications.* (Oxford University Press, Oxford, 2011).

Paper III

Continuum model applied to granular analogs of droplets and puddles

J.-C. Ono-dit-Biot, T. Lorand and K. Dalnoki-Veress, Phys. Rev. Lett., **125**, 228001 (2020).

This work examines the spreading of aggregates made of lightly attractive frictionless oil droplets on a surface. Droplets are produced in a liquid cell and rise to the top due to buoyancy where they accumulate. Instead of forming a conical heap as expected with granular materials, we find that, after an initial stage, the aggregates spread in 2D along the horizontal direction. The growth of the aggregates is analogous to one of a liquid puddle (see discussion in section 1.4.3) and the height of the droplet aggregate remains constant in the later stage of the growth. The height of the aggregates is set by a balance between the buoyancy and the adhesion between the droplets which can be tuned experimentally. In analogy with the the capillary length of liquid, κ^{-1}, (see section 1.4.2), we define a "granular capillary length" which captures the balance between adhesion strength and buoyancy. The granular capillary length set a natural length scale for the experiment which can be used to describe the geometry of the aggregate. To measure the granular capillary length as a function of the different experimental parameters, we developed an experiment to precisely measure the adhesion between two oil droplets.

For this research project, I designed the experimental setup in collaboration with Kari Dalnoki-Veress. I collected and analyzed all the data related to the spreading of aggregates. I designed the setup for the adhesion measurement between droplets and conducted preliminary experiments. This measurement was then handed-off to Tanel Lorand, a summer student under the supervision of Kari Dalnoki-Veress and myself. Tanel Lorand determined the ideal experimental parameters for the measurement, collected and analyzed the adhesion experiment data. I developed the theoretical model that allows to capture the geometry of the aggregate of droplets that spread on the top glass slide with help from Kari Dalnoki-Veress. I prepared the first draft of the manuscript which was then revised by Kari Dalnoki-Veress.

Continuum Model Applied to Granular Analogs of Droplets and Puddles

Jean-Christophe Ono-dit-Biot,[1] Tanel Lorand,[1] and Kari Dalnoki-Veress[1,2,*]
[1] *Department of Physics and Astronomy, McMaster University, 1280 Main Street West, Hamilton, Ontario, L8S 4M1, Canada*
[2] *UMR CNRS Gulliver 7083, ESPCI Paris, PSL Research University, 75005 Paris, France*

(Received 13 July 2020; revised 28 September 2020; accepted 16 October 2020; published 24 November 2020)

We investigate the growth of aggregates made of adhesive frictionless oil droplets, piling up against a solid interface. Monodisperse droplets are produced one by one in an aqueous solution and float upward to the top of a liquid cell where they accumulate and form an aggregate at a flat horizontal interface. Initially, the aggregate grows in 3D until its height reaches a critical value. Beyond a critical height, adding more droplets results in the aggregate spreading in 2D along the interface with a constant height. We find that the shape of such aggregates, despite being granular in nature, is well described by a continuum model. The geometry of the aggregates is determined by a balance between droplet buoyancy and adhesion as given by a single parameter, a "granular" capillary length, analogous to the capillary length of a liquid.

DOI: 10.1103/PhysRevLett.125.228001

From playing with sand, sugar, or salt, to the large piles that can be observed in an industrial or agricultural context, the formation of granular piles is familiar to all. Granular materials are of particular interest as they can exhibit both liquid or solidlike behaviors [1–3]. Such systems give rise to unusual properties such as a characteristic angle of repose [4,5], clogging through an opening [6,7], intermittent flow and avalanches [8–10], force chains [10–13], and dynamical heterogeneities [1,14–16]. These properties are strongly affected by modifying the interaction between grains; for example, the water added to sand forms interstitial capillary bridges which facilitate adhesion strong enough to build exquisite sand castles [17–19]. The adhesion forces can originate from diverse mechanisms: depletion interactions [20,21], capillary forces [22,23], electrostatic forces [24,25], or simply van der Waals interactions [21,26]. Understanding these interactions and the effects on structure formation impacts a range of fields; for example, colloidal gels can be used as models to understand biological systems [27–33] or geophysical flows [34], and aggregates of dust particles are studied in the context of planet formation [35].

Here, we are specifically interested in piles and aggregates that form at an obstacle. In many cases piles grow in 3D with a characteristic shape defined by the angle of repose. The angle of repose and its dependence on surface roughness [5,36] or the shape of the grains [37] has been extensively studied. Recent studies have shown that even without friction, spheres can pack and exhibit granular properties such as the angle of repose. For example, Ortiz *et al.* [38] observed sandpilelike structures when flowing repulsive colloids against an obstacle in a microfluidic channel. Similar structures were also observed with glass beads colliding on a target where friction cannot be discounted [39]. In another experiment, Shorts and Feitosa [40] defined an angle of repose when floating bubbles in a container. A feature of both studies with frictionless particles was that the angle of repose was not sustained when the flow was turned off. Lespiat and co-workers [41] showed that the mechanical behavior of granular materials can be extended to assemblies of frictionless bubbles, including the existence of a critical angle at which the assembly transitions from a solidlike to a liquidlike behavior. Finally, nonzero angles of repose have also been reported in numerical simulations of frictionless particles [42,43]. We contrast these granular piles with the familiar spreading of a continuum liquid on a surface. Instead of forming a 3D pile, a liquid droplet grows in 3D as a spherical cap to a maximum height, after which the liquid spreads in 2D as a pancakelike puddle, with a constant height. This height is set by a balance between surface tension and gravity, and of order the capillary length $\kappa^{-1} = \sqrt{\gamma/\rho g}$ [44], where γ is the surface tension, ρ is the density of the liquid, and g the gravitational acceleration.

Here we introduce adhesion between frictionless athermal oil droplets. Droplets are produced one by one and rise by buoyancy to the top of a liquid cell where they accumulate against a horizontal glass surface and form an aggregate. Surprisingly, the aggregate does not assume a 3D sandpilelike structure as is typical of granular materials. Instead, after an initial regime, the height of the aggregate saturates and the aggregate grows in 2D, spreading along the interface. We find that the growth is analogous to the growth of a liquid puddle, and that the shape of the aggregate is determined by a balance between buoyancy and adhesion between the droplets. In analogy with the capillary length of a liquid κ^{-1}, we introduce a "granular" capillary length, which captures the relative importance of the droplet's buoyancy and adhesion strength in the formation of the aggregates. This granular analog of the

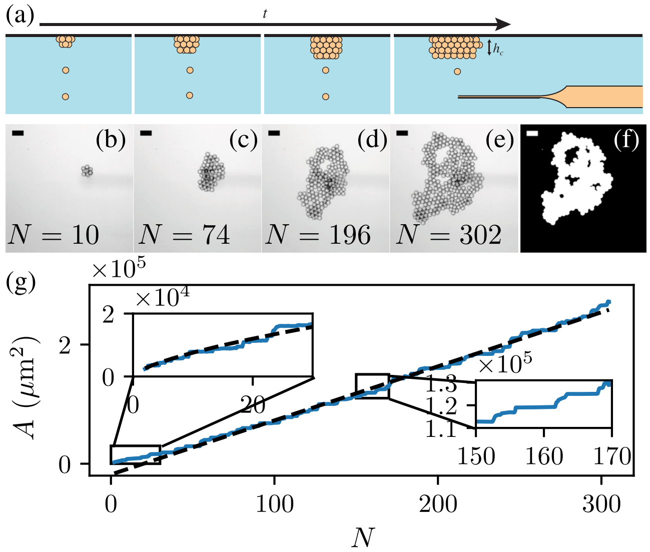

FIG. 1. (a) Schematic side view of the experimental chamber. A glass pipette produces monodisperse oil droplets with a radius of ~10 μm in an aqueous solution. Droplets float to the top and form an aggregate that spreads on the top glass slide over time. (b)–(e) Optical microscopy images of the aggregate at different stage of the growth (scale bars are 100 μm). (f) Images are binarized to measure the area covered by the droplet aggregate A. (g) Evolution of the aggregate area as a function of the number of droplets N (here $R = 17.8$ μm, $C = 0.10$ mol/l). The black dashed line is a linear fit of the data for $N > 30$. Left inset: early growth of the aggregate with best fit of the model presented in the main text for $N_{\text{droplets}} \leq 30$. Right inset: the stepwise increase of the area corresponds to collapsing events.

capillary length is found to well predict the equilibrium shape of the aggregates.

The experimental setup is illustrated in Fig. 1(a) and consists of a chamber (55×30 mm^2) made from two glass slides separated by a gap of 2.5 mm (larger than the size of the droplets by 10^3). The chamber is filled with an aqueous solution of NaCl at 1.5% (w/w) and a surfactant sodium dodecyl sulfate (SDS). The concentration of SDS, C, is varied from 0.07 to 0.21 mol/l in the experiment. In this concentration range, SDS not only stabilizes the oil droplets, but also forms micelles which act as a depletant resulting in a short-ranged attraction between the droplets [20]. A pipette is inserted into the chamber to produce droplets. The pipette is pulled from a glass capillary tube (World Precision Instruments, U.S.) with a pipette puller (Narishige, Japan) to a tip diameter of ~10 μm. Mineral oil is pushed through the pipette to produce monodisperse droplets, with radius R using the snap-off instability [45]. The variation in R within each experimental trial is less than 1%. The pipette is connected to an open reservoir of mineral oil placed at a fixed height ensuring a constant pressure, and hence a constant volumic flow rate. Because of buoyancy, droplets float to the top of the chamber where they accumulate under the top glass slide [Fig. 1(a)]. Over time, the aggregate grows and spreads horizontally at the top glass slide as illustrated in Fig. 1(a). Droplets are produced a constant rate of about one droplet every 20 s. The slow rate ensures that the aggregate has time to rearrange and that the results upon addition of each droplet are quasiequilibrium. The friction between droplets and the top glass slide is negligible and droplets can freely move along the horizontal direction [46]. The chamber is placed atop of an inverted microscope for imaging while the aggregates are growing. The aggregate is a 3D object which is imaged with an optical microscope; thus the images shown in Figs. 1(b)–1(e) are 2D projections. The darker regions show areas where the aggregate has more layers of droplets in the vertical direction, which corresponds to a thicker aggregate. As shown in Fig. 1(e), the aggregates are not always dense and patches without droplets can form within the aggregate. Raw images are analyzed to measure the area covered by droplets A. Holes within the aggregate are excluded from the measured area, as shown in Fig. 1(f) [47].

The evolution of the area A as a function of the number of droplets N in the aggregate is shown in Fig. 1(g). The aggregate does not spread continuously on the glass slide. Rather, the system alternates between droplets which accumulate vertically to some critical height, followed by small avalanches which collapse the aggregate. During the vertical growth the area remains constant while the pressure due to buoyancy grows. Eventually the aggregate reaches a critical height when the pressure cannot be sustained and the structure collapses. These avalanches are accompanied by an increases in the area of the cluster. Alternating between these two stages results in the "avalanche steps" shown in Fig. 1(g) and continues as long as droplets are added to the aggregate.

Figure 1(g) reveals two stages in the evolution of $A(N)$. Clearly, for $N \gtrsim 30$, $A(N)$ is linear, when smoothing over the underlying avalanche steps. Since the change in area is linear in N, the growth is in 2D with a constant average height h_c. This linear growth is analogous to the spreading of a liquid puddle once the height of the droplet exceeds a critical value set by κ^{-1} where the area grows linearly with the volume of the liquid. At early stages, for $N \lesssim 30$, a deviation from the linear growth is observed in Fig. 1(g). Again this stage is analogous to the growth of a liquid droplet prior to reaching a critical height: just as a droplet grows in all three dimensions as a self-similar spherical cap, the granular system should follow 3D growth with $A \propto N^{2/3}$. The 3D growth scaling is verified in the inset of Fig. 1(g) for $N \leq 30$, while a best fit line to the 2D growth regime for $N > 30$ is shown in the main plot. Despite the aggregate being granular in nature, its shape and growth is analogous to that observed with continuous media: an initial 3D growth regime is followed by the aggregate growing horizontally in 2D along the top glass slide [see schematics Fig. 1(a)]. Underlying the two general

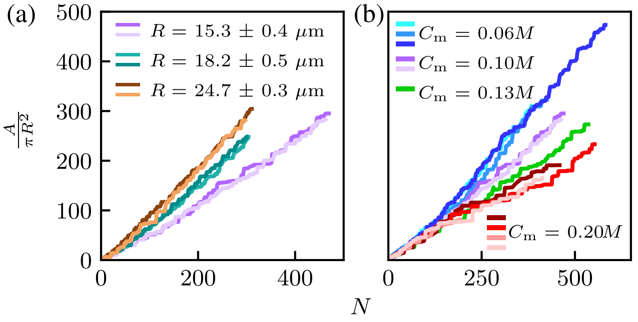

FIG. 2. (a) Normalized aggregate area as a function of the number of droplets for different droplet radii, while the strength of adhesion is kept constant ($C_m = 0.10$ mol/l). (b) Normalized aggregate area as a function of the number of droplets for different adhesion strengths, while the droplet radius ($R = 15.3 \pm 0.4$ μm) is kept constant. The strength of adhesion increases with SDS concentration. The purple curves correspond to the same data shown in (a).

growth laws are the avalanche steps resulting from the collapsing events, similar to that observed in traditional granular materials.

In order to investigate the role of buoyancy and adhesion, we first consider adjusting the droplet radius while keeping the adhesion between droplets constant. Data for the area of the aggregate normalized by the size of the droplet $A/\pi R^2$ are shown in Fig. 2(a) for three different radii at a constant concentration of SDS. The uncertainty in the droplet radius originates from the variability from one experimental trial to another. In Fig. 2(a) it is observed that the growth rate increases with droplet radii, and hence buoyancy. In the limit of the puddlelike regime, a faster growth indicates a thinner aggregate with a smaller average critical height of the aggregate h_c. We now change the strength of adhesion by varying the concentration of SDS while keeping the radius of the droplets (or buoyancy) fixed. A larger volume fraction of micelles in solution leads to stronger adhesion between droplets due to the depletion interaction. The volume fraction of micelles is given by $\phi_m = (C - C_{\mathrm{CMC}})N_A/N_a$, with Avogadro's constant N_A, the critical micelle concentration $C_{\mathrm{CMC}} = 8$ mM [20], and the number of SDS molecules in one micelle $N_a \approx 120$ [48]. For simplicity, the control parameter to quantify the adhesion strength is taken as $C_m = C - C_{\mathrm{CMC}}$ as it is directly proportional to the micelle volume fraction ϕ_m. Figure 2(b) shows the effect of the micelle concentration for a fixed droplet size ($R = 15.3 \pm 0.4$ μm). Thicker aggregates (larger h_c) are formed when the strength of adhesion is increased. Thus from Fig. 2 we can conclude that the equilibrium shape of the aggregates is dictated by a balance between buoyancy and adhesion: (i) increasing buoyancy results in thinner aggregates and (ii) increasing adhesion increases the thickness of aggregates.

The balance between buoyancy and adhesion, which determines h_c, is reminiscent of how the height of a liquid puddle is governed by a balance between gravity and surface tension given by the capillary length $\kappa^{-1} = \sqrt{\gamma/\rho g}$ [44]. In the granular system the adhesion $\mathcal{A}$ (J/m^2) favors contact between droplets and stabilizes aggregates. Droplets at the surface of the aggregate have a higher free energy as they are missing neighbors in analogy with the definition of surface tension [21]. We can then define a granular capillary length as $\delta = \sqrt{\mathcal{A}/\Delta\rho g}$, with $\Delta\rho$ the difference in density between the aqueous solution and mineral oil. Within a geometrical factor of order one, the height of the aggregate, $h_c \approx \delta$. The volume of the aggregate can be written as the product of the volume of one droplet V_s and the number of droplets, $V \approx V_s N/\phi$, where ϕ is the packing fraction of the aggregate. Since ϕ ranges from ~0.64 to ~0.74 for random-close-packed and hexagonal-close-packed spheres, we take $\phi \approx 0.7$. We can approximate that the transition from 3D growth to 2D growth occurs once the aggregate reaches a volume V^* corresponding to, roughly, a hemisphere with radius δ. This crossover corresponds to an aggregate area $A^* \approx \pi\delta^2$ and characteristic number of droplets $N^* \approx \phi(V^*/V_s) = (\phi/2)(\delta/R)^3$. Thus N^* and A^* represent the crossover from 3D to 2D growth. In the initial growth regime we have $A \approx \pi[(3/2\pi)V]^{2/3}$, which can be renormalized as $A/A^* \approx (N/N^*)^{2/3}$. Similarly, for the puddlelike 2D regime, excluding edge effects [49], the volume of the aggregate $V \approx A\delta$, which leads to $A/A^* \approx \frac{2}{3}(N/N^*)$. To summarize, to within geometric prefactors of order one, there is a crossover from $A/A^* \propto (N/N^*)^{2/3}$ at early growth of the aggregate to $A/A^* \propto N/N^*$ at late stages of the growth, with a crossover at (A^*, N^*). The parameters A^* and N^* depend on the granular capillary length δ. To calculate δ, and thus (A^*, N^*), the adhesion strength $\mathcal{A}$ due to the depletion force must be measured.

Depletion forces have been shown to scale linearly with the concentration of SDS micelles, proportional to C_m, and the radius R [50]. To characterize the droplet-droplet interaction, the adhesion force was measured directly following a method outlined in Ref. [51] as follows. Individual droplets are manipulated using pulled glass micropipettes with modest suction to hold the droplets. The left pipette [see Fig. 3(a)] moves at a constant velocity ($v = 0.3$ μm/s). The right micropipette is long (~1 cm), thin (~10 μm), and bent into an "L" shape so that its deflection (spring constant, $k = 0.12$ nN/μm) can be used to measure the adhesion force. Figure 3(a) shows images of the experiment. The left droplet is initially displaced to the right ($0 < t < 20$ s). As contact is made, $t \sim 15$ s, the force sensing pipette deflects to the right and the force increases [Fig. 3(b)]. After keeping the droplets in contact for about 10 s, the motion is reversed and the force decreases $t > 30$, eventually becoming negative due to adhesion forces. The contact between droplets is broken when a critical unbinding force F_c is reached [see Fig. 3(b)] [52].

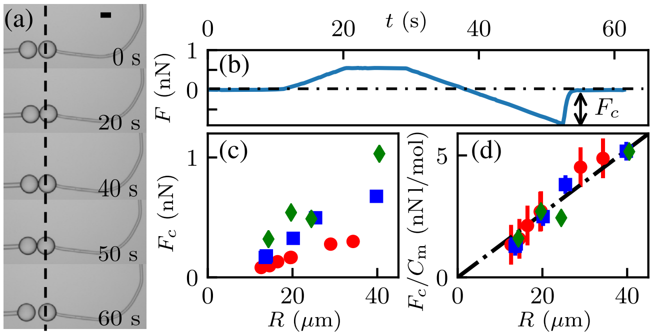

FIG. 3. (a) Adhesion force measurement: two droplets are pushed into contact by the left pipette, held constant, and then pulled apart. The dashed line marks the equilibrium position of the right droplet. The deflection of the sensing pipette (right) is converted to a force. The scale bar is 100 μm. (b) Force measurement between two droplets of oil ($R = 39.8$ μm, $C_m = 0.13$ mol/l). The force rises as the droplets are pushed together, and then decreases as the droplets are pulled apart (negative slope). A negative force results from adhesion between the droplets. The contact between droplets is broken when the force suddenly jumps to 0. (c) Unbinding force as a function of the droplet radius for various concentrations in SDS: red circles, $C_m = 0.06$ mol/l; blue squares, $C_m = 0.13$ mol/l; green diamonds, $C_m = 0.20$ mol/l. (d) Collapse of the unbinding force by normalizing by the concentration in micelles. The black dashed line corresponds to the linear fit including all three datasets.

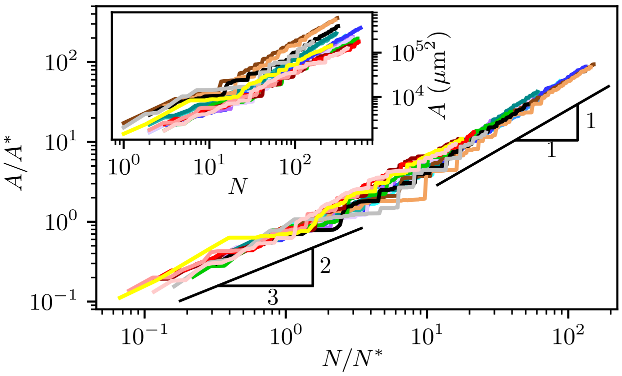

FIG. 4. Double-logarithmic plot of the renormalized aggregate area versus the renormalized number of droplets for various droplet sizes R and adhesion strength $\mathcal{A}$. The aggregate growth transitions from $(N/N^*)^{2/3}$ to N/N^* at (A^*, N^*) (nonrenormalized data shown in inset). The data correspond to those presented in Fig. 2 using the same color code, and three further datasets are included: black ($R = 24.7$ μm, $C_m = 0.20$ mol/l), gray ($R = 24.7$ μm, $C_m = 0.20$ mol/l), and yellow ($R = 18.7$ μm, $C_m = 0.20$ mol/l).

Results for F_c as a function of droplet radius and SDS concentration are shown in Fig. 3(c). The expected normalization of the force F_c/C_m results in the collapse of the different curves onto a single line [Fig. 3(d)], which confirms $F_c \propto C_m R$. Since the unbinding force between two vesicles is $F_c = \pi R \mathcal{A}$ [53], the slope of the dashed line in Fig. 3(d) is used to obtain the adhesion strength $\mathcal{A}(C_m)$. For the system studied here, $\Delta\rho \approx 200$ kg m^{-3}, and the measured values for δ range from ~36 to ~65 μm. The crossover values (A^*, N^*) can now be calculated for each experiment. In Fig. 4 we show the renormalized area A/A^* as a function of N/N^* on a double-logarithmic plot. We observe not only an excellent collapse of all the data, but a transition from 3D growth, $A/A^* \propto (N/N^*)^{2/3}$, to 2D puddlelike growth at long times, $A/A^* \propto N/N^*$, with a crossover at (A^*, N^*), as expected from the model.

Here we have explored using a continuum model for an aggregate of athermal droplets, but such liquidlike behaviors have been observed in other granular systems also. For example, a column of glass beads can break up into clusters of grains [54], which is reminiscent of the Plateau-Rayleigh instability observed as a liquid jet breaks into droplets. Analogs to the Rayleigh-Taylor instability have also been reported during the sedimentation of thermal colloids [55]. Other surface-tension-dependent phenomena found at liquid interfaces are capillary fluctuations and capillary waves. Similar fluctuations can be seen at the interface between a granular particle-rich condensed and a particle-poor gas phase [56–58]. A fundamental advantage of the system described in this study is that the interactions between particles are easily tunable and particles can be imaged and tracked individually. The model is not specific to depletion interactions and can be generalized to other sources of adhesion such as capillary interactions, van der Waals, or biological interactions between cells. Indeed, foams and emulsions have been widely used to model complex biological systems [27–33]. The theoretical framework developed here can be applied to a broad range of systems through defining a granular capillary length, provided that the adhesion $\mathcal{A}$ can be defined.

While the continuum model presented well explains the growth rate of the aggregate, the model coarse grains the underlying avalanches which result in the discrete growth steps. The literature suggests that the statistics of such discreet events are independent of the length scale of the system [59–62]. The droplet experiment provides an ideal system to study such behaviors and the dependence on the granular capillary length. The noncircular shape of the puddle shown in Fig. 1 is also a direct result of the granular nature of the aggregates not captured by the simple model presented. It is expected that both the avalanche dynamics and shape of the aggregates depends on the granular capillary length; however, these aspects remain outstanding questions.

In summary, we present a study of the growth of an aggregate of adhesive oil droplets. Because of buoyancy forces, the aggregate spreads horizontally along the top surface of the chamber. However, the adhesion between the droplets stabilizes the aggregate along the vertical direction. Aggregates initially grow in 3D until they reach a maximum height, after which the growth occurs in 2D.

This growth is analogous to that of a liquid puddle. The height of the aggregates is entirely determined by the balance between buoyancy and the adhesion strength between droplets. We introduce the granular capillary length, $\delta = \sqrt{\mathcal{A}/\Delta\rho g}$, the granular equivalent of the capillary length for liquids. Using the analogy with a liquid puddle, we developed a simple model that fully captures the aggregate geometry as a function of the adhesion strength and the droplet size. Despite the aggregates being granular in nature, displaying avalanches in the growth dynamics, the shape of the aggregates can be captured using the physics of continuous media.

We gratefully acknowledge financial support by the Natural Science and Engineering Research Council of Canada. We also thank Karen Daniels, Ramin Golestanian, Johnathan Hoggarth, James Forrest, Elie Raphael, Thomas Salez, An-Chang Shi, and Eric Weeks for discussions.

---

[*] dalnoki@mcmaster.ca

[1] A. D. Gopal and D. J. Durian, Nonlinear Bubble Dynamics in a Slowly Driven Foam, Phys. Rev. Lett. **75**, 2610 (1995).

[2] H. M. Jaeger, S. R. Nagel, and R. P. Behringer, Granular solids, liquids, and gases, Rev. Mod. Phys. **68**, 1259 (1996).

[3] P. Jop, Y. Forterre, and O. Pouliquen, A constitutive law for dense granular flows, Nature (London) **441**, 727 (2006).

[4] C. Coulomb, An attempt to apply the rules of maxima and minima to several problems of stability related to architecture, Mem. Math. Acad. R. Sci. (Paris) **7**, 343 (1776).

[5] B. Andreotti, Y. Forterre, and O. Pouliquen, *Granular Media: Between Fluid and Solid* (Cambridge University Press, Cambridge, England, 2013).

[6] I. Zuriguel, D. R. Parisi, R. C. Hidalgo, C. Lozano, A. Janda, P. A. Gago, J. P. Peralta, L. M. Ferrer, L. A. Pugnaloni, E. Clément, D. Maza, I. Pagonabarraga, and A. Garcimarín, Clogging transition of many-particle systems flowing through bottlenecks, Sci. Rep. **4**, 7324 (2014).

[7] X. Hong, M. Kohne, M. Morrell, H. Wang, and E. R. Weeks, Clogging of soft particles in two-dimensional hoppers, Phys. Rev. E **96**, 062605 (2017).

[8] V. Frette, K. Christensen, A. Malthe-Sørenssen, J. Feder, T. Jøssang, and P. Meakin, Avalanche dynamics in a pile of rice, Nature (London) **379**, 49 (1996).

[9] P.-A. Lemieux and D. J. Durian, From Avalanches to Fluid Flow: A Continuous Picture of Grain Dynamics Down a Heap, Phys. Rev. Lett. **85**, 4273 (2000).

[10] R. Kozlowski, C. M. Carlevaro, K. E. Daniels, L. Kondic, L. A. Pugnaloni, J. E. S. Socolar, H. Zheng, and R. P. Behringer, Dynamics of a grain-scale intruder in a two-dimensional granular medium with and without basal friction, Phys. Rev. E **100**, 032905 (2019).

[11] C.-h. Liu, S. R. Nagel, D. Schecter, S. Coppersmith, S. Majumdar, O. Narayan, and T. Witten, Force fluctuations in bead packs, Science **269**, 513 (1995).

[12] A. A. Zadeh, J. Barés, T. A. Brzinski, K. E. Daniels, J. Dijksman, N. Docquier, H. O. Everitt, J. E. Kollmer, O. Lantsoght, D. Wang, M. Workamp, Y. Zhao, and H. Zheng, Enlightening force chains: A review of photoelasticimetry in granular matter, Granular Matter **21**, 83 (2019).

[13] Y. Zhao, J. Barés, H. Zheng, J. E. S. Socolar, and R. P. Behringer, Shear-Jammed, Fragile, and Steady States in Homogeneously Strained Granular Materials, Phys. Rev. Lett. **123**, 158001 (2019).

[14] W. K. Kegel and A. van Blaaderen, Direct observation of dynamical heterogeneities in colloidal hard-sphere suspensions, Science **287**, 290 (2000).

[15] A. R. Abate and D. J. Durian, Topological persistence and dynamical heterogeneities near jamming, Phys. Rev. E **76**, 021306 (2007).

[16] X. Cao, H. Zhang, and Y. Han, Release of free-volume bubbles by cooperative-rearrangement regions during the deposition growth of a colloidal glass, Nat. Commun. **8**, 362 (2017).

[17] D. Hornbaker, R. Albert, I. Albert, A.-L. Barabási, and P. Schiffer, What keeps sandcastles standing?, Nature (London) **387**, 765 (1997).

[18] T. G. Mason, A. J. Levine, D. Ertaş, and T. C. Halsey, Critical angle of wet sandpiles, Phys. Rev. E **60**, R5044 (1999).

[19] M. Scheel, R. Seemann, M. Brinkmann, M. Di Michiel, A. Sheppard, B. Breidenbach, and S. Herminghaus, Morphological clues to wet granular pile stability, Nat. Mater. **7**, 189 (2008).

[20] J. Bibette, D. Roux, and B. Pouligny, Creaming of emulsions: The role of depletion forces induced by surfactant, J. Phys. II **2**, 401 (1992).

[21] R. A. L. Jones, R. Jones, R. A. Jones *et al.*, *Soft Condensed Matter* (Oxford University Press, New York, 2002), Vol. 6.

[22] M. G. Nikolaides, A. R. Bausch, M. F. Hsu, A. D. Dinsmore, M. P. Brenner, C. Gay, and D. A. Weitz, Electric-field-induced capillary attraction between like-charged particles at liquid interfaces, Nature (London) **420**, 299 (2002).

[23] J. C. Loudet, A. M. Alsayed, J. Zhang, and A. G. Yodh, Capillary Interactions between Anisotropic Colloidal Particles, Phys. Rev. Lett. **94**, 018301 (2005).

[24] J. Q. Feng, Electrostatic interaction between two charged dielectric spheres in contact, Phys. Rev. E **62**, 2891 (2000).

[25] U. Konopka, F. Mokler, A. V. Ivlev, M. Kretschmer, G. E. Morfill, H. M. Thomas, H. Rothermel, V. E. Fortov, A. M. Lipaev, V. I. Molotkov, A. P. Nefedov, Y. M. Baturin, Y. Budarin, A. I. Ivanov, and M. Roth, Charge-induced gelation of microparticles, New J. Phys. **7**, 227 (2005).

[26] S. C. Du Pont, P. Gondret, B. Perrin, and M. Rabaud, Wall effects on granular heap stability, Europhys. Lett. **61**, 492 (2003).

[27] K. Guevorkian, M.-J. Colbert, M. Durth, S. Dufour, and F. Brochard-Wyart, Aspiration of Biological Viscoelastic Drops, Phys. Rev. Lett. **104**, 218101 (2010).

[28] O. Lieleg, J. Kayser, G. Brambilla, L. Cipelletti, and A. R. Bausch, Slow dynamics and internal stress relaxation in bundled cytoskeletal networks, Nat. Mater. **10**, 236 (2011).

[29] J. Colombo and E. Del Gado, Stress localization, stiffening, and yielding in a model colloidal gel, J. Rheol. **58**, 1089 (2014).

[30] T. Hayashi and R. W. Carthew, Surface mechanics mediate pattern formation in the developing retina, Nature (London) **431**, 647 (2004).

[31] D. Gonzalez-Rodriguez, K. Guevorkian, S. Douezan, and F. Brochard-Wyart, Soft matter models of developing tissues and tumors, Science **338**, 910 (2012).

[32] L.-L. Pontani, I. Jorjadze, V. Viasnoff, and J. Brujic, Biomimetic emulsions reveal the effect of mechanical forces on cell–cell adhesion, Proc. Natl. Acad. Sci. U.S.A. **109**, 9839 (2012).

[33] S. Douezan and F. Brochard-Wyart, Active diffusion-limited aggregation of cells, Soft Matter **8**, 784 (2012).

[34] D. J. Jerolmack and K. E. Daniels, Viewing earth's surface as a soft-matter landscape, Nat. Rev. Phys. **1**, 716 (2019).

[35] T. Steinpilz, K. Joeris, F. Jungmann, D. Wolf, L. Brendel, J. Teiser, T. Shinbrot, and G. Wurm, Electrical charging overcomes the bouncing barrier in planet formation, Nat. Phys. **16**, 225 (2020).

[36] N. A. Pohlman, B. L. Severson, J. M. Ottino, and R. M. Lueptow, Surface roughness effects in granular matter: Influence on angle of repose and the absence of segregation, Phys. Rev. E **73**, 031304 (2006).

[37] B.-B. Dai, J. Yang, and C.-Y. Zhou, Micromechanical origin of angle of repose in granular materials, Granular Matter **19**, 24 (2017).

[38] C. P. Ortiz, R. Riehn, and K. E. Daniels, Flow-driven formation of solid-like microsphere heaps, Soft Matter **9**, 543 (2013).

[39] J. Ellowitz, H. Turlier, N. Guttenberg, W. W. Zhang, and S. R. Nagel, Still Water: Dead Zones and Collimated Ejecta from the Impact of Granular Jets, Phys. Rev. Lett. **111**, 168001 (2013).

[40] D. C. Shorts and K. Feitosa, Experimental measurement of the angle of repose of a pile of soft frictionless grains, Granular Matter **20**, 2 (2018).

[41] R. Lespiat, S. Cohen-Addad, and R. Höhler, Jamming and Flow of Random-Close-Packed Spherical Bubbles: An Analogy with Granular Materials, Phys. Rev. Lett. **106**, 148302 (2011).

[42] T. Hatano, Power-law friction in closely packed granular materials, Phys. Rev. E **75**, 060301(R) (2007).

[43] P.-E. Peyneau and J.-N. Roux, Frictionless bead packs have macroscopic friction, but no dilatancy, Phys. Rev. E **78**, 011307 (2008).

[44] P.-G. De Gennes, F. Brochard-Wyart, and D. Quéré, *Capillarity and Wetting Phenomena: Drops, Bubbles, Pearls, Waves* (Springer Science & Business Media, New York, 2013).

[45] S. Barkley, E. R. Weeks, and K. Dalnoki-Veress, Snap-off production of monodisperse droplets, Eur. Phys. J. E **38**, 138 (2015).

[46] J.-C. Ono-dit-Biot, P. Soulard, S. Barkley, E. R. Weeks, T. Salez, E. Raphael, and K. Dalnoki-Veress, Rearrangement of two dimensional aggregates of droplets under compression: Signatures of the energy landscape from crystal to glass, Phys. Rev. Research **2**, 023070 (2020).

[47] Holes smaller than the projected area of a single droplet are included in the covered area, an overestimate which introduces a small uncertainty, especially as holes are typically observed for large aggregates made of ~100 droplets.

[48] B. L. Bales, L. Messina, A. Vidal, M. Peric, and O. R. Nascimento, Precision relative aggregation number determinations of sds micelles using a spin probe. a model of micelle surface hydration, J. Phys. Chem. B **102**, 10347 (1998).

[49] At early times, near the crossover from 3D to 2D growth, the edge effects cannot be ignored. The edge effects become insignificant as the aggregate grows and the relationship between A/A^* and N/N^* is linear.

[50] A. Vrij, Polymers at interfaces and the interactions in colloidal dispersions, Pure Appl. Chem. **48**, 471 (1976).

[51] M. Backholm and O. Bäumchen, Micropipette force sensors for *in vivo* force measurements on single cells and multicellular microorganisms, Nat. Protoc. **14**, 594 (2019).

[52] See Supplemental Material at http://link.aps.org/supplemental/10.1103/PhysRevLett.125.228001 for a movie that illustrates the experimental procedure for measuring the strength of adhesion between two droplets.

[53] F. Brochard-Wyart and P.-G. de Gennes, Unbinding of adhesive vesicles, C.R. Phys. **4**, 281 (2003).

[54] J. R. Royer, D. J. Evans, L. Oyarte, Q. Guo, E. Kapit, M. E. Möbius, S. R. Waitukaitis, and H. M. Jaeger, High-speed tracking of rupture and clustering in freely falling granular streams, Nature (London) **459**, 1110 (2009).

[55] A. Wysocki, C. P. Royall, R. G. Winkler, G. Gompper, H. Tanaka, A. van Blaaderen, and H. Löwen, Direct observation of hydrodynamic instabilities in a driven non-uniform colloidal dispersion, Soft Matter **5**, 1340 (2009).

[56] D. G. Aarts, M. Schmidt, and H. N. Lekkerkerker, Direct visual observation of thermal capillary waves, Science **304**, 847 (2004).

[57] Y. Amarouchene, J.-F. Boudet, and H. Kellay, Capillarylike Fluctuations at the Interface of Falling Granular Jets, Phys. Rev. Lett. **100**, 218001 (2008).

[58] L.-H. Luu, G. Castillo, N. Mujica, and R. Soto, Capillary-like fluctuations of a solid-liquid interface in a noncohesive granular system, Phys. Rev. E **87**, 040202(R) (2013).

[59] J. P. Sethna, K. A. Dahmen, and C. R. Myers, Crackling noise, Nature (London) **410**, 242 (2001).

[60] J. T. Uhl, S. Pathak, D. Schorlemmer, X. Liu, R. Swindeman, B. A. Brinkman, M. LeBlanc, G. Tsekenis, N. Friedman, R. Behringer *et al.*, Universal quake statistics: From compressed nanocrystals to earthquakes, Sci. Rep. **5**, 16493 (2015).

[61] R. Benzi, P. Kumar, F. Toschi, and J. Trampert, Earthquake statistics and plastic events in soft-glassy materials, Geophys. J. Int. **207**, 1667 (2016).

[62] P. Kumar, E. Korkolis, R. Benzi, D. Denisov, A. Niemeijer, P. Schall, F. Toschi, and J. Trampert, On interevent time distributions of avalanche dynamics, Sci. Rep. **10**, 626 (2020).

Chapter 4

Conclusions

The research presented in this thesis shows how aggregates of adhesive droplets can be used as model systems to study fundamental questions. Our ability to produce highly monodisperse oil droplets of a controlled size enabled us to assemble ideal model aggregates with arbitrary geometry and various amounts of disorder. Using the deflection of a glass micropipette, we are able to measure the force applied on the aggregates as they are compressed with a resolution of $\sim$ 100 pN. Being able to precisely measure small forces, we were able to measure the interaction at play between oil droplets as a function of their size and the concentration of surfactant in the solution.

In Paper I, we take advantage of the high degree of monodispersity of the oil droplets, produced via the snap-off instability, and the small size aggregates to build ordered, defect-free crystals. The compression force is used to define the purely crystalline mechanical response of the aggregates. A crystal deforms elastically until the force reaches a critical value at which the aggregate fails in a single coordinated event. All bonds between droplets break simultaneously to allow the crystal to rearrange into a new geometry with one less row of droplets. The elastic properties of the aggregates are well captured by an assembly of springs, each representing a droplet. Finally, by balancing the elastic energy stored in the equivalent spring with the total adhesion energy released by breaking bonds between droplets, the yield force, at which the crystal breaks, can be accurately predicted. This study provides a mechanical signature of the crystalline behaviour and was the starting point for the study of the crystal-to-glass transition.

In Paper II, the amount of disorder is progressively increased in the aggregates, keeping other parameters, such as adhesion and geometry constant. Defects are introduced by substituting large droplets by smaller ones and *vice versa*. As aggregates are built droplet-by-droplet, the location and number of defects is precisely controlled. Aggregates are then compressed and the force measured. Adding defects results in a rapid increase in the number of peaks in the force measurement as well as a decrease in the magnitude of the force peaks. By measuring the work required to break the aggregates, we find that a large energy barrier must be overcome to break a crystal while glasses fracture in several steps with smaller energy barriers. The work analysis provides a picture of the substructure introduced in the energy landscape as the aggregate transitions from a crystal to a glass. The increase in the number of peaks is surprisingly well described by a simple analytical formula. The energy dissipated during compression can also be predicted by a minimal analytical model. The main conclusion of this study is that even a small amount of disorder has a significant impact on the mechanical properties of the aggregates.

In Paper III, we study the spreading of aggregates of adhesive oil droplets on an interface. Droplets are added one-by-one and the area covered by the droplets on the glass slide is monitored. Despite the aggregates being made of discrete particles, it was found that after an initial 3D growth, the height of the aggregates saturates and the growth only occurs in 2D, along the interface. This type of growth is analogous to the growth of a puddle of liquid which height is set by the capillary length. By analogy, we define the granular capillary length, a balance between buoyancy and the adhesion between droplets, which fully captures the geometry of the aggregates.

In these works, there were two overarching goals: 1) to understand how a system transition form a crystal to a glass using the mechanical properties of aggregates with various amounts of defects; and 2) study the connection and analogies between simple liquids and granular systems. We have shown that aggregates of oil droplets in water are ideal model systems to study these fundamental questions.

During the course of my studies, I have explored several experiments which ranges from those where preliminary experiments were carried out, to those that I am confident would lead to interesting results but have not had the time to pursue. Below is a list of those experiments:

- A natural follow-up project to Paper I and II would be to pull the aggregates apart and see how and where they rupture. I have tried this experiment. The main technical challenge is to ensure good adhesion between the droplets and the glass pipette. In the preliminary experiments I conducted, the contact with the glass pipette and the droplets was always broken before any inter-droplet bonds would break.
- Another idea would be to shear the droplet aggregates instead of compressing them. Suspensions are often studied under shear and it would be particularly interesting to study the behaviour of these model aggregates, as a function of disorder for example, under this type of external constrain. Again the main challenge is to ensure a good adhesion between the droplets and the pipettes. Another way to conduct the shearing experiment would be to create a small hook at the very tip of the pipette which would allow to drag the first one or two layers of droplets. Once again, this is experimentally challenging as all bends would need to remain in-plane to prevent the pipettes from touching the top glass slide. The micro-forging of the accordion pipette is already a challenge and while adding an extra bend is doable, it would not be an easy task.
- One could also imagine using the microscopy pictures to conduct a more detailed analysis of the spacial rearrangement of droplets. For example, in aggregates with a single defect, the position of the defect could be followed and see how peaks in the force measurement correlate with the rearrangement around the defect. Droplets can easily be tracked individually and preliminary results have shown that the trajectories of droplets in a glass and a crystal are vastly different.
- In collaboration with a summer student, Tanel Lorand, we started to investigate the hexagonal packing of monodisperse oil droplets on a curved surface. Small droplets of oil are produced on the surface of a large oil droplet, called the bearing droplet, which is held in place using a glass pipette. Small droplets adhere to one another and to the large droplet due to depletion interactions. These small droplets accumulate on the top hemisphere of the bearing droplet

due to buoyancy (see Fig. 4.1). The volume of the large oil droplet can be decreased by sucking oil into the glass micropipette. As the volume of the large droplet decreases, the curvature of the surface increases. The small droplets, hexagonally packed, must accommodate for this increase in curvature as they are confined to the surface. We conducted preliminary experiments where seven droplets, six droplets surrounding a central droplet, were confined to the surface of a larger oil droplet. We found that a bond between the center droplet and one of the surrounding droplets must break to accommodate for the increase in curvature [Fig. 4.1 (b)]. The position of each droplet can be tracked over time as shown in Fig. 4.1.

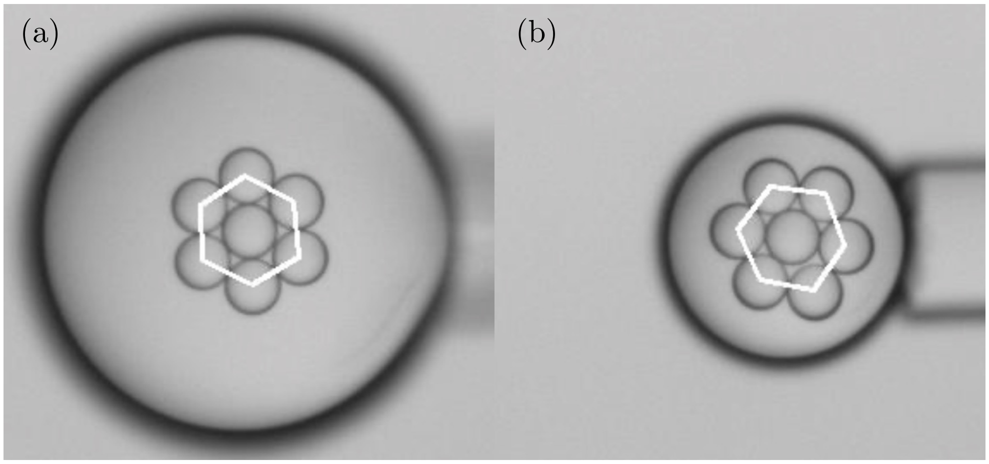

Figure 4.1: (a) Seven small oil droplets adhered to a large oil droplet, called bearing droplet, held in place by a glass micropipette. The droplets are monodisperse and pack hexagonally. The position of the six surrounding droplets can be tracked over time and the white lines connect the centers of these droplets. (b) The curvature of the confining surface is increased by decreasing the volume of the bearing droplet. As the curvature increases the small droplets must rearrange and a bond between the droplet in the center and one of the surrounding is broken.

The preliminary results from this experiment warrant a more detailed investigation. In this version of the experiment, it can be challenging to hold such a large oil droplet in place in the chamber with the micropipette. Perhaps an easier experiment would be to produce oil droplets in a spherical cap of water on a substrat. The volume of the spherical cap can be varied by removing liquid with a pipette or due to evaporation. The later would be the easiest method but the concentration in SDS would vary and thus the strength of interaction between droplets would increase over time.

- A follow-up to the work presented in Paper III would be to confine the growing aggregate within well defined boundaries of various thicknesses and geometries. While this experiment is conceptually easy, I faced several challenges in the preliminary experiments I conducted. The confining boundaries must be relatively small (of the order of 10-100 droplet radii) and have well defined edges. I used optical pinholes with diameter $\sim 400\ \mu$m. The main difficulty was to adhere the pinhole to the top glass slide to prevent the droplets from escaping while not affecting the edges with overflowing glue for example. From the preliminary videos I was able to record, the most interesting stage of the experiment is when the pinhole is filled with several layers of droplets and droplets must rearrange due to the confinement and move cooperatively.

- The work presented in Paper III has strong implications. If aggregates of adhesive oil droplets can be described as a continuous medium, experiments typically conducted with liquids can be reproduced with these emulsions. I am currently studying a granular equivalent to the pendant drop experiment. Instead of pushing a liquid out of a pipette, I am pushing a suspension of oil droplets in a liquid bath. The droplets are pulled out of the pipette due to buoyancy but held together by the depletion forces. Preliminary results show that aggregates of droplets regularly come out of the pipette. The next steps in this study are to measure the characteristic size of the aggregates as a function of the adhesion strength and the size of the droplets (strength of buoyancy).

- Another idea would consist of trying to replicate liquid instabilities, such as the Rayleigh-Taylor instability, using a suspension of droplets.

- Finally, fingering instabilities have been observed when injecting a low viscosity fluid into a highly viscous fluid. It would be interesting to inject the emulsion of oil into another liquid to see if the same instability occurs.

Chapter 5

Appendix A

Paper AI

Hydroelastic wake on a thin elastic sheet floating on water

J.-C. Ono-dit-Biot, M. Trejo, E. Loukiantcheko, M Lauch, E. Raphaël, K. Dalnoki-Veress and T. Salez, Phys. Rev. Fluids, **4**, 014808 (2019).

In this article, we study hydroelastic waves that form on a thin elastic sheet floating on water as it moves past a stationary perturbation. We measure the wavelength of the waves, using a high-resolution 2D cross-correlation technique, as a function of the speed of the perturbation for sheets with various thicknesses. From the measurement of the wavelength, we are able to measure experimentally the dispersion relation of hydroelastic waves. The theoretical dispersion relation predicts that three contributions are relevant to the propagation of the waves: gravity, tension and bending. While the gravity term remains the same for the different sheets, the bending modulus changes with the thickness of the sheet and varies over two orders of magnitude in the experiment. The tension in the sheet is set by the surface tension of water. Both the bending modulus for each sheet thickness and the surface tension of water are measured independently. Using these measured values, we are able to calculate the theoretical dispersion relation for the different elastic sheets. We find excellent agreement between the experimental and the theoretical dispersion relations of hydroelastic waves with no adjustable parameters. All three contributions are important to describe the propagation of such waves. However, we find that for thin elastic sheets (under 100 μm), tension plays a significant role in the propagation of the waves while bending becomes the dominant term for thicker sheets (over 100 μm).

The original idea for this experiment was suggested by Thomas Salez. Kari Dalnoki-Veress designed the first version of the experimental setup. With help from Max Launch, an undergraduate student, I improved the experimental setup to use the 2D image cross-correlation technique called the schlieren method to image the waves. Max Launch and myself conducted preliminary measurements and determined the best parameters to use in the open source software that was used to analyze the raw data. I wrote additional scripts to further analyze the data. Elsie Loukiantcheko, an undergraduate student under the supervision of Kari Dalnoki-Veress and myself, collected and analyzed the wavelength data. Miguel Trejo, Elie Raphaël and Thomas Salez developed the theoretical model for the dispersion relation of hydroelastic waves. I prepared the first draft of the manuscript which was revised by all contributors.

PHYSICAL REVIEW FLUIDS **4**, 014808 (2019)

Hydroelastic wake on a thin elastic sheet floating on water

Jean-Christophe Ono-dit-Biot,[1] Miguel Trejo,[2] Elsie Loukiantcheko,[1] Max Lauch,[1] Elie Raphaël,[2]
Kari Dalnoki-Veress,[1,2] and Thomas Salez[3,4,*]

[1] *Department of Physics and Astronomy, McMaster University, 1280 Main Street West,*
Hamilton, Ontario, Canada L8S 4M1

[2] *UMR CNRS Gulliver 7083, ESPCI Paris, PSL Research University, 75005 Paris, France*

[3] *Univ. Bordeaux, CNRS, LOMA, UMR 5798, F-33405 Talence, France*

[4] *Global Station for Soft Matter, Global Institution for Collaborative Research and Education,*
Hokkaido University, Sapporo, Hokkaido 060-0808, Japan

(Received 19 June 2018; published 24 January 2019)

We investigate the hydroelastic waves created by a perturbation moving at constant speed along a thin elastic sheet floating at the surface of deep water. Using a high-resolution cross-correlation imaging technique, we characterize the waves as a function of the perturbation speed, for different sheet thicknesses. The general theoretical expression for the dispersion relation of hydroelastic waves includes three components: gravity, bending, and tension. The bending modulus and the tension in the sheet are independently measured. The experiments represent a direct test of the theory where all components, bending, stretching, and gravity, cannot be neglected. Excellent agreement is found between the experimental data and the theoretical expression.

DOI: 10.1103/PhysRevFluids.4.014808

I. INTRODUCTION

Feynman described water waves as "the worst possible example [of waves], because they are in no respect like sound and light; they have all the complications that waves can have" [1]. Several decades later, some questions remain unanswered and the study of water waves continues to be an area of great interest. For example, Kelvin's gravity wake behind a ship [2] still stimulates fundamental questions [3,4]. Surface tension of the liquid-air interface also influences the wave propagation, resulting in gravitocapillary waves [5–8]. Unlike the gravity wake, the capillary waves appear ahead of the perturbation [6]. This is particularly relevant for the locomotion of insects [9–13], as well as for nanorheological applications involving, e.g., atomic-force microscopy probes moving along thin viscous samples [14–16].

Other waves of interest are the ones that propagate on elastic plates and membranes. Their properties are dictated by both the bending and stretching rigidities of the material [17]. Floating such an elastic sheet on a liquid further leads to the coupling of the elastic waves to hydrodynamics. The resulting hydroelastic waves are of particular interest, as elastic sheets surrounded by fluids are ubiquitous in nature. Examples can be found in fluid mechanics [18,19], geophysics [20–23], and biophysics [24]. Hydroelastic waves are also relevant to practical applications in civil engineering [25,26], as well as in energy harvesting through piezoelectric flags [27] and control of energy radiation by trucks moving on ice sheets [28]. Interestingly, the propagation of such waves can be finely controlled in an optical-like fashion by using model thin sheets with heterogeneous elastic properties [29]. Different properties of these waves, such as the wave resistance or nonlinear effects,

---

[*] thomas.salez@u-bordeaux.fr

have been further studied theoretically [30,31], including the overdamped limit of lubrication settings where viscosity dominates over fluid inertia [32–38]. The dispersion relation in the inertial case was analytically derived and found to depend on three components: gravity, bending, and stretching [39]. A few experimental studies developed in different contexts have studied the limiting cases where only bending and stretching [40,41], or gravity and bending [20,21], contribute.

In this article we study the hydroelastic waves created by a perturbation moving at constant speed relative to an elastic sheet floating on deep water. The waves are imaged using a high-resolution optical method. By using elastic sheets with different thicknesses, the bending modulus of the sheet is varied over more than two orders of magnitude. We find excellent agreement between experimental data and the general theoretical dispersion relation, accounting for the three different contributions: gravity, bending, and tension.

II. EXPERIMENTAL METHODS

A transparent annular tank (outer radius $R_{\mathrm{out}} = 50\,\mathrm{cm}$, inner radius $R_{\mathrm{in}} = 30\,\mathrm{cm}$) is filled with water to a depth of about 16 cm, as shown in Fig. 1. Thin elastic sheets of Elastosil® Film 2030 (Wacker Chemie AG) with nominal thicknesses h of 50, 100, 200, 250, and 350 μm and lateral dimensions of $20\times16\,\mathrm{cm}^2$ are floated onto the surface of water. Thin rigid plastic supports ($18\times1\times0.1\,\mathrm{cm}^3$) are placed atop the radial edges of the elastic sheet (shown in black in Fig. 1) to ensure that the sheets do not crumple.

We experimentally verify that adding the supports does not introduce an anisotropic tension in the sheet, by ensuring that the deformation induced by ball bearings placed atop the sheet is axially symmetric (see Appendix C). The tank is rotated at constant angular speed Ω, ranging from 0 to $2.5\,\mathrm{rad\,s^{-1}}$, causing the water to flow and the sheet to move. We take advantage of the opaque plastic supports to measure the angular speed of the sheet, using an infrared beam-breaking technique. Because of inertia, both the sheet and water do not follow the tank's speed instantaneously. Hence, all experiments are performed only once the speed of the sheet is constant and equal to the speed of the tank.

A glass capillary (World Precision Instruments, USA) is pulled to a diameter of about 100 μm at one end with a pipette puller (Narishige, Japan) and used to blow air normal to the surface of

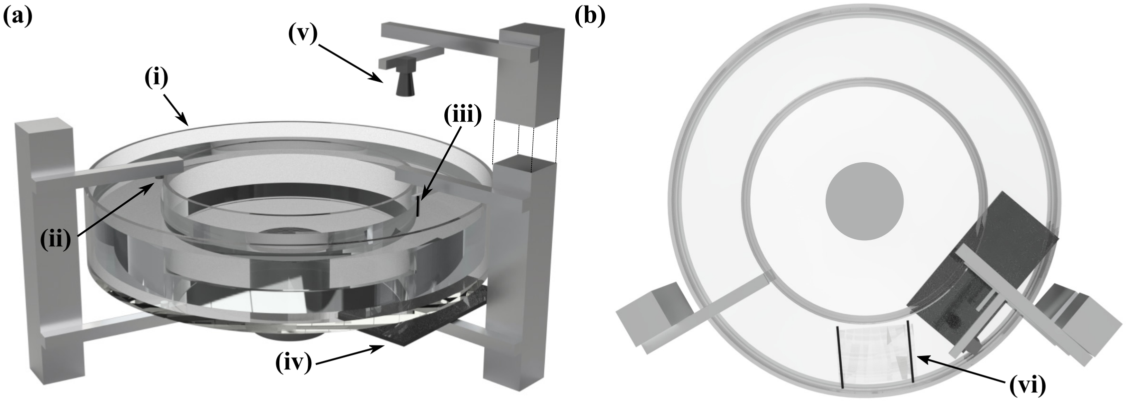

FIG. 1. (a) Three-dimensional schematics of the experimental setup. (i) Rotating transparent annular tank (outer radius $R_{\mathrm{out}} = 50\,\mathrm{cm}$, inner radius $R_{\mathrm{in}} = 30\,\mathrm{cm}$) filled with water to a depth of about 16 cm and with an elastic sheet floating atop. (ii) Infrared beam-breaking setup to measure the angular speed Ω of the elastic sheet. (iii) A pipette perturbs the surface by blowing air normal to the surface, causing waves to form. (iv) Light sheet and dot pattern used to characterize the waves using the schlieren method [42]. (v) A camera is placed $\sim$2 m above the tank to image the dot pattern. (b) Top-view schematics of the experimental setup. The elastic sheet (vi) only covers a small portion of the water surface. Plastic beams are placed along the radial edges of the elastic sheet as shown in black.

the sheet [Fig. 1(a iii)]. The pipette is placed in the middle of the tank, i.e., at a radius $R_\mathrm{p} = 40\,\mathrm{cm}$ from the center. The air jet acts as a perturbation moving at speed $v = \Omega R_\mathrm{p}$ in the reference frame of the elastic sheet, which generates hydroelastic waves. The latter is imaged using a synthetic schlieren method [42] involving a random dot pattern refracted by the surface topography. The dot pattern is generated using MATLAB [42,43] and printed onto a transparency film. Light shines through the dot pattern [Fig. 1(a iv)] and the waves, before being collected by a camera above the tank [Fig. 1(a v)]. The schlieren method consists in measuring the apparent displacement of the dots due to light refraction by the waves. The displacement is measured relative to a reference image of the unperturbed surface (i.e., no air jet) moving at angular speed Ω, which ensures that the collected information is only due to the waves. This measurement is performed using an open-source digital two-dimensional (2D) image-correlation algorithm (Ncorr, MATLAB) [44]. From the displacement of the dots, one can access the slope of the surface and thus the surface topography [42].

III. RESULTS AND DISCUSSION

A. Measurement of the wavelength

Figures 2(a) and 2(b) show a typical vectorial displacement field. The air jet creates a localized perturbation in the sheet, as evidenced by the large magnitude of the displacement field therein.

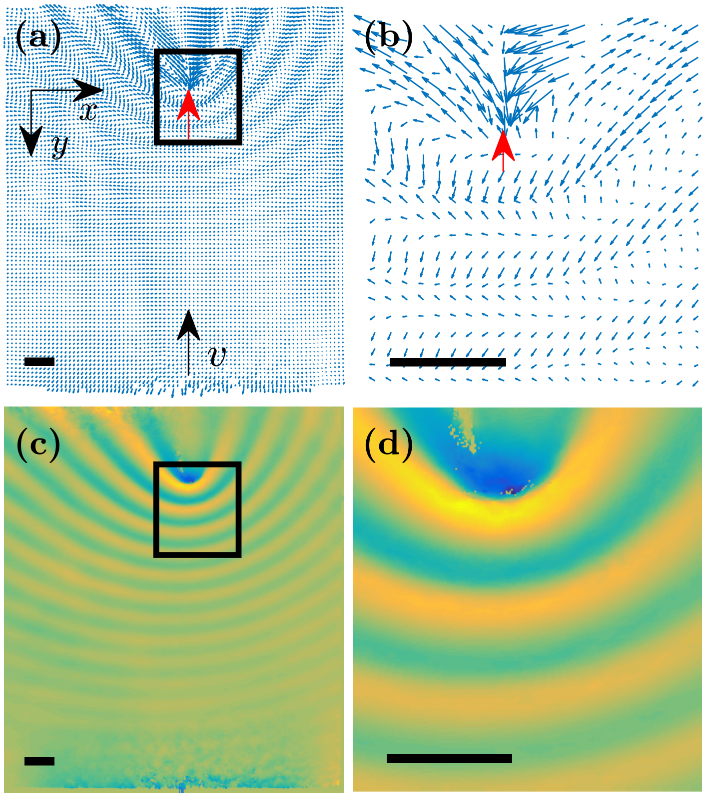

FIG. 2. (a) Raw 2D dot-displacement data measured with Ncorr [44], for an elastic sheet of nominal thickness $h \approx 200\,\mu\mathrm{m}$ moved at speed $v = 0.9\,\mathrm{m\,s^{-1}}$. The displacement vectors are only shown every ten pixels for clarity. The bottom arrow indicates the speed of the sheet with respect to the stationary air jet whose position is indicated by the red arrow. (b) Close-up around the perturbation, corresponding to the black square in (a). (c) The y component d of the displacement field. Warm colors (green to orange) correspond to positive displacements, while cold colors (green to blue) correspond to negative ones. (d) Close-up around the perturbation, corresponding to the black square in (c). All scale bars correspond to 1 cm.

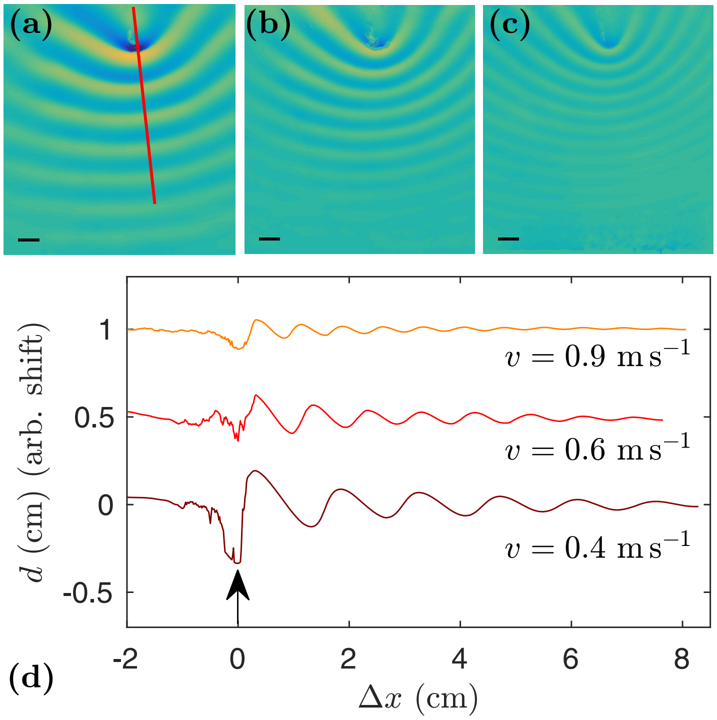

FIG. 3. The y component d of the displacement field (see Fig. 2), for speeds (a) $v = 0.4$, (b) $v = 0.6$, and (c) $v = 0.9\,\mathrm{m\,s^{-1}}$, on an elastic sheet of nominal thickness $h \approx 200\ \mu\mathrm{m}$. All scale bars correspond to 1 cm. (d) The y component d of the displacement field normal to the wave front [see the red line in (a)], as a function of the distance Δx from the perturbation, for the three speeds as indicated (shifted vertically for clarity). The position of the air-jet perturbation is indicated by the black arrow.

Ahead of the perturbation, in the reference frame of the elastic sheet, the upstream wave pattern of the hydroelastic wave appears clearly, with a dominant, centimetric, wavelength λ. Note that the displacement data plotted in Fig. 2 are directly related to the slope of the interface through the Snell-Descartes law and that the amplitude of the waves is at least an order of magnitude smaller than the wavelength. As the hydroelastic waves propagate along the y direction, the projection of the displacement along that direction provides the strongest signal for analysis. Figures 2(c) and 2(d) thus focus only on the y component d of the displacement field.

To characterize experimentally the dispersion relation of the hydroelastic wave, the wavelength λ is measured as a function of the speed v. Figures 3(a)–3(c) show the y component d of the displacement field, for various speeds. The wave is slightly tilted and not symmetric about the y axis, because of the centrifugal force and the surface of water assuming a parabolic profile when rotated. This distortion is avoided in the wavelength measurement by analyzing the displacement field normal to the wave front, as shown in Figs. 3(a) and 3(d). We observe both the wavelength and the displacement magnitude to decrease as the speed increases. The general shape of the wave is consistent with a sinusoid with an exponential decay envelope (see Appendix B). However, near the source of the perturbation, where the amplitude of the wave is the largest, the shape deviates from this description. The deviation may be ascribed to a loss of resolution for steep slopes and nonuniform strains in the elastic sheet near the source.

B. Theoretical dispersion relation

In order to quantify further and rationalize these observations, we now introduce the relevant theoretical framework which follows that of Schulkes *et al.* [39]. The mechanical system we consider is the thin elastic sheet in its reference frame. The out-of-plane displacement field $z = \zeta(\boldsymbol{r}, t)$ with respect to its flat horizontal state $z = 0$ satisfies a simplified version of the Föppl–von Kármán equation [17]

$$B\nabla_{\boldsymbol{r}}^4\zeta - \sigma\nabla_{\boldsymbol{r}}^2\zeta + \rho_{\mathrm{e}}h\partial_{tt}\zeta = P + P_{\mathrm{ext}}, \tag{1}$$

along the 2D horizontal space coordinate $\boldsymbol{r} = (x, y)$ and for time t, where $\boldsymbol{\nabla}_{\boldsymbol{r}}$ is the nabla operator in two dimensions, ∂_{tt} is the second partial derivative with respect to time, B is the bending stiffness of the sheet, σ represents the tension in the sheet, and ρ_{e} is the sheet's density. The first and second terms respectively account for bending and tension of the sheet, while the third term accounts for the solid inertia. The elastic sheet is further subjected to two external forces: the excess hydrodynamic pressure $P(\boldsymbol{r}, t)$ (with respect to the atmospheric one) exerted on the sheet by the water flow under gravity and the driving pressure $P_{\mathrm{ext}}(x, y - vt)$ modeling the perturbation by the air jet translating at constant speed v along y. Note that we treat the motion as rectilinear and that in particular we neglect the inertial effects due to rotation in view of the large radius of the tank and the moderate speed.

The water contribution $P(\boldsymbol{r}, t)$ is calculated by assuming an incompressible and irrotational flow of an inviscid fluid, in a semi-infinite half space located at $z < \zeta(\boldsymbol{r}, t)$. In this context, the fluid velocity field can be written as $\boldsymbol{\nabla}\varphi$, where $\varphi(\boldsymbol{r}, z, t)$ is a potential that vanishes in the far field and that satisfies Laplace's equation [45] $\nabla^2\varphi = (\nabla_{\boldsymbol{r}}^2 + \partial_z^2)\varphi = 0$. At lowest order in the flow (i.e., for small-amplitude hydroelastic waves), the linearized Bernoulli equation for unsteady potential flows provides the excess hydrodynamic pressure exerted on the sheet, $P = -\rho\partial\varphi/\partial t|_{z=0} - \rho g\zeta$, with ρ the liquid density and g the acceleration due to gravity.

To obtain the dispersion relation, one substitutes the expression for P into Eq. (1) in the absence of driving ($P_{\mathrm{ext}} = 0$) and invokes the kinematic condition $\partial\varphi/\partial z|_{z=0} = \partial\zeta/\partial t$ at the water-sheet interface. Finally, the solid inertia can be neglected for films that are thin enough in comparison to the wavelength of the wave [39]. Considering a plane wave $\varphi \propto \exp[i(ky - \omega t - ikz)]$ satisfying Laplace's equation, with angular wave number k and angular frequency $\omega(k)$, yields [39]

$$\omega = \sqrt{\frac{Bk^5}{\rho} + \frac{\sigma k^3}{\rho} + gk}. \tag{2}$$

We now consider the waves created by the driving perturbation P_{ext} traveling at constant speed v along y. In the comoving frame of the perturbation, the angular frequency ω' of a plane-wave component of the waves is shifted by the Doppler effect and thus reads $\omega' = \omega - kv$. Furthermore, since in that comoving frame the wave is stationary, $\omega' = 0$ is a necessary condition. Using Eq. (2), one thus obtains the central relation connecting the angular wave number k and the perturbation speed v, for a hydroelastic wave on deep water:

$$v = \sqrt{\frac{Bk^3}{\rho} + \frac{\sigma k}{\rho} + \frac{g}{k}}. \tag{3}$$

An extensive analysis of this relation, similar to the one performed for the gravitocapillary case [7], reveals the main features of the present waves (see also Fig. 4). First, below a certain minimal speed v^* (see Appendix D) wave propagation is impossible. Second, at a given speed $v > v^*$ there are two possible values for the observed wavelength. (i) The smallest value corresponds to a group velocity that is higher than the perturbation speed v and therefore the waves propagate upstream of the perturbation. This is the situation studied in the present work (see Figs. 2 and 3), which is dominated by bending and tension at sufficiently large speed. (ii) The largest value corresponds to a group velocity that is lower than the perturbation speed v and therefore the waves propagate downstream of the perturbation. This situation corresponds to Kelvin's classical wake [2], which is dominated by gravity at sufficiently large speed.

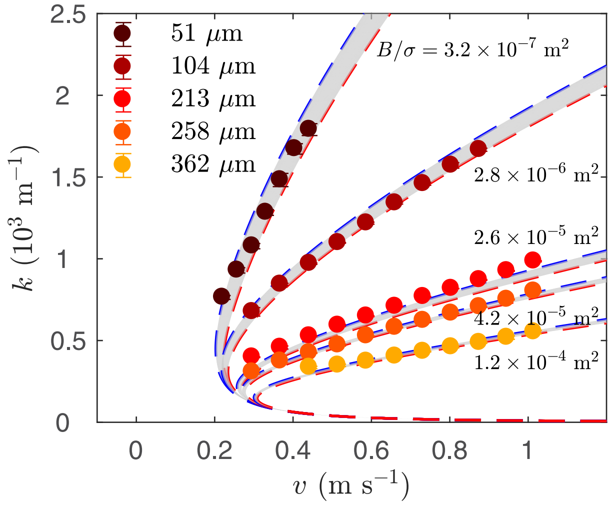

FIG. 4. Angular wave number $k = 2\pi/\lambda$ as a function of perturbation speed v, for five different sheet thicknesses h as indicated in the legend. Each data point was obtained using the procedure detailed in Fig. 3 and an average over four different experimental displacement profiles. The error bars correspond to the standard deviation, which is comparable to the marker size. For each thickness h, the blue and red dashed lines separated by a gray region indicate the upper and lower theoretical predictions obtained from Eq. (3), using the independently measured values of B and σ (see the main text) and their uncertainties. The relative importance of bending to stretching is quantified with the ratio B/σ and is displayed next to the corresponding curve. As the elastic sheet gets thicker (top to bottom curves), bending becomes more significant.

C. Experimental verification of the dispersion relation

The values of the bending modulus B and the tension σ are measured independently. The bending modulus $B = Eh^3/[12(1-\nu^2)]$ depends on three parameters: (i) Young's modulus $E = 1.11 \pm 0.06$ MPa of Elastosil® Film 2030, measured using the stress-strain curve; (ii) the sheet thickness h, depending on the sample and measured through optical microscopy; and (iii) Poisson's ratio $\nu = 0.5$, assuming that Elastosil® Film 2030 is an incompressible elastomer. The values of h (μm) and B (N m) for our five different samples are found to be $(h, B) = \{[51 \pm 1, (1.6 \pm 0.1) \times 10^{-8}], [104 \pm 2, (1.4 \pm 0.1) \times 10^{-7}], [213 \pm 7, (1.2 \pm 0.1) \times 10^{-6}], [258 \pm 2, (2.1 \pm 0.1) \times 10^{-6}], [362 \pm 3, (5.9 \pm 0.3) \times 10^{-6}]\}$. We note that the 362-$\mu$m film was obtained by stacking two films with nominal thicknesses of 250 and 100 μm. In addition, as the sheet is freely floating on water, the tension in the sheet is equal to the water-air surface tension: $\sigma = \gamma$. The latter is measured to be $\gamma = 50 \pm 10\,\mathrm{mN\,m^{-1}}$, as in [29], from two different techniques (see Appendix C): (i) using a Wilhelmy-plate setup and (ii) characterizing the dispersion relation of gravitocapillary waves on water. The low value of γ and the large uncertainty are attributed to the fact that the tank is filled with an important volume of tap water and thus subject to contamination by surfactants. We also note that recent works have shown that wrinkles can develop when a freely floating film is indented [46,47]. In such a case, the tension in the film is no longer uniform and in particular is not equal to the water-air surface tension. In contrast, in our work, the typical stress introduced by the perturbation is of order $\sim A^2/\lambda^2 \ll 1$ (as estimated for a triangular indentation of sizes A and λ), with A the amplitude of the wave, and is negligible in comparison to the water-air surface tension.

As shown in Fig. 4 (dashed lines), using the above measured values of B and σ, one can predict the evolution of the angular wave number k as a function of the perturbation speed v. The uncertainties in B and σ are taken into account through two limiting predictions and an interval in between. Note that the uncertainty on σ accounts for most of the spread between the two limiting predictions. Finally, as expected from Eq. (3), all the theoretical curves for different h (and thus B) collapse onto Kelvin's gravity-dominated branch [2], at both large v and small k.

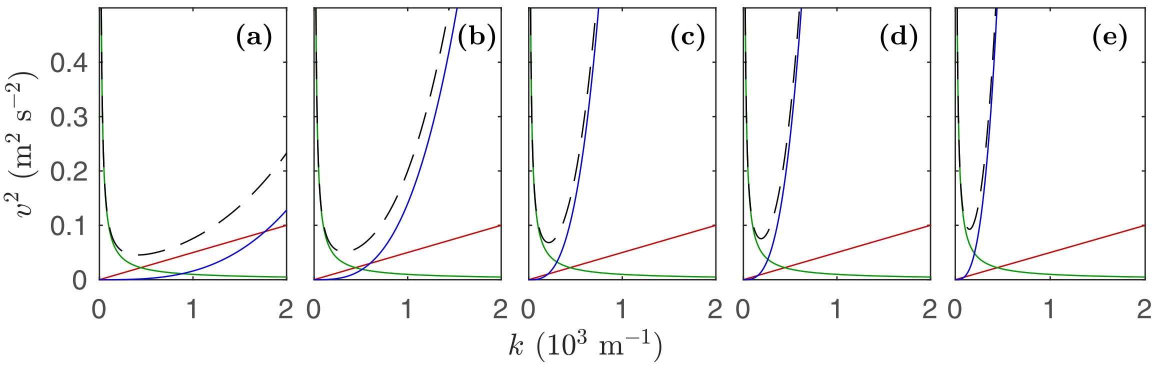

FIG. 5. Contributions of bending, tension, and gravity in Eq. (3), corresponding to different thicknesses (and thus bending moduli B): (a) $h = 50$, (b) $h = 100$, (c) $h = 200$, (d) $h = 250$, and (e) $h = 350\,\mu$m. The blue line corresponds to bending (Bk^3/ρ), the red line to tension ($\sigma k/\rho$), and the green line to gravity (g/k), while the dashed line represents the sum of the three contributions.

The wavelength λ (see Fig. 3), or equivalently the angular wave number $k = 2\pi/\lambda$, is measured by fitting the experimental profile to a sinusoid with a decay envelope as a function of v (see Appendix B for more details) or by measuring the peak-to-peak distance. The results for the five different sheet thicknesses h are shown in Fig. 4 (data points). We find excellent agreement between the experimental data and the theoretical prediction, which includes bending, tension, and gravity, with no adjustable parameter. The relative contributions of the three terms in Eq. (3) are discussed in detail in the next section. The experimental data points for the two thinnest sheets seem to be in slightly better agreement with the upper prediction at low speed and with the lower prediction at high speed. This observation could perhaps be related to a slight, but not quantifiable, increase in the sheet tension due to the increase in curvature of the water-air interface. Another interesting feature of Fig. 4 is that the difference between the upper and lower predictions decreases as the thickness h of the sheet is increased. Indeed, the relative contribution of bending to Eq. (3) increases and the difference between both predictions, which is mainly due to the uncertainty in tension, decreases. Note that Kelvin's classical gravity-dominated branch [2] corresponds to (i) a wake propagating behind the perturbation and (ii) a wavelength that would almost reach the meter range in our experiments, which is not attainable with the current setup.

D. Relative contributions of bending, tension, and gravity

Let us consider Eq. (3) in more detail. The first term under the square root corresponds to the bending of the sheet, the second one to the tension in the sheet, and the third one to gravity. Using all the measured values for B and the value of σ, the respective contributions of those three terms, as well as their sum (dashed lines), are computed from Eq. (3) and plotted in Fig. 5. We experimentally measure angular wave numbers ranging from 400 to 2000 m^{-1} (see Fig. 4). For the thinnest film $h = 50\,\mu$m [Fig. 5(a)], all three terms do contribute in that range. This highlights the counterintuitive role of gravity in the wavelength selection of the upstream hydroelastic waves. The elastic sheet with $h = 100\,\mu$m shows an interesting behavior [Fig. 5(b)]: At low angular wave numbers ($k < 1000\,$m^{-1}), all three terms are also relevant, while bending becomes predominant at larger angular wave numbers. For the three largest thicknesses, $h = 200$, 250, and 350 μm [Figs. 5(c)–5(e), respectively], bending clearly dominates.

IV. CONCLUSION

In this article we have studied the hydroelastic waves formed by moving a thin elastic sheet, floating on water, past a stationary air jet. Specifically, we experimentally measured the wavelength of the wave as a function of the perturbation speed, for sheets with bending moduli varying over two orders of magnitude. For thin elastic sheets (thickness smaller than 100 μm), the tension in the sheet plays a significant role in the propagation of the waves. For thicker elastic sheets (thickness larger than 100 μm), the bending contribution becomes dominant, a regime that is particularly relevant for floating ice [20,21,28]. The results are found to be in excellent agreement with theoretical predictions, based on the elasticity of slender structures coupled to the hydrodynamics of inviscid incompressible flows, with no adjustable parameter. Interestingly, for thin elastic sheets, bending, tension, and gravity all contribute to the hydroelastic waves, a result with practical consequences in geophysics, biophysics, and civil engineering.

ACKNOWLEDGMENTS

Financial support from the Natural Science and Engineering Research Council of Canada and the Joliot Chair of ESPCI Paris is gratefully acknowledged. The authors also thank Andreas Koellnberger and Wacker Chemie AG for technical information and the donation of Elastosil® Film 2030 films, as well as Antonin Eddi, Lucie Domino, Andreas Carlson, and Yacine Amarouchene for stimulating discussions. The excellent collaboration with the McMaster Engineering Machine Shop is also gratefully acknowledged.

APPENDIX A: IMAGE ANALYSIS

As described in the main text, the waves are imaged using the schlieren method [42]. Specifically, the apparent displacement of the dots due to refraction at the interface is measured when hydroelastic waves are propagating on the elastic sheet. The displacement of the dots is measured by comparing the image of the dot pattern when waves are propagating [Figs. 6(b) and 6(f)] to a reference [Figs. 6(a) and 6(e)]. For both images, the elastic sheet is rotating at speed Ω in the tank and the measured displacement is only a result of the waves propagating at the interface. The apparent displacement can be seen more easily when zooming closer to the perturbation [Fig. 6(f)] where the magnitude is larger. Processing these images with the open-source digital 2D image-correlation algorithm (Ncorr, MATLAB) [44], Figs. 6(c) and 6(g) are obtained. Finally, the strongest signal for measuring the wavelength of the waves is obtained by looking at the vertical component of the displacement vectors [Figs. 6(d) and 6(h)].

APPENDIX B: WAVE PROFILE ANALYSIS

As explained in Sec. III A, the displacement profiles normal to the wave front can be extracted and used to measure the wavelength of the hydroelastic waves. The displacement profiles can be empirically described by

$$d = A\exp(-\kappa x)\sin(kx+\phi), \tag{B1}$$

where κ is the inverse of the characteristic length scale of the decay, $k = 2\pi/\lambda$ is the angular wave number, and ϕ is the phase of the wave. The fit is performed one wavelength away from where the perturbation is applied. Indeed, the imaging technique is optimized in order to measure precisely small deformations of the surface. Near the perturbation, the magnitude of the displacement is too large and cannot be measured precisely by the algorithm. Fitting away from the perturbation minimizes experimental artifacts as well as possible nonlinearities near the perturbation. Figure 7 shows excellent agreement between this empirical description of the wave and the experimental data, indicating that the wave is dominated by a single wavelength λ. The wavelength is extracted from the fit and is consistent with a peak-to-peak measurement of the wavelength. In addition, we have performed measurements of the wavelength near and far away from the perturbation using the peak-to-peak method. Both measurements agree well within 5%, the difference being most significative at lower speed ($\lambda \sim 1$ cm). Another parameter of interest is κ, which characterizes the

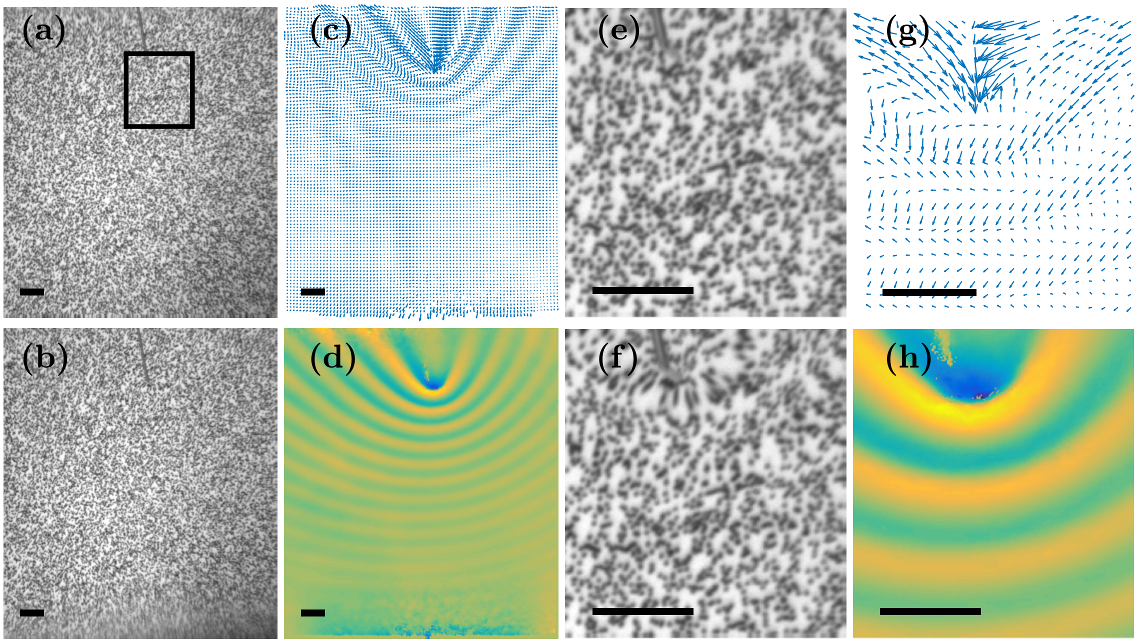

FIG. 6. (a) Raw picture of the dot pattern placed underneath the tank when no perturbation is applied (no wave propagating), called the reference image. The gray line at the top middle of the image, just extending into the black square, is the pipette used to blow air at the surface of the elastic sheet. (b) Raw picture of the dot pattern when a perturbation is applied and hydroelastic waves are propagating [note that shear is hard to discern at this magnification; compare with (e) and (f)]. (c) Two-dimensional dot-displacement data obtained with Ncorr [44] using the images shown in (a) and (b). (d) The y component of the displacement field. Warm colors (green to orange) correspond to positive displacements, while cold colors (green to blue) correspond to negative ones. (e)–(h) Close-up around the perturbation, corresponding to the black square in (a), for (a)–(d), respectively. Notice that the dot pattern [see (e)] is distorted [see (f)] as the waves propagate on the elastic sheet. This is the dot displacement quantified using Ncorr. All scale bars correspond to 1 cm.

exponential decay of the wave amplitude away from the perturbation. The profiles shown in Fig. 7 indicate that κ increases with the speed of the perturbation, i.e., the amplitude of the wave decays faster as v increases. This trend seems to hold for the different sets of experiments conducted during this study. However, a quantitative analysis of the decay constant for the different elastic sheets is beyond the scope of the present work.

APPENDIX C: TENSION IN THE FILM

1. Tension isotropy

A schematic of the elastic sheet is shown in Fig. 8(a). The tensions along the x and y axes are denoted by σ_{xx} and σ_{yy}, respectively. We place ball bearings directly on the sheet floating on water and we image the resulting deformation using the optical schlieren method [42]. We then calculate the magnitude of the displacement vector field, which is directly linked to the deformation of the elastic sheet. Sample isodisplacement lines are shown in Fig. 8(b). We quantify the anisotropy of the deformation by fitting the isodisplacement lines to ellipses. We define the aspect ratio $\epsilon = r_x/r_y$, where r_x and r_y are the radii along the x and y axes, respectively, to quantify how circular the isodisplacement lines are. The best fit to ellipses for the four cases shown in Fig. 8(b) are all found to be $\epsilon = 1 \pm 0.02$, meaning that the isodisplacement lines are, within experimental error, equivalent to circles. Thus the tension in the sheet is isotropic. Indeed, if σ_{xx} or σ_{yy} was larger than the other, the deformation would be elongated along the low-tension direction, leading to an aspect ratio ϵ different from 1.

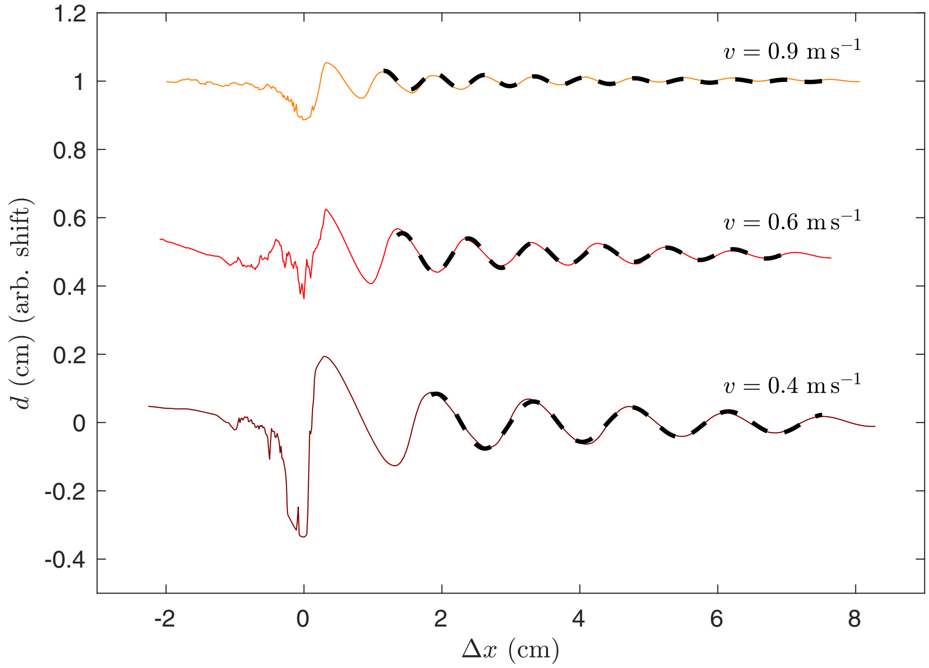

FIG. 7. The y component d of the displacement field normal to the wave front, already shown in Fig. 3(d), for three different speeds $v = 0.4$, 0.6, and 0.9 m s^{-1}. The black dashed lines show the best fit of Eq. (B1) to the experimental profiles.

2. Tension measurement

The tension σ_{xx} along the x axis is set by the water-air surface tension γ, as both the left and right edges are free [see Fig. 8(a)]. Since all the experiments presented in the study are performed on sheets where the tension is isotropic, one can safely assume that $\sigma = \sigma_{yy} = \sigma_{xx} = \gamma$. The tabulated value for the pure water-air surface tension under ambient conditions is $\gamma = 72\,\mathrm{mN\,m^{-1}}$,

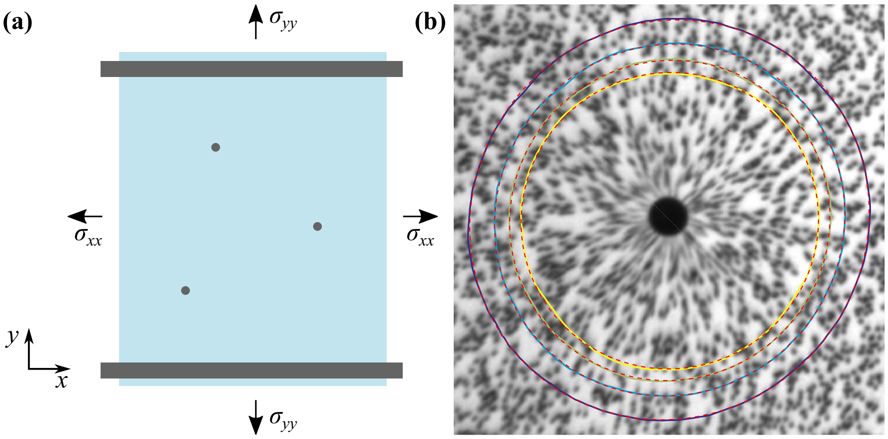

FIG. 8. (a) Top-view schematic of the elastic sheet floating on water. Plastic beams are placed along the radial edges of the elastic sheet as shown in black to ensure that the sheet does not crumple. Ball bearings are dropped atop the sheet to verify that no anisotropy is introduced when placing the beams. (b) Picture of the reference dot pattern, seen through the water and the sheet, around a ball bearing. The solid lines are sample isodisplacement lines. The dashed lines are the best fits of the isodisplacement lines to ellipses. The best-fit ellipticities are found to be equal to 1 for all cases.

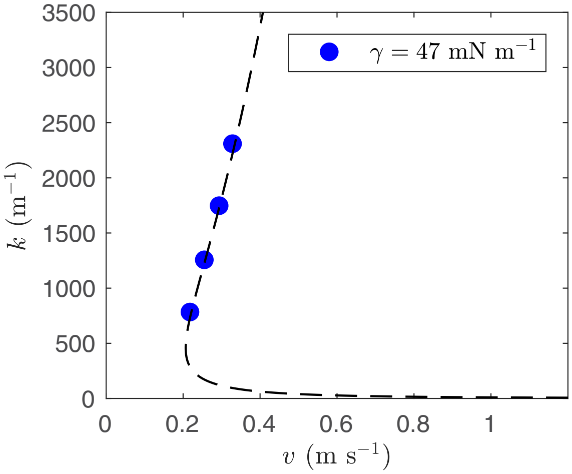

FIG. 9. Angular wave number k as a function of perturbation speed v, for the gravitocapillary waves at the surface of deep water. The dashed line shows the best fit of Eq. (C1) to the experimental data points. The water-air surface tension $\gamma = 47\,\mathrm{mN\,m^{-1}}$ is obtained as the only adjustable parameter.

but it is extremely sensitive to contamination by all kinds of surfactants. Since the experiments are conducted in an open tank containing ∼200 L of water, contamination is unavoidable. Therefore, γ is measured from two independent methods.

First, using a Wilhelmy-plate setup, γ is found to be between 40 and 55 $\mathrm{mN\,m^{-1}}$, for water from three different sources: water from the tank after one day, tap water, and deionized water. The largest value of γ is obtained for deionized water and the smallest one for the water from the tank, which is consistent with tank contamination over time.

Another approach to measure γ is to invoke the gravitocapillary waves formed at the surface of deep water by a perturbation moving at constant speed v. In such a case, the analog of Eq. (3) is [7]

$$v = \sqrt{\frac{\gamma k}{\rho} + \frac{g}{k}}. \tag{C1}$$

Therefore, γ can be evaluated by fitting Eq. (C1) to the experimental evolution of the angular wave number k as a function of speed v for gravitocapillary waves. In fact, as the elastic sheet only covers a small portion of the water in the tank, the hydroelastic waves are only observed once a lap when the sheet moves across the stationary perturbation at speed v. Otherwise, water flowing at speed v is directly exposed to the perturbation and gravitocapillary waves are instead formed at the surface. Using the schlieren method, the wavelength $\lambda = 2\pi/k$ of the upstream gravitocapillary waves is measured as a function of speed v. The measurements of the wavelengths for both the hydroelastic and the gravitocapillary waves are thus performed simultaneously. Figure 9 shows the evolution of the angular wave number k as a function the speed v, for the gravitocapillary waves. By fitting the experimental data to Eq. (C1), we find $\gamma = 47\,\mathrm{mN\,m^{-1}}$.

Note that the last measurement is performed during the characterization of the hydroelastic waves on a sheet of thickness $h = 50\,\mu\mathrm{m}$. Similar measurements are also performed during the characterization of the hydroelastic waves on sheets with larger thicknesses $h = \{100; 200; 250\}\,\mu\mathrm{m}$. However, in those cases, the wavelength for the gravitocapillary waves is measurable only for the lowest speed, $v \approx 0.2\,\mathrm{m\,s^{-1}}$. For all those three measurements, we get $\gamma = 47\,\mathrm{mN\,m^{-1}}$. Considering all the measured values from both methods, we reach the conclusion that $\gamma = 50 \pm 10\,\mathrm{mN\,m^{-1}}$.

APPENDIX D: THEORETICAL EXPRESSION FOR THE MINIMAL VELOCITY AND ANGULAR WAVE NUMBER

As explained in Sec. III B, there exists a minimal velocity v^* below which there is no wave propagation. It is given by

$$v^* = \left(\frac{2}{27}\right)^{1/4} \sqrt{\frac{\sigma\left(\sqrt{12Bg\rho + \sigma^2} - \sigma\right) + 12Bg\rho}{\rho\sqrt{B\left(\sqrt{12Bg\rho + \sigma^2} - \sigma\right)}}}. \tag{D1}$$

This minimal velocity is reached at an angular wave number k^*, given by

$$k^* = \sqrt{\frac{\sqrt{12Bg\rho + \sigma^2} - \sigma}{6B}}. \tag{D2}$$

[1] R. P. Feynman, R. B. Leighton, and M. Sands, *The Feynman Lectures on Physics* (Basic Books, New York, 2011), Vol. I.

[2] W. Thomson, On ship waves, Proc. Inst. Mech. Eng. **38**, 409 (1887).

[3] M. Rabaud and F. Moisy, Ship Wakes: Kelvin or Mach Angle? Phys. Rev. Lett. **110**, 214503 (2013).

[4] A. Darmon, M. Benzaquen, and E. Raphaël, Kelvin wake pattern at large Froude numbers, J. Fluid Mech. **738**, R3 (2014).

[5] L. D. Landau and E. M. Lifshitz, *Fluid Mechanics*, 2nd ed. (Pergamon Press, Oxford, 1987).

[6] D. J. Acheson, *Elementary Fluid Dynamics* (Oxford University Press, Oxford, 1990).

[7] E. Raphaël and P.-G. de Gennes, Capillary gravity waves caused by a moving disturbance: Wave resistance, Phys. Rev. E **53**, 3448 (1996).

[8] F. Dias and C. Kharif, Nonlinear gravity and capillary-gravity waves, Annu. Rev. Fluid Mech. **31**, 301 (1999).

[9] D. L. Hu, B. Chan, and J. W. M. Bush, The hydrodynamics of water strider locomotion, Nature (London) **424**, 663 (2003).

[10] A. D. Chepelianskii, F. Chevy, and E. Raphaël, Capillary-Gravity Waves Generated by a Slow Moving Object, Phys. Rev. Lett. **100**, 074504 (2008).

[11] F. Closa, A. D. Chepelianskii, and E. Raphaël, Capillary-gravity waves generated by a sudden object motion, Phys. Fluids **22**, 052107 (2010).

[12] J. Voise and J. Casas, The management of fluid and wave resistances by whirligig beetles, J. R. Soc. Interface **7**, 343 (2010).

[13] T. Steinmann, M. Arutkin, P. Cochard, E. Raphaël, J. Casas, and M. Benzaquen, Unsteady wave pattern generation by water striders, J. Fluid Mech. **848**, 370 (2018).

[14] K. Wedołowski and M. Napiórkowski, Dynamics of a liquid film of arbitrary thickness perturbed by a nano-object, Soft Matter **11**, 2639 (2015).

[15] R. Ledesma-Alonso, M. Benzaquen, T. Salez, and E. Raphaël, Wake and wave resistance on viscous thin films, J. Fluid Mech. **792**, 829 (2016).

[16] R. Ledesma-Alonso, E. Raphaël, T. Salez, P. Tordjeman, and D. Legendre, van der Waals interaction between a moving nano-cylinder and a liquid thin film, Soft Matter **13**, 3822 (2017).

[17] L. D. Landau and E. M. Lifshitz, *Theory of Elasticity*, 3rd ed. (Elsevier, New York, 1986), Vol. 7.

[18] M. J. Shelley and J. Zhang, Flapping and bending bodies interacting with fluid flows, Annu. Rev. Fluid Mech. **43**, 449 (2011).

[19] E. Virot, X. Amandolese, and P. Hémon, Fluttering flags: An experimental study of fluid forces, J. Fluid Struct. **43**, 385 (2013).

[20] T. Takizawa, Deflection of a floating sea ice sheet induced by a moving load, Cold Reg. Sci. Technol. **11**, 171 (1985).

[21] V. A. Squire, W. H. Robinson, P. J. Langhorne, and T. G. Haskell, Vehicles and aircraft on floating ice, Nature (London) **333**, 159 (1988).

[22] V. A. Squire, J. P. Dugan, P. Wadhams, P. J. Rottier, and A. K. Liu, Of ocean waves and sea ice, Annu. Rev. Fluid Mech. **27**, 115 (1995).

[23] E. Părău and F. Dias, Nonlinear effects in the response of a floating ice plate to a moving load, J. Fluid Mech. **460**, 281 (2002).

[24] J. B. Grotberg and O. E. Jensen, Biofluid mechanics in flexible tubes, Annu. Rev. Fluid Mech. **36**, 121 (2004).

[25] M. Murai, H. Kagemoto, and M. Fujino, On the hydroelastic responses of a very large floating structure in waves, J. Mar. Sci. Technol. **4**, 123 (1999).

[26] E. Watanabe, T. Utsunomiya, and C. M. Wang, Hydroelastic analysis of pontoon-type VLFS: A literature survey, Eng. Struct. **26**, 245 (2004).

[27] D. T. Akcabay and Y. L. Young, Hydroelastic response and energy harvesting potential of flexible piezoelectric beams in viscous flow, Phys. Fluids **24**, 054106 (2012).

[28] J. W. Davys, R. J. Hosking, and A. D. Sneyd, Waves due to a steadily moving source on a floating ice plate, J. Fluid Mech. **158**, 269 (1985).

[29] L. Domino, M. Fermigier, E. Fort, and A. Eddi, Dispersion-free control of hydroelastic waves down to sub-wavelength scale, Europhys. Lett. **121**, 14001 (2018).

[30] F. Milinazzo, M. Shinbrot, and N. W. Evans, A mathematical analysis of the steady response of floating ice to the uniform motion of a rectangular load, J. Fluid Mech. **287**, 173 (1995).

[31] E. I. Părău and J.-M. Vanden-Broeck, Three-dimensional waves beneath an ice sheet due to a steadily moving pressure, Philos. Trans. R. Soc. A **369**, 2973 (2011).

[32] A. E. Hosoi and L. Mahadevan, Peeling, Healing, and Bursting in a Lubricated Elastic Sheet, Phys. Rev. Lett. **93**, 137802 (2004).

[33] H. Vandeparre, S. Gabriele, F. Brau, C. Gay, K. K. Parker, and P. Damman, Hierarchical wrinkling patterns, Soft Matter **6**, 5751 (2010).

[34] J. R. Lister, G. G. Peng, and J. A. Neufeld, Viscous Control of Peeling an Elastic Sheet by Bending and Pulling, Phys. Rev. Lett. **111**, 154501 (2013).

[35] T. T. Al-Housseiny, I. C. Christov, and H. A. Stone, Two-Phase Fluid Displacement and Interfacial Instabilities under Elastic Membranes, Phys. Rev. Lett. **111**, 034502 (2013).

[36] A. Carlson and L. Mahadevan, Similarity and singularity in adhesive elastohydrodynamic touchdown, Phys. Fluids **28**, 011702 (2016).

[37] M. Arutkin, R. Ledesma-Alonso, T. Salez, and E. Raphaël, Elastohydrodynamic wake and wave resistance, J. Fluid Mech. **829**, 538 (2017).

[38] O. Kodio, I. M. Griffiths, and D. Vella, Lubricated wrinkles: Imposed constraints affect the dynamics of wrinkle coarsening, Phys. Rev. Fluids **2**, 014202 (2017).

[39] R. M. S. M. Schulkes, R. J. Hosking, and A. D. Sneyd, Waves due to a steadily moving source on a floating ice plate. Part 2, J. Fluid Mech. **180**, 297 (1987).

[40] L. Deike, J.-C. Bacri, and E. Falcon, Nonlinear waves on the surface of a fluid covered by an elastic sheet, J. Fluid Mech. **733**, 394 (2013).

[41] L. Deike, M. Berhanu, and E. Falcon, Experimental observation of hydroelastic three-wave interactions, Phys. Rev. Fluids **2**, 064803 (2017).

[42] F. Moisy, M. Rabaud, and K. Salsac, A synthetic schlieren method for the measurement of the topography of a liquid interface, Exp. Fluids **46**, 1021 (2009).

[43] F. Moisy and M. Rabaud, Free-surface synthetic schlieren (FS-SS): A tutorial, available at http://www.fast.u-psud.fr/~moisy/sgbos/tutorial.php

[44] J. Blaber, B. Adair, and A. Antoniou, Ncorr: Open-source 2D digital image correlation Matlab software, Exp. Mech. **55**, 1105 (2015).

[45] G. K. Batchelor, *An Introduction to Fluid Dynamics* (Cambridge University Press, Cambridge, 1967).

[46] J. D. Paulsen, E. Hohlfeld, H. King, J. Huang, Z. Qiu, T. P. Russell, N. Menon, D. Vella, and B. Davidovitch, Curvature-induced stiffness and the spatial variation of wavelength in wrinkled sheets, Proc. Natl. Acad. Sci. USA **113**, 1144 (2016).
[47] D. Vella and B. Davidovitch, Regimes of wrinkling in an indented floating elastic sheet, Phys. Rev. E **98**, 013003 (2018).

Paper AII

Self-organization and convection of confined magnetotactic bacteria

A. Théry, L. Le Nagard*, J.-C. Ono-dit-Biot*, C. Fradin, K. Dalnoki-Veress and E. Lauga, Scientific Reports, **10**, 1-9 (2020).

* These authors contributed equally

In this paper, we study a new type of collective motion, the bacterial magneto-convection, in a population of magnetotactic bacteria (MTB) confined in a capillary. Upon applying a magnetic field perpendicular to the confining walls, MTB self-organize into bacterial plumes perpendicular to the capillary walls. The formation of these plumes generates flow which resembles Rayleigh-Benard convection cells. Convection cells are imaged by Particle Image Velocimetry. The spacing between plumes coarsens over time before reaching an equilibrium distance which scales linearly with the width of the confining channel. Similar plumes of bacteria are observed in a phenomenon called bioconvection. The difference between the Rayleigh-Benard instability or bioconvection patterns and the new instability reported here, is that no external net force is applied to the system. The magnetic field only applies a torque to align the bacteria with the direction of the field. A theoretical model based on hydrodynamic singularities and their images is used to describe the bacteria-bacteria and bacteria-wall interactions. The model captures the growth of the plumes as well as the evolution of the spacing between plumes observed experimentally.

Lucas Le Nagard and I designed the experimental setup and conducted preliminary experiments on MTB which lead to the discovery of this instability in collaboration with Kari Dalnoki-Veress and Cécile Fradin. Albane Théry, a visiting graduate student, optimized the various experimental parameters, conducted the experiments and analyzed the data presented in this article in collaboration with Lucas Le Nagard, Kari Dalnoki-Veress, Cécile Fradin and myself. Albane Théry and Eric Lauga developed the theoretical model which describes the instability. Albane Théry prepared the first manuscript with was subsequently revised by all authors.

www.nature.com/scientificreports

SCIENTIFIC REPORTS

natureresearch

Check for updates

Self-organisation and convection of confined magnetotactic bacteria

Albane Théry[1,2], Lucas Le Nagard[2,4], Jean-Christophe Ono-dit-Biot[2,4], Cécile Fradin[2], Kari Dalnoki-Veress[2,3] & Eric Lauga[1]✉

Collective motion is found at all scales in biological and artificial systems, and extensive research is devoted to describing the interplay between interactions and external cues in collective dynamics. Magnetotactic bacteria constitute a remarkable example of living organisms for which motion can be easily controlled remotely. Here, we report a new type of collective motion where a uniform distribution of magnetotactic bacteria is rendered unstable by a magnetic field. A new state of "bacterial magneto-convection" results, wherein bacterial plumes emerge spontaneously perpendicular to an interface and develop into self-sustained flow convection cells. While there are similarities to gravity driven bioconvection and the Rayleigh–Bénard instability, these rely on a density mismatch between layers of the fluids. Remarkably, here no external forces are applied on the fluid and the magnetic field only exerts an external torque aligning magnetotactic bacteria with the field. Using a theoretical model based on hydrodynamic singularities, we capture quantitatively the instability and the observed long-time growth. Bacterial magneto-convection represents a new class of collective behaviour resulting only from the balance between hydrodynamic interactions and external alignment.

Examples of collective motion can be found in many biological systems over a wide range of length scales[1], from animal herds[2], bird flocks[3] and schools of fish[4], to individual cells[5]. Microorganisms swimming in viscous fluids at low Reynolds numbers can form coherent patterns that depend on the propulsion modes of the swimmers[6–8]. For instance, randomly-swimming cells such as bacteria[9] and spermatozoa[10] are able to self-organise into large-scale coherent structures.

In contrast with the random motion of many cells, micro-swimmers and artificial swimmers can also bias their movement in response to external cues. The bias can arise actively, as in the cases of chemotaxis[11] and phototaxis[12], or passively, for example gyrotactic swimmers[13], resulting in emergent pattern-formation in dense systems—a characteristic of collective locomotion. A classic example in this case is bioconvection, an instability initiated by the accumulation at an interface of gyrotactic[14] or phototactic[15] swimmers that are denser than the surrounding fluid. The resulting density stratification is unstable[16], which leads to the formation of downward falling plumes[17, 18]. Boundaries and confinement[19, 20] also strongly affect the swimming of microorganisms and their hydrodynamic interactions[21]. Although back-flow generated by boundaries tends to screen swimmer-swimmer interactions, the emergence of wall-driven attractive interactions has been observed, leading to orbiting[22] and large-scale clustering at a wall[23].

Magnetotactic bacteria (MTB) are prokaryotic micro-swimmers found in abundance in freshwater and marine habitats[24]. These bacteria can synthesize magnetosomes, membrane-bounded, magnetic nanocrystals often assembled into chain-like structures within the cytoplasm[25]. Magnetosomes confer to each cell a permanent magnetic dipole moment, forcing the swimming bacterium to align with external magnetic fields. The orientation and direction of motion of MTB can thus be manipulated remotely using controlled magnetic fields[26–28]. MTB can be used as a source of magnetosomes, which have demonstrated a great potential for medical applications due to their unmatched chemical purity and magnetic properties[29]. Furthermore, MTB have even been proposed as potential agents for targeted drug delivery[30]. A thorough understanding of the individual and collective properties of MTB is thus needed to fully exploit their potential for practical applications. The wall-mediated behaviour of single and pairs of MTB has been explored[31], and attractive hydrodynamic interactions lead to clustering

[1]Department of Applied Mathematics and Theoretical Physics, University of Cambridge, Cambridge CB3 0WA, UK. [2]Department of Physics and Astronomy, McMaster University, 1280 Main St. W, Hamilton, ON L8S 4M1, Canada. [3]UMR CNRS Gulliver 7083, ESPCI Paris, PSL Research University, 75005 Paris, France. [4]These authors contributed equally: Lucas Le Nagard and Jean-Christophe Ono-dit-Biot. ✉email: e.lauga@damtp.cam.ac.uk

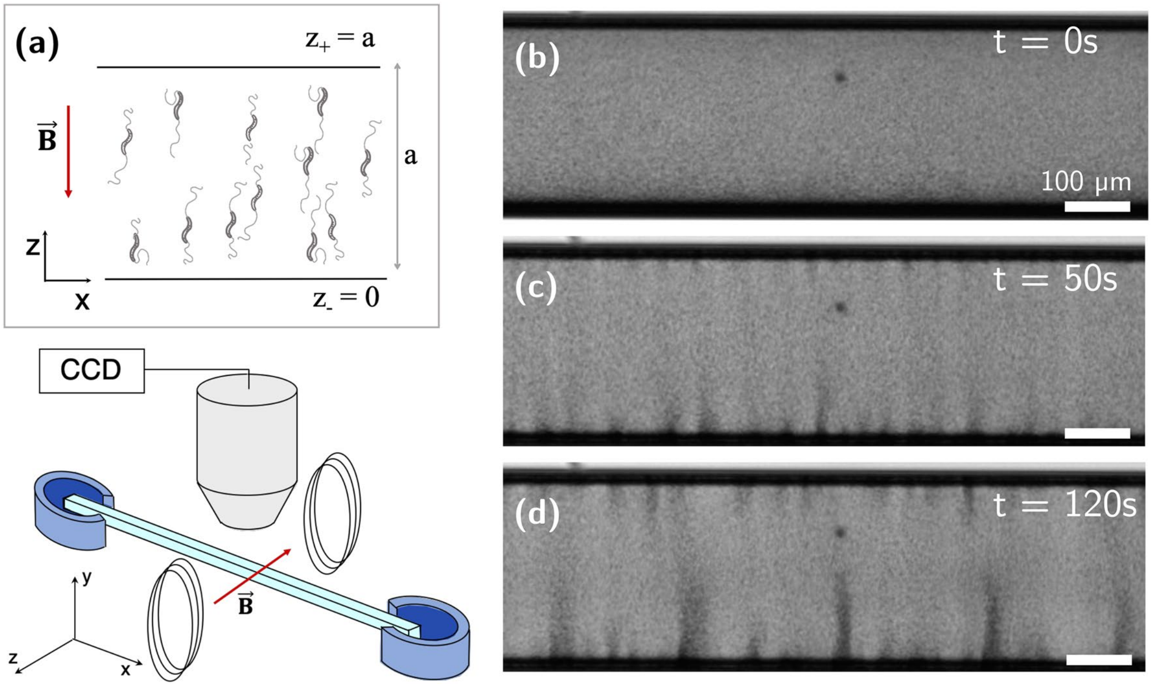

Figure 1. (**a**) Experimental set up and schematic view of the observed bacteria in the microscope under the magnetic field **B**. A glass capillary with square cross-section and pore size ranging from 80 μm to 500 μm, is held and sealed at both ends by two reservoirs filled with mineral oil. Two Helmholtz coils generate a uniform magnetic field and a microscope is used to image the bacteria. (**b**) Uniform distribution of bacteria in a capillary with dimensions 300 μm square at $t < 0$. The magnetic field magnetic field is then turned on at $t = 0$. (**c**) At $t = 50$ s, bacteria accumulate near the z_- wall, and the concentration instability emerges. (**d**) At longer times, plumes grow and cluster until a steady flow is obtained at $t = 2$ min.

near a wall[32]. Various patterns and instabilities can be induced by the control and orientation of large swimmer populations[33], including pearling of focused MTB in a thin capillary[34, 35] or vortex formation in droplets[36].

Here we report on a new type of collective motion observed in a population of confined MTB induced by the application of a magnetic field perpendicular to the confining walls. We find that a uniform distribution of magnetotactic bacteria is observed to self-organise spontaneously into bacterial plumes perpendicular to the wall, resulting in self-sustained convection cells. The observed plumes are reminiscent of bioconvection patterns and the flow generated resembles Rayleigh–Bénard convection cells[37]. However, an important difference exists between the phenomenon reported here and these well-studied instabilities. Both bioconvection and the Rayleigh–Bénard instability rely on a density mismatch between layers of the fluids, and thus on net (gravitational) forces applied to the fluid. In both these cases, removing the external force from the governing equations results in the absence of convective cells. In contrast, for the phenomenon reported here, no external forces are applied on the fluid and the magnetic field only exerts an external torque aligning MTB with the field[34]. A different mechanism thus needs to be proposed to describe the plumes and flow patterns observed.

Using a theoretical model based on hydrodynamic singularities, we show that the plumes result solely from the balance between the ordered state of the swimmers and both cell-cell and cell-wall hydrodynamic interactions. An instance of biased active matter related to previous examples in biological (phototactic, gyrotactic and chemotactic cells) and artificial systems (active phoretic particles in shear flows near surfaces), the self-sustained state reported here, which we term bacterial magneto-convection, represents therefore a new class of collective behaviour resulting only from the balance between hydrodynamic interactions and external alignment.

Results

Bacteria self organisation and plume formation.

In our experiments, bacteria of the strain *Magnetospirillum magneticum* AMB-1[38] are confined to square capillary channels aligned along the x-axis. Capillaries are filled with a concentrated solution of MTB and an external magnetic field, **B**, is applied normal to the channel wall along the positive z direction (see schematic in Fig. 1a and Methods section). The field **B** is uniform throughout the capillary, with strength ranging from 1×10^{-4} T to 20×10^{-4} T (Fig. 1). The bacteria are confined within the tube by the walls z_- and z_+ perpendicular to **B**, and by the walls y_- and y_+ in the orthogonal directions. Images are acquired at 10 fps and particle image velocimetry (PIV) is used to study the flow in the tubes, using bacteria as tracers. Some of the bacteria are non-motile and we observe the fluid flow generated by the plumes in the capillary. Cultures of motile and magnetic MTB were obtained through a racetrack selection method[39] which results in a bacteria population dominated by a preferred polarity and therefore in bacteria that predominantly swim in one direction. Despite the selection, there is always a small minority population present

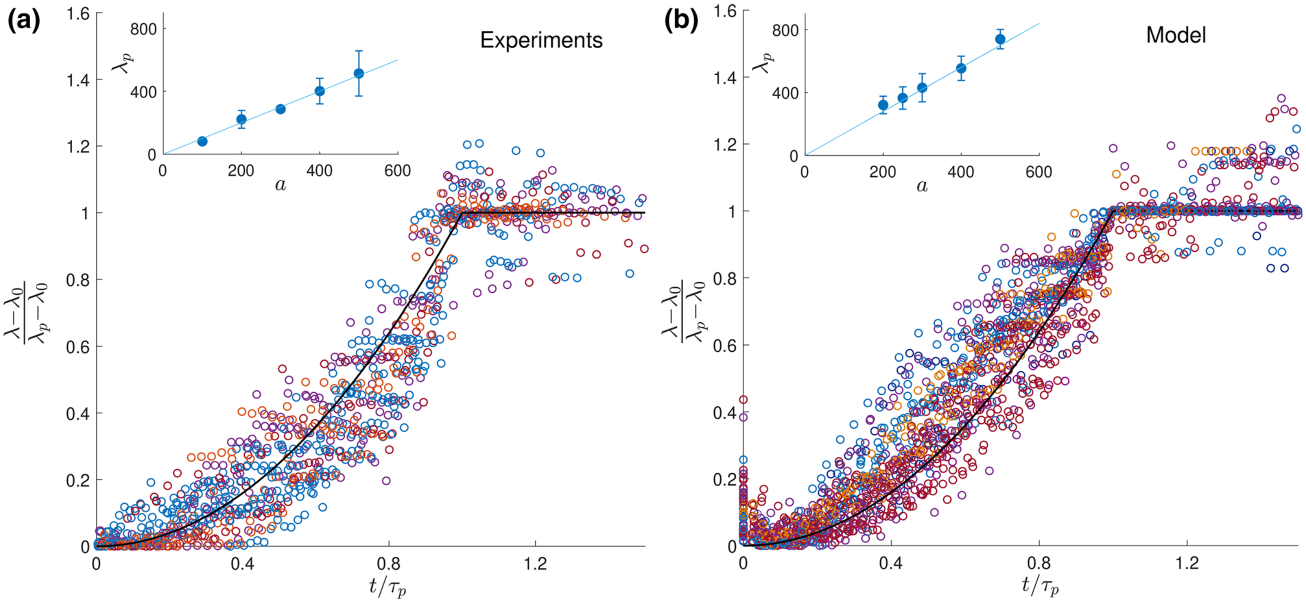

Figure 2. Time evolution of the wavelength in experiments (**a**) and model (**b**). In both cases, the wavelength λ is rescaled using its initial (λ_0) and final values (λ_p) and is plotted as a function of the reduced time, t/τ_p, where τ_p is the time at which λ plateaus. Colours correspond to different confinement sizes. The black line is $y = x^2$ for $x < 1$ and $y = 1$ after. Insets show final wavelengths scaling linearly with channel size, with error bars showing standard deviation.

with the reverse polarity which swims in the opposite direction. Due to the small size of that minority population, the reverse swimmers are neglected in our analysis.

In the absence of magnetic field, the bacteria are homogeneously distributed in the channel (Fig. 1b) with bacteria swimming in random directions. When the magnetic field is switched on, swimmers orient along the magnetic field **B**, and most motile bacteria start swimming towards the z_- wall (Fig. 1a) with velocities ranging from ~ 4 to $10\,\mu\text{ms}^{-1}$. As bacteria accumulate at the z_- wall, small clusters form and start growing. The time before the instability becomes visible depends strongly on both concentration and population of the bacteria, and ranges from a few seconds to 50 s. As the clusters grow, they start forming plumes which advect bacteria through a strong backward flow (Fig. 1c). The plumes interact with their nearest neighbours and attract each other, leading to merging and formation of larger plumes, with ultimate separations between plumes comparable to the channel size (Fig. 1d) (see Supplementary movies SM1, SM2 and SM3). In the larger 500 μm capillaries we observe by changing the focus of the microscope along the y-direction, that the plumes form in the central region of the channel, as opposed to close to the walls.

We observe the plumes and measure their dynamics in 26 experiments carried out in different capillary sizes and bacterial concentrations. In a few experiments, the plumes do not appear or do not grow. The mobility of bacteria and their sensitivity to the magnetic field are two key parameters that impact the dynamics of the instability and the plume formation. The dynamical properties of the instability are quantified by the characteristic time, τ_p, to reach the steady state. Experimentally τ_p ranges from 170s to 600s. Although no critical bacterial concentration can be determined, we find that lower concentrations of bacteria lead to larger τ_p, and to formation of smaller plumes that do not reach the same late-time wavelength as concentrated systems.

Below a critical magnetic field, which depends on the bacteria population and concentration and ranges from 2.6×10^{-4}T to 10×10^{-4}T, no plumes are observed. Above this critical field, plumes grow and evolve with dynamics unaltered by field strength (see Supplementary Material). The existence of a critical magnetic field can be understood by the necessity to have the bacteria aligned within a narrow orientation distribution along the magnetic field direction. All our experiments are carried out with magnetic fields much larger than the observed critical fields (2 mT) to rule out any influence of the field strength and ensure that the bacteria remain perfectly aligned with the field (see details in Supplementary Material). We also note that at this field strength, magnetic dipole-dipole interactions between neighbouring bacteria are negligible compared to those with the applied magnetic field.

In order to quantify the dynamics of the emergent patterning, we measure the wavelength λ of the plumes, defined as the average distance between neighbouring plumes, as a function of time. We locate the plumes in the experimental data by finding peaks in the intensity profile averaged along z. While we sometimes observe short-lived smaller plumes forming later in the experiments, we focus on the larger ones by defining an intensity threshold for the measured peaks (see details in Supplementary Material). Depending on the size of the channel, we observe between a few tens of plumes to two plumes at late times. As shown in Fig. 2a, the wavelength $\lambda(t)$ starts from an initial value λ_0, grows, and this growth accelerates until it reaches a plateau value at λ_p, after a time denoted by τ_p. Remarkably, this final wavelength is found to scale linearly with the size of the capillary (Fig. 2a, inset). We note that in traditional convection, it is common for external length scales, including those due to confinement, to set the late-time convection wavelength[37]. Plotting the normalised wavelength $(\lambda - \lambda_0)/(\lambda_p - \lambda_0)$

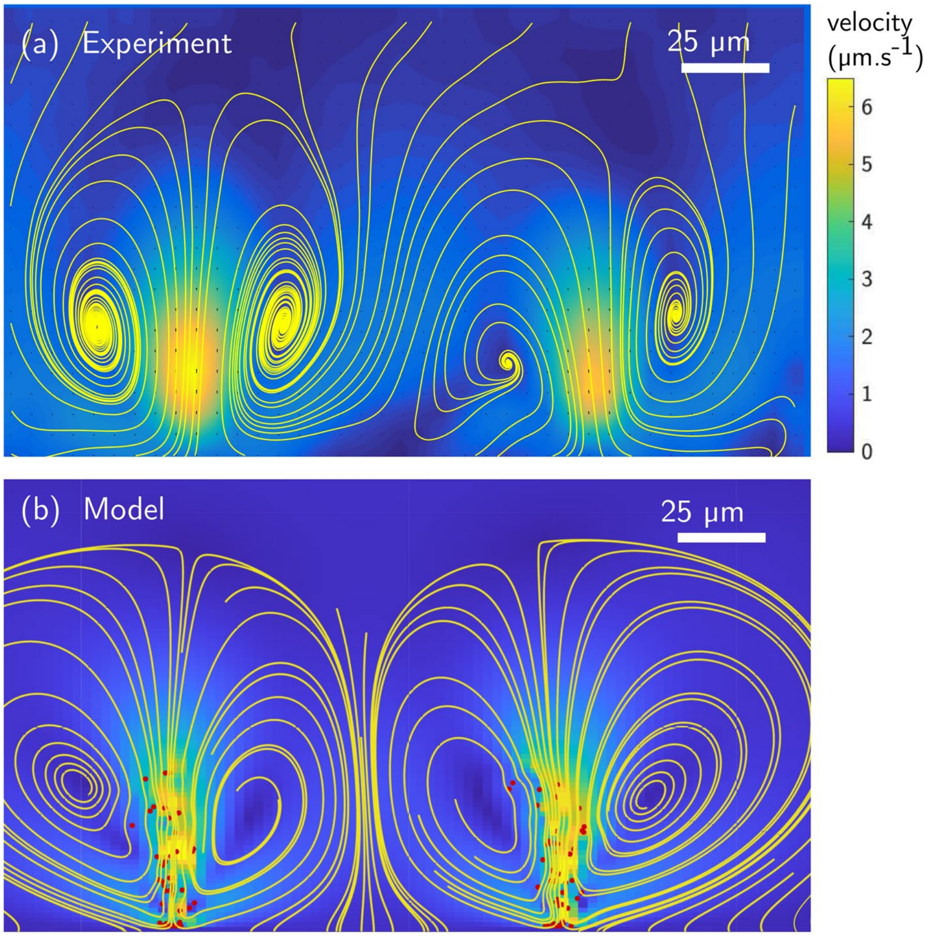

Figure 3. Convection cells created by two plumes in a 200 μm glass capillary. (**a**) Experimental measurements showing magnitude (colormap) and streamlines of the flow field averaged over one minute. (**b**) Convection cells and flow obtained with the theoretical model, with red dots representing the instantaneous location of the swimmers.

as a function of the reduced time t/τ_p exemplifies the two regimes of the wavelength time evolution: monotonic growth followed by a plateau, as shown in Fig. 2a.

We next use PIV to measure the flow field and plot the streamlines and flow magnitude in Fig. 3a. Plumes are generated as soon as the characteristic flow velocities induced by the layer of accumulating bacteria are of the same order of magnitude as the downward velocity of the swimmers. When the wavelength becomes on the order of the channel width, hydrodynamic interactions with the walls screen the cellular flows and plumes stop growing, resulting in stable convection cells of size comparable to the channel.

Hydrodynamic singularities model. To further understand the mechanism for the instability and its time evolution, we develop a theoretical model which successfully describes the emergence of collective behaviour and the formation of plumes in the suspension. We model AMB-1 as pusher swimmers[31, 40]. Each free-swimming bacterium is modelled as two opposite regularized point forces (known as stokeslets[41]) of strength s_0 separated by a distance l_0, taken as the characteristic size of the swimmer[42] (see Supplementary Material and movies SM4 and SM5). The force-free swimmers are confined in a channel with square section a and aspect ratio 10 with periodic boundary conditions along the x direction (see Fig. 1a), and are subject to both steric and hydrodynamic interactions[20]. Magnetic interactions between swimmers are negligible compared to those with the external field, and are therefore neglected. We assume that the swimmers remain aligned with the external magnetic field and always tend to swim preferentially in the negative z direction at a constant speed $-u_0\hat{z}$. However, their speeds are modified by the dipolar flow fields induced by the other swimmers and by hydrodynamic interactions with walls. Our model investigates the system for values of the magnetic field above the critical field for bacterial alignment, consistent with what was done in the experiments. The model is non-dimensionalised using characteristic length scale l_0, velocity u_0 and dynamic viscosity μ. For comparison with experiments, we use a characteristic bacterium size $l_0 = 5\,\mu\text{m}$[32]. Steric interactions are included using soft pair-repulsive forces[43] between the centres of each bacteria. These interactions decay as A/r and, to speed up computation times, are only taken into account for bacteria closer than $2l_0$ and generate a speed with upper bound $5u_0$. In addition to bacterium-bacterium interactions, hydrodynamic interactions also occur between bacteria and channel walls.

We include the two walls normal to the magnetic field, z_- and z_+, and use the method of images for regularized stokeslets (algebraic regularization function with a core of size $\delta = 0.3l_0$) in order to enforce the no-slip boundary condition on the walls exactly (see Ref.[44] and Supplementary Material). The image system for a stokeslet consists of a stokeslet, an irrotational dipole and a stokeslet dipole[45] with adequate regularization. As a result, the position $\boldsymbol{x}^{(j)}$ of the j^{th} bacterium evolves with its velocity, $\boldsymbol{u}^{(j)}$, sum of its intrinsic swimming speed $-u_0\boldsymbol{e}_z$, the hydrodynamic and steric interactions with other bacteria, denoted $\boldsymbol{u}_{\mathrm{hydro}}$ and $\boldsymbol{u}_{\mathrm{steric}}$ respectively, and the flow created by interactions of all swimmers with the walls, $\boldsymbol{u}_{\mathrm{wall}}$, leading to

$$\frac{\mathrm{d}\boldsymbol{x}^{(j)}}{\mathrm{d}t} = \boldsymbol{u}^{(j)} = -u_0\boldsymbol{e}_z + \sum_{i=1}^{N}\boldsymbol{u}^{(j)}_{\mathrm{wall}}(\boldsymbol{x}^{(i)};\boldsymbol{x}^{(j)}) + \sum_{i\neq j}\left[\boldsymbol{u}^{(j)}_{\mathrm{steric}}(\boldsymbol{x}^{(i)}-\boldsymbol{x}^{(j)}) + \boldsymbol{u}^{(j)}_{\mathrm{hydro}}(\boldsymbol{x}^{(i)}-\boldsymbol{x}^{(j)})\right]. \tag{1}$$

Our simulations have N swimmers, with N ranging from 500 to 8000, with different values of N used for each channel size a. Bacteria are initially distributed uniformly in the channel and their position is then integrated explicitly from Eq. (1) using the dimensionless time step $\mathrm{d}t = 0.5$. Swimmers are confined laterally in the channel by ensuring that, after each time step, they remain inside the walls along y_+ and y_-, i.e. $-a/2 < y^{(i)} < a/2$. Note that in practice this constraints is rarely invoked in our simulations because hydrodynamic interactions between swimmers in the (x-z) plane are attractive and thus quickly lead to clustering within the channel. In the simulations, we take the bacteria to have identical swimming speed and therefore identical effect on the surrounding fluid. To account for the heterogeneity of the population, simulations were also carried out with bacteria velocities normally distributed around u_0 with standard deviation $u_0/3$ and we obtained the same plume patterns and dynamics.

The dynamics of the convective cells in the numerical model is illustrated in Fig. 4. Similar to the experimental observations, the randomly distributed bacteria (Fig. 4a) first swim in the $-z$ direction and accumulate at the wall (Fig. 4b). Neighbouring wall-bound bacteria experience attractive interactions and start clustering. The origin of this attraction lies in the hydrodynamic interactions between the bacteria and the wall. When a swimmer is located at the no-slip wall, the point force closer to the surface nearly cancels with its image, leaving only a stokeslet pushing the surrounding fluid away from the wall[22]. In other words, a bacterium stuck near a surface imposes a net force away from the wall on the surrounding fluid. Due to mass conservation, the flow created by this force induces a secondary attractive flow along the wall and directed toward the swimmer. Attractive interactions disturb the uniform distribution of wall-bound swimmers and lead to clustering. Attractive interactions between point forces located near a surface have been described in the past in both physics[46] and biology[22], including for MTB[31]. Similar hydrodynamic clustering has also been observed for *Thiovulum majus* (*T. majus*), a larger almost-spherical bacterium, swimming near walls[23]. While the mechanism for the initial attraction to the surface is the same, the evolution of the two systems differ significantly. The back-flow generated by the MTB in our experiments is strong enough to detach some of the swimmers and advect them away from the surface. Additionally, the *T. majus* bacteria in Ref.[23] remain bound to the surfaces, possibly due to stronger interaction with the surfaces or because of their spherical shape, and form two-dimensional rotating crystals. In contrast, for both our experiments and model, detached MTB cells form plumes (Fig. 4c) which in turn generate stronger attractive flows, resulting in plume-plume attraction and merging. Finally, the increasing number of swimmers within each plume leads to the formation of elongated vertical plumes. This instability is predicted to occur at any bacterium concentration, as any two swimmers at the wall will experience attraction. Besides, cell detachment from the wall can occur for clusters of as little as three swimmers, which means that in our model, we predict no critical concentration for the instability. However, for very dilute systems, the timescale for plume formation becomes very long, and exceeds the time of our observations. The time-sequence from initial swimmer distribution to final plumes is illustrated in Fig. 4d with time-lapse representation of the swimmers position within the $x - y$ plane perpendicular to the plumes. Ultimately, a steady flow state is reached when plumes are separated by a length scale similar to the channel height, creating flows with convection cells similar to experimental observations (Fig. 3b). Note that, beyond the final state, we find a good qualitative agreement between the flow structures created by the plumes in our experiments and in the numerical model, as further detailed in the Supplementary Material.

To further compare the experimental data with the model, we study the dynamics of the plume wavelength, λ. In order to compute the wavelength, a histogram of the bacteria positions is obtained for each time point in the simulation. For consistency with experimental data analysis, plumes are identified where a peak is greater than 1/5 of the highest peak. Similarly to experiments, simulations reveal a sharp change in wavelength evolution, corresponding to a transition from accelerating growth to a plateau in the wavelength. Rescaling the wavelength leads to collapse of the numerical results for various concentrations and system sizes in excellent agreement with the experimental data (Fig. 2). In particular, the late-time wavelength scales with the size of the channels in both cases (we obtain $\lambda_p \sim a$ in the experiments and $\lambda_p \sim 1.4a$ for the simulations). Our simulations support an intuitive physical explanation for the existence of a plateau value wherein the transition occurs when plumes interact with their hydrodynamic images on the opposing wall, which limits the range of the flow created by all swimmers in a plume and thereby plume growth. The confinement thus sets the limit for the accelerating merging of the plumes. To validate this hypothesis, we carried out simulations without an upper wall (i.e. unconfined) and obtain, for sufficiently large concentrations, uninterrupted growth until only a single plume emerges (see Supplementary Material). We note that the presence of walls parallel to the magnetic field, y_- and y_+, is neglected in simulations and would further slow the growth of the biggest plumes due to additional flow confinement.

Focusing on wavelength dynamics before reaching the plateau regime, $\lambda(t)$, we observe some scatter in the curves of Fig. 2 for both experiments and in our model, showing that the precise wavelength growth dynamics vary with the channel size a and the cell concentration (see Supplementary Material). This shows that the time

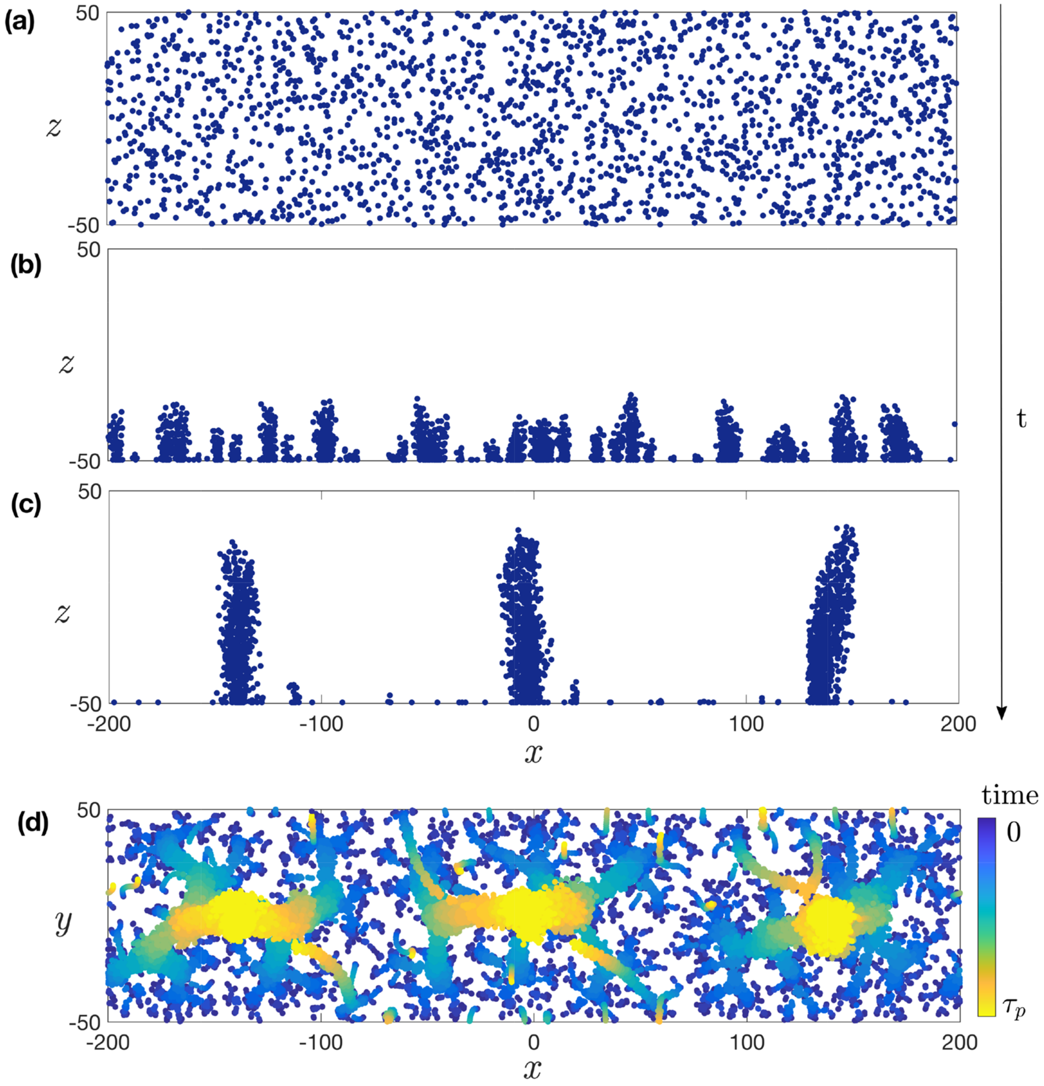

Figure 4. (**a**) Growth of plumes in the model starting from randomly distributed bacteria. (**b**) Swimmers accumulate at the wall and cluster due to hydrodynamic interactions. (**c**) The flows induced by the swimmers are sufficiently strong to detach some bacteria from the wall, leading to elongated plumes. (**d**) $x - y$ plane view showing the time-lapse evolution of the swimmers positions, from initially random (dark blue) to plumes in a steady flow state (light yellow) (dimensionless units).

to reach the plateau τ_p does not fully govern the early dynamics of the system. Indeed, we identify two regimes in the simulations, one of accelerating growth and one of approximately constant growth. Their relative duration sets the shape of the $\lambda(t)$ curves in Fig. 2. In the first one, some bacteria have not yet reached the z_- region of the channel as the first plumes start forming. The duration of this first regime can be estimated by computing the average of the lowest z value previously reached by each bacterium, and we see that it is higher than for free swimming bacteria due to repulsive hydrodynamic interactions in the z direction. Increasing swimmers concentration in the z_- region accelerates plume growth (see Fig. 5), and this first regime coincides with an increasing rate of growth of the wavelength, as further detailed in the Supplementary Material.

At later times, all bacteria are in the z_- region of the channel. If the flow created by a plume was the sum of all flows generated by individual bacteria at the wall, then $\lambda \propto t^{1/2}$, due to localised hydrodynamic forcing (Stokeslets) near surfaces interacting as r^{-2}, which matches neither the experiments nor the simulations. However, when in a plume, swimmers are advected away from the wall and their contribution to the flow is modified and decays more slowly. Because of this, the flow created by a plume does not scale linearly with the number of swimmers in the plume, which leads to more complex dynamics without a single scaling law. Plume-plume interactions depend on the position of individual swimmers relative to the wall and hence on the density profile of plumes. We find that plumes are systematically denser near the wall, with some bacteria sticking on it (see Supplementary Material). Integrating the inverse of the flow velocity in the x direction from simulations of a single stratified plume yields an approximation for the merging time of two plumes, given their initial separation x_0. Due to mass conservation, for a given system where plumes gradually merge, x_0 scales with the number of swimmers in a plume, N_p. We intuitively expect the merging time for two plumes to be linear with N_p, and

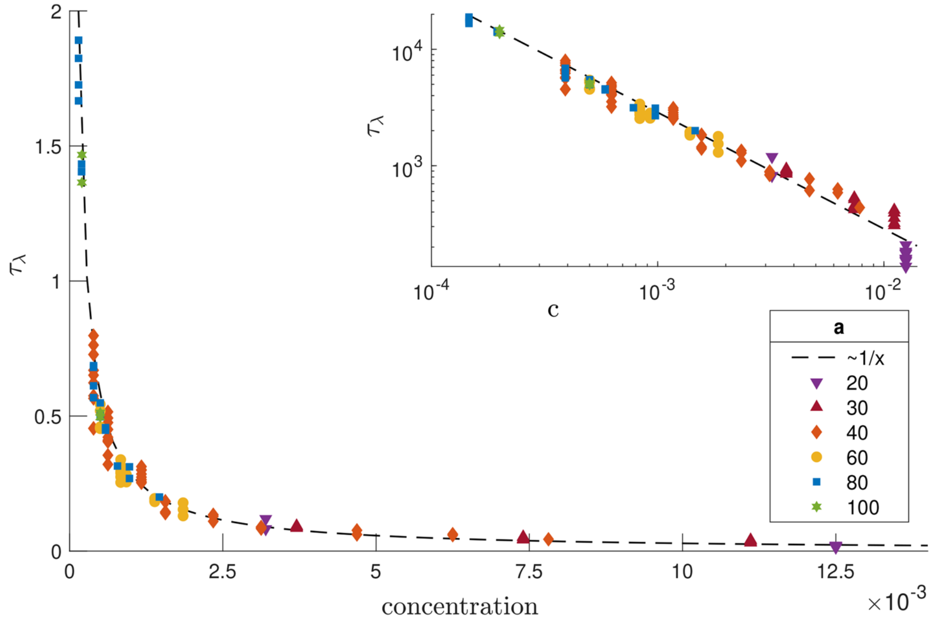

Figure 5. Characteristic time for the growth of the wavelength, τ_λ, as a function of the concentration, *c*, in our simulations (both quantities are plotted in dimensionless units). The time scale τ_λ is obtained using a least-square quadratic fit of the wavelength of the form $\lambda(t)/a = \lambda_0/a + (t/\tau_\lambda)^2$. The dotted line is a fit to an inverse scaling as $\tau_\lambda \propto 1/c$. Inset: same plot in log-log scale.

this is observed for sufficiently large swimmer concentrations, corresponding to the concentrations used in our simulations to match experimental observations. In contrast, lower concentrations lead to longer merging times for the plumes and therefore smaller plumes, as observed both in experiments and simulations. In the regime where the bacteria have reached the z_- part of the channel, the wavelength varies linearly with time. This linear scaling is confirmed by simulations where all bacteria were initially positioned on the z_- surface. In that case, the wavelength depends linearly on time from the beginning of the simulation (see Supplementary Material). The time scale of the dynamics τ_p is therefore larger than the time for a single bacterium to swim to the wall but smaller than the time for bacteria at the wall to attract each other on distance comparable to the cross section *a*. To quantify the influence of the concentration on plume growth in our model, we estimate a characteristic time scale, τ_λ, for wavelength growth obtained from a quadratic fit of the wavelength $\lambda(t)$, with results shown in Fig. 5. We see that τ_λ scales as the inverse of the concentration, which shows that the dynamics of the system are governed by the plume-plume merging time scaling as N_p, as described above. Overall, the nonlinear shape of the wavelength dependence on time can thus be explained by the time it takes for swimmers to reach the plumes region and the advection of bacteria away from their hydrodynamic images, which tends to increase their contribution to the flow and thus the attractive interactions between plumes.

In summary, we have identified experimentally a new type of collective motion, bacterial magneto-convection. MTB driven by an external magnetic field start by accumulating at the surface of a microfluidic channel. The initial random distribution of bacteria is unstable due to hydrodynamic attraction between swimmers, which cluster and form dynamic plumes. The resulting self-sustained flow resembles convection cells, with a late-time characteristic size linearly dependent on the confinement length scale, with the crucial difference that here no external forces are applied to the system, only external torques aligning the cells with the external field. A model based on hydrodynamic singularities and their images describes interactions between bacteria and with channel walls and successfully reproduces the growth and long-time dynamics of the interacting plumes. We expect this model to be useful in understanding other observed collective motions of magnetotactic bacteria as well as any confined swimmers oriented by external fields, leading to a better understanding of the respective role of swimmer-swimmer interaction and external cues. Since bacterial magneto-convection represents a new class of collective behaviour resulting only from the balance between hydrodynamic interactions and external alignment, it helps elucidate the synergy between particle-particle interactions and external cues and can be compared to other systems of biased biological or artificial swimmers to shed a light on their own collective dynamics.

Methods

Bacteria are grown in a liquid medium with controlled nutrients and O_2 conditions, following Ref.[47]. To ensure that most of the bacterium population remains magnetotactic and motile, we use a racetrack selection method[39], keeping only bacteria that swim through a filter while guided by an external magnetic field. This also selects bacteria with a preferred polarity. Before the experiments reported in the present study, we measured the magnetic moment of bacteria grown in the same conditions and obtained $\mu = 10^{-15} \pm 4 \times 10^{-16}$ A m^2 (mean ± standard deviation)[48]. High concentrations of motile bacteria are then obtained by centrifugation (1.5ml, 2000 rcf, 2 min) and subsequent re-dispersion in approximately 10% of the supernatant. After this procedure, a majority of the obtained bacteria are motile and magnetic, however the solution also contains non motile and dead bacteria. We fill the glass capillaries (Vitrotubes, VitroCom, New Jersey, USA) by capillarity with a drop of the concentrated suspension. Both sides of the capillary are then sealed by placing them on a support with two cells filled with mineral oil, to avoid evaporation.

Two Helmholtz coils are mounted on the platform of a microscope (Nikon eclipse E200) to generate a uniform magnetic field normal to the capillary tube. We verify that the magnetic field was indeed uniform on the whole length of the capillary and calibrated the set up to obtain fields ranging from 1×10^{-4} T to 20×10^{-4} T. Images are then acquired with a CCD camera (Allied Vision Technology GE680) at 10 fps. The images are then analysed through PIV[49], using bacteria as tracers. While motile magnetic bacteria accumulate at the surface of the capillary and in the plumes, the presence of non-motile bacteria enables us to observe the flow field in the capillary throughout the experiments, and obtain streamlines in the channel.

Data availability

The data that support the findings of this study as well as the Matlab code (for image analysis and simulations) are available from the corresponding author upon reasonable request.

Received: 15 May 2020; Accepted: 27 July 2020

References

1. Vicsek, T. & Zafeiris, A. Collective motion. *Phys. Rep.* **517**, 71–140. https://doi.org/10.1016/j.physrep.2012.03.004 (2012).
2. Sumpter, D. J. The principles of collective animal behaviour. *Philos. Trans. R. Soc. B Biol. Sci.*https://doi.org/10.1098/rstb.2005.1733 *(2005)*.
3. Mora, T. *et al.* Local equilibrium in bird flocks. *Nat. Phys.* **12**, 1153. https://doi.org/10.1038/nphys3846 (2016).
4. Lopez, U., Gautrais, J., Couzin, I. D. & Theraulaz, G. From behavioural analyses to models of collective motion in fish schools. *Interface Focus* **2**, 693–707. https://doi.org/10.1098/rsfs.2012.0033 (2012).
5. Trepat, X. *et al.* Physical forces during collective cell migration. *Nat. Phys.* **5**, 426. https://doi.org/10.1038/nphys1269 (2009).
6. Lauga, E. & Powers, T. R. The hydrodynamics of swimming microorganisms. *Rep. Prog. Phys.* **72**, 096601. https://doi.org/10.1088/0034-4885/72/9/096601 (2009).
7. Cisneros, L. H., Cortez, R., Dombrowski, C., Goldstein, R. E. & Kessler, J. O. Fluid dynamics of self-propelled micro-organisms, from individuals to concentrated populations. *Exp. Fluids* **43**, 737–753. https://doi.org/10.1007/s00348-007-0387-y (2007).
8. Koch, D. L. & Subramanian, G. Collective hydrodynamics of swimming microorganisms: living fluids. *Annu. Rev. Fluid Mech.* **43**, 637–659. https://doi.org/10.1146/annurev-fluid-121108-145434 (2011).
9. Sokolov, A., Aranson, I. S., Kessler, J. O. & Goldstein, R. E. Concentration dependence of the collective dynamics of swimming bacteria. *Phys. Rev. Lett.* **98**, 158102. https://doi.org/10.1103/physrevlett.98.158102 (2007).
10. Riedel, I. H., Kruse, K. & Howard, J. A self-organized vortex array of hydrodynamically entrained sperm cells. *Science* **309**, 300–303. https://doi.org/10.1016/j.physrep.2012.03.0040 (2005).
11. Keller, E. F. & Segel, L. A. Model for chemotaxis. *J. Theor. Biol.* **30**, 225–234. https://doi.org/10.1016/j.physrep.2012.03.0041 (1971).
12. Witman, G. B. Chlamydomonas phototaxis. *Trends Cell Biol.* **3**, 403–408. https://doi.org/10.1016/j.physrep.2012.03.0042 (1993).
13. Kessler, J. O. Hydrodynamic focusing of motile algal cells. *Nature* **313**, 218. https://doi.org/10.1016/j.physrep.2012.03.0043 (1985).
14. Pedley, T. & Kessler, J. Hydrodynamic phenomena in suspensions of swimming microorganisms. *Annu. Rev. Fluid Mech.* **24**, 313–358. https://doi.org/10.1016/j.physrep.2012.03.0044 (1992).
15. Vincent, R. & Hill, N. Bioconvection in a suspension of phototactic algae. *J. Fluid Mech.* **327**, 343–371. https://doi.org/10.1016/j.physrep.2012.03.0045 (1996).
16. Childress, S., Levandowsky, M. & Spiegel, E. A. Pattern formation in a suspension of swimming microorganisms: equations and stability theory. *J. Fluid Mech.* **69**, 591–613. https://doi.org/10.1016/j.physrep.2012.03.0046 (1975).
17. Hill, N. & Pedley, T. Bioconvection. *Fluid Dyn. Res.* **37**, 1–20. https://doi.org/10.1016/j.physrep.2012.03.0047 (2005).
18. Mogami, Y., Yamane, A., Gino, A. & Baba, S. A. Bioconvective pattern formation of tetrahymena under altered gravity. *J. Exp. Biol.* **207**, 3349–3359. https://doi.org/10.1016/j.physrep.2012.03.0048 (2004).
19. Wioland, H., Lushi, E. & Goldstein, R. E. Directed collective motion of bacteria under channel confinement. *New J. Phys.* **18**, 075002. https://doi.org/10.1016/j.physrep.2012.03.0049 (2016).
20. Lushi, E., Wioland, H. & Goldstein, R. E. Fluid flows created by swimming bacteria drive self-organization in confined suspensions. *Proc. Natl. Acad. Sci.*https://doi.org/10.1073/pnas.1405698111 *(2014)*.
21. Drescher, K., Dunkel, J., Cisneros, L. H., Ganguly, S. & Goldstein, R. E. Fluid dynamics and noise in bacterial cell-cell and cell-surface scattering. *Proc. Natl. Acad. Sci.* **108**, 10940–10945. https://doi.org/10.1073/pnas.1019079108 (2011).
22. Drescher, K. *et al.* Dancing volvox: hydrodynamic bound states of swimming algae. *Phys. Rev. Lett.* **102**, 168101. https://doi.org/10.1103/physrevlett.102.168101 (2009).
23. Petroff, A. P., Wu, X.-L. & Libchaber, A. Fast-moving bacteria self-organize into active two-dimensional crystals of rotating cells. *Phys. Rev. Lett.* **114**, 158102. https://doi.org/10.1103/physrevlett.114.158102 (2015).
24. Klumpp, S., Lefèvre, C. T., Bennet, M. & Faivre, D. Swimming with magnets: from biological organisms to synthetic devices. *Phys. Rep.* **789**, 1–54. https://doi.org/10.1016/j.physrep.2018.10.007 (2019).
25. Uebe, R. & Schüler, D. Magnetosome biogenesis in magnetotactic bacteria. *Nat. Rev. Microbiol.* **14**, 621. https://doi.org/10.1038/nrmicro.2016.99 (2016).
26. Bazylinski, D. A. & Trubitsyn, D. Magnetotactic bacteria and magnetosomes. In *Magnetic Nanoparticles in Biosensing and Medicine* (eds Darton, N. J. *et al.*) 251–284 (Cambridge University Press, Cambridge, 2019). https://doi.org/10.1017/9781139381222.009.
27. Blakemore, R. P. Magnetotactic bacteria. *Annu. Rev. Microbiol.* **36**, 217–238. https://doi.org/10.1146/annurev.mi.36.100182.001245 (1982).
28. Lefevre, C. T., Song, T., Yonnet, J.-P. & Wu, L.-F. Characterization of bacterial magnetotactic behaviors by using a magnetospectrophotometry assay. *Appl. Environ. Microbiol.* **75**, 3835–3841. https://doi.org/10.1128/aem.00165-09 (2009).
29. Alphandéry, E. Applications of magnetosomes synthesized by magnetotactic bacteria in medicine. *Front. Bioeng. Biotechnol.* **2**, 5. https://doi.org/10.3389/fbioe.2014.00005 (2014).
30. Felfoul, O. *et al.* Magneto-aerotactic bacteria deliver drug-containing nanoliposomes to tumour hypoxic regions. *Nat. Nanotechnol.* **11**, 941. https://doi.org/10.1038/nnano.2016.137 (2016).
31. Pierce, C. *et al.* Tuning bacterial hydrodynamics with magnetic fields. *Phys. Rev. E* **95**, 062612 (2017).
32. Pierce, C. *et al.* Hydrodynamic interactions, hidden order, and emergent collective behavior in an active bacterial suspension. *Phys. Rev. Lett.* **121**, 188001. https://doi.org/10.1103/physreve.95.062612 (2018).

33. Belovs, M., Livanovics, R. & Cēbers, A. Synchronized rotation in swarms of magnetotactic bacteria. *Phys. Rev. E* **96**, 042408. https://doi.org/10.1103/physreve.96.042408 (2017).
34. Waisbord, N., Lefèvre, C. T., Bocquet, L., Ybert, C. & Cottin-Bizonne, C. Destabilization of a flow focused suspension of magnetotactic bacteria. *Phys. Rev. Fluids* **1**, 053203. https://doi.org/10.1103/physrevfluids.1.053203 (2016).
35. Meng, F., Matsunaga, D. & Golestanian, R. Clustering of magnetic swimmers in a poiseuille flow. *Phys. Rev. Lett.* **120**, 188101. https://doi.org/10.1103/physrevlett.120.188101 (2018).
36. Vincenti, B. *et al.* Magnetotactic bacteria in a droplet self-assemble into a rotary motor. *Nat. Commun.* **10**, 1–8. https://doi.org/10.1017/9781139381222.0090 (2019).
37. Normand, C., Pomeau, Y. & Velarde, M. G. Convective instability: a physicists approach. *Rev. Mod. Phys.* **49**, 581. https://doi.org/10.1103/RevModPhys.49.581 (1977).
38. Matsunaga, T., Sakaguchi, T. & Tadakoro, F. Magnetite formation by a magnetic bacterium capable of growing aerobically. *Appl. Microbiol. Biotechnol.* **35**, 651–655. https://doi.org/10.1007/bf00169632 (1991).
39. Wolfe, R., Thauer, R. & Pfennig, N. A capillary racetrack method for isolation of magnetotactic bacteria. *FEMS Microbiol. Lett.* **3**, 31–35. https://doi.org/10.1111/j.1574-6968.1987.tb02335.x (1987).
40. Murat, D. *et al.* Opposite and coordinated rotation of amphitrichous flagella governs oriented swimming and reversals in a magnetotactic spirillum. *J. Bacteriol.* **197**, 3275–3282. https://doi.org/10.1128/jb.00172-15 (2015).
41. Cortez, R. The method of regularized stokeslets. *SIAM J. Sci. Comput.* **23**, 1204–1225. https://doi.org/10.1137/s106482750038146x (2001).
42. Drescher, K., Goldstein, R. E., Michel, N., Polin, M. & Tuval, I. Direct measurement of the flow field around swimming microorganisms. *Phys. Rev. Lett.* **105**, 168101. https://doi.org/10.1103/PhysRevLett.105.168101 (2010).
43. Costanzo, A., Di Leonardo, R., Ruocco, G. & Angelani, L. Transport of self-propelling bacteria in micro-channel flow. *J. Phys. Condens. Matter* **24**, 065101. https://doi.org/10.1088/0953-8984/24/6/065101 (2012).
44. Ainley, J., Durkin, S., Embid, R., Boindala, P. & Cortez, R. The method of images for regularized stokeslets. *J. Comput. Phys.* **227**, 4600–4616. https://doi.org/10.1016/j.jcp.2008.01.032 (2008).
45. Blake, J. A note on the image system for a stokeslet in a no-slip boundary. *Math. Proc. Cambr. Philos. Soc.* **70**, 303–310. https://doi.org/10.1017/s0305004100049902 (1971).
46. Squires, T. M. & Brenner, M. P. Like-charge attraction and hydrodynamic interaction. *Phys. Rev. Lett.* **85**, 4976. https://doi.org/10.1103/physrevlett.85.4976 (2000).
47. Le Nagard, L., Morillo-López, V., Fradin, C. & Bazylinski, D. A. Growing magnetotactic bacteria of the genus magnetospirillum: strains msr-1, amb-1 and ms-1. *J. Vis. Exper.*https://doi.org/10.3791/58536 *(2018).*
48. Le Nagard, L. *et al.* Misalignment between the magnetic dipole moment and the cell axis in the magnetotactic bacterium magnetospirillum magneticum amb-1. *Phys. Biol.* **16**, 066008. https://doi.org/10.1088/1478-3975/ab2858 (2019).
49. Thielicke, W. & Stamhuis, E. J. Pivlab-towards user-friendly, affordable and accurate digital particle image velocimetry in matlab. *J. Open Res. Softw.*https://doi.org/10.5334/jors.bl *(2014).*

Acknowledgements

This work was funded by the European Research Council (ERC) under the EU's Horizon 2020 research and innovation program (Grant Agreement No. 682754 to EL) and the Natural Science and Engineering Research Council of Canada. The Joliot Chair of the ESPCI Paris is gratefully acknowledged. We also thank Dennis Bazylinski and Adam Hitchcock for fruitful discussions.

Author contributions

A.T., L.L.N. and J.-C.O.B. carried out the experiments under the direction of K.D.V. and C.F.. A.T. and E.L. developed the theoretical model and the simulations. All authors contributed to the writing of the manuscript and reviewed it.

Competing interests

The authors declare no competing interests.

Additional information

Supplementary information is available for this paper at https://doi.org/10.1038/s41598-020-70270-0.

Correspondence and requests for materials should be addressed to E.L.

Reprints and permissions information is available at www.nature.com/reprints.

Publisher's note Springer Nature remains neutral with regard to jurisdictional claims in published maps and institutional affiliations.

Bibliography

[1] Robert J Hunter. *Foundations of colloid science*. Oxford university press, 2001.

[2] Brent S Murray and Rammile Ettelaie. Foam stability: proteins and nanoparticles. *Curr. Opin. Colloid Interface Sci.*, 9(5):314–320, 2004.

[3] Eric Dickinson. Food emulsions and foams: Stabilization by particles. *Curr. Opin. Colloid Interface Sci.*, 15(1-2):40–49, 2010.

[4] Anthony Edward Gregory, Diane Williamson, and Richard Titball. Vaccine delivery using nanoparticles. *Front. Cell. Infect. Microbiol*, 3:13, 2013.

[5] John S Huang and Ramesh Varadaraj. Colloid and interface science in the oil industry. *Curr. Opin. Colloid Interface Sci.*, 1(4):535–539, 1996.

[6] Gary L Hunter and Eric R Weeks. The physics of the colloidal glass transition. *Rep. Prog. Phys.*, 75(6):066501, 2012.

[7] Lea-Laetitia Pontani, Ivane Jorjadze, Virgile Viasnoff, and Jasna Brujic. Biomimetic emulsions reveal the effect of mechanical forces on cell–cell adhesion. *Proc. Natl. Acad. Sci. U.S.A*, 109(25):9839–9844, 2012.

[8] W. L. Bragg and J. F. Nye. A dynamical model of a crystal structure. *Proc. R. Soc. A*, 190(1023):474–481, 1947.

[9] John C Crocker and David G Grier. Methods of digital video microscopy for colloidal studies. *J. Colloid Interface Sci.*, 179(1):298–310, 1996.

[10] J Zhou, S Long, Q Wang, and AD Dinsmore. Measurement of forces inside a three-dimensional pile of frictionless droplets. *Science*, 312(5780):1631–1633, 2006.

[11] Kenneth W Desmond, Pearl J Young, Dandan Chen, and Eric R Weeks. Experimental study of forces between quasi-two-dimensional emulsion droplets near jamming. *Soft Matter*, 9(12):3424–3436, 2013.

[12] Douglas J Jerolmack and Karen E Daniels. Viewing earth's surface as a soft-matter landscape. *Nat. Rev. Phys.*, pages 1–15, 2019.

[13] David Gonzalez-Rodriguez, Karine Guevorkian, Stéphane Douezan, and Françoise Brochard-Wyart. Soft matter models of developing tissues and tumors. *Science*, 338(6109):910–917, 2012.

[14] L Guy, S Daudey, and Y Bomal. New insights in the dynamic properties of precipitated silica filled rubber using a new high surface silica. *Kautsch. Gummi Kunstst.*, 62:383–391, 2009.

[15] HH Hassan, E Ateia, NA Darwish, SF Halim, and AK Abd El-Aziz. Effect of filler concentration on the physico-mechanical properties of super abrasion furnace black and silica loaded styrene butadiene rubber. *Materials & Design*, 34:533–540, 2012.

[16] Dennis Miller, Eva-Maria Wiener, Angelika Turowski, Christine Thunig, and Heinz Hoffmann. O/w emulsions for cosmetics products stabilized by alkyl phosphates—rheology and storage tests. *Colloids Surf. A*, 152(1-2):155–160, 1999.

[17] Dennis J Miller, Torsten Henning, and Wolfgang Grünbein. Phase inversion of w/o emulsions by adding hydrophilic surfactant—a technique for making cosmetics products. *Colloids Surf. A*, 183:681–688, 2001.

[18] Yanjun Zhao, Stuart A Jones, and Marc B Brown. Dynamic foams in topical drug delivery. *J. Pharm. and Pharmacol.*, 62(6):678–684, 2010.

[19] Solomon Barkley, Eric R Weeks, and Kari Dalnoki-Veress. Snap-off production of monodisperse droplets. *Eur. Phys. J. E*, 38(12):1–4, 2015.

[20] P.N. N Pusey. The effect of polydispersity on the crystallization of hard spherical colloids. *J. Phys-Paris*, 48(5):709–712, 1987.

[21] S Auer and D Frenkel. Suppression of crystal nucleation in polydisperse colloids due to increase of the surface free energy. *Nature*, 413(6857):711–713, 2001.

[22] Selwyn J Rehfeld. Adsorption of sodium dodecyl sulfate at various hydrocarbon-water interfaces. *J. Phys. Chem*, 71(3):738–745, 1967.

[23] W Ramsden. Separation of solids in the surface-layers of solutions and 'suspensions'(observations on surface-membranes, bubbles, emulsions, and mechanical coagulation).—preliminary account. *Proc. R. Soc. Lond.*, 72(477-486):156–164, 1904.

[24] Spencer Umfreville Pickering. Cxcvi.—emulsions. *J. Chem. Soc.*, 91:2001–2021, 1907.

[25] Bernard P Binks and SO Lumsdon. Influence of particle wettability on the type and stability of surfactant-free emulsions. *Langmuir*, 16(23):8622–8631, 2000.

[26] Stephanie Lam, Krassimir P Velikov, and Orlin D Velev. Pickering stabilization of foams and emulsions with particles of biological origin. *Curr. Opin. Colloid Interface Sci.*, 19(5):490–500, 2014.

[27] Thomas G Mason, James N Wilking, Kieche Meleson, Connie B Chang, and Sara M Graves. Nanoemulsions: formation, structure, and physical properties. *J. Phys. Condens. Matter*, 18(41):R635, 2006.

[28] Piotr Garstecki, Michael J Fuerstman, Howard A Stone, and George M Whitesides. Formation of droplets and bubbles in a microfluidic t-junction—scaling and mechanism of break-up. *Lab Chip*, 6(3):437–446, 2006.

[29] Andrew S Utada, Alberto Fernandez-Nieves, Howard A Stone, and David A Weitz. Dripping to jetting transitions in coflowing liquid streams. *Phys. Rev. Lett.*, 99(9):094502, 2007.

[30] Koen van Dijke, Riëlle de Ruiter, Karin Schroën, and Remko Boom. The mechanism of droplet formation in microfluidic edge systems. *Soft Matter*, 6(2):321–330, 2010.

[31] R. A. L Jones. *Soft condensed matter*, volume 6. Oxford University Press, 2002.

[32] Eric R Weeks, John C Crocker, Andrew C Levitt, Andrew Schofield, and David A Weitz. Three-dimensional direct imaging of structural relaxation near the colloidal glass transition. *Science*, 287(5453):627–631, 2000.

[33] VC Martelozzo, Andrew B Schofield, WCK Poon, and PN Pusey. Structural aging of crystals of hard-sphere colloids. *Physical Review E*, 66(2):021408, 2002.

[34] Brent S Murray. Stabilization of bubbles and foams. *Curr. Opin. Colloid Interface Sci.*, 12(4-5):232–241, 2007.

[35] J Bergan, L Pascarella, and L Mekenas. Venous disorders: treatment with sclerosant foam. *J. Cardiovasc. Surg.*, 47(1):9–18, 2006.

[36] Luigi Lazzeri, Maria Grazia Cascone, Serena Danti, Lorenzo Pio Serino, Stefania Moscato, and Nunzia Bernardini. Gelatine/plla sponge-like scaffolds: morphological and biological characterization. *J. Mater. Sci: Mater. Med.*, 18(7):1399–1405, 2007.

[37] W. L. Bragg and W. M. Lomer. A dynamical model of a crystal structure. ii. *Proc. R. Soc. A*, 196(1045):171–181, 1949.

[38] Kai Zhang, Meng Fan, Yanhui Liu, Jan Schroers, Mark D Shattuck, and Corey S O'Hern. Beyond packing of hard spheres: The effects of core softness, non-additivity, intermediate-range repulsion, and many-body interactions on the glass-forming ability of bulk metallic glasses. *J. Chem. Phys.*, 143(18):184502, 2015.

[39] Dmitry V Denisov, Kinga A Lőrincz, Wendelin J Wright, Todd C Hufnagel, Aya Nawano, Xiaojun Gu, Jonathan T Uhl, Karin A Dahmen, and Peter Schall. Universal slip dynamics in metallic glasses and granular matter–linking frictional weakening with inertial effects. *Sci. Rep.*, 7(1):1–8, 2017.

[40] Corey S. O'Hern, Leonardo E. Silbert, Andrea J. Liu, and Sidney R. Nagel. Jamming at zero temperature and zero applied stress: The epitome of disorder. *Phys. Rev. E*, 68(1):011306, jul 2003.

[41] Martin van Hecke. Jamming of soft particles: geometry, mechanics, scaling and isostaticity. *J. Phys.: Condens. Matter*, 22(3):033101, 2009.

[42] Hugo C Hamaker. The london—van der waals attraction between spherical particles. *physica*, 4(10):1058–1072, 1937.

[43] A Vrij. Polymers at interfaces and the interactions in colloidal dispersions. *Pure Appl. Chem.*, 48(4):471–483, 1976.

[44] J Bibette, D Roux, and B Pouligny. Creaming of Emulsions - the Role of Depletion Forces Induced By Surfactant. *J. Phys. II*, 2(3):401–424, 1992.

[45] Sho Asakura and Fumio Oosawa. Interaction between particles suspended in solutions of macromolecules. *J. Polym. Sci.*, 33(126):183–192, 1958.

[46] John C Crocker, Joseph A Matteo, Anthony D Dinsmore, and Arjun G Yodh. Entropic attraction and repulsion in binary colloids probed with a line optical tweezer. *Phys. Rev. Lett.*, 82(21):4352, 1999.

[47] Jacob N Israelachvili. *Intermolecular and surface forces.* Academic press, 2011.

[48] Bruno Andreotti, Yoël Forterre, and Olivier Pouliquen. *Granular media: between fluid and solid.* Cambridge University Press, 2013.

[49] Heinrich M Jaeger, Sidney R Nagel, and Robert P Behringer. Granular solids, liquids, and gases. *Rev. Mod. Phys.*, 68(4):1259, 1996.

[50] Hamzah M Beakawi Al-Hashemi and Omar S Baghabra Al-Amoudi. A review on the angle of repose of granular materials. *Powder Technol.*, 330:397–417, 2018.

[51] Bei-Bing Dai, Jun Yang, and Cui-Ying Zhou. Micromechanical origin of angle of repose in granular materials. *Granul. Matter*, 19(2):24, 2017.

[52] Nicholas A Pohlman, Benjamin L Severson, Julio M Ottino, and Richard M Lueptow. Surface roughness effects in granular matter: Influence on angle of repose and the absence of segregation. *Phys. Rev. E*, 73(3):031304, 2006.

[53] Takahiro Hatano. Power-law friction in closely packed granular materials. *Phys. Rev. E*, 75(6):060301, 2007.

[54] Pierre-Emmanuel Peyneau and Jean-Noël Roux. Frictionless bead packs have macroscopic friction, but no dilatancy. *Phys. Rev. E*, 78(1):011307, 2008.

[55] Carlos P Ortiz, Robert Riehn, and Karen E Daniels. Flow-driven formation of solid-like microsphere heaps. *Soft Matter*, 9(2):543–549, 2013.

[56] Daniel C Shorts and Klebert Feitosa. Experimental measurement of the angle of repose of a pile of soft frictionless grains. *Granul. Matter*, 20(1):2, 2018.

[57] Rémi Lespiat, Sylvie Cohen-Addad, and Reinhard Höhler. Jamming and flow of random-close-packed spherical bubbles: an analogy with granular materials. *Phys. Rev. Lett.*, 106(14):148302, 2011.

[58] P-A Lemieux and Douglas J Durian. From avalanches to fluid flow: A continuous picture of grain dynamics down a heap. *Phys. Rev. Lett.*, 85(20):4273, 2000.

[59] C Cassar, M Nicolas, and O Pouliquen. Submarine granular flows down inclined planes. *Phys. Fluids*, 17(10):103301, 2005.

[60] Pierre-Gilles De Gennes, Françoise Brochard-Wyart, and David Quéré. *Capillarity and wetting phenomena: drops, bubbles, pearls, waves.* Springer Science & Business Media, 2013.

[61] Joshua D McGraw, Nicholas M Jago, and Kari Dalnoki-Veress. Capillary levelling as a probe of thin film polymer rheology. *Soft Matter*, 7(17):7832–7838, 2011.

[62] Matilda Backholm, Michael Benzaquen, Thomas Salez, Elie Raphaël, and Kari Dalnoki-Veress. Capillary levelling of a cylindrical hole in a viscous film. *Soft Matter*, 10(15):2550–2558, 2014.

[63] Mark Ilton, Miles MP Couchman, Cedric Gerbelot, Michael Benzaquen, Paul D Fowler, Howard A Stone, Elie Raphaël, Kari Dalnoki-Veress, and Thomas Salez. Capillary leveling of freestanding liquid nanofilms. *Phys. Rev. Lett.*, 117(16):167801, 2016.

[64] Vincent Bertin, John Niven, Howard A Stone, Thomas Salez, Elie Raphael, and Kari Dalnoki-Veress. Symmetrization of thin freestanding liquid films via a capillary-driven flow. *Phys. Rev. Lett.*, 124(18):184502, 2020.

[65] Antonin Marchand, Joost H Weijs, Jacco H Snoeijer, and Bruno Andreotti. Why is surface tension a force parallel to the interface? *Am. J. Phys.*, 79(10):999–1008, 2011.

[66] Joshua B Bostwick, Michael Shearer, and Karen E Daniels. Elastocapillary deformations on partially-wetting substrates: rival contact-line models. *Soft Matter*, 10(37):7361–7369, 2014.

[67] MER Shanahan. The influence of solid micro-deformation on contact angle equilibrium. *J. Phys. D: Appl. Phys.*, 20(7):945, 1987.

[68] Su Ji Park, Byung Mook Weon, Ji San Lee, Junho Lee, Jinkyung Kim, and Jung Ho Je. Visualization of asymmetric wetting ridges on soft solids with x-ray microscopy. *Nat. Commun.*, 5(1):1–7, 2014.

[69] Bruno Andreotti and Jacco H Snoeijer. Statics and dynamics of soft wetting. *Annu. Rev. Fluid Mech.*, 52:285–308, 2020.

[70] Rafael D Schulman and Kari Dalnoki-Veress. Droplets capped with an elastic film can be round, elliptical, or nearly square. *Phys. Rev. Lett.*, 121(24):248004, 2018.

[71] T.G. Mason, J Bibette, and D.A. Weitz. Yielding and flow of monodisperse emulsions. *J. Colloid. Interface Sci.*, 179(2):439–448, 1996.

[72] Julie Goyon, Annie Colin, G Ovarlez, A Ajdari, and L Bocquet. Spatial cooperativity in soft glassy flows. *Nature*, 454(7200):84–87, 2008.

[73] Daniel Bonn, Morton M Denn, Ludovic Berthier, Thibaut Divoux, and Sébastien Manneville. Yield stress materials in soft condensed matter. *Rev. Mod. Phys.*, 89(3):035005, 2017.

[74] PN Pusey, E Zaccarelli, C Valeriani, E Sanz, Wilson CK Poon, and Michael E Cates. Hard spheres: crystallization and glass formation. *Phil. Trans. R. Soc. A*, 367(1909):4993–5011, 2009.

[75] T.G. Mason, J Bibette, and D.A. Weitz. Elasticity of compressed emulsions. *Phys. Rev. Lett.*, 75(10):2051, 1995.

[76] Cong Cao, Jianshan Liao, Victor Breedveld, and Eric R Weeks. Rheology finds distinct glass and jamming transitions in emulsions. *Soft Matter*, 17(9):2587–2595, 2021.

[77] Corey S O'Hern, Stephen A Langer, Andrea J Liu, and Sidney R Nagel. Random packings of frictionless particles. *Phys. Rev. Lett.*, 88(7):075507, 2002.

[78] Douglas J Durian. Foam mechanics at the bubble scale. *Phys. Rev. Lett.*, 75(26):4780, 1995.

[79] TG Mason, Martin-D Lacasse, Gary S Grest, Dov Levine, J Bibette, and DA Weitz. Osmotic pressure and viscoelastic shear moduli of concentrated emulsions. *Phys. Rev. E*, 56(3):3150, 1997.

[80] Andrea J Liu and Sidney R Nagel. Jamming is not just cool any more. *Nature*, 396(6706):21–22, 1998.

[81] Veronique Trappe, V Prasad, Luca Cipelletti, PN Segre, and David A Weitz. Jamming phase diagram for attractive particles. *Nature*, 411(6839):772–775, 2001.

[82] Romain Mari, Florent Krzakala, and Jorge Kurchan. Jamming versus glass transitions. *Phys. Rev. Lett.*, 103(2):1–4, 2009.

[83] José Paredes, Matthias AJ Michels, and Daniel Bonn. Rheology across the zero-temperature jamming transition. *Phys. Rev. Lett.*, 111(1):015701, 2013.

[84] M Dinkgreve, MAJ Michels, TG Mason, and D Bonn. Crossover between athermal jamming and the thermal glass transition of suspensions. *Phys. Rev. Lett.*, 121(22):228001, 2018.

[85] Eugene Cook Bingham. *Fluidity and plasticity*, volume 2. McGraw-Hill, 1922.

[86] Winslow H Herschel and Ronald Bulkley. Konsistenzmessungen von gummibenzollösungen. *Kolloid Z.*, 39(4):291–300, 1926.

[87] Georgios Petekidis, Dimitris Vlassopoulos, and Peter N Pusey. Yielding and flow of colloidal glasses. *Faraday discuss.*, 123:287–302, 2003.

[88] C-h Liu, Sydney R Nagel, DA Schecter, SN Coppersmith, Satya Majumdar, Onuttom Narayan, and TA Witten. Force fluctuations in bead packs. *Science*, 269(5223):513–515, 1995.

[89] Corey S O'Hern, Stephen A Langer, Andrea J Liu, and Sidney R Nagel. Force distributions near jamming and glass transitions. *Phys. Rev. Lett.*, 86(1):111, 2001.

[90] Leonardo E Silbert, Gary S Grest, and James W Landry. Statistics of the contact network in frictional and frictionless granular packings. *Phys. Rev. E*, 66(6):061303, 2002.

[91] Srdjan Ostojic, Ellák Somfai, and Bernard Nienhuis. Scale invariance and universality of force networks in static granular matter. *Nature*, 439(7078):828–830, 2006.

[92] H.M. Princen. Rheology of foams and highly concentrated emulsions: I. elastic properties and yield stress of a cylindrical model system. *J. Colloid. Interface Sci.*, 91(1):160–175, 1983.

[93] Jasna Brujić, Sam F Edwards, Dmitri V Grinev, Ian Hopkinson, Djordje Brujić, and Hernán A. Makse. 3D bulk measurements of the force distribution in a compressed emulsion system. *Faraday Discuss.*, 123(3):207–220, jan 2003.

[94] Junfei Geng, G Reydellet, E Clément, and RP Behringer. Green's function measurements of force transmission in 2d granular materials. *Physica D*, 182(3-4):274–303, 2003.

[95] Trushant S Majmudar and Robert P Behringer. Contact force measurements and stress-induced anisotropy in granular materials. *Nature*, 435(7045):1079–1082, 2005.

[96] Karen E Daniels, Jonathan E Kollmer, and James G Puckett. Photoelastic force measurements in granular materials. *Rev. Sci. Instrum.*, 88(5):051808, 2017.

[97] Daniel L Blair, Nathan W Mueggenburg, Adam H Marshall, Heinrich M Jaeger, and Sidney R Nagel. Force distributions in three-dimensional granular assemblies: Effects of packing order and interparticle friction. *Phys. Rev. E*, 63(4):041304, 2001.

[98] Eric I Corwin, Heinrich M Jaeger, and Sidney R Nagel. Structural signature of jamming in granular media. *Nature*, 435(7045):1075–1078, 2005.

[99] Adam Ross Abate and DJ Durian. Topological persistence and dynamical heterogeneities near jamming. *Phys. Rev. E*, 76(2):021306, 2007.

[100] AD Gopal and Douglas J Durian. Nonlinear bubble dynamics in a slowly driven foam. *Phys. Rev. Lett.*, 75(13):2610, 1995.

[101] Willem K Kegel and Alfons van Blaaderen. Direct observation of dynamical heterogeneities in colloidal hard-sphere suspensions. *Science*, 287(5451):290–293, 2000.

[102] Xin Cao, Huijun Zhang, and Yilong Han. Release of free-volume bubbles by cooperative-rearrangement regions during the deposition growth of a colloidal glass. *Nat. Commun.*, 8(1):362, 2017.

[103] G Marty and Olivier Dauchot. Subdiffusion and cage effect in a sheared granular material. *Phys. Rev. Lett.*, 94(1):015701, 2005.

[104] Eric R Weeks and DA Weitz. Properties of cage rearrangements observed near the colloidal glass transition. *Phys. Rev. Lett.*, 89(9):095704, 2002.

[105] Luca Cipelletti and Laurence Ramos. Slow dynamics in glassy soft matter. *J. Phys. Condens. Matter*, 17(6):R253, 2005.

[106] Rachel E Courtland and Eric R Weeks. Direct visualization of ageing in colloidal glasses. *J. Phys. Condens. Matter*, 15(1):S359, 2002.

[107] W Van Megen, TC Mortensen, SR Williams, and J Müller. Measurement of the self-intermediate scattering function of suspensions of hard spherical particles near the glass transition. *Phys. Rev. E*, 58(5):6073, 1998.

[108] Nikoleta B Simeonova and Willem K Kegel. Gravity-induced aging in glasses of colloidal hard spheres. *Phys. Rev. Lett.*, 93(3):035701, 2004.

[109] Matthew C Jenkins and Stefan U Egelhaaf. Confocal microscopy of colloidal particles: towards reliable, optimum coordinates. *Adv. Colloid Interface Sci.*, 136(1-2):65–92, 2008.

[110] Morgane Houssais, Carlos P Ortiz, Douglas J Durian, and Douglas J Jerolmack. Rheology of sediment transported by a laminar flow. *Phys. Rev. E*, 94(6):062609, 2016.

[111] Nicholas W Hayman, Lucie Ducloué, Kate L Foco, and Karen E Daniels. Granular controls on periodicity of stick-slip events: kinematics and force-chains in an experimental fault. *Pure Appl. Geophys.*, 168(12):2239–2257, 2011.

[112] James P Sethna, Karin A Dahmen, and Christopher R Myers. Crackling noise. *Nature*, 410(6825):242–250, 2001.

[113] Jonathan T Uhl, Shivesh Pathak, Danijel Schorlemmer, Xin Liu, Ryan Swindeman, Braden AW Brinkman, Michael LeBlanc, Georgios Tsekenis, Nir Friedman, Robert Behringer, et al. Universal quake statistics: From compressed nanocrystals to earthquakes. *Sci. Rep.*, 5(16493):1–10, 2015.

[114] Roberto Benzi, Pinaki Kumar, Federico Toschi, and Jeannot Trampert. Earthquake statistics and plastic events in soft-glassy materials. *Geophys. J. Int.*, 207(3):1667–1674, 2016.

[115] Pinaki Kumar, Evangelos Korkolis, Roberto Benzi, Dmitry Denisov, André Niemeijer, Peter Schall, Federico Toschi, and Jeannot Trampert. On interevent time distributions of avalanche dynamics. *Sci. Rep.*, 10(1):1–11, 2020.

[116] Takashi Hayashi and Richard W Carthew. Surface mechanics mediate pattern formation in the developing retina. *Nature*, 431(7009):647–652, 2004.

[117] Oliver Lieleg, Jürgen Kayser, Gianfranco Brambilla, Luca Cipelletti, and Alexandra R Bausch. Slow dynamics and internal stress relaxation in bundled cytoskeletal networks. *Nat. Mater.*, 10(3):236–242, 2011.

[118] Karine Guevorkian, Marie-Josée Colbert, Mélanie Durth, Sylvie Dufour, and Françoise Brochard-Wyart. Aspiration of biological viscoelastic drops. *Phys. Rev. Lett.*, 104(21):218101, 2010.

[119] Duke Duguay, Ramsey A Foty, and Malcolm S Steinberg. Cadherin-mediated cell adhesion and tissue segregation: qualitative and quantitative determinants. *Dev. Biol.*, 253(2):309–323, 2003.

[120] Ramsey A Foty and Malcolm S Steinberg. Cadherin-mediated cell-cell adhesion and tissue segregation in relation to malignancy. *Int. J. Dev. Biol.*, 48(5-6):397–409, 2004.

[121] Michael Rubinstein, Ralph H Colby, et al. *Polymer physics*, volume 23. Oxford university press New York, 2003.

[122] Thomas Salez, Justin Salez, Kari Dalnoki-Veress, Elie Raphaël, and James A Forrest. Cooperative strings and glassy interfaces. *Proc. Natl. Acad. Sci. U.S.A*, 112(27):8227–8231, 2015.

[123] Louise Marshall and Charles F Zukoski. Experimental studies on the rheology of hard-sphere suspensions near the glass transition. *J. Phys. Chem.*, 94(3):1164–1171, 1990.

[124] Stephen A Langer and AJ Liu. Sheared foam as a supercooled liquid? *Europhys. Lett.*, 49(1):68, 2000.

[125] Claudio Donati, Jack F Douglas, Walter Kob, Steven J Plimpton, Peter H Poole, and Sharon C Glotzer. Stringlike cooperative motion in a supercooled liquid. *Phys. Rev. Lett.*, 80(11):2338, 1998.

[126] Ranko Richert. Heterogeneous dynamics in liquids: fluctuations in space and time. *J. Phys. Condens. Matter*, 14(23):R703, 2002.

[127] Jacob D Stevenson, Jörg Schmalian, and Peter G Wolynes. The shapes of cooperatively rearranging regions in glass-forming liquids. *Nat. Phys.*, 2(4):268–274, 2006.

[128] Smarajit Karmakar, Chandan Dasgupta, and Srikanth Sastry. Growing length and time scales in glass-forming liquids. *Proc. Natl. Acad. Sci. U.S.A*, 106(10):3675–3679, 2009.

[129] S Kawana and RAL Jones. Effect of physical ageing in thin glassy polymer films. *Eur. Phys. J. E*, 10(3):223–230, 2003.

[130] Daniel M Mueth, Heinrich M Jaeger, and Sidney R Nagel. Force distribution in a granular medium. *Phys. Rev. E.*, 57(3):3164, 1998.

[131] A. W. Philips. *Amorphous Solids: Low-Temperature Properties*. Springer, 1981.

[132] Carl P Goodrich, Andrea J Liu, and Sidney R Nagel. Solids between the mechanical extremes of order and disorder. *Nat. Phys.*, 10(July):1–4, 2014.

[133] Hua Tong, Peng Tan, and Ning Xu. From Crystals to Disordered Crystals: A Hidden Order-Disorder Transition. *Sci. Rep.*, pages 1–8, 2015.

[134] Jeetu S Babu, Chandana Mondal, Surajit Sengupta, and Smarajit Karmakar. Excess vibrational density of states and the brittle to ductile transition in crystalline and amorphous solids. *Soft Matter*, 12(4):1210–1218, 2016.

[135] Huijun Zhang and Yilong Han. Compression-induced polycrystal-glass transition in binary crystals. *Phys. Rev. X*, 8(4):041023, 2018.

[136] Patrick Charbonneau, Eric I Corwin, Lin Fu, Georgios Tsekenis, and Michael van Der Naald. Glassy, gardner-like phenomenology in minimally polydisperse crystalline systems. *Phys. Rev. E*, 99(2):020901, 2019.

[137] Peter J. Yunker, Zexin Zhang, and A. G. Yodh. Observation of the disorder-induced crystal-to-glass transition. *Phys. Rev. Lett.*, 104(1):2–5, 2010.

[138] Ruben Higler, Jeroen Appel, and Joris Sprakel. Substitutional impurity-induced vitrification in microgel crystals. *Soft Matter*, 9:5372–5379, 2013.

[139] Peter J Yunker, Ke Chen, Matthew D Gratale, Matthew A Lohr, Tim Still, and A G Yodh. Physics in ordered and disordered colloidal matter composed of poly(N-isopropylacrylamide) microgel particles. *Rep. Prog. Phys.*, 77(5):056601, 2014.

[140] M Hanifpour, N Francois, S M Vaez Allaei, T Senden, and M Saadatfar. Mechanical Characterization of Partially Crystallized Sphere Packings. *Phys. Rev. Lett.*, 113(October):1–5, 2014.

[141] Nathan C. Keim and Paulo E. Arratia. Role of disorder in finite-amplitude shear of a 2D jammed material. *Soft Matter*, 11(8):1539–1546, 2015.

[142] Ya Gai, Chia Min Leong, Wei Cai, and Sindy K Y Tang. Spatiotemporal periodicity of dislocation dynamics in a two-dimensional microfluidic crystal flowing in a tapered channel. *Proc. Natl. Acad. Sci. U.S.A.*, 113(43):12082–12087, 2016.

[143] Iaroslava Golovkova, Lorraine Montel, Elie Wandersman, Thibault Bertrand, Alexis Michel Prevost, and Lea-Laetitia Pontani. Depletion attraction impairs the plasticity of emulsions flowing in a constriction. *Soft Matter*, 16(13):3294–3302, 2020.

[144] M Emilia Rosa and MA Fortes. Nucleation and glide of dislocations in a monodisperse two-dimensional foam under uniaxial deformation. *Philos. Mag. A*, 77(6):1423–1446, 1998.

[145] Andrew Gouldstone, Krystyn J Van Vliet, and Subra Suresh. Simulation of defect nucleation in a crystal. *Nature*, 411(6838):656–656, 2001.

[146] Charles Kittel et al. *Introduction to solid state physics*, volume 8. Wiley New York, 1976.

[147] Xiang Cheng, German Varas, Daniel Citron, Heinrich M Jaeger, and Sidney R Nagel. Collective behavior in a granular jet: Emergence of a liquid with zero surface tension. *Phys. Rev. Lett.*, 99(18):188001, 2007.

[148] Xiang Cheng, Lei Xu, Aaron Patterson, Heinrich M Jaeger, and Sidney R Nagel. Towards the zero-surface-tension limit in granular fingering instability. *Nature Physics*, 4(3):234–237, 2008.

[149] L Mandelstam. Über die rauhigkeit freier flüssigkeitsoberflächen. *Ann. Phys.*, 41(8):609, 1913.

[150] John Shipley Rowlinson and Benjamin Widom. *Molecular theory of capillarity*. Dover, New York, 2002.

[151] Dirk G.A.L. Aarts, Matthias Schmidt, and Henk N.W. Lekkerkerker. Direct visual observation of thermal capillary waves. *Science*, 304(5672):847–850, 2004.

[152] A Vrij. Demixed phases of colloid plus polymer systems in a common solvent calculation of the interfacial tension. *Physica A*, 235(1-2):120–128, 1997.

[153] Els HA de Hoog and Henk NW Lekkerkerker. Measurement of the interfacial tension of a phase-separated colloid- polymer suspension. *The Journal J. Phys. Chem B*, 103(25):5274–5279, 1999.

[154] Yacine Amarouchene, Jean-François Boudet, and Hamid Kellay. Capillary-like fluctuations at the interface of falling granular jets. *Phys. Rev lett.*, 100(21):218001, 2008.

[155] Li-Hua Luu, Gustavo Castillo, Nicolás Mujica, and Rodrigo Soto. Capillarylike fluctuations of a solid-liquid interface in a noncohesive granular system. *Phys. Rev. E*, 87(4):040202, 2013.

[156] Matthias E Möbius. Clustering instability in a freely falling granular jet. *Phys. Rev. E*, 74(5):051304, 2006.

[157] John R Royer, Daniel J Evans, Loreto Oyarte, Qiti Guo, Eliot Kapit, Matthias E Möbius, Scott R Waitukaitis, and Heinrich M Jaeger. High-speed tracking of rupture and clustering in freely falling granular streams. *Nature*, 459(7250):1110–1113, 2009.

[158] Adam Wysocki, C Patrick Royall, Roland G Winkler, Gerhard Gompper, Hajime Tanaka, Alfons van Blaaderen, and Hartmut Löwen. Direct observation of hydrodynamic instabilities in a driven non-uniform colloidal dispersion. *Soft Matter*, 5(7):1340–1344, 2009.

[159] Camilla Völtz, Werner Pesch, and Ingo Rehberg. Rayleigh-taylor instability in a sedimenting suspension. *Phys. Rev. E*, 65(1):011404, 2001.

[160] Jan Ludvig Vinningland, Øistein Johnsen, Eirik G Flekkøy, Renaud Toussaint, and Knut Jørgen Måløy. Granular rayleigh-taylor instability: Experiments and simulations. *Phys. Rev. Lett.*, 99(4):048001, 2007.

[161] Jacques Duran. Rayleigh-taylor instabilities in thin films of tapped powder. *Phys. Rev. Lett.*, 87(25):254301, 2001.

[162] Matilda Backholm and Oliver Bäumchen. Micropipette force sensors for in vivo force measurements on single cells and multicellular microorganisms. *Nat. Protoc.*, 14(2):594–615, 2019.

[163] O Mondain-Monval, F Leal-Calderon, J Phillip, and J Bibette. Depletion forces in the presence of electrostatic double layer repulsion. *Phys. Rev. Lett.*, 75(18):3364, 1995.

[164] RM Pashley and BW Ninham. Double-layer forces in ionic micellar solutions. *J. Phys. Chem.*, 91(11):2902–2904, 1987.

[165] Solomon Barkley, Samantha J. Scarfe, Eric R. Weeks, and Kari Dalnoki-Veress. Predicting the size of droplets produced through Laplace pressure induced snap-off. *Soft Matter*, 12(35):7398–7404, 2016.

[166] M-J Colbert, A.N. Raegen, C Fradin, and K Dalnoki-Veress. Adhesion and membrane tension of single vesicles and living cells using a micropipette-based technique. *Eur. Phys. J. E*, 30(2):117–121, 2009.

[167] Matilda Backholm, William S Ryu, and Kari Dalnoki-Veress. Viscoelastic properties of the nematode caenorhabditis elegans, a self-similar, shear-thinning worm. *Proc. Natl. Acad. Sci. U.S.A*, 110(12):4528–4533, 2013.

[168] Rafael D Schulman, Matilda Backholm, William S Ryu, and Kari Dalnoki-Veress. Dynamic force patterns of an undulatory microswimmer. *Phys. Rev. E*, 89(5):050701, 2014.